J. Hydrol. Hydromech., 67, 2019, 4, 297–304
DOI: 10.2478/johh-2019-0018

The dominant runoff processes on grassland versus bare soil hillslopes in a temperate environment - An experimental study

Gabriel Minea[1, 2*], Gabriela Ioana-Toroimac[3], Gabriela Moroşanu[3, 4, 5]

[1] Research Institute of the University of Bucharest, University of Bucharest, 36-46 Bd. M. Kogălniceanu, Sector 5, 050107, Bucharest, Romania.
[2] National Institute of Hydrology and Water Management, 97 E Bucureşti - Ploieşti Road, Sector 1, 013686, Bucharest, Romania.
[3] Faculty of Geography, University of Bucharest, 1 Nicolae Bălcescu Avenue, Sector 1, 010041, Bucharest, Romania.
[4] Institute of Environmental Sciences, University of Grenoble Alpes, CS 40700, 38058 Grenoble Cedex 9, France.
[5] Institute of Geography, Romanian Academy, 12 Dimitrie Racoviță, Sector 2, 023994, Bucharest, Romania.
[*] Corresponding author. Tel.: +40213181115. Fax: +40213181116. E-mail: gabriel.minea@hidro.ro

Abstract: This paper aimed to investigate the dominant runoff processes (DRP's) at plot-scale in the Curvature Subcarpathians under natural rainfall conditions characteristic for Romania's temperate environment.

The study was based on 32 selected rainfall-runoff events produced during the interval April–September (2014–2017). By comparing water balance on the analyzed Luvisol plots for two types of land use (grassland vs. bare soil), we showed that DRP's are mostly formed by Hortonian Overland Flow (HOF), 47% vs. 59% respectively. On grassland, HOF is followed by Deep Percolation (DP, 31%) and Fast Subsurface Flow (SSF, 22%), whereas, on bare soil, DP shows a higher percentage (38%) and SSF a lower one (3%), which suggests that the soil-root interface controls the runoff generation.

Concerning the relationship between antecedent precipitation and runoff, the study indicated the nonlinearity of the two processes, more obvious on grassland and in drought conditions than on bare soil and in wet conditions (as demonstrated by the higher runoff coefficients). Moreover, the HOF appeared to respond differently to rainfall events on the two plots - slightly longer lag-time, lower discharge and lower volume on grassland - which suggests the hydrologic key role of vegetation in runoff generation processes.

Keywords: Dominant runoff processes; Grassland; Soil water balance plot; Rainfall-runoff event.

INTRODUCTION

The conversion of precipitation into runoff on hillslopes represents dynamic processes, highly variable in space and time (Weyman, 1973; Bachmair and Weiler, 2012; Rodrigo-Comino et al. 2019). The hydrological relevance of understanding hillslope runoff processes lies in the practical necessity to predict river discharge in ungauged basins.

The determination of dominant runoff processes (DRP's) is an important approach in investigating and analyzing soil-hydrological parameters in detail, with respect to hydrological predictions in ungauged basins, water conservation management, flood and erosion hazards prevention (Müller et al., 2009; Hümann and Müller, 2013; Rodrigo-Comino et al. 2017; Ferreira et al., 2018).

Several methods have been developed to determine the DRP's and characterize the spatial extent and distribution of areas where a specific runoff process occurs. Naef et al. (2002) have defined DRP on a site as being the process that mostly contributes to the runoff for a given rainfall event. In recent decades, a large number of intensive plot-scale experiments have been conducted in the field to identify DRP's (e.g., Scherrer et al., 2007; Müller et al., 2009; Jost et al., 2012).

The DRP's literature includes two approaches: (i) manual field investigation; (ii) automatic GIS-based, also called GIS-DRP. Hümann and Müller (2013) considered that the *field investigations* approach is the best way to analyze dominant runoff processes and Antonetti et al. (2016) added that it is reliable but time-consuming. To foster investigations on runoff formation, Schmocker-Fackel et al. (2007) conducted sprinkling experiments at plot scale in Switzerland, while Antonetti et al. (2016) performed measurements of soil profile properties in Germany, on grassland hillslopes with varying slopes, geology, and soils. On the basis of the above-mentioned approaches, a number of studies have been carried out to obtain a decision scheme and a spatial distribution (mapping) of DRP's on grassland sites. Significant results from Scherrer and Naef (2003) have shown that, by studying the four main processes in a catchment, they were able to separate their different effects on floods in terms of location and spatial extent of the DRP's. Also, the authors proposed a decision tree to define the dominant hydrological flow processes on a variety of grassland sites in Switzerland. Likewise, Scherrer et al. (2007) concluded from the sprinkling experiments on several grassland plots in Switzerland that overland flow was dominant in most of the studied runoff events followed by subsurface flow at a few sites. Schmocker-Fackel et al. (2007) designed an experiment to determine the potential of each grassland plot to produce a given runoff process. However, the experiment failed to establish the hydrological connectivity occurring between them. Antonetti et al. (2016) tested the suitability of different automatic DRP's mapping approaches for mapping ungauged catchments and quantified the uncertainties of hydrological simulations due to different spatial representations of DRP.

In Romania, regarding the hydrological influence of vegetation on runoff generation, few field investigations at microscale were initiated within the Curvature Subcarpathians (e.g., Stanciu and Zlate-Podani, 1987; Minea et al., 2018), and different results on runoff processes such as runoff coefficients, overland flow volume, and discharge or infiltration rates were found. These hydrologic experimental studies on hillslopes were marked by the pioneering work of Blidaru (1965).

Bereitgestellt von University Library Bratislava | Heruntergeladen 31.01.20 12:21 UTC

While the Romanian literature has shown valuable information on the role of land use on the overland flow occurrence (e.g., Stanciu and Zlate-Podani, 1987; Miţă and Mătreaţă, 2016), other runoff pathways (e.g., subsurface flow and deep percolation) have remained little explored. The data on DRP's on hillslopes are nearly unknown in the Romanian literature.

Therefore, this work is based on the following hypothesis: (i) dominant runoff processes on Romanian hillslopes reflect the complex relationship between rainfall and runoff; (ii) a relationship between rainfall and runoff exists for the grassland and can be used to predict water flow pathways. In the present study, we used field data to identify DRP's at plot-scale. The objectives of this paper are to: (i) identify the dominant runoff processes at plot and event scales, and (ii) examine how grassland influences the peak discharge and lag-time of water flow pathways, in the typical case of the Voineşti Experimental Basin, Romania.

MATERIAL AND METHODS

Site description

The study area is located in the Curvature Subcarpathians (hilly region), dominated by Dacian sedimentary rocks (e.g., sands and clays and sandstones with marnes), about 110 km northwest of Bucharest, on the left side of Dâmboviţa River (Figure 1). The experimental site (45°05'07.27" N and 25°15'15.43" E) of Voineşti Experimental Basin – VEB is operated and maintained by the National Institute of Hydrology and Water Management. The experimental basin is situated in grassland at an elevation of 500 m a.s.l., in an area highly exposed to erosion (Zaharia and Ioana-Toroimac, 2009). The underneath soil is classified as Luvisol (Florea et al., 1971; Florea and Munteanu, 2012), and it is composed of 51% sand, 21% silt, and 28% clay. Luvisols have a well-developed Ao-Ea-Bt-C profile with a sandy clay loam texture (USDA-NRCS, 1999). The parental material is represented by clays (Maftei et al., 2002). According to the Köppen System for climate classification, the Curvature Subcarpathians are described by "Dfb" subtype or temperate humid continental climate (Peel et al., 2007).

Average annual precipitation and air temperature are 822 mm and 9.8°C (1980–2017), with the highest monthly average temperature of 20.2°C in July, and the lowest average of –0.6°C in January (Figure 2). Most rainfall events (64%) occur during the vegetation season (April–September 1967–2017: average precipitation depth = 510 mm, standard deviation SD 142 mm), and the highest number of rainfalls was recorded in June (13.1%) and July (12.6%). June is the wettest month receiving an average of 103.7 mm (SD ±46 mm), while February is the driest month, recording only 40 mm (SD ±28.5 mm) of precipitation.

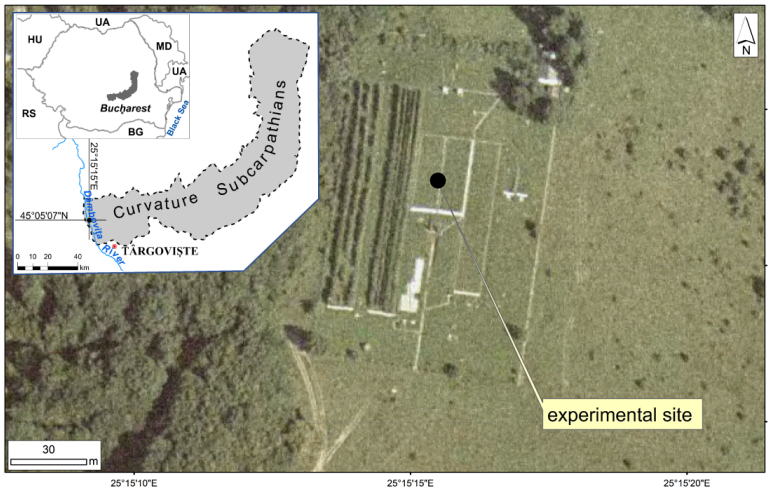

Fig. 1. Location of the study site in the Romania and Curvature Subcarpathians with the point of the experimental site - Voineşti Experimental Basin.

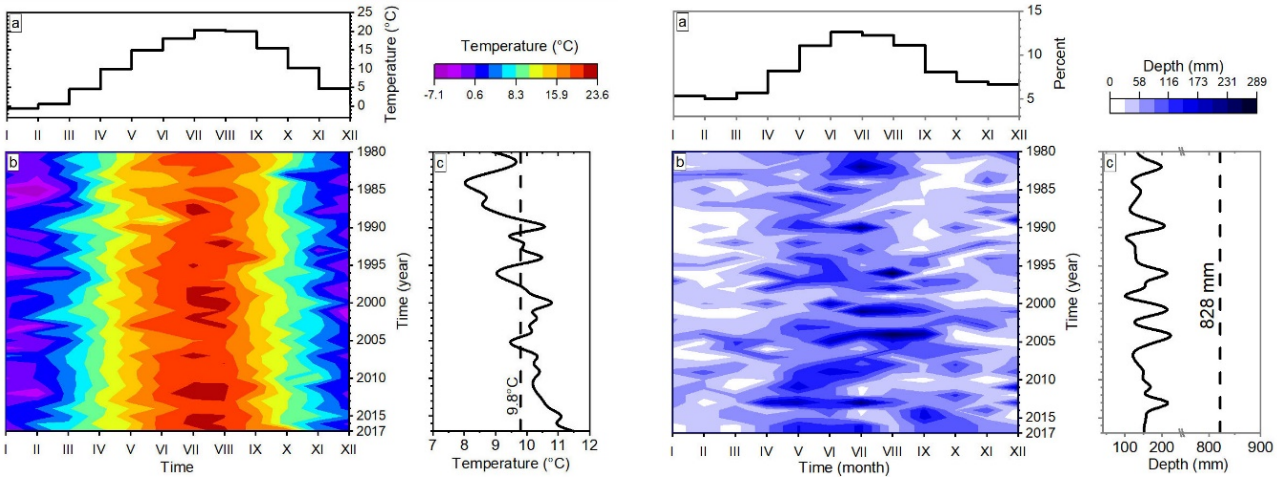

Fig. 2. Temporal distribution of mean air temperature (monthly - a, daily - b, annual - c) on the left; and daily precipitation (monthly average - a, daily amounts - b, and the highest monthly amounts - c) on the right; dashed line represents the multiannual average value. Period: 1980–2017, location: Voineşti Experimental Basin.

Bereitgestellt von University Library Bratislava | Heruntergeladen 31.01.20 12:21 UTC

Methods

In order to answer our research questions, measurements of rainfall, overland flow, subsurface flow, and base flow were made during the period April to September 2014–2017. The measurements had a temporal resolution of 1 minute (2016–2017) or 10 minutes (2014–2015).

Runoff - soil water balance plots cover an area of 300 sq m (length = 30 m and width = 10 m), N-S aspect with a 13% planar slope and 500 m a.s.l. The land use of the soil water balance plots falls in the following categories:

(i) grasslands – corresponding to secondary perennial grass (Figure 1); this plot was never grazed, but herbage was cut in June, according to traditional practices in the region; the average height of grass species surrounding the plot was about 40 cm and an abundant superficial network of grass roots dominated in the top ~ 20 cm of the soil (see Minea et al., 2018);

(ii) bare soil or *"working soil"* – the plot was spaded annually in March; the spading created microdepressions (depth of less than 20 cm) and enabled infiltration of rainfall and water retention in the eroded soil; regular application of the herbicide treatments may sometimes lead to the formation of a soil crust covering the plot.

The soil water balance plots were bordered by an impervious (concrete) wall. A number of ditches, drainage and conveyance underground pipes (subsurface and base flow/deep percolation), and, at their lower part, shelters containing calibration water tanks with drainage installation for evacuated water were used. The concrete walls were dug in at a depth of 1.50 m and raised above ground by 0.20 m. The concrete ditches were covered by metal caps to avoid the rain falling directly into these. The overland flow (*HOF*) across the soil water balance plots was collected by one concrete cutslope ditch, situated at the outlet of the plot, a few centimeters below the surface. Subsurface flow (*SSF*) was represented by water collected at the depth of 0.4 m (below the effective root zone and at sandy clay Bt horizon) and deep percolation/base flow (*DP*) was collected at the depth of 1.3 m in the soil (Blidaru, 1965).

Six calibration metal measuring tanks were installed in a shelter below the plots: (i) 2 big tanks (0.380 m^3) with 45° V-notch sharp-crested weir after volumetric retention level (Q_{max} = 10 l/sec with a head of 20 cm) for the overland flow measurement; (ii) smaller tanks with the capacity of 0.120 m^3 capacity for measurement of the *SSF* and *DP*. Each tank contained a device (OTT float-cable counterweight followed by 2016 Nivotrack probes) for the continuous detection of the water level with a resolution of 0.001 m.

The rain gauge devices were located at the height of 1.5 m above the ground, between the two plots, and included a pluviometer (stage non-recording) and a pluviograph used to continuously record rainfall.

Supplementary data about the setup and handling of the runoff devices and rain gauges were given by Minea and Moroşanu (2016) and Minea et al. (2016; 2018).

Data calculation and analysis

The first step in the analysis was to convert continuous water level measurements (overland flow, subsurface flow, and base flow/deep percolation) into flow rate by a volumetric method $V = f(H)$ and rating curve $Q = f(H)$. Then, the flow data obtained (e.g., volumes, discharges) were compared.

Considering the rainfall-runoff analysis, we only used rainfall events defined by precipitation ≥ 0.2 mm. The rainfall events were considered finished when there was no precipitation during the following 1 hour. Event duration, rainfall depth and intensity (average and maximum) were determined for each event. We analyzed data from period 2014–2017. In 2014, only the data from April were used due to technical difficulties in the rest of the year.

In order to assess the influence of antecedent conditions (e.g., soil moisture) within a plot before a runoff event, the Antecedent Precipitation Index (API) (Kohler and Linsley, 1951; Rodríguez-Caballero et al., 2014) was calculated as a weighted sum of the total rainfall during three days preceding an event (API_3):

$$API_3 = \sum_{t=-1}^{-i} P_t \, k^{-t}$$

where API_3 is the antecedent precipitation index on day t, k is an empirical decay parameter (0.9 in this study), P_t is the total rainfall for the day t, and i = 3; k was fixed to 0.9, based on previous studies (Miţă and Mătreaţă, 2016).

For the specific runoff response, different flow processes and DRP's were determined for the rainfall-runoff events following the approach and terminology used by Scherrer et al. (2007). Water flow pathways during an event were denoted as the "Hortonian Overland Flow" (*HOF*), "Fast Subsurface Flow" (*SSF*) or interflow, and "Deep Percolation" (*DP*) or base flow. The process that mostly contributed to total runoff was assumed to be the "dominant" one (Schmocker-Fackel et al., 2007). Several additional runoff characteristics were determined for each event (rainfall and runoff durations, depths and volumes, and runoff coefficients – *RC's*).

The land use influence during the rainfall-runoff events was analyzed using the peak discharge and volume response to the rainfall, and the lag-time between the maximum rainfall and the peak flow (*HOF, SSF*, and *DP*).

Descriptive statistics (frequency distribution; relationships between rainfall and runoff characteristics) have also been employed. The relations between the rainfall and runoff characteristics were studied by using the coefficient of determination/regression (r^2).

RESULTS

Characteristics of rainfall events

Runoff process mainly depends on the rainfall event characteristics, in particular on rainfall intensity (Woolhiser and Goodrich, 1988; Bronstert and Bárdossy, 2003). The characteristics of natural rainfall events (duration, average, and maximum rainfall intensity) from April–September 2015–2017, are given in Table 1. More precisely, 297 rainfall events were measured (e.g., 94 events in 2015; 101 in 2016, and 102 in 2017). In April 2014, 37 rainfall events were recorded. Those of 18/4/2014 (32.2 mm; I_{max} = 6 mm/h) and 19/4/2014 (22.8 mm; I_{max} = 6 mm/h) produced runoff. As a rule, in April, the rainfall events were characterized by small depths and low intensities. Following periods with no precipitation, most of the rainfall events from this month did not produce runoff or significant runoff events, but have contributed to restoring the soil moisture storage.

The most important pluviometric feature of the rainfall events was represented by the small rainfall depth (see Table 1). Thus, in warm/growing period of April–September 2015 around 8 cases of rainfall events with rainfall depth over *P90* (90th percentile) were registered, 4 of which being even over

Bereitgestellt von University Library Bratislava | Heruntergeladen 31.01.20 12:21 UTC

P95; in 2016 a greater number of small rainfalls was registered (*P90* = 9.70 mm, 11 events; *P95* = 16.1 mm, 2 events); whereas in 2017, the number of the rainfalls with total rainfall depth exceeding *P90* (14.96 mm) was bigger (*P90* = 14.96 mm, 11 events in total, 6 of which exceeded *P95*).

The intensity of rainfall events, especially those with the highest peak values, was generally characterized by low values in the warm/growing period of April–September 2015 and somewhat higher in 2016 and 2017. In the warm/growing period of April–September 2016, 10 rainfalls with a maximum intensity ≥ *P90* were registered (24.6 mm/h), 5 of which were higher than *P95* (28.2 mm/h), and in 2017 there were 11 rainfalls with maximum intensity ≥ *P90* (33.2 mm/h), 7 of which from June – July being superior to *P95* (45.6 mm/h).

Several rainfall events were remarkable in terms of quantity (depth and maximum intensities). The events with hydrological impact corresponded to those characterized by a high rainfall intensity (see Figure 3a).

Dominant runoff processes at plot scale

Figure 3 gives an overview of the runoff response observed during the experiments performed under natural rainfall. The 32 rainfall-runoff events were produced by very different rainfall amounts (4.40 – 51.9 mm; SD = ± 12.2 mm) at wetness state characterized by API_3 (0 – 65.5 mm amounts). Very variable rainfall amounts and wetness states led to high differences in runoff characteristics (e.g., volume and runoff coefficients). As expected, infiltration processes on the hillslope, given the two land use categories, played an important role, especially in dry conditions ($API_3 \leq 10$ mm).

Moreover, the runoff rates and response times were affected by API_3 values. The results show that *RC's* of 32 selected events were low, despite the occurrence of heavy rainfall events and potentially erosive rains (Figure 3). The major part of the total runoff is produced by *HOF*. Cumulative runoff depth values on grassland plot are low, which indicates the role of the grass retention and the water consumption affected by the plants, associated with drier soil moisture conditions compared to the bare soil. However, cumulative runoff depths from grassland plot in a few cases showed high values of up to 25.4 mm (3/7/2017), if topsoil saturation occurred. Vertical flow dynamics indicated *HOF* as the fastest runoff generation mechanism delivering the greatest volumes of water (maximum value observed on 3/7/2017, 15.9 mm or 4791 l), followed by *DP* (3108 l or 10.3 mm on 19/4/2014).

The bare soil cumulative runoff depth plot depicted considerable runoff value, mainly based on *HOF* (24.3 mm on 20/9/2016), followed by *DP* (e.g., 3/7/2017 event) and significantly by *SSF* (e.g., 1.14 mm on 20/9/2016 event). *HOF* was the dominant runoff generation process on the bare soil plot,

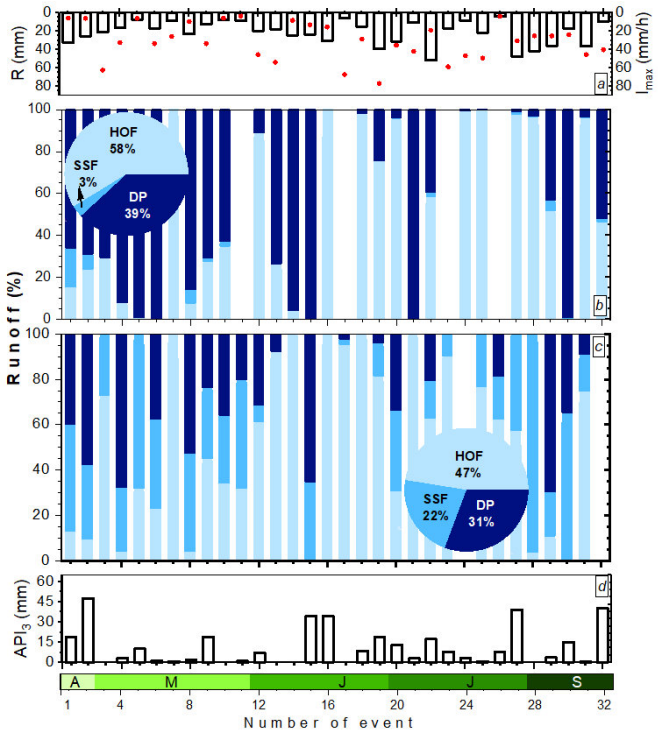

Fig. 3. Rainfall and runoff plot characteristics for 32 events sorted by months (April to September); a) - rainfall depth (*R*) and red dots represent maximum intensities of rainfall events, I_{max} (mm/h); runoff and its components (*HOF, SSF, DP*) from the runoff plots with the bare soil b) and grass c); the blank stacked column means that no flow occurred; d) - API_3.

especially in dry conditions. The greatest volumes correspond to the *DP* and were generated by the rainfall events that occurred at high soil moisture conditions (e.g., 19/4/2014; 20/9/2016, 3/7/2017 rainfall events).

The minor contribution of *SSF* – particularly on the bare soil plot – was observed, and 55% of the rainfall events did not generate any runoff (total). *SSF* was quantitatively dominant for the grassland plot.

On the bare soil plot, *SSF* is a relatively absent and less important process in terms of peak discharges. This situation is probably due to soil matrix, macropore system and pipe flow, water from infiltration passing to the deeper storage.

We assume that the important volume of water was transported from the topsoil into the matrix macropores to *DP*. *HOF, DP,* and *SSF* contributed to total water volume during the analyzed 32 rainfall-runoff events by 47%, 31%, and 22%, respectively at the grass plot. The *HOF, DP* and *SSF* contributions on the bare soil plot were 59%, 38%, and 3%, respectively.

Table 1. The rainfall events parameters from April–September, 2015/17 at Voineşti Experimental Basin.

Year (IV-IX)	2015				2016				2017			
Percentile	Parameters											
	D (min)	De (mm)	Intensity Avg (mm/h)	Intensity Max (mm/h	D (min)	De (mm)	Intensity Avg (mm/h)	Intensity Max (mm/h)	D (min)	De (mm)	Intensity Avg. (mm/h)	Intensity Max (mm/h)
Min	10	0.30	1.80	0.30	10	0.30	1.80	0.42	10	0.30	1.80	0.30
25th	30	0.70	1.40	1.20	20	0.60	1.80	1.20	40	0.80	1.20	1.20
50th	60	2.20	2.20	2.22	60	1.60	1.60	1.98	70	2.35	2.01	2.94
75th	170	5.75	2.03	5.40	110	4.00	2.18	7.80	130	7.58	3.50	9.60
90th	401	19.1	2.86	15.7	210	9.70	2.77	24.6	307	14.9	2.91	33.2
95th	667	24.3	2.19	25.7	300	16.1	3.22	28.2	499	21.6	2.60	45.6
Max	1310	35.9	1.64	62.4	910	81.8	5.39	62.4	920	51.9	3.38	76.8

D = Duration; De = Depth; Avg = average; Max = maximum.

Bereitgestellt von University Library Bratislava | Heruntergeladen 31.01.20 12:21 UTC

The relationship between rainfall and runoff coefficients

The boxplots of *RC's* of 32 rainfall-runoff events experiments grouped by land use are shown in Figure 4. We found a greater variability of *RC's* on bare soil than on grassland. The maximum and median were higher on the bare soil plot, while the minimum was slightly smaller on the grassland plot.

The 75th percentile of *RC's* at the bare soil plot was more than two times higher than at the grassland plot. The high *RC's* on bare soil could be explained by the soil water repellency on *HOF*. The 90th percentile values of cumulative runoff coefficient of events were 0.37 for the grassland and 0.60 for the bare soil (Figure 4). This indicates an increase in water retention capacity at the grassland plot under extreme conditions.

It was found that in very dry conditions (API_3 < 4 mm) grassland plot runoff coefficients (*HOF, SSF, DP*) are greatly reduced to 0, and in extreme wetness conditions, the *RC's* went up to 0.50 (e.g., 0.49 on 3/7/2017; 0.42 on 27/5/2017). Runoff coefficients on the bare soil plot have generally higher values than on the grassland plot. The bare soil plot release more than half of the rainfall volume in extreme conditions (e.g., *RC* = 0.65 on 9/5/2017 and *RC* = 0.63 on 3/7/2017). On the grassland, when API_3 was up to 4 mm, more than 8 mm of rainfall was needed to produce a minor *RC's*, while on the bare soil, minor RC's was produced by the rainfall event of 8 mm already at API_3 of 1 mm (Figure 4).

The relationship between rainfall and water flow pathways

The relationship between rainfall and water flow pathways (*HOF, SSF, DP* and cumulative) based on the 32 events is shown in Figure 5. These results reflect the nonlinearity of the rainfall-runoff processes, particularly on grassland (r^2 = 0.09) when compared to the bare soil (r^2 = 0.45).

Lag-time and peak discharge

The results concerning the lag-time to peak discharge at the two runoff plots for the same events are presented in Table 2.

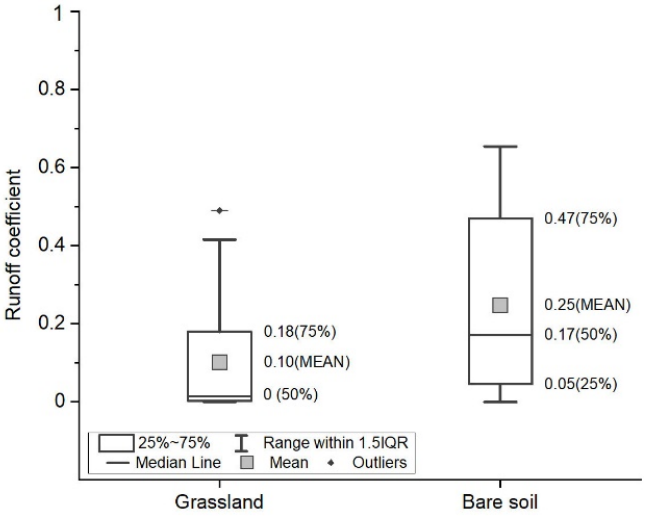

Fig. 4. Boxplots of the runoff coefficients of 32 rainfall-runoff events grouped by the land-use.

The lag-times differed from one case to another. The *HOF* hydrographs of a few events showed a rapid response to rainfall at the bare soil plot. However, in some cases, the *HOF* hydrographs had approximately the same lag-time on both plots (e.g., the 30/5/16 15:00 and 5/5/17 20:07 events).

The peak flow after the long rainless periods with high transpiration at the bare soil plot occurred earlier than at the grassland plot, e.g., after 12 and 18 min, respectively on 26 June 2017. Concerning the response time in the case of *SSF*, a lower drainage capacity was recorded on grassland than on the bare soil. This finding could be explained by the influence of the root system (Ghestem et al., 2011). *DP* occurring only after substantial rainfall events shows in most cases intermittent flow (dripping) which was quantitatively significant, but had no clear peak.

One of the most notable runoff elements is *HOF* peak discharge. In our pedoclimatic conditions, we observed that *HOF* peak discharges at grassland and bare soil plots do not respond

Table 2. Lag-time (min) of water flow pathways for grasslands and bare soil.

Events time	Grassland				Bare soil		
	HOF	SSF	DP	Growth stage	HOF	SSF	DP
13/5/16 4:00	NR	NR	NR	Initial	66	NR	IR
16/5/16 8:00	70	383	IR		59	NR	IR
30/5/16 15:00	50	NR	IR	Mid	50	NR	IR
2/6/16 4:00	104	NR	NR		81	NR	NR
17/7/16 3:30	69	NR	NR		NR	NR	NR
19/9/16 10:50	48	64	IR	Late	38	62	IR
20/9/16 0:40	151	154	IR		120	120	IR
20/9/16 7:00	39	72	IR		40	300	IR
25/9/16 15:00	NR	159	368		NR	IR	IR
5/5/17 20:07	187	206	232	Initial	187	653	653
7/5/17 17:30	91	111	162		5	160	810
9/5/17 8:00	141	164	219		121	340	905
27/5/17 15:17	163	173	188	Mid	154	IR	177
26/6/17 20:10	18	34	115		12	IR	2090
3/7/17 6:00	5	295	1500		0	60	858
25/7/17 13:50	87	160	289	Late	NR	NR	NR
19/9/17 10:40	758	792	803		771	826	1220
22/9/17 10:20	NR	NR	NR		186	299	304

HOF = Hortonian Overland Flow; SSF = Fast Subsurface Flow; DP = Deep Percolation; NR = no runoff; IR = intermittent runoff.

Bereitgestellt von University Library Bratislava | Heruntergeladen 31.01.20 12:21 UTC

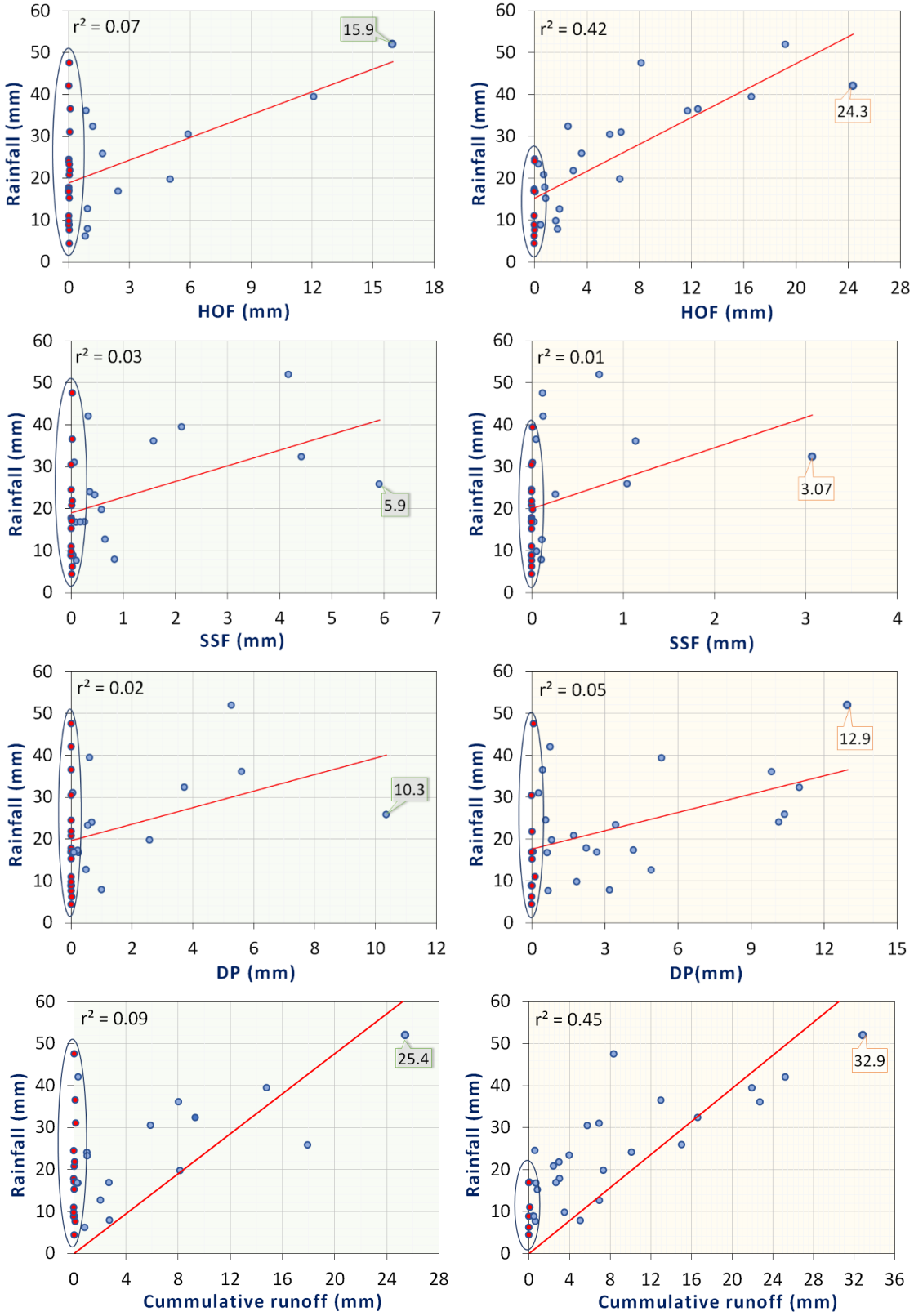

Fig. 5. The relationship at the event scale between rainfall and runoff (*HOF, SSF, DP*, and cummulative) for grassland (left row) and bare soil (right row); red dots show dry conditions (API_3 < 4 mm).

to rainfall events in a similar way (e.g. hydrograph shapes, peak discharges). In some cases, the *HOF* runoff peak was relatively synchronous on both plots (e.g., 30/5/2016; 5/5/2017). The decrease of *HOF* is more intense under dry conditions and it shows the hydrological key role of grassland for the water regulatory function.

Under extreme rainfall conditions in an unsaturated soil, a few major runoff events were produced. The *HOF* peak discharges at the grassland plots were smaller than at the bare soil plots. The *HOF* hydrograph shapes were very similar to those of hyetographs (see the double peaks in Fig. 6. The peak discharge of the *SSF* on grassland and bare soil plots was also (Figure 6).

Bereitgestellt von University Library Bratislava | Heruntergeladen 31.01.20 12:21 UTC

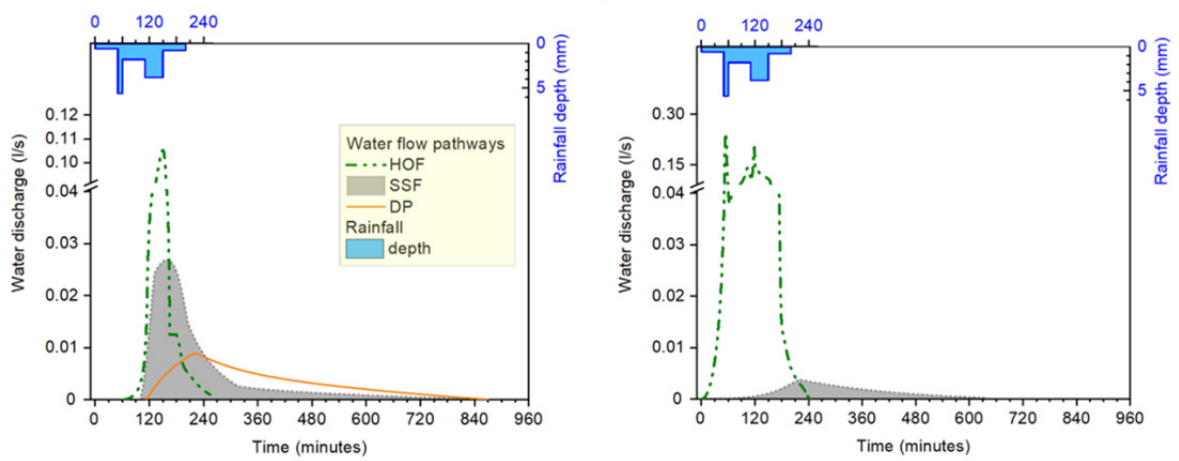

Fig. 6. Hydrographs during the rainfall-runoff event on July 5, 2017, on the grassland (left) and bare soil (right) plots.

The grassland plot had a fast *SSF* response. On the bare soil plot, reduction and flattening of the *SSF* peak discharge was a characteristic process, sometimes followed by bypass flow to *DP*. *SSF* does not occur under light rainfall intensities. On the bare soil plot, the *DP* peak discharge was insignificant and the *DP* hydrograph had flat rising and falling limbs.

DISCUSSION

Role of antecedent wetness on DRP's

Our study contributes to the improvement of knowledge on water flow pathways, namely DRP's, in relation to land use in a hilly temperate environment.

On the grassland plot, a strong control of antecedent wetness conditions for drainage paths was observed, by reducing the volumes of drained water (5% of the rain). The most visible hydrologic influences in dry conditions are on *SSF* (often absent) and *HOF,* which has often been severely diminished. However, the initial conditions did not control the flow response. Also, Scherrer et al. (2007), analyzing the RC's, observed that the DRP was not affected by antecedent wetness and that runoff volume increased only slightly at higher soil moisture. However, in their study of cambisol plots (10 sq m), Leitinger et al. (2010) found a mean surface runoff coefficient of 0.18 on pastures. Likewise, our results show similarly low values, with the P75 runoff coefficient of 0.18 for *HOF* (see Figure 4).

Rainfall characteristics such as depth (e.g., 26/6/2017 events), maximum intensities (e.g., 27/6/2015; 26/6/2017 events) had an important role in the occurrence and dynamics of DRP, particularly *HOF*. Compared to bare soil plot during drying period conditions, the DRP changed from *DP* in grassland plot to *HOF*. Dominant *HOF* (64%) on bare soil plot occurs when water repellent soils restrict (soil crust) infiltration and increase runoff. A subordinate process was *DP* (35%), whereas *SSF* were negligible (~ 1%).

In a case study of grassland DRP's, Scherrer et al. (2012) found that on grassland plots the dominant process changed from very delayed infiltration excess overland flow under dry conditions to delayed saturation excess overland flow under wet conditions. Also, several authors found that temporary *HOF* occurred only at the beginning under dry conditions (Scherrer et al., 2007; Leitinger et al., 2010; Ries et al., 2017). Therefore, results at plot-scale confirm the expectations that grassland on hillslopes influenced runoff and can modify the peak discharge and lag-time.

How does vegetation growth stage influence the DRP's?

From a hydrological point of view, an uncertain relationship between vegetation growth stage (initial, mid and late) and lag-time of runoff was observed.

In June–July period (months characterized by a pluviometric maximum), after the grass cutting on the grassland plot, a relatively variable lag time was observed. Statistical analysis of the vegetation stage and runoff coefficients did not show significant differences between the two periods (pre-cut and growth, respectively cut off).

The growth stage did not seem to have a great influence on runoff (e.g., thrugh water uptake by transpiration and percolation). One possible explanation is that the grass root system does not change by grass cutting. As for the runoff peak time, the grassland plot has a higher effect on the runoff peak attenuation, suggesting a stronger regulatory effect of grassland on the runoff process. We observed that most of the *HOF* grassland hydrographs had steep rising and falling limbs and narrow peak discharges. It was also noticed that the *HOF* lag-time on grassland was greater than on the bare soil. A possible explanation could be related to the dynamics and interactive behavior of soil characteristics, e.g., water repellency, vertical movement of water etc. (Lichner et al., 2011).

CONCLUSIONS

Our results suggest that runoff process on the grassland plot was dominated by *HOF* (47%) followed by *DP* (31%) and *SSF* (22%). Runoff on the bare soil plot was dominated by *HOF* (59%) followed by *DP* (38%) and *SSF* (3%).

These results indicate that *HOF* is actually the dominant runoff generation mechanism for both land uses. The vertical distribution of water in the soil gradually decreases in the case of grassland, whereas on bare soil, gravitational drainage of water changes *HOF* into *DP*.

Antecedent wetness conditions do not affect the DRP, but reduce the peak runoff rate during dry conditions. On the grassland plot, most of the rainfall percolated through the root zones into Luvisols and formed *SSF*. The soil-root interface has a strong hydrologic control there. On bare soil plot, where the grass root system was absent, the *SSF* was minor.

Runoff coefficients (for *HOF, SSF* and *DP*) indicated the influence of the antecedent conditions which were more important on the grassland plot. On the contrary, on the bare soil plot, higher runoff coefficients were observed (up to 0.65).

Bereitgestellt von University Library Bratislava | Heruntergeladen 31.01.20 12:21 UTC

Lag-time of peak flow was not strongly influenced by the land use. Grasslands had the biggest effect on the peak discharge and volume reduction, particularly on *HOF*. Clear influence of the vegetation growth stage on the runoff generation mechanism was not identified.

To conclude, grasslands have both positive (e.g., lag-time and attenuation of discharge volumes) and negative (e.g., retention and consumption of water in the soil-root zone during dry conditions) aspects (Lobet et al., 2014; Ries et al., 2017).

Acknowledgements. The authors would like to express their gratitude to Research Institute of the University of Bucharest for financial support of Gabriel Minea's postdoctoral research, and to the National Institute of Hydrology and Water Management for the continuous support in carrying out the research at microscale. We thank the Associate Editor and two anonymous reviewers for their thoughtful comments and time devoted to the improvement of our manuscript.

REFERENCES

Antonetti, M., Buss, R., Scherrer, S., Margreth, M., Zappa, M., 2016. Mapping dominant runoff processes: an evaluation of different approaches using similarity measures and synthetic runoff simulations. Hydrology and Earth System Sciences, 20, 7, 2929–2945.

Bachmair, S., Weiler, M., 2012. Hillslope characteristics as controls of subsurface flow variability. Hydrology and Earth System Sciences, 16, 10, 3699–3715.

Blidaru, S., 1965. Emploi des bassins représentatifs et des stations expérimentales a l'étude des phénomènes hydrologiques. Studies and reports in hydrology, IAHS, 66, 2, 107–115.

Bronstert, A., Bárdossy, A., 2003. Uncertainty of runoff modelling at the hillslope scale due to temporal variations of rainfall intensity. Physics and Chemistry of the Earth, Parts A/B/C, 28, 6–7, 283–288.

Ferreira, C.S.S., Keizer, J.J., Santos, L.M.B., Serpa, D., Silva, V., Cerqueira, M., Ferreira, A.J.D., Abrantes, N., 2018. Runoff, sediment and nutrient exports from a Mediterranean vineyard under integrated production: An experiment at plot scale. Agriculture, Ecosystems & Environment, 256, 184–193.

Florea, N., Conea, A., Munteanu, I. (coord.), 1971. Soil Map Romania, sc. 1: 500,000. Inst. Geol. Bucureşti, Bucharest.

Florea, N., Munteanu, I., (Eds.), 2012. Romanian System of Soil Taxonomy/Sistemul Român de Taxonomie a Solurilor (SRTS-2012). Publish House Sitech, Craiova.

Ghestem, M., Sidle, R. C., Stokes, A., 2011. The influence of plant root systems on subsurface flow: implications for slope stability. BioScience, 61, 11, 869–879.

Hümann, M., Müller, C., 2013. Improving the GIS-DRP Approach by Means of Delineating Runoff Characteristics with New Discharge Relevant Parameters. ISPRS International Journal of Geo-Information, 2, 1, 27–49.

Jost, G., Schume, H., Hager, H., Markart, G., Kohl, B., 2012. A hillslope scale comparison of tree species influence on soil moisture dynamics and runoff processes during intense rainfall. Journal of Hydrology, 420, 112–124.

Kohler, M.A., Linsley, R.K., 1951. Predicting the runoff from storm rainfall (Vol. 30). US Department of Commerce, Weather Bureau. Washington, DC, 9 p.

Leitinger, G., Tasser, E., Newesely, C., Obojes, N., Tappeiner, U., 2010. Seasonal dynamics of surface runoff in mountain grassland ecosystems differing in land use. Journal of Hydrology, 385, 1–4, 95–104.

Lichner, L., Eldridge, D.J., Schacht, K., Zhukova, N., Holko, L., Sir, M., Pecho, J., 2011. Grass cover influences hydrophysical parameters and heterogeneity of water flow in a sandy soil. Pedosphere, 21, 6, 719–729.

Lobet, G., Couvreur, V., Meunier, F., Javaux, M., Draye, X., 2014. Plant water uptake in drying soils. Plant Physiology, 164, 1619–1627.

Maftei, C., Chevalier, P., Ciurea, C., Roşu, L., 2002. Considerations Concerning the Characteristics of Permeability of the Podzolic soil in Voineşti Catchment. Analele Universitatii "OVIDIUS" Constanta, Seria Constructii, I, 3–4, 525–530.

Minea, G., Iliescu, M., Dedu, F., 2016. Temporal rainfall properties at events scale in the Curvature Subcarpathians (Romania). Forum Geografic, XV, Suppl. 2, 115–123. DOI:10.5775/fg.2016.

Minea, G., Moroşanu, G.A., 2016. Micro-scale hydrological field experiments in Romania. Open Geosciences, 8, 1, 154–160.

Minea, G., Tudor, G., Stan F-I., Ioana-Toroimac, G., Zamfir, R., 2018. How can the grasslands under rainfall events modify water balance in drought conditions. Journal of Water and Land Development, 38, 53–65.

Miţă, P., Mătreaţă, S., 2016. Representative Basins in Romania: Synthesis of Research Result. Didactica Publishing House, Bucharest, 36 p.

Müller, C., Hellebrand, H., Seeger, M., Schobel, S., 2009. Identification and regionalization of dominant runoff processes-a GIS-based and a statistical approach. Hydrology and Earth System Sciences, 13, 6, 779–792.

Naef, F., Scherrer, S., Weiler, M., 2002. A process based assessment of the potential to reduce flood runoff by land use change. Journal of Hydrology, 267, 1, 74–79.

Peel, M.C., Finlayson, B.L., McMahon, T.A., 2007. Updated world map of the Köppen-Geiger climate classification. Hydrol. Earth Syst. Sci., 11, 5, 1633–1644. https://doi.org/10.5194/hess-11-1633-2007

Ries, F., Schmidt, S., Sauter, M., Lange, J., 2017. Controls on runoff generation along a steep climatic gradient in the Eastern Mediterranean. Journal of Hydrology: Regional Studies, 9, 18–33.

Rodrigo-Comino, J., Senciales, J. M., Sillero-Medina, J. A., Gyasi-Agyei, Y., Ruiz-Sinoga, J. D., & Ries, J. B. 2019. Analysis of Weather-Type-Induced Soil Erosion in Cultivated and Poorly Managed Abandoned Sloping Vineyards in the Axarquía Region (Málaga, Spain). Air, Soil and Water Research, 12, 1–-11.

Rodrigo-Comino, J., Wirtz, S., Brevik, E.C., Ruiz-Sinoga, J., Ries, J.B. 2017. Assessment of agri-spillways as a soil erosion protection measure in Mediterranean sloping vineyards. J. Mt. Sci. 14, 6,1009–1022.

Rodríguez-Caballero, E., Cantón, Y., Lazaro, R., Solé-Benet, A., 2014. Cross-scale interactions between surface components and rainfall properties. Non-linearities in the hydrological and erosive behavior of semiarid catchments. Journal of Hydrology, 517, 815–825.

Scherrer, S., Naef, F., 2003. A decision scheme to indicate dominant hydrological flow processes on temperate grassland. Hydrological processes, 17, 2, 391–401.

Scherrer, S., Naef, F., Faeh, A.O., Cordery, I., 2007. Formation of runoff at the hillslope scale during intense precipitation. Hydrology and Earth System Sciences Discussions, 11, 2, 907–922.

Schmocker-Fackel, P., Naef, F., Scherrer, S., 2007. Identifying runoff processes on the plot and catchment scale. Hydrology and Earth System Sciences, 11, 2, 891–906.

Stanciu, P., Zlate-Podani, I., 1987. A study of hydrological regimes in experimental basins in relation to cultivation practices. Water for the Future: Hydrology in Perspective (Proceedings of the Rome Symposium, April 1987). IAHS, 164,193–203.

USDA-NRCS, 1999. Guide to Texture by Feel. https://www.nrcs.usda.gov/wps/portal/nrcs/detail/soils/edu/?cid=nrcs142p2_054311, Accessed on November 27, 2018.

Weyman, D.R., 1973. Measurements of the downslope flow of water in a soil. Journal of Hydrology, 20, 3, 267–288.

Woolhiser, D.A., Goodrich, D.C., 1988. Effect of storm rainfall intensity patterns on surface runoff. Journal of Hydrology, 102, 1–4, 335–354.

Zaharia, L., Ioana-Toroimac, G., 2009. Erosion dynamics – precipitation relationship in the Carpathian's Curvature Region (Romania). Geografia Fisica e Dinamica Quaternaria, 32, 95–10.

Received 23 May 2018
Accepted 19 December 2018

Bereitgestellt von University Library Bratislava | Heruntergeladen 31.01.20 12:21 UTC

J. Hydrol. Hydromech., 67, 2019, 4, 305–313
DOI: 10.2478/johh-2019-0019

Long term variations of river temperature and the influence of air temperature and river discharge: case study of Kupa River watershed in Croatia

Senlin Zhu[1], Ognjen Bonacci[2], Dijana Oskoruš[3], Marijana Hadzima-Nyarko[4*], Shiqiang Wu[1]

[1] State Key Laboratory of Hydrology-Water resources and Hydraulic Engineering, Nanjing Hydraulic Research Institute, Nanjing 210029, China.
[2] Faculty of Civil Engineering and Architecture, University of Split, Matice hrvatske 15, 21000 Split, Croatia.
[3] Meteorological and Hydrological Service, Gric 3, 10000 Zagreb, Croatia.
[4] Josip Juraj Strossmayer University of Osijek, Faculty of Civil Engineering and Architecture Osijek, Vladimira Preloga 3, 31000 Osijek, Croatia.
[*] Corresponding author. E-mail: mhadzima@gfos.hr

Abstract: The bio-chemical and physical characteristics of a river are directly affected by water temperature, which therefore affects the overall health of aquatic ecosystems. In this study, long term variations of river water temperatures (RWT) in Kupa River watershed, Croatia were investigated. It is shown that the RWT in the studied river stations increased about 0.0232–0.0796ºC per year, which are comparable with long term observations reported for rivers in other regions, indicating an apparent warming trend. RWT rises during the past 20 years have not been constant for different periods of the year, and the contrasts between stations regarding RWT increases vary seasonally. Additionally, multilayer perceptron neural network models (MLPNN) and adaptive neuro-fuzzy inference systems (ANFIS) models were implemented to simulate daily RWT, using air temperature (T_a), flow discharge (Q) and the day of year (DOY) as predictors. Results showed that compared to the individual variable alone with T_a as input, combining T_a and Q in the MLPNN and ANFIS models explained temporal variations of daily RWT more accurately. The best accuracy was achieved when the three inputs (T_a, Q and the DOY) were included as predictors. Modeling results indicate that the developed models can well reproduce the seasonal dynamics of RWT in each river, and the models may be used for future projections of RWT by coupling with regional climate models.

Keywords: Climate change; Machine learning models; River water temperature.

INTRODUCTION

River water temperature (RWT) is one of the most important indicators to determine the overall health of aquatic ecosystems since it affects various physical and biochemical processes in rivers (Rice and Jastram, 2015). For example, RWT significantly impacts dissolved oxygen dynamics (Cox and Whitehead, 2009), the formation of potentially toxic ammonia (Kim et al., 2017), and the evolution and distribution of aquatic organisms (Fullerton et al., 2018). Cingi et al. (2010) stressed that relatively small increases in RWT during the spawning period of Coregonus lavaretus may lead to fatal impacts on its recruitment and population persistence.

Understanding the factors impacting RWT and how thermal regimes have changed in the past and how they can be modified in the future is therefore of great significance for the sustainable management of river ecosystems. This is especially important in recent decades considering the rising of air temperatures due to climate change (van Vliet et al., 2013), the impacts of extreme climate events such as heatwaves (Feng et al., 2018; Schär et al., 2004) and anthropogenic activities such as land use change (DeWeber and Wagner, 2014; LeBlanc et al., 1997), urbanization (DeWeber and Wagner, 2014; Chen et al., 2016) and damming (Ayllón et al., 2012). Rising RWT is strongly related to climate warming with various time scales for different type of rivers, which have been reported in a lot of studies (Bonacci et al., 2008; Chen et al., 2016; Gooseff et al., 2005; Null et al., 2013; Webb et al., 2003). For example, Chen et al. (2016) indicated that RWT in the Yongan watershed increased by 0.029−0.046°C year^{-1} due to a ~0.050°C year^{-1} increase of air temperature over the 1980−2012 period.

Although the air-water temperature relationship is generally strong, the strength of such a relationship varies regionally and temporally, and can be highly site specific due to additional influences from local hydrology and human activities (DeWeber and Wagner, 2014; Zhu et al., 2019). It is commonly observed that RWT is inversely related to river discharge, and a global assessment indicated that a decrease in river discharge by 20% and 40% would exacerbate water temperature increases by 0.3°C and 0.8°C on average, respectively (van Vliet et al., 2011). Additionally, it was found that river discharge played a relevant role mainly in snow-fed and regulated rivers with higher altitude hydropower reservoirs, while it played a minor role in lowland rivers for RWT dynamics (Zhu et al., 2019). Depending on the river type and time scale, the air-water temperature relationships can be explained by linear or logistic functions (Hadzima-Nyarko et al., 2014; Webb et al., 2003), machine learning models (DeWeber and Wagner, 2014; Hadzima-Nyarko et al., 2014; Piotrowski et al., 2015; Zhu et al., 2019), and hybrid statistically and physically based models (Toffolon and Piccolroaz, 2015).

Kupa River watershed is one of the most important water resources in Croatia, and quantifying thermal dynamics in this particular river catchment is thus of great significance to water resources managers. Previously, Bonacci et al. (2008) analyzed water temperature regime of the Danube and its tributaries in Croatia, including the main stem of the Kupa River. However, the RWT data from the main stem hydrological stations were only limited to 1951–2003. In this study, the latest RWT and flow discharge data from 6 hydrological stations on the main tributaries of Kupa River were evaluated to describe and identify changes in the thermal regime of the watershed. In addition,

Bereitgestellt von University Library Bratislava | Heruntergeladen 31.01.20 12:22 UTC

we developed predictive water temperature models using the multilayer perceptron neural network (MLPNN) and adaptive neuro-fuzzy inference system (ANFIS) machine learning tools following their use by Zhu et al. (2019) for the Drava River. In the Drava River model (Zhu et al., 2019), the components of the Gregorian calendar (*CGC*) which include year, month, and day were used as suggested by Heddam (2016) and Heddam and Kisi (2017) for water quality modelling. For RWT forecasting, the day of year (*DOY*) was used in the forwards and backwards stepwise model for Scotland's Atlantic salmon rivers (Jackson et al., 2018). In this study, air temperature, river discharge, and *DOY* were used as inputs to predict RWT. The objective of this study is to analyze thermal regimes of rivers in the Kupa River watershed, develop models which can be used for future RWT projections and further test the performance of MPLNN and ANFIS for predicting water temperatures under different hydrologic conditions than those of Zhu et al. (2019).

MATERIALS AND METHODS

Study area

The study covers the Kupa River basin, situated between Croatia (86% of total basin area) and Slovenia (14% of total basin area) in the hinterland of the Northern Adriatic Sea (Fig. 1). The region is characterized by complex karst hydrological/hydrogeological behavior common to the deep and developed Croatian Dinaric karst, resulting in a weakly defined hydrological drainage area (Bonacci and Andrić, 2010). A mix of continental and Mediterranean climate influences the upper part of the basin, while Pannonian climate is the most important in the lower part. The patterns of land use in the Kupa River basin include mountains (26%), forests (33%), pasture (26%) and agriculture (15%) (Frančišković-Bilinski et al., 2012). Hydrological parameters (water temperature and river discharge) were regularly monitored at six gauging stations in the Kupa River selected for this study. Table 1 presents the main characteristics of the 6 studied gauging stations (station name, station elevation, drainage area, period of available data for water temperature and flow discharge). River water temperature data was monitored once-daily at 7.30 am. Daily river discharge was calculated based on measurements of water level using the water level-river discharge RK method. Daily average air temperatures (T_a) were obtained from the nearby meteorological station in Ogulin for 1990–2017.

Analysis methods

In this study, annual variations of T_a and T_w in each river station were analyzed using linear models with year as effect for trend analysis. The correlations between the RWT increase rates and annual averaged flow discharges, and relationships between the mean annual RWT and the station elevation for the six river stations were investigated using linear models. Changes in T_a, T_w and Q for annual and seasonal average values were compared between five years averages for two sub-periods (1996–2000 and 2011–2015). Since the Čabranka River only has data till 2008, data from 1990–1994 and 2004–2008 was compared. The seasonal dynamics of T_w, T_a and Q are analyzed through the climatological year, which is defined by averaging for each day of the calendar year all measurements available over the observation period for that same specific day (Zhu et al., 2019).

Table 1. Main characteristics of the 6 studied water temperature gauging stations in the Kupa River watershed.

River name	Station name	Elevation (m a.s.l.)	Drainage area (km^2)	Period of available data	Long term averages	
					T_w	Q
Čabranka	Zamost 2	297.540	134.451[a]	T_w Q: 1990–1999 2002–2008	8.14	3.50
Donja Dobra	Stative Donje	116.456	49.344[a]	T_w Q: 1994–2017	12.34	37.28
Donja Mrežnica	Mrzlo Polje	113.967	257.953[a]	T_w Q: 1990–2017	13.80	26.14
Gornja Dobra	Luke	353.668	162.00[b]	T_w Q: 1991–1992 1994–2015	9.01	6.78
Korana	Slunj Uzvodni	212.167	572.341[a]	T_w Q: 1996–2004 2007–2017	12.41	9.97
Slunjčica	Rastoke	226.899	273.00[b]	T_w Q: 1996–2017	10.78	8.32

T_w: water temperature; Q: flow discharge; a Hydrological drainage area, b Topographical drainage area

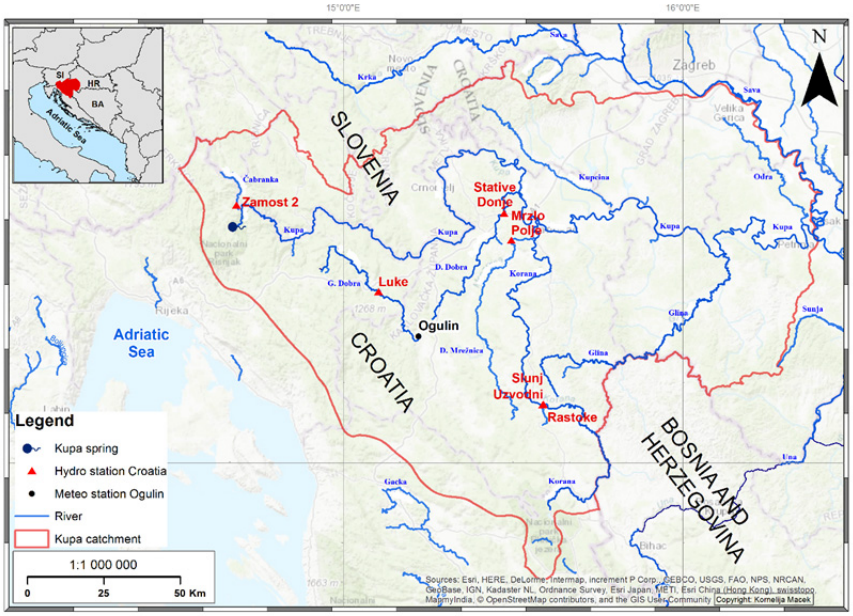

Fig. 1. Location map indicating the studied river catchment.

Bereitgestellt von University Library Bratislava | Heruntergeladen 31.01.20 12:22 UTC

Machine learning models

In the present study, the MLPNN and ANFIS models applied previously by Zhu et al. (2019) were used. For the MLPNN model, the weights (w_{ij}) and bias levels (δ_0) are the only parameters that need to be adjusted when the structure of the neural network has been defined (number of layers, number of neurons in each layer, activation function for each layer). Modification of these parameters will change the output values of the designed network. The weights (w_{ij}) and bias levels (δ_0) are iteratively adjusted during model training to minimize error. The root mean squared error (RMSE) and the mean squared error (MSE) is often used to define the network error. Similar to Zhu et al. (2019), the MLPNN model has one hidden layer with sigmoidal activation function, and one output layer with linear activation function. We tried to vary the number of neurons in the hidden layer from 10 and 13, and it was found that there is no any significant improvement for model performance, thus, the number of neurons in the hidden layer is set as 10. To develop ANFIS model, it is important to create the fuzzy rule base. The number of fuzzy rule for any ANFIS model is directly related to the identification method used for partitioning the input space. According to the previous research results (Zhu et al., 2019), the fuzzy c-means clustering (FC) was used. When using FC method, the number of fuzzy rules is equal to the clusters and fixed by the user. Detailed information about the two models can be found in Zhu et al. (2019).

In this study, both the scripts of the MLPNN and ANFIS models were implemented in Matlab.

Besides air temperature (T_a) and flow discharge (Q), the day of the year (DOY) was also used as input variable. Three MLPNN and three ANFIS models were developed with the following predictors: (i) version 1 with only one input variable (T_a), (ii) version 2 with two inputs variable (T_a and Q) and (iii) version 3 with three inputs (T_a, Q and the DOY). For the six river stations, data period for model training and testing are respectively: (1) 1990–1999 and 2002–2008 for Čabranka River, (2) 1994–2009 and 2010–2017 for Donja Dobra River, (3) 1990–2007 and 2008–2017 for Donja Mrežnica River, (4) 1991–1992 plus1994–2007 and 2008–2015 for Gornja Dobra River, (5) 1996–2004 plus 2008–2010 and 2011–2017 for Korana River, and (6) 1996–2009 and 2010–2017 for Slunjčica River.

Model evaluation metrics

Model performances were evaluated using the following four indicators: the coefficient of correlation (R), the Willmott index of agreement (d), the root mean squared error (RMSE), and the mean absolute error (MAE).

$$R = \left[\frac{\frac{1}{n}\sum_{i=1}^{n}(O_i - O_m)(P_i - P_m)}{\sqrt{\frac{1}{n}\sum_{i=1}^{n}(O_i - O_m)^2}\sqrt{\frac{1}{n}\sum_{i=1}^{n}(P_i - P_m)^2}} \right] \quad (1)$$

$$d = 1 - \frac{\sum_{i=1}^{n}(P_i - O_i)^2}{\sum_{i=1}^{n}\left(|P_i - O_m| + |O_i - O_m|\right)^2} \quad (2)$$

$$RMSE = \sqrt{\frac{1}{n}\sum_{i=1}^{n}(O_i - P_i)^2} \quad (3)$$

$$MAE = \frac{1}{n}\sum_{i=1}^{n}|O_i - P_i| \quad (4)$$

where n is the number of data samples, O_i is the observed and P_i is the predicted water temperatures. O_m and P_m are the average values of O_i and P_i.

RESULTS AND DISCUSSION

Dynamic variations of water temperature and air temperature

The annual variations of T_a and T_w are presented in Fig. 2. Air temperatures increased about 0.0449ºC year^{-1}, while RWT increases differed between the studied river stations from 0.0232–0.0796ºC per year. The RWT increase rate (ºC year^{-1}) negatively correlated with annual averaged flow discharge (Fig. 3). The observed RWT increases are comparable with long term observations reported for rivers in China (0.029–0.046ºC year^{-1}, Chen et al. 2016), USA (0.009–0.077ºC year^{-1}, Isaak et al., 2012; van Vliet et al., 2013; Rice and Jastram, 2015) and Europe (0.006–0.18ºC year^{-1}, Albek and Albek, 2009; Hardenbicker et al., 2017; Lepori et al., 2014; Markovic et al., 2013; Moatar and Gailhard, 2006; Orr et al., 2015; Pekárová et al., 2011; Žganec, 2012).

Fig. 4 presents changes in T_a, T_w and Q for annual and seasonal average values. For all the rivers, annual averaged T_a, T_w and Q increased during the two sub-periods (1996–2000 and 2011–2015) except for the decreased Q in the Slunjcica River. With an increase of 0.94ºC for air temperature, the annual mean of RWT increased about 0.146–1.287ºC. Increases in annual mean RWT was highest for the Korana River (1.287ºC) and least for the Donja Dobra River (0.146ºC). Repeating this analysis for different seasonal quarters revealed that RWT rises during the two sub-periods have not been constant for different periods of the year, and the contrasts between river stations regarding RWT increases vary seasonally. For the Čabranka river (Fig. 4(a)), though air temperature in January-March and July-September decreased, RWT in different seasons still increased between 0.386 and 0.878ºC. For the other five rivers, the greatest rises in average RWT ranged from 0.626 to 5.221ºC. Particularly, RWT increases in July–September exceeded 5.0ºC and 2.0ºC for the Korana River (Fig. 4(e)) and the Gornja Dobra River (Fig. 4(d)) respectively.

Fig. 5 presents a linear relationship between the mean annual RWT and the station elevation for the six river stations. Results showed that the mean annual RWT negatively correlated with station elevation, which is consistent with previous analysis for river stations in the main stem of the Kupa River (Bonacci et al., 2008). However, the mean annual RWT presented no significant correlation with the drainage area listed in Table 1 (the coefficient of correlation R = 0.36), which may be explained by the complex karst hydrological/hydrogeological behavior and weakly defined hydrological drainage areas (Bonacci and Andrić 2010).

The seasonal dynamics of water temperature (T_w), air temperature (T_a) and flow discharge (Q) are presented in Fig. 6 through the climatological year. River flow mainly was generally higher in the spring and winter period for the six rivers, when air and water temperatures are lower. However, river flow is generally low when air temperatures are high, which may further intensify RWT increases. The response of T_w to changes in T_a is almost linear for the Donja Dobra River (Fig. 6(b)), the Donja Mrežnica River (Fig. 6(c)) and Korana River (Fig. 6(e)). Typically for the Donja Mrežnica River (Fig. 6(c)),

Bereitgestellt von University Library Bratislava | Heruntergeladen 31.01.20 12:22 UTC

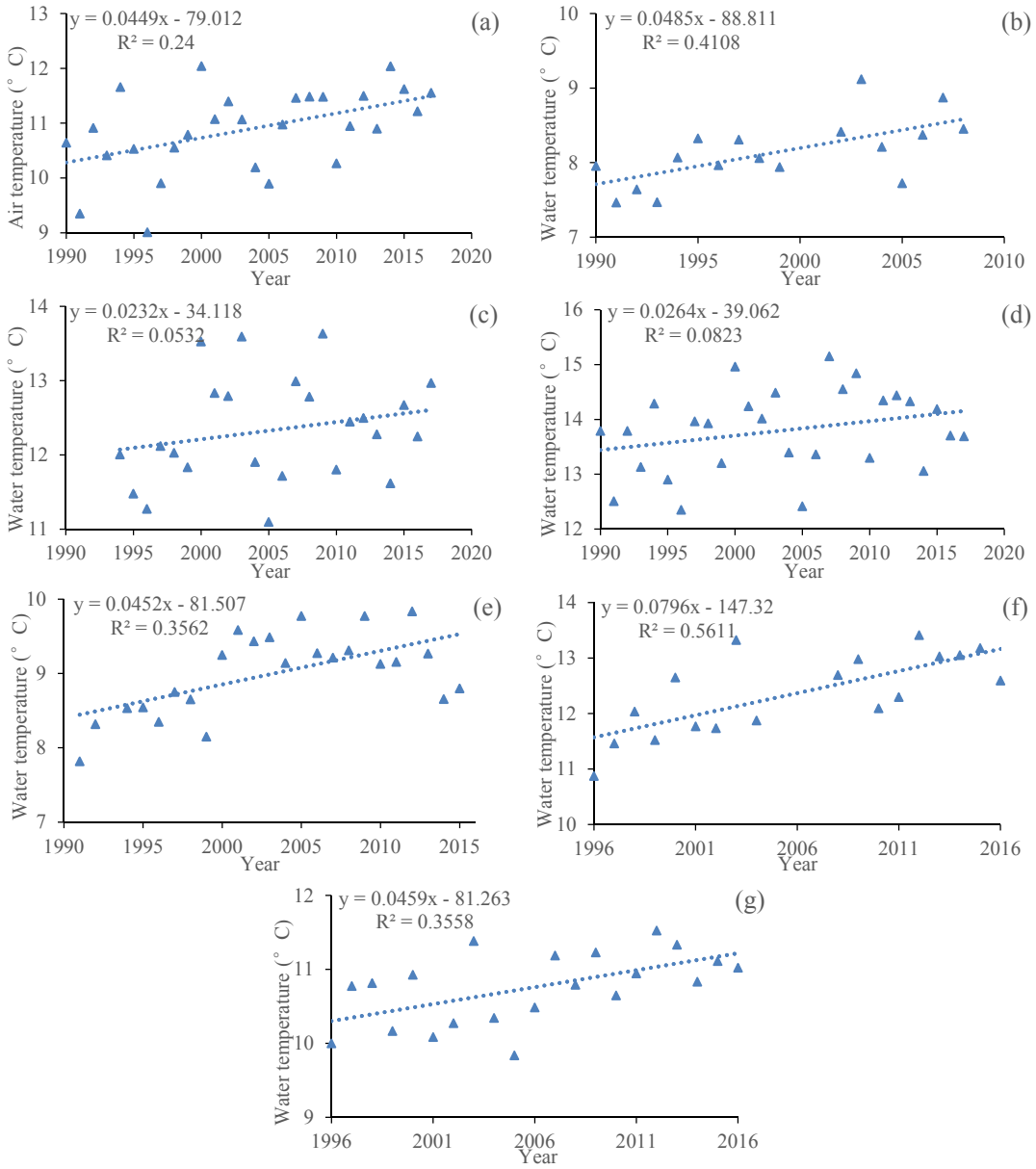

Fig. 2. Annual variations of T_a and T_w: (a) T_a in Ogulin, (b) T_w in Čabranka, (c) T_w in Donja Dobra, (d) T_w in Donja Mrežnica, (e) T_w in Gornja Dobra, (f) T_w in Korana and (g) T_w in Slunjčica.

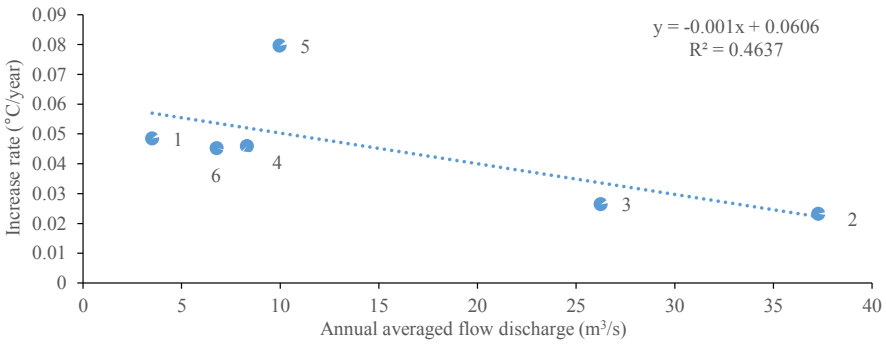

Fig. 3. Linear relationship between increase rate of river temperature and annual averaged flow discharge for the six rivers (1-Čabranka, 2-Donja Dobra, 3-Donja Mrežnica, 4-Gornja Dobra, 5-Korana, 6- Slunjčica).

T_w in the climatological year were larger than T_a all the year round. The Čabranka River (Fig. 6(a)), Gornja Dobra River (Fig. 6(d)), and Slunjčica River (Fig. 6(f)) presented a clear flattening of the seasonal pattern of T_w, especially in summer.

Bereitgestellt von University Library Bratislava | Heruntergeladen 31.01.20 12:22 UTC

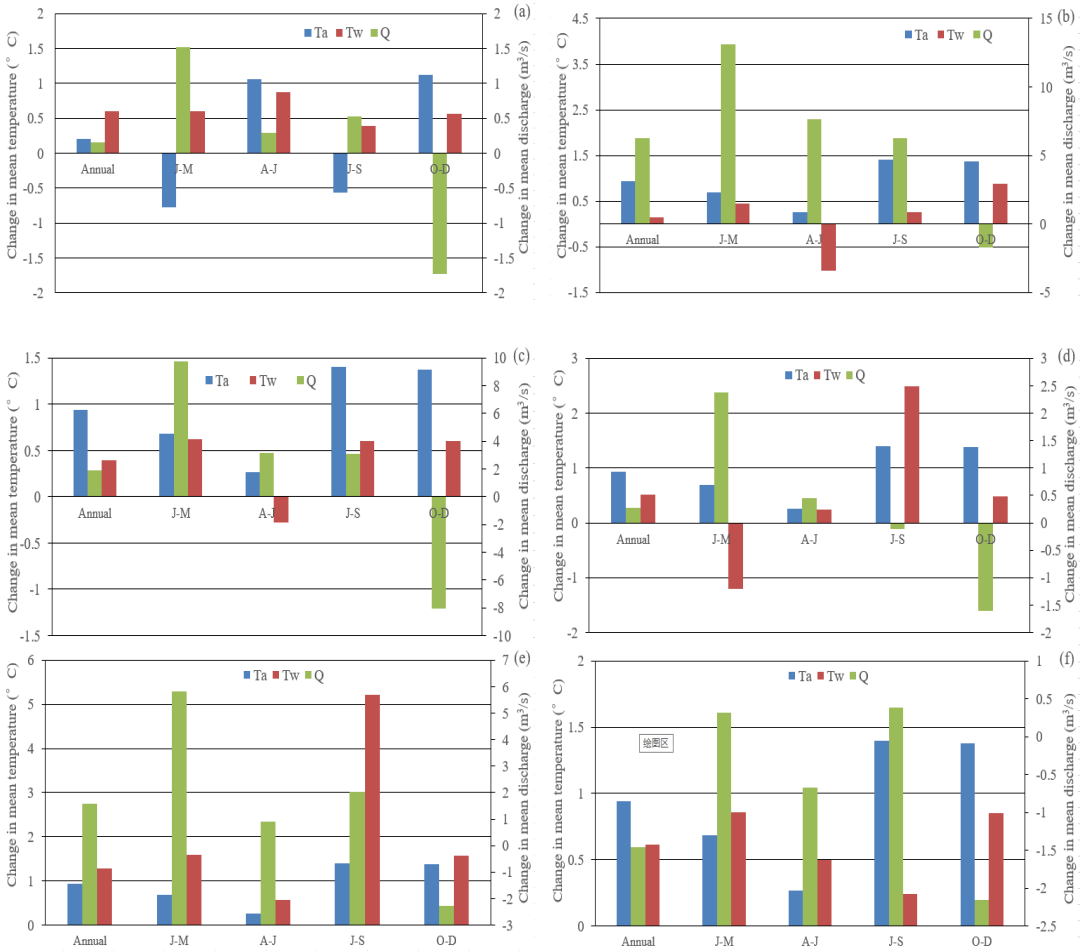

Fig. 4. Changes in T_a, T_w and Q between two sub-periods for annual and seasonal average values (J-M: January–March; A-J: April–June; J-S: July–September; O-D: October–December): (a) Čabranka, (b) Donja Dobra, (c) Donja Mrežnica, (d) Gornja Dobra, (e) Korana, (f) Slunjčica.

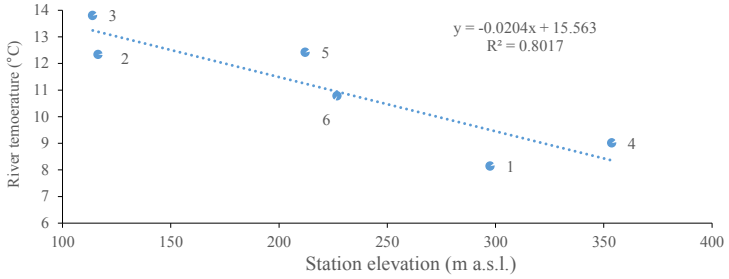

Fig. 5. Linear relationship between mean annual river temperature and station elevation for the studied river station in each river (1-Čabranka, 2-Donja Dobra, 3-Donja Mrežnica, 4-Gornja Dobra, 5-Korana, 6- Slunjčica).

Machine learning models for modeling daily river water temperature

Models performance was similar but MLPNN model performed slightly better (Table 2), conforming the previous conclusion of Zhu et al. (2019). Compared to the models with only T_a as input (version 1), combining T_a and Q in the version 2 models explained temporal variations of RWT more accurately (Table 2), especially for the Donja Dobra, Donja Mrežnica and Slunjčica rivers. For example, for the Slunjčica River, the MLPNN2 model decreased the RMSE and MAE values of MLPNN1 by 25.90% and 26.97% in the training phase, and 14.97% and 17.48% in the testing phase. By including *DOY* as model input, modeling performances dramatically improved (Table 2), which indicates that the seasonal component *DOY* plays an important role for RWT forecasting. For the Donja Mrežnica River, the ANFIS2 model decreased the RMSE and MAE values of ANFIS1 by 18.58% and 23.00% in the training phase, and 21.30% and 25.64% in the testing phase. Generally, the two models performed well for RWT predictions. For model version 3, in the testing phase, R and d values varied between 0.907 and 0.978, and 0.951 and 0.989 respectively, and RMSE and MAE values ranged from 0.872 to 1.793ºC, and 0.627 to 1.435ºC. The modeling performances are comparable with that for the two river stations in the Drava River that had RMSE varying between 1.227 and 1.69ºC (Zhu et al., 2019). Fig. 7 shows the variation of annual RMSE values (MLPNN3) for the whole modeling period in each river, which indicates that the annual RMSE values varied between years. The averaged RMSE values for the studied time periods were 1.077, 1.419, 1.285, 1.356, 1.583 and 0.794ºC for the Čabranka, Donja

Bereitgestellt von University Library Bratislava | Heruntergeladen 31.01.20 12:22 UTC

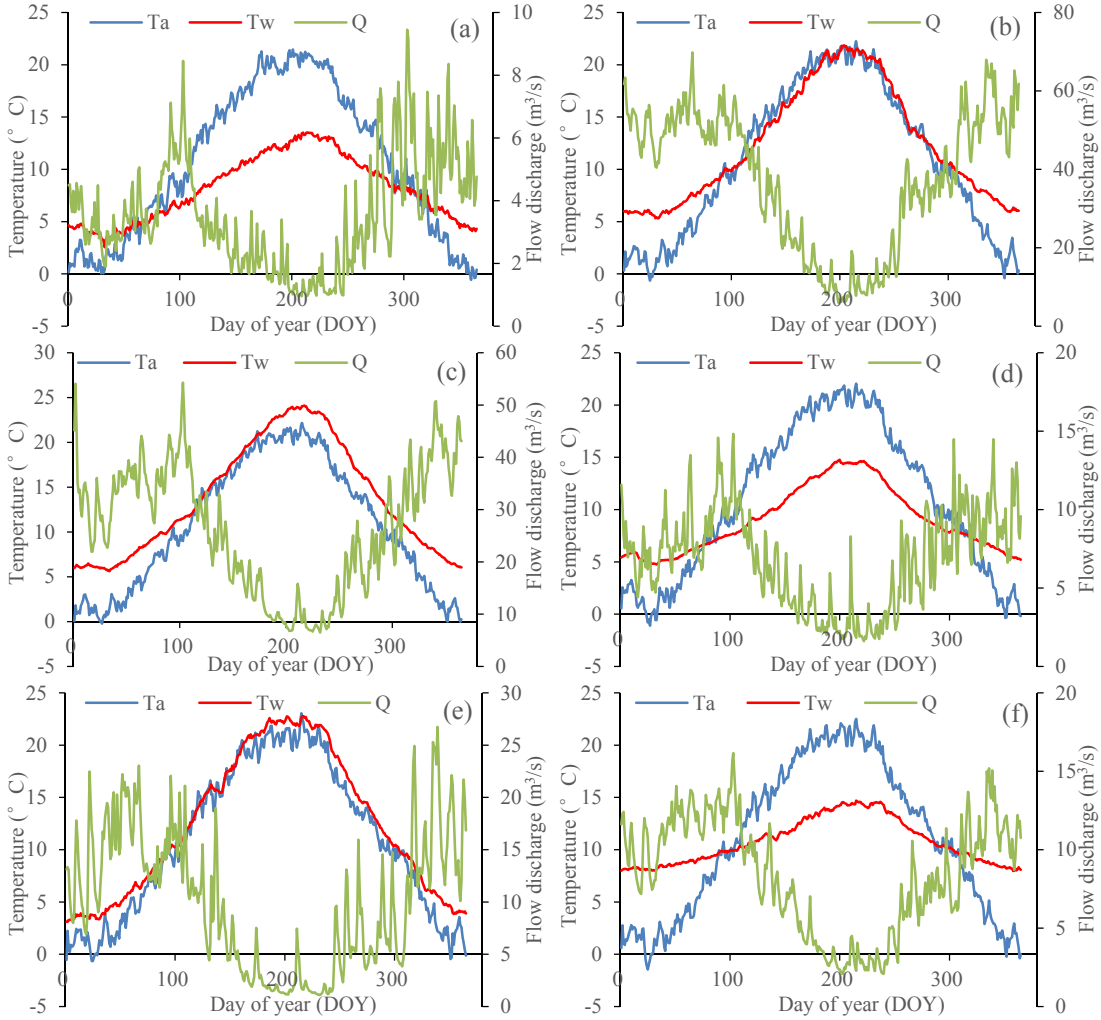

Fig. 6. Climatological (reference) year for the six rivers: (a) Čabranka, (b) Donja Dobra, (c) Donja Mrežnica, (d) Gornja Dobra, (e) Korana, (f) Slunjčica.

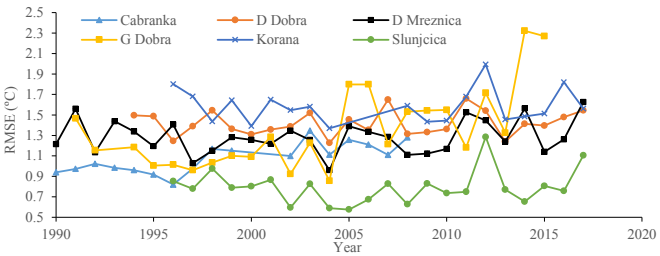

Fig. 7. Variation of annual RMSE values for the MLPNN3 models.

Dobra, Donja Mrežnica, Gornja Dobra, Korana, and Slunjčica respectively. The RMSE values compare reasonably with that in Jackson et al. (2018) (1.57ºC) and Sohrabi et al. (2017) (1.25ºC), and far better than that of Temizyurek and Dadaser-Celik (2018) (2.10–2.64ºC). Fig. 8 presents the modeling performances of the MLPNN3 for the climatological year at the six river stations. As is shown, the MLPNN3 model can well reproduce the seasonal dynamics of RWT in each river. The further test of modeling methods used in our previous research (Zhu et al., 2019) indicate that the models can be successfully applied for RWT forecasting for rivers characterized by different hydrological conditions. The models can be further coupled with regional climate models for future projections of RWT in the Kupa River watershed, which can help to inform water resources management in Croatia.

CONCLUSIONS

In this study, long term changes of RWT from six river stations in Kupa River watershed, Croatia were investigated. Results showed that RWT in the six studied river stations increased about 0.0232–0.0796ºC per year with an increasing trend of air temperatures of 0.0449ºC year^{-1}, indicating an apparent warming trend. The results are comparable with long term observations for rivers in other regions (China, USA and Europe etc.). With an increase of 0.94ºC for air temperature, the annual mean of RWT increased about 0.146–1.287ºC in the two sub-periods (1996–2000 and 2011–2015). Results for different seasonal quarters revealed that temperature rises during the two sub-periods have not been constant for different periods of the year, and the contrasts between stations regarding temperature increases vary seasonally. In addition, MLPNN and ANFIS models were developed to predict daily RWT, using T_a, Q and DOY as model inputs. Results showed that compared to the model version 1 with T_a only, adding Q better explained temporal variations of daily RWT. Using the three inputs as predictors (T_a, Q and the DOY) yielded the best accuracy among all the developed models. RMSE and MAE values ranged from 0.872 to 1.793ºC, and 0.627 to 1.435ºC respectively in the testing phase. Modeling results indicate that the developed models can well reproduce the seasonal dynamics of RWT. For further research, the models can be coupled with regional climate models for future projections of RWT.

Bereitgestellt von University Library Bratislava | Heruntergeladen 31.01.20 12:22 UTC

Table 2. Performances of different models in modelling water temperature (T_w °C) for the studied rivers in the Kupa River watershed.

River name	Model version	Training				Testing			
		R	*d*	*RMSE* (°C)	*MAE* (°C)	*R*	*d*	*RMSE* (°C)	*MAE* (°C)
Čabranka	MLPNN3	0.956	0.977	0.986	0.774	0.941	0.970	1.262	0.979
	MLPNN2	0.916	0.955	1.342	1.037	0.908	0.953	1.585	1.242
	MLPNN1	0.882	0.934	1.576	1.261	0.884	0.937	1.715	1.370
	ANFIS3	0.954	0.976	1.005	0.787	0.943	0.971	1.233	0.965
	ANFIS2	0.918	0.956	1.330	1.020	0.908	0.953	1.571	1.230
	ANFIS1	0.882	0.934	1.577	1.261	0.887	0.938	1.699	1.361
Donja Dobra	MLPNN3	0.972	0.986	1.406	1.047	0.964	0.982	1.460	1.083
	MLPNN2	0.935	0.966	2.118	1.545	0.919	0.957	2.167	1.619
	MLPNN1	0.890	0.939	2.724	2.061	0.874	0.931	2.659	2.040
	ANFIS3	0.972	0.985	1.416	1.056	0.963	0.981	1.469	1.088
	ANFIS2	0.935	0.966	2.117	1.544	0.918	0.956	2.174	1.630
	ANFIS1	0.891	0.940	2.721	2.060	0.873	0.930	2.673	2.048
Donja Mrežnica	MLPNN3	0.980	0.990	1.274	0.990	0.978	0.989	1.334	1.040
	MLPNN2	0.923	0.959	2.479	1.828	0.923	0.959	2.450	1.801
	MLPNN1	0.882	0.934	3.042	2.374	0.873	0.930	3.115	2.417
	ANFIS3	0.980	0.990	1.297	1.002	0.978	0.989	1.334	1.034
	ANFIS2	0.923	0.959	2.476	1.828	0.923	0.959	2.453	1.798
	ANFIS1	0.882	0.934	3.041	2.374	0.873	0.930	3.117	2.418
Gornja Dobra	MLPNN3	0.919	0.956	1.225	0.925	0.907	0.951	1.724	1.361
	MLPNN2	0.852	0.915	1.630	1.200	0.823	0.901	2.323	1.838
	MLPNN1	0.839	0.906	1.693	1.265	0.794	0.884	2.492	1.874
	ANFIS3	0.916	0.954	1.251	0.948	0.907	0.951	1.716	1.377
	ANFIS2	0.852	0.915	1.630	1.198	0.824	0.902	2.316	1.830
	ANFIS1	0.838	0.906	1.696	1.267	0.814	0.894	2.364	1.858
Korana	MLPNN3	0.975	0.987	1.552	1.222	0.969	0.982	1.763	1.408
	MLPNN2	0.932	0.964	2.537	1.933	0.917	0.950	2.831	2.227
	MLPNN1	0.915	0.954	2.823	2.175	0.904	0.949	2.960	2.322
	ANFIS3	0.974	0.986	1.603	1.258	0.968	0.982	1.793	1.435
	ANFIS2	0.933	0.964	2.530	1.933	0.917	0.951	2.823	2.200
	ANFIS1	0.915	0.954	2.823	2.175	0.904	0.949	2.961	2.324
Slunjčica	MLPNN3	0.952	0.975	0.767	0.580	0.938	0.956	0.882	0.655
	MLPNN2	0.922	0.958	0.967	0.715	0.909	0.939	1.028	0.765
	MLPNN1	0.853	0.915	1.305	0.979	0.851	0.920	1.209	0.927
	ANFIS3	0.951	0.974	0.771	0.582	0.939	0.957	0.872	0.627
	ANFIS2	0.922	0.958	0.965	0.715	0.909	0.939	1.024	0.764
	ANFIS1	0.853	0.915	1.305	0.978	0.852	0.920	1.208	0.926

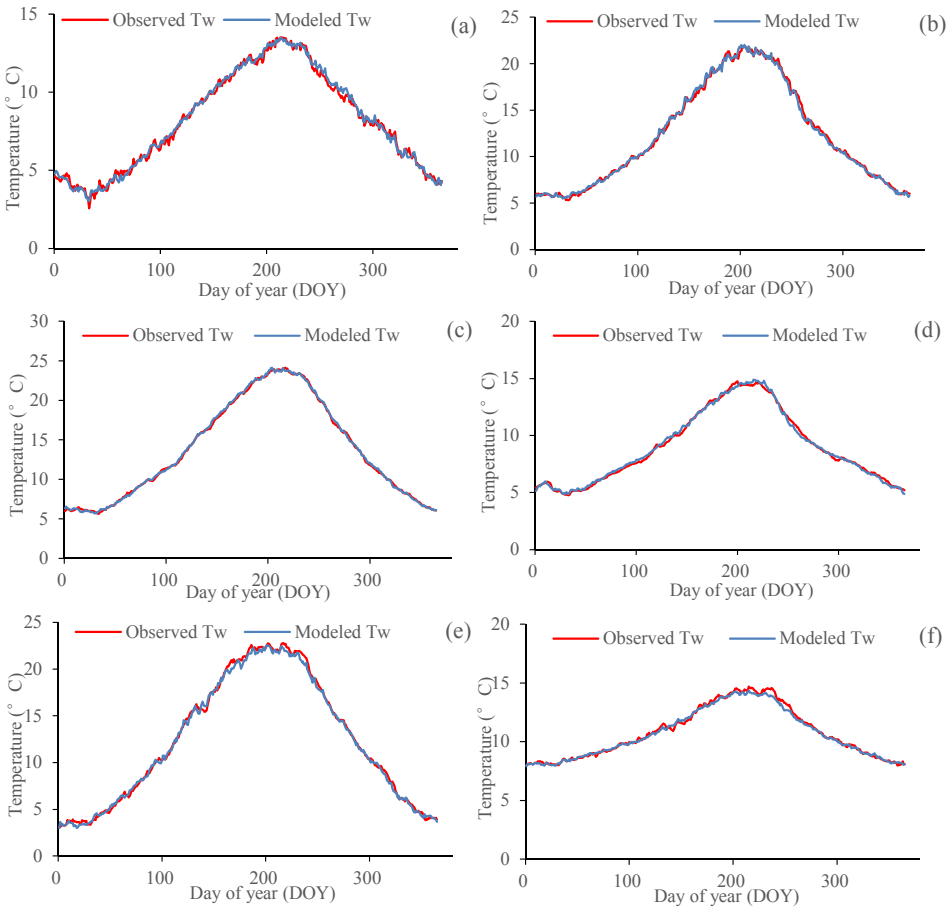

Fig. 8. Modeling performances of the MLPNN3 for the climatological year at the six rivers: (a) Čabranka, (b) Donja Dobra, (c) Donja Mrežnica, (d) Gornja Dobra, (e) Korana, and (f) Slunjčica.

Bereitgestellt von University Library Bratislava | Heruntergeladen 31.01.20 12:22 UTC

Acknowledgements. We acknowledge the Croatian Meteorological and Hydrological Service for providing the water temperature, air temperature and river flow discharge data used in this study. This work was jointly funded by the National Key R&D Program of China (2018YFC0407203, 2016YFC0401506), China Postdoctoral Science Foundation (2018M640499) and the research project from Nanjing Hydraulic Research Institute (Y118009).

REFERENCES

Albek, M., Albek, E., 2009. Stream temperature trends in Turkey. Clean Soil Air & Water, 37, 142–149.

Ayllón, D., Almodóvar, A., Nicola, G.G., Parra, I., Elvira, B., 2012. A new biological indicator to assess the ecological status of Mediterranean trout type streams. Ecological Indicators, 20, 295–303.

Bonacci, O., Andrić, I., 2010. Impact of an inter-basin water transfer and reservoir operation on a karst open streamflow hydrological regime: an example from the Dinaric karst (Croatia). Hydrological Processes, 24, 3852–3863.

Bonacci, O., Trninić, D., Roje-Bonacci, T., 2008. Analysis of the water temperature regime of the Danube and its tributaries in Croatia. Hydrological Processes, 22, 1014–1021.

Chen, D., Hu, M., Guo, Y., Dahlgren, R.A., 2016. Changes in river water temperature between 1980 and 2012 in Yongan watershed, eastern China: magnitude, drivers and models. Journal of Hydrology, 533, 191–199.

Cingi, S., Keinänen, M., Vuorinen, P.J., 2010. Elevated water temperature impairs fertilization and embryonic development of whitefish Coregonus lavaretus. Journal of Fish Biology, 76, 502–521.

Cox, B.A., Whitehead, P.G., 2009. Impacts of climate change scenarios on dissolved oxygen in the River Thames, UK. Hydrology Research, 40, 138–152.

DeWeber, J.T., Wagner, T., 2014. A regional neural network ensemble for predicting mean daily river water temperature. Journal of Hydrology, 517, 187–200.

Feng, M., Zolezzi, G., Pusch, M., 2018. Effects of thermopeaking on the thermal response of alpine river systems to heatwaves. Science of the Total Environment, 612, 1266–1275.

Frančišković-Bilinski, S., Bhattacharya, A.K., Bilinski, H., Bhattacharya, B.D., Mitra, A., Sarkar, S.K., 2012. Fluvial geomorphology of the Kupa River drainage basin, Croatia: a perspective of its application in river management and pollution studies. Zeitschrift für Geomorphologie, 56, 93–119.

Fullerton, A.H., Torgersen, C.E., Lawler, J.J., Steel, E.A., Ebersole, J.L., Lee, S.Y., 2018. Longitudinal thermal heterogeneity in rivers and refugia for coldwater species: effects of scale and climate change. Aquatic Sciences, 80, 3.

Gooseff, M.M., Strzepek, K., Chapra, S.C., 2005. Modeling the potential effects of climate change on water temperature downstream of a shallow reservoir, lower Madison River, MT. Climatic Change, 68, 331–353.

Hadzima-Nyarko, M., Rabi, A., Šperac, M., 2014. Implementation of artificial neural networks in modeling the water-air temperature relationship of the river Drava. Water Resources Management, 28, 1379–1394.

Hardenbicker, P., Viergutz, C., Becker, A., Kirchesch, V., Nilson, E., Fischer, H., 2017. Water temperature increases in the river Rhine in response to climate change. Regional Environmental Change, 17, 299–308.

Heddam, S., 2016. New modelling strategy based on radial basis function neural network (RBFNN) for predicting dissolved oxygen concentration using the components of the Gregorian calendar as inputs: case study of Clackamas River, Oregon, USA. Modeling Earth Systems & Environment, 2, 1–5.

Heddam, S., Kisi, O., 2017. Extreme learning machines: a new approach for modeling dissolved oxygen (DO) concentration with and without water quality variables as predictors. Environmental Science and Pollution Research, 24, 16702–16724.

Isaak, D.J., Wollrab, S., Horan, D., Chandler, G., 2012. Climate change effects on stream and river temperatures across the northwest U.S. from 1980–2009 and implications for salmonid fishes. Climatic Change, 113, 499–524.

Jackson, F.L., Fryer, R.J., Hannah, D.M., Millar, C.P., Malcolm, I.A., 2018. A spatio-temporal statistical model of maximum daily river temperatures to inform the management of Scotland's Atlantic salmon rivers under climate change. Science of the Total Environment, 621, 1543–1558.

Kim, J.H., Park, H.J., Hwang, I.K., Han, J.M., Kim, D.H., Oh, C.W., Lee, J.S., Kang, J.C., 2017. Toxic effects of juvenile sablefish, *Anoplopoma fimbria* by ammonia exposure at different water temperature. Environmental Toxicology and Pharmacology, 54, 169–176.

Leblanc, R.T., Brown, R.D., Fitzgibbon, J.E., 1997. Modeling the effects of land use change on the water temperature in unregulated urban streams. Journal of Environmental Management, 49, 445–469.

Lepori, F., Pozzoni, M., Pera, S., 2014. What drives warming trends in streams? A case study from the Alpine Foothills. River Research and Applications, 31, 663–675.

Markovic, D., Scharfenberger, U., Schmutz, S., Pletterbauer, F., Wolter, C., 2013. Variability and alterations of water temperatures across the Elbe and Danube River Basins. Climatic Change, 119, 375–389.

Moatar, F., Gailhard, J., 2006. Water temperature behaviour in the River Loire since 1976 and 1881. Comptes Rendus Geoscience, 338, 319–328.

Null, S.E., Viers, J.H., Deas, M.L., Tanaka, S.K., Mount, J.F., 2013. Stream temperature sensitivity to climate warming in California's Sierra Nevada: impacts to coldwater habitat. Climatic Change, 116, 149–170.

Orr, H.G., Simpson, G.L., des Clers, S., Watts, G., Hughes, M., Hannaford, J., Dunbar, M.J., Laizé, C.L.R., Wilby, R.L., Battarbee, R.W., Evans, R., 2015. Detecting changing river temperatures in England and Wales. Hydrological Processes, 29, 752–766.

Pekárová, P., Miklánek, P., Halmová, D., Onderka, M., Pekár, J., Kučárová, K., Liová, S., Škoda, P., 2011. Long-term trend and multi-annual variability of water temperature in the pristine Bela River basin (Slovakia). Journal of Hydrology, 400, 333–340.

Piotrowski, A.P., Napiorkowski, M.J., Napiorkowski, J.J., Osuch, M., 2015. Comparing various artificial neural network types for water temperature prediction in rivers. Journal of Hydrology, 529, 302–315.

Rice, K.C., Jastram, J.D., 2015. Rising air and stream-water temperatures in Chesapeake Bay region, USA. Climatic Change, 128, 127–138.

Schär, C., Vidale, P.L., Lüthi, D., Frei, C., Häberli, C., Liniger, M.A., Appenzeller, C., 2004. The role of increasing temperature variability in European summer heatwaves. Nature, 427, 332–336.

Sohrabi, M.M., Benjankar, R., Tonina, D., Wenger, S.J., Isaak, D.J., 2017. Estimation of daily stream water temperatures with a Bayesian regression approach. Hydrological Processes, 31, 1719–1733.

Temizyurek, M., Dadaser-Celik, F., 2018. Modelling the effects of meteorological parameters on water temperature using artificial neural networks. Water Science and Technology, 77, 1724–1733.

Bereitgestellt von University Library Bratislava | Heruntergeladen 31.01.20 12:22 UTC

Toffolon, M., Piccolroaz, S., 2015. A hybrid model for river water temperature as a function of air temperature and discharge. Environmental Research Letters, 10, 114011.

van Vliet, M.T.H., Ludwig, F., Zwolsman, J.J.G., Weedon, G.P., Kabat, P., 2011. Global river temperatures and sensitivity to atmospheric warming and changes in river flow. Water Resources Research, 47, 247–255.

van Vliet, M.T.H., Franssen, W.H.P., Yearsley, J.R., Ludwig, F., Haddeland, I., Lettenmaier, D.P., Kabat, P., 2013. Global river discharge and water temperature under climate change. Global Environmental Change, 23, 450–464.

Webb, B.W., Clack, P.D., Walling, D.E., 2003. Water–air temperature relationships in a Devon river system and the role of flow. Hydrological Processes, 17, 3069–3084.

Žganec, K., 2012. The effects of water diversion and climate change on hydrological alteration and temperature regime of karst rivers in central Croatia. Environmental Monitoring and Assessment, 184, 5705–5723.

Zhu, S., Heddam, S., Nyarko, E.K., Hadzima-Nyarko, M., Piccolroaz, S., Wu, S., 2019. Modeling daily water temperature for rivers: comparison between adaptive neuro-fuzzy inference systems and artificial neural networks models. Environmental Science and Pollution Research, 26, 402–420.

Received 17 January 2019
Accepted 13 March 2019

Bereitgestellt von University Library Bratislava | Heruntergeladen 31.01.20 12:22 UTC

J. Hydrol. Hydromech., 67, 2019, 4, 314–321
DOI: 10.2478/johh-2019-0021

Adaptive stochastic management of the storage function for a large open reservoir using an artificial intelligence method

Tomas Kozel*, Milos Stary

Brno University of Technology, Faculty of Civil Engineering, Institute of Landscape Water Management, Veveří 331/95, Brno, Czech Republic.
*Corresponding author. E-mail: kozel.t@fce.vutbr.cz

Abstract: The design and evaluation of algorithms for adaptive stochastic control of reservoir function of the water reservoir using artificial intelligence methods (learning fuzzy model and neural networks) are described in this article. This procedure was tested on an artificial reservoir. Reservoir parameters have been designed to cause critical disturbances during the control process, and therefore the influences of control algorithms can be demonstrated in the course of controlled outflow of water from the reservoir. The results of the stochastic adaptive models were compared. Further, stochastic model results were compared with a resultant course of management obtained using the method of classical optimisation (differential evolution), which used stochastic forecast data from real series (100% forecast). Finally, the results of the dispatcher graph and adaptive stochastic control were compared. Achieved results of adaptive stochastic management provide inspiration for continuing research in the field.

Keywords: Stochastic; Artificial intelligence; Storage function; Optimisation.

INTRODUCTION

Water shortage problems have begun to appear in the whole of the Czech Republic (Crhová et al., 2019). Water shortage manifests from the prolonging and deepening of dry seasons. This reality leads to growing tension between capacity of water resources and water user demand. Many problems with water demand occurred in 2015, 2016 and 2018. Long-term average flow Q_a is decreasing due to lower values of flow in river networks and prolonging of the dry season, because the low flow rates will not be able to sufficiently dilute the pollutants entering into them.

Assumed future values could decrease to 0.8 Q_a or even lower values (Kašpárek, 2005). This decrease will not only impact water supply, but it could even influence quality of water. Some rivers can be transformed to drains in the worst scenario, because the low flow rates will not be able to sufficiently dilute the pollutants entering into them. If new large water reservoirs were built, it would lead to an improvement of the current situation. But construction of new large water reservoirs is complicated nowadays. Therefore, optimised current management of reservoirs is required.

Controlling the outflow of water from the reservoir will be understood in the following text as a strategic management of storage function of the reservoir using monthly time steps. Reservoir control is the management of an isolated reservoir with a single inflow of water and one regulated flow.

At the level of average monthly flows, water flows in streams can be considered as random (stochastic) processes (sequences) for which their future values cannot be accurately determined (Hirsh, 1979; Svanidze, 1961). Probability of their future occurrence can be estimated. Therefore, it is a great simplification to predict their values deterministically. However, a deterministic prediction of a random process can be burdened with a major error, and its use for system control can be misleading. This problem should be approached stochastically, at least to quantify the range of their possible occurrence with a certain probability distribution. A range of possible occurrences increases with increasing prediction length.

It follows from the previous paragraph that, when using only one value (deterministic control), there is a significant simplification of the problem, loss of management accuracy or mistaken assessment of the situation (values of real inflow to reservoir may differ significantly from what was assumed). On the other hand, stochastic control allows us to work with a certain scatter of values of controlled outflows (with a given probability distribution). Proper risk assessment and grasping of the options offered by the approach is able to significantly reduce failure risk of the managed reservoir's supply function. A range of controlled outflows will therefore provide us with a choice of managed outflow based on the probability of overtaking. Therefore, it is desirable to shift from a deterministic control to a stochastic one.

METHODS

Managing the storage function of the reservoir in an adaptive way (one of the methods of artificial intelligence) allows the problem of controlling the storage function of the reservoir, with a consideration of stochastic flow forecasting, to be very well described. In the transition from deterministic to stochastic control of outflows in adaptive management, use of models based on the Monte Carlo method is offered. The principle of the Monte Carlo method is applied in constructing forecasts that are extrapolations of historically measured flow lines to which a random component is repeatedly added. In this way, a fan of possible future combinations of water inflows into the reservoir is created. Use of optimisation algorithms to control outflow of water from a reservoir brings the problem of computer performance limitations (high machine time requirements for calculation). For a reasonable evaluation of repeated random states, at least 300 repetitions of the calculation are required. Stochastic adaptive control will be understood in the following text as a control of storage function of reservoir, in which future controlled outflows are calculated from actual value of storage volume and the spectrum of random generated inflows of given length (number of members of the series of forecasted average flows). Therefore, for each forecast the

Bereitgestellt von University Library Bratislava | Heruntergeladen 31.01.20 12:22 UTC

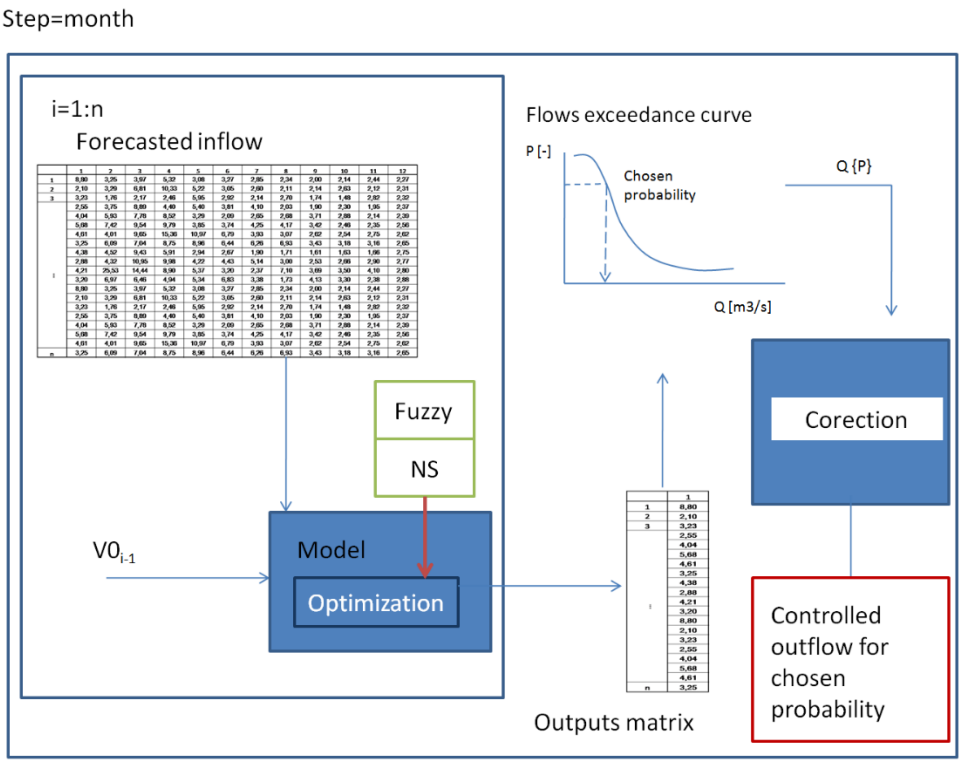

Fig. 1. Schema of main algorithm.

optimal course of controlled outflow is repeatedly sought. Controlled outflow values are then processed into an exceedance curve, and a controlled outflow value with a specified probability of exceedance is used for control. Simplified schema of the main process is in Figure 1.

If the reservoir fill volume values are considered based on actual measured values and inflow forecasts based on the measured data, control algorithms described in the article can be used for operational control of the reservoir's storage function in real time.

Here, the Differential Evolution method DE as an optimization method for controlling was chosen (Price et al., 2005; Storn and Price, 1997), and the DE method search area of acceptable solutions Ω, with a number of dimensions equal to number of forecasted members in forecasted inflow line, was used. The DE method quantifies a series of outflows of water from the reservoir for specified initial volume of water in the reservoir and predicted water inflows into the reservoir during the solving period. The optimisation criterion is the sum of differences of second powers between target (improved) average monthly water outflow from the reservoir O_p and a series of controlled average monthly outflows of water from reservoir O which is minimized:

$$\pi = \left[\sum_{j=1}^{N} \left(O_P - O_j \right)^2 \right] \rightarrow MIN, \qquad (1)$$

where O_P is value of the target outflow (mean monthly improved outflow), O_j is value of the calculated controlled average monthly outflow, N is number of months, j is number of months and π is value of the critical function.

The choice of this criterion implicitly introduces long and shallow disturbances in the malfunctioning fault periods (which is desirable) in an effort to avoid short deep failures that are problematic from the point of view of reservoir management.

The disadvantage of this control method using the DE optimisation method is the large machine demands for calculation. It is possible to use Artificial Intelligence (UI) methods, which are capable of replacing the DE method with a certain loss of accuracy.

From Artificial Intelligence Methods, a learning fuzzy model of the Mamdani type (Sugeno, 1977; Tagaki and Sugeno, 1985) was chosen and a neural network containing a three-layer perceptron network (Caudill and Butler, 1992) was selected. UI methods are very well described (Donald et al., 1994). Model schemes are shown in Figures 2 and 3. The learned fuzzy model uses the step-by-step aggregation of inputs described (Janál and Starý, 2009; Janál and Starý, 2012), which allows easy creation of a matrix of rules for fuzzy models with more than two inputs.

For this purpose, the DE method was used in advance to construct a matrix of target behaviour patterns of the controlled reservoir (training matrix). It then served to train the learning system, i.e. to find a generalised relationship between the status of the reservoir and the used controlled outflow. The state of the reservoir is described by its immediate filling and the predicted monthly inflow vector.

When using the basic equation of the reservoir in differential shape, the relation between the average monthly inflows Q^τ and the average monthly outflows O^τ and the volume of the water in the tank at the beginning of the time step $V^{\tau-1}$ and the volume at the end of the time step V^τ is given in the time step τ with duration Δt by relationship (2)

$$Q^\tau - O^\tau = \frac{V^\tau - V^{\tau-1}}{\Delta t} \qquad (2)$$

For the time step $\tau = 1$, V_0 is the initial condition. The members of the series O^τ for $\tau = 1, 2, ..., N$ can acquire infinitely many values that depend on the filling reservoir and how to control outflow of water from the reservoir.

Bereitgestellt von University Library Bratislava | Heruntergeladen 31.01.20 12:22 UTC

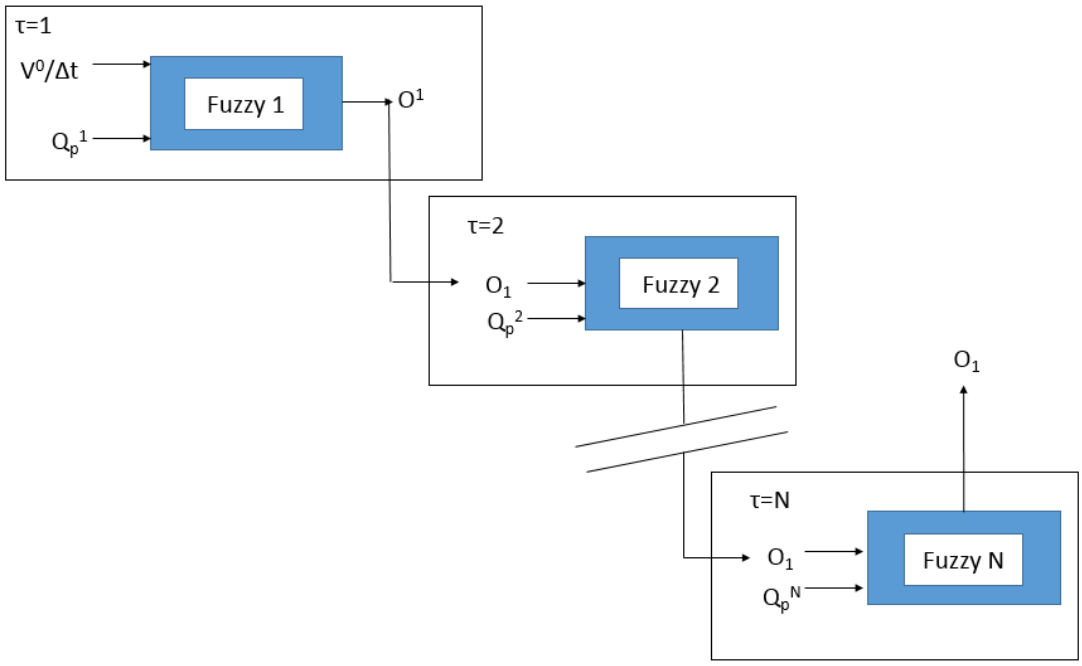

Fig. 2. Schema of learned fuzzy model SA for forecast with length N.

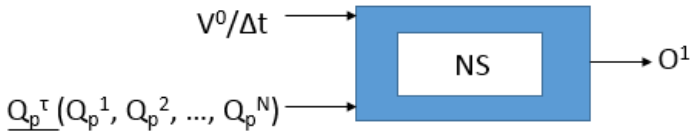

Fig. 3. Schema of trained NS model for forecast with length N.

For the control algorithm alone, Q series (boundary conditions) is replaced by a series of forecast Q_p (inflow forecasting vector) for each solution of task in relation (2) at each step and adaptive recurrent control is performed for all time steps τ. The initial volume of water in reservoir V_0 is replaced by volume obtained in the real-time operation. For simulation of control, V_0 for repeated calculation is replaced by V^1 of the previous calculation.

If the value of $\tau > 1$ is the initial condition, $V^{\tau-1}$ for each additional time step τ is calculated according to Equation (2) in which the predicted value is used instead of real inflow value, which is considered to be a real value for calculation, and the value of the outflow is calculated from the previous time step. Before starting the next calculation step, it is necessary to calculate actual value of the storage volume according to Equation (2). The outflow of the water from the reservoir, which is controlled to O_p (target outflow) value, can take values from the interval (0, O_p >. If the capacity of the reservoir volume is unable to absorb excess water, the outflow of water from reservoir may be higher than O_p. If the controlled outflow values discharged from the reservoir are lower than O_p, a fault occurs. The aim of the algorithm is to perform a control in which the value of the π criterion is minimised according to Equation (1).

Forecasts are generated by the hybrid zonal model described (Kozel and Starý, 2016). In the following text, the forecasting model is only briefly indicated. The forecasting model is a combination of the linear autoregression model described, for example, by Brockwell and Davis (1991) and the zonal model described by Marton et al., 2015. Average monthly flows of historical series are sorted from the smallest to the largest by month with the last measured flow and divided into a predetermined number of zones. Average monthly flows of the real flow line in the given zone and their subsequent course (the length is determined by length of the flow forecast) form the working area of flows (zones). Other historical flows of the real flow line are not used for forecasts. The modified zonal model differs by applying a linear autoregressive model to the selected zone. Historically, measured flows are converted to the level Z (standard normal distribution), so the first data is deprived of asymmetry by the Box-Cox equation (level Y, assumption of the normalised distribution) (Box and Cox, 1964) and subsequently transformed to level Z by standard transformation relationships between normal and normal standard divisions. The zone is determined for the working month according to the latest measured flow. The correlation matrix, which is the basic input for Yule-Walker equations (Yule, 1927; Walker, 1931), is calculated only from historically measured flows occurring in the assigned zone. For the rest of the data, the model does not have access to the correlation matrix. From the assembled correlation matrix, using the Yule-Walker equations, regression coefficients and Q_p predictions are calculated for a given period. When applying a forecasting model, simplistic assumptions have been introduced so that average monthly inflow to the reservoir is considered a random process.

During construction of artificial flow generators, the uncertainty of flow measurement in the measurement station profile was neglected. To simplify the task, the uncertainties of input data as well as water losses associated with the reservoir operation were neglected.

All of these algorithms have been programmed in the Matlab software environment.

Bereitgestellt von University Library Bratislava | Heruntergeladen 31.01.20 12:22 UTC

APPLICATION

Fig. 4. Location of measured profile Bílovice nad Svitavou.

Stochastic control was applied to a fictitious water tank designed for this purpose in the measuring profile of Bílovice nad Svitavou. Figure 4 shows the position of the profile. The profile was chosen due to availability of data at the workplace and a long series of real average monthly flows that is very little influenced by management of the large water reservoir located at the top of the river basin. Reservoir parameters and target outflow are designed to cause sufficiently long and deep failures during its management, allowing the methods used to control its storage function to demonstrate their effectiveness. The storage volume was set at 51 811 000 m^3 and the target outflow from the reservoir O_p at a constant value of 4.25 m^3/s.

An 89-year long series of average monthly flows (from 1921 to 2009) was used for construction and subsequent validation of the forecasting model of water inflow into the reservoir. The series was made by measuring the profile of Bílovice nad Svitavou, located on the Svitavy river. The series was divided into two parts. The first 75 years were used to calibrate forecasting models (modules) and were used for model validation for the last 14 years. Flows in each month have different probability distributions, so their transformation has been transformed into a single distribution (normalised normal distribution). There were 12 transformational relationships. The transformation itself was described in the previous text.

For the construction of the target matrix TM, the period 1981–1995 was chosen and the years 1996–2009 were used as the validation period. The TM construction period was selected in view of increased occurrence of drought periods, which are problematic from the point of view of the storage function of reservoir management. If an entire real series (outside the validation period) is selected for the TM construct, the TM would contain a large amount of data which is not problematic from the point of view of storage function, and would obscure the relationship between inputs and outputs. The TM was created from results of the DE method which used real-time series segment (100% forecast). For each forecasting length (number of forward months to be driven) 1 to 12, TM was compiled. For the training of models based on NS neural networks, the backward propagation method was used and fuzzy C-means methods (Bezdec, 1981) were used to learn the fuzzy model for a pre-assembled matrix of rules.

After calibration of both models based on the UI methods (fuzzy model SA, a model containing the NS neural network) validation was made, where progressive slides from the real flow line (100% forecast) were used instead of average monthly flow forecasts. In this way, the maximum achievable effects of management using UI methods were determined. The results for the SA model are shown in Figure 5 (prediction length is 6 months). There is a certain loss of accuracy over the DE method shown in Figure 5 which consists of three graphs. The first contains the average monthly inflows for the validation period. The other two charts show the course of controlled volumes (middle chart) and controlled outflow for the SA model and DE method for the same period.

After learning the SA and NS control models, they were applied in the validation period using stochastic predictions of water inflows into the reservoir. As inputs to the models, the volume of water in the reservoir at the start of the solution has always been used for each predicted period and a set of corresponding forecasted vectors (created by the hybrid zonal model). For each predicted period, 1000 prediction vectors were always created. After the model provided control for all predictions, an empirical overflow line was constructed for the first controlled outflow of water from the reservoir by Čegodajev formula (Keylock, 2012). The overflow line was further smoothed out by polynomial using the built-in function of program matlab pchip (Kahaner et al., 1988). Then, the value of the controlled outflow that was applied for the first step was deducted for the chosen probability of the exceedance. The above procedure was applied for given probability of overrun at all time steps of the validation period of successive validation. In the first phase of validation, a probability of exceedance of outflow P was maintained at all times. In order to test sensitivity of the achieved effects arising out of control, depending on probability of exceeding, the value gradually changed. The elected P values were 99.9, 99, 95, 90, ..., 5, 1.

The EA model was the first to be applied. The results show that the model is not capable of managing a malfunction and generates a very short but deep fault. That is why correction was introduced in the application of controlled outflows. The correction consisted in averaging calculated controlled flow value with its previous realisations (idea taken from the conjugate gradient method). After the correction was introduced, the results improved significantly.

Bereitgestellt von University Library Bratislava | Heruntergeladen 31.01.20 12:22 UTC

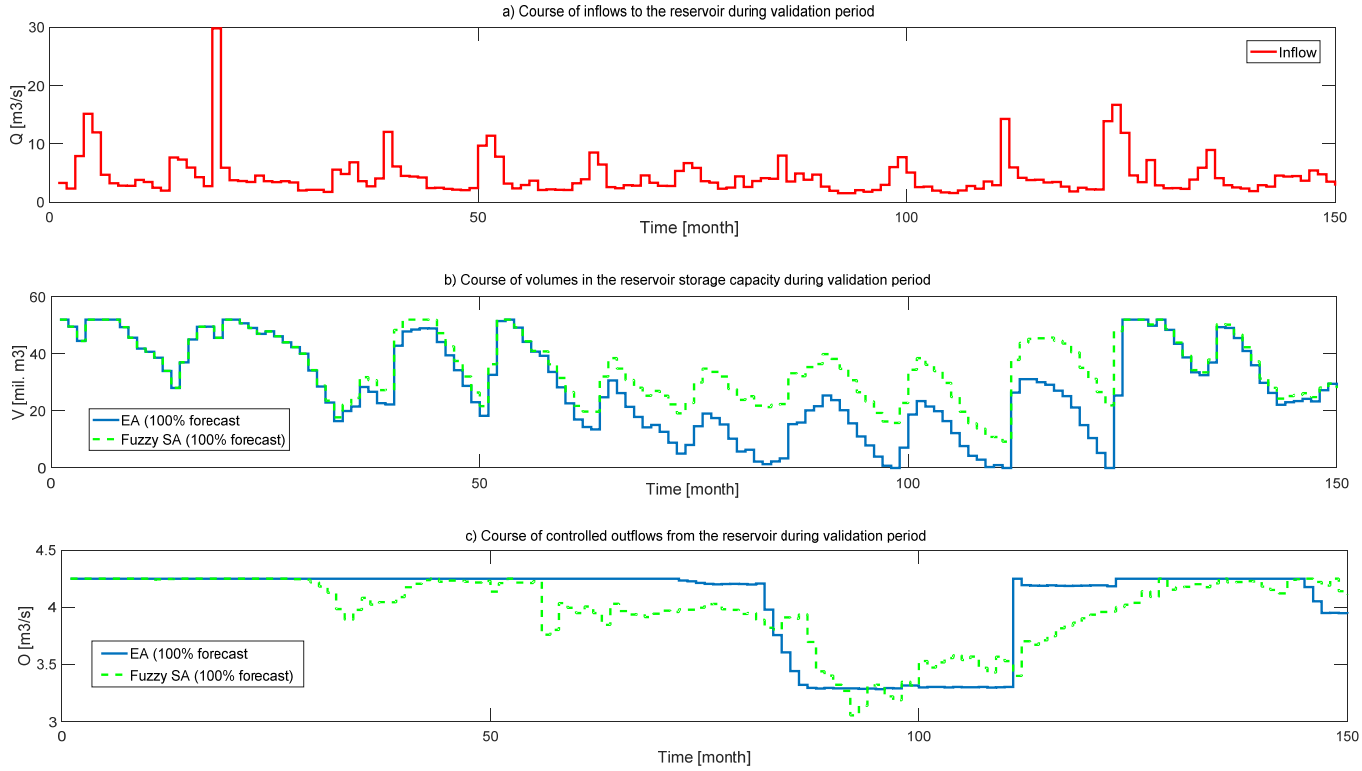

Fig. 5. Results of chosen models (for 100% forecast).

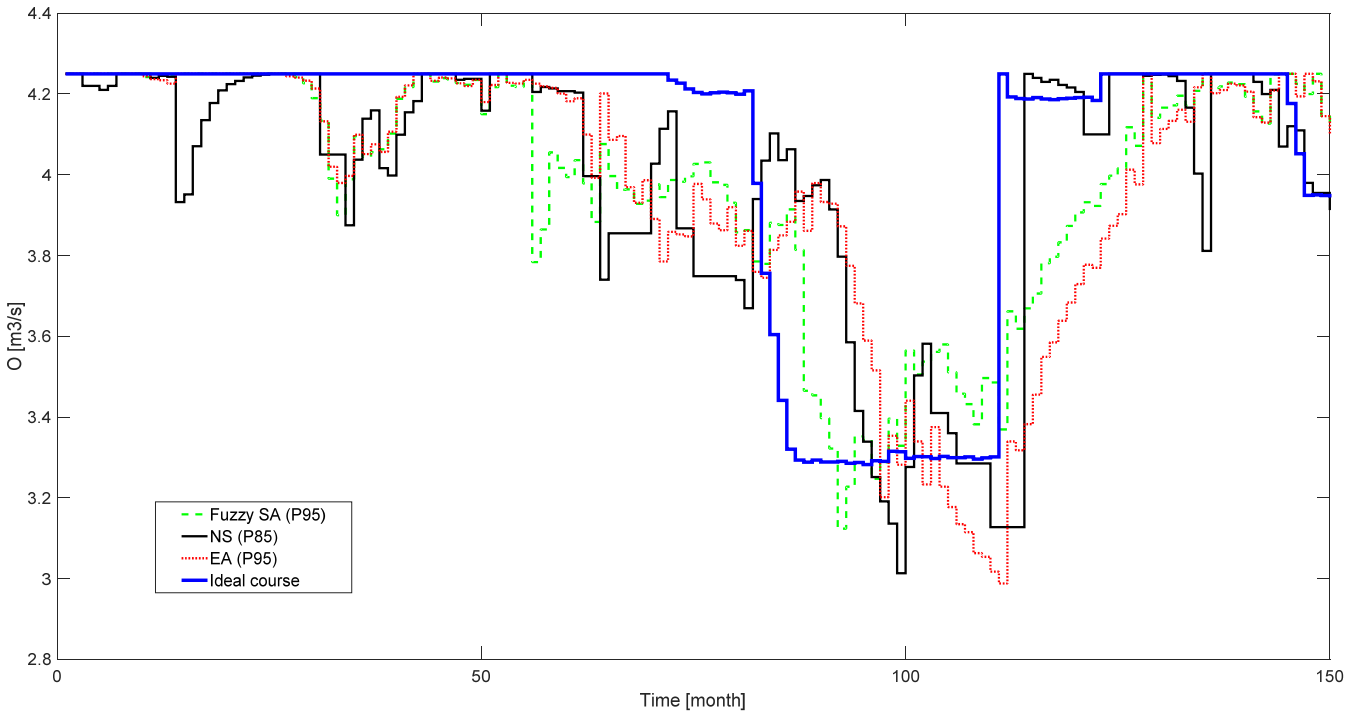

Fig. 6. Results of chosen models.

Additionally, the SA and NS models were applied. Both models again use described correction. After the correction was introduced, the results of both UI models resembled the results provided by the EA model. Selected results of models are plotted in Figure 6; the horizontal axis shows time in months and the vertical axis shows the average monthly discharge control water in the tank in m^3/s. The following figures always show the best course for the model achieved for the chosen probability of exceeding P.

It can be seen from Figure 6 that all the used control models give a similar course of controlled outflows. Therefore, other criteria were introduced to assess success. Figure 6 shows the results of the individual models and also draws the course obtained by the EA model, which used the real-time series segment as forecast (100% forecast). These results (course) will be referred to as an ideal course in the following text. The criterion E was the sum of the second powers of differences between controlled outflow provided by stochastic control using sto-

Bereitgestellt von University Library Bratislava | Heruntergeladen 31.01.20 12:22 UTC

chastic inflow forecasts and the value of the target outflow. This is the application of the relationship (1) over the entire validation period. The second criterion was the sum of the undelivered water flow rate *Er* [m^3/s]. The resulting values of 1 and 2 are shown in Table 1. In Table 1 the values for Criteria 1 and 2 (*E* and *Er*) are given for the individual methods used for control.

Table 1 shows that for the criterion 1, better results were achieved by the SA model than the ideal course (EA model with 100% predictions). According to criterion 2, the best result was the ideal management.

During the validation of the model, the total number of forecasts used and their influence on control were also tested. If the total forecasts were less than 400, there were significant differences between different control patterns for generated forecasts. For a total number of 500 or more forecasts, individual courses of controlled outflows for repeated generated predictions varied only slightly.

Furthermore, in the second phase of validation, the changes of values *P* (*P95* and *P60* quantile) during the management process were tested. Selecting P leads to change of strength management (reduction of controlled outflow at a time when enough water is in the reservoir is unnecessary). If the volume of water in the reservoir drops below 0.6 from storage volume, the value *P* changes from *P60* to *P95* and vice versa. The combination above illustrates the possibility of using a fan of possible values that provide stochastic control. The resulting process was then compared to the results of the first validation phase.

The comparison between the results of the SA model is shown in Figure 7.

Furthermore, a comparison was made between the results of the ideal course and the results provided by the stochastic control of the SA model using the combination *P* and the stochastic prediction. The results are shown in Figure 7. Finally, a comparison of the method of adaptive stochastic control (model SA with correction) with the method of dispatcher graphs, which is shown in Figure 8, was performed. The dispatcher charts were designed as zonal (five zones) according to the method mentioned (Broža, 1981).

Table 1. Values of criteria for chosen results.

Model/criterium	E [m^3/s]^2	Er [m^3/s]
SA P95	23.8	39.8
NS P85	25.6	37.9
EA P95	28.6	41.6
DG	50.5	46.5
EA 100% forecast	24.6	28.6
SA 100% forecast	24.4	40.1
SA combination P95+P60	21.6	33.7

DISCUSSION AND CONCLUSION

Stochastic adaptive control is an appropriate method for controlling the storage function of a large open reservoir. In particular, its contribution to suppressing the influence of uncertainties in development of future trends of water inflow into the reservoir can be expected. It is to be expected that future climate change and subsequent flow changes will not work well with the commonly used dispatching graph (DG) methods.

Future changes occurring in flow lines are not contained in existing historical flow lines from which DG are constructed. On the other hand, the stochastic adaptive control described is able to capture high diversity and variability of future inflows. The strong aspect of the processed algorithms is primarily generalization of input/output relationships contained in the matrix of patterns that implicitly carry artificial intelligence methods (learning fuzzy models, neural networks). Adaptive stochastic control is able to capture future climate change if the adaptive principle is applied to the target behaviour matrix and construction of forecast generation.

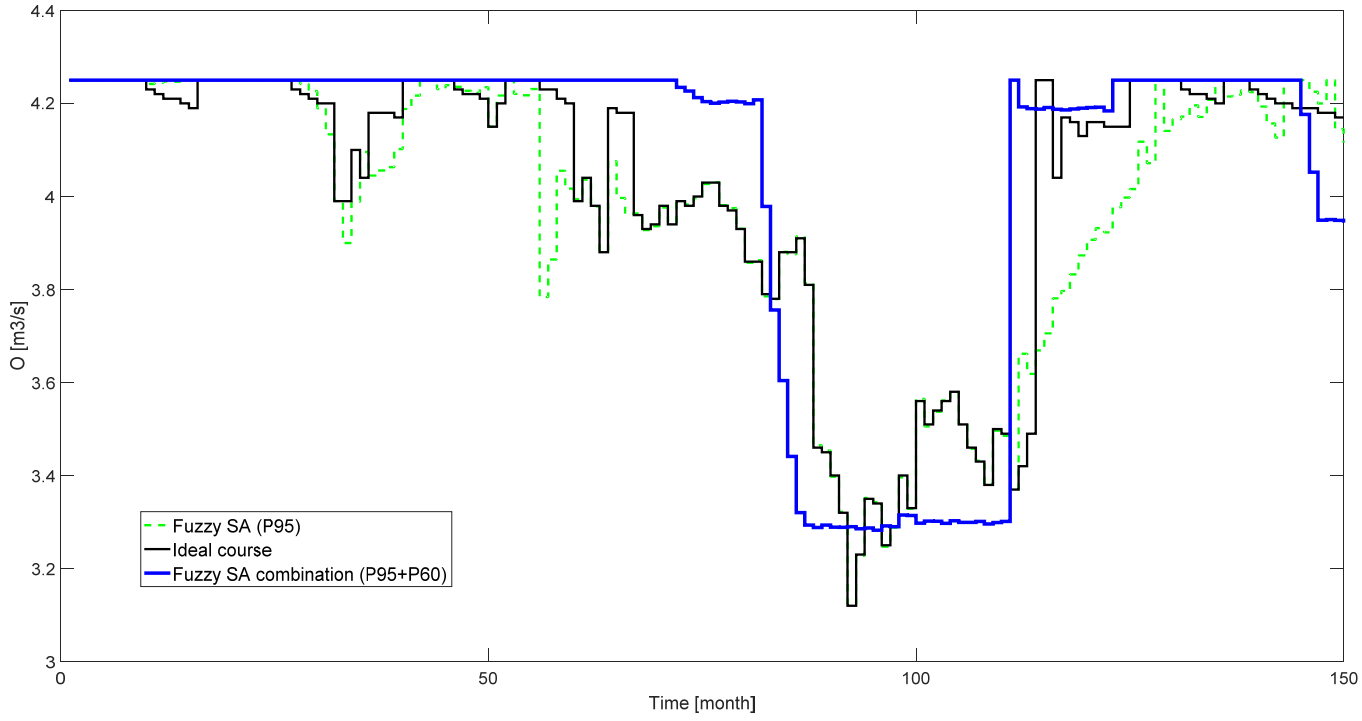

Fig. 7. Results of chosen models.

Bereitgestellt von University Library Bratislava | Heruntergeladen 31.01.20 12:22 UTC

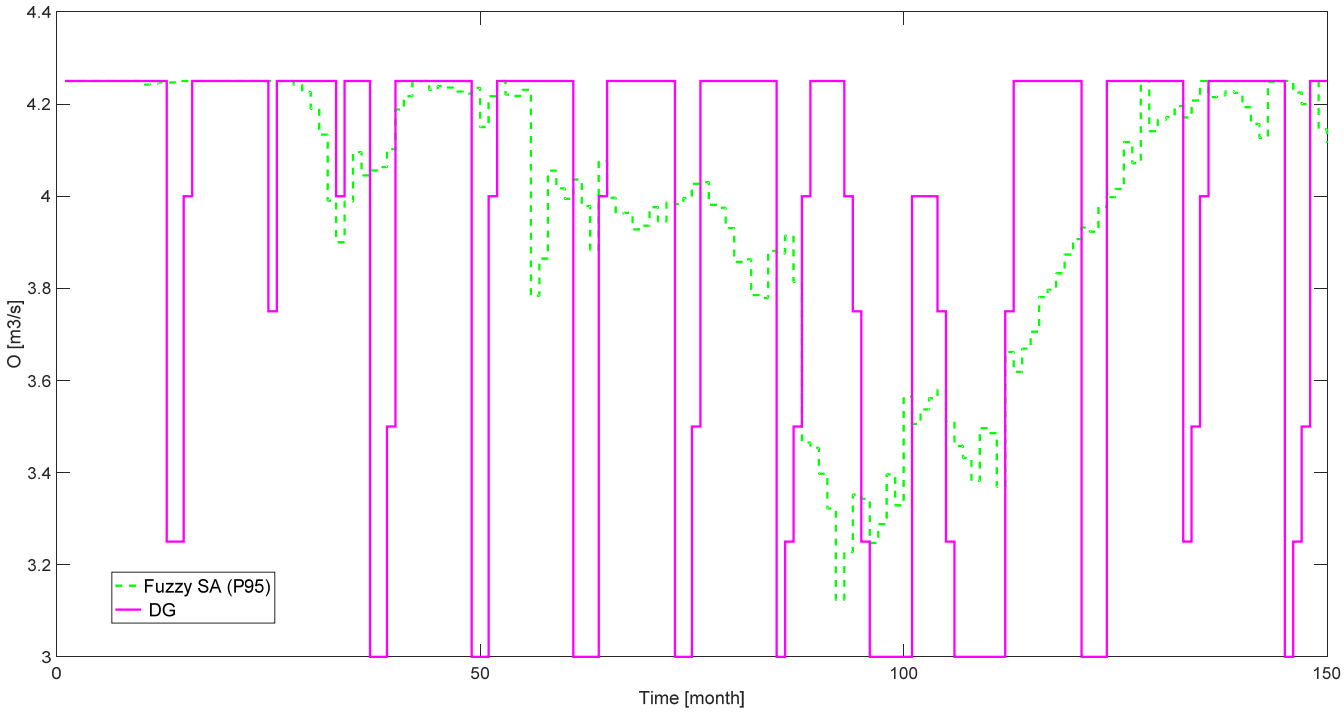

Fig. 8. Results of chosen models.

The initially poor EA results were attributed to the optimization that used the entire volume of water in the reservoir, including forecasted inflow values. This property led to lower values of *P* for emptying storage volume of the reservoir in longer dry periods. Applying the described correction has made it possible to overcome this deficiency. The correction used has proven to be very effective and desirable. The results of the SA model were even better than the ideal course for criterion E. A better result can be attributed to generalizing capabilities of the learned fuzzy model.

From the results obtained (see Table 1 and Figure 6), after introduction of the correction, SA and NS models are able to replace the EA optimization model, with a significant shortening of calculation time. The calculation time EA needed was about 7 hours for one P value. Model SA needed only 15 minutes for the same calculation and the NS model needed about 16 minutes. During stochastic control, the suitability of using parallel computations in clusters (EA model), which are able to significantly speed up often very time-consuming operations, has been proven. When using a cluster (6 PC, AMD Phenom X4 9550, 4 cores), the time required to calculate, from 7 hours to 25 minutes, has been shortened to 45 minutes. The use of the cluster opens up possibilities for using methods that would otherwise be inappropriate for their time-consuming performance. The cluster price may be considerably lower than the cost of a powerful computing centre, as clusters can be built from older PCs.

The benefit of stochastic adaptive control over use of DG is excellent in the multi-annual management of water outflow from the reservoir where use of DG is problematic. The method of adaptive stochastic control is suitable for multi-year management and, on the basis of the results obtained, it is able to successfully manage the outflow of the water in the reservoir in short and long drought seasons with suitably adjusted strength of control.

In the work, a suitable probability of exceeding outflow (the appropriate quantity) was searched for each model. The results showed that the models provided very good results for *P85* to *P95*. Higher probabilities of exceedance represent higher strength of control used. If higher probabilities of exceedance are used for choosing the controlled outflow, the corresponding value of controlled outflow is given from exceeding curve (Higher value of P corresponding with lower values of controlled outflow). It cannot be forgotten that the results depend on the total number and length of the forecast. For most models, the best results were achieved for a forecasting period of six months and a value of 3 for the correction. At the value of three for the correction, the calculated controlled outflow is averaged with the two previously controlled water outflows that were used to control two previous time steps. When replacing predictions with real inflows from the real flow line (when testing models), a longer series of average monthly flows is of course a benefit. Using stochastic predictions, the extension of a range of predicted inflow lines is beneficial only to a certain length, then increasing forecast length acts counterproductively as the forecast becomes largely inaccurate.

Additionally, a suitable number of forecasts vectors was tested. Tests have shown that it is appropriate to use at least 500 forecast vectors so that the course of controlled outflows does not vary significantly with repeated generated forecasts. A higher number of forecasts generated did not lead to a significant increase in the effects of management.

The method described above is applicable to any reservoir with a storage function. Some reservoirs in the world must work with a very high state of stress between inflows and controlled outflows. In general, the situation in the Czech Republic is different and the operation of the reservoirs is safe. The storage volume of reservoirs was designed for very high security. In operating anomalies or large changes in climate development and increasing demand for water supply, we can expect an increase and a higher frequency of disturbances and the methods described may be used.

In conclusion, the results provided by the adaptive stochastic control of the storage function of the reservoir were sufficiently positive to justify further examination.

Bereitgestellt von University Library Bratislava | Heruntergeladen 31.01.20 12:22 UTC

Acknowledgements. The article was supported by SEDECO - Sediments, ecosystem services and interrelation with floods and droughts in the AT-CZ border region, ATCZ28.

REFERENCES

Bezdec, J.C., 1981. Pattern Recognition with Fuzzy Objective Function Algorithms. Plenum Press, New York.

Box, G.E.P., Cox, D.R., 1964. An analysis of transformations. Journal of the Royal Statistical Society, Series B, 26, 211-252.

Brockwell, P.J., Davis, R.A., 1991. Time Series: Theory and Methods. 2nd edition. Springer.

Broža, V., 1981. Methodological instructions for water management solutions of reservoirs (Metodické návody k vodohospodářským řešením nádrží). ČVUT v Praze, Praha.

Caudill, M., Butler, C., 1992. Understanding Neural Networks: Computer Explorations. Vols. 1 and 2. MIT Press, Cambridge, MA.

Crhová, L., Čekal, R., Černá, L., Kimlová, M., Krejčová, K., Šádková, E., Štěpánková, B., Vrabec, M., 2019. Annual report on the hydrometeorological situation in the Czech Republic 2018. Czech Hydrometeorological Institute, Prague, Czech Republic. http://portal.chmi.cz/files/portal/docs/hydro/sucho/Zpravy/ROK_2018.pdf

Donald, M., Spiegelhalter, D.J., Taylor, C.C., 1994. Machine Learning, Neural and Statistical Classification. NJ, USA. ISBN 0-13-106360-X.

Hirsh, R.M., 1979. Synthetic hydrology and water supply reliability. Water Resources Research, 15, 6, 1603–1615.

Janál, P., Starý, M., 2009. Fuzzy model for predicting the degree of vulnerability basin flooding from torrential rains. Journal of Hydrology and Hydromechanics, 57, 3, 145–153. (In Czech.)

Janál, P., Starý, M., 2012. Fuzzy model used for the prediction of a state of emergency for a river basin in the case of a flash flood - PART 2. Journal of Hydrology and Hydromechanic, 60, 3, 162–173.

Kahaner, D., Moler, C., Stephen, N., 1988. Numerical Methods and Software. Prentice Hall, Upper Saddle River, NJ.

Kašpárek, L., 2005. Estimation of the volume of reservoir required to compensate for the drop in runoff due to climate change. VÚV, Prague. (In Czech.)

Keylock, C.J., 2012. A resampling method for generating synthetic hydrological time series with preservation of cross-correlative structure and higher-order, Properties. Water Resour. Res., 48, 12.

Kozel, T., Starý, M., 2016. Zone stochastic forecasting model for management of large open water reservoir with storage function. In: SGEM Conference Proceedings. STEF92 Technology Ltd., Sofia, Bulgaria.

Marton, D., Menšík, P., Starý, M., 2015. Using predictive model for strategic control of multi-reservoir system storage capacity. Procedia Engineering, 119, 994–1002.

Price, K., Storn, R., Lampinen, J., 2005. Differential Evolution: A Practical Approach to Global Optimization. Springer-Verlag Berlin.

Storn, R., Price, K., 1997. Differential evolution - a simple and efficient heuristic for global optimization ov er continuous spaces. Journal of Global Optimization, 11, 341–359.

Sugeno, M., 1977. Fuzzy Measures and Fuzzy Integrals. In: Gupta M.M., Saridis, G.N., Ganies, B.R. (Eds.): Fuzzy Automata and Decision Processes. North-Holand, New York, pp. 89–102.

Svanidze, G.G., 1961. Mathematical Modelling of Hydrological Series and Some Problems of Long-Term River Runoff Control, AN Gruz. SSSR, 1961, Vol. 14. p. 189–216.

Tagaki, H., Sugeno, M., 1985. Fuzzy identification of systems and its applications to modelling and control. IEEE Transactions on Systems, Man and Cybernetics, SMC-15, 1, 116–132.

Yule, G.U., 1927. On a method of investigating periodicities in disturbed series, with special reference to Wolfer's sunspot numbers. Philosophical Transactions of the Royal Society of London, Series A, 226, 267–298.

Walker, G., 1931. On periodicity in series of related terms. Proceedings of the Royal Society of London, Series A, 131, 518–532.

Received 9 November 2018
Accepted 9 September 2019

Bereitgestellt von University Library Bratislava | Heruntergeladen 31.01.20 12:22 UTC

J. Hydrol. Hydromech., 67, 2019, 4, 322–328
DOI: 10.2478/johh-2019-0014

Performance of a shallow-water model for simulating flow over trapezoidal broad-crested weirs

Jaromír Říha[1*], David Duchan[1], Zbyněk Zachoval[1], Sébastien Erpicum[2], Pierre Archambeau[2], Michel Pirotton[2], Benjamin Dewals[2]

[1] Faculty of Civil Engineering, Brno University of Technology, Brno, Czech Republic.
[2] Hydraulics in Environmental and Civil Engineering (HECE), Research unit Urban & Environmental Engineering, University of Liege (ULiège), Belgium.
[*] Corresponding author. E-mail: riha.j@fce.vutbr.cz

Abstract: Shallow-water models are standard for simulating flow in river systems during floods, including in the near-field of sudden changes in the topography, where vertical flow contraction occurs such as in case of channel overbanking, side spillways or levee overtopping. In the case of stagnant inundation and for frontal flow, the flow configurations are close to the flow over a broad-crested weir with the trapezoidal profile in the flow direction (i.e. inclined upstream and downstream slopes). In this study, results of shallow-water numerical modelling were compared with seven sets of previous experimental observations of flow over a frontal broad-crested weir, to assess the effect of vertical contraction and surface roughness on the accuracy of the computational results. Three different upstream slopes of the broad-crested weir (V:H = 1:Z_1 = 1:1, 1:2, 1:3) and three roughness scenarios were tested. The results indicate that, for smooth surface, numerical simulations overestimate by about 2 to 5% the weir discharge coefficient. In case of a rough surface, the difference between computations and observations reach up to 10%, for high relative roughness. When taking into account mentioned the differences, the shallow-water model may be applied for a range of engineering purposes.

Keywords: Discharge coefficient; Frontal broad-crested weir; Shallow flow modelling; Rough weir crest.

INTRODUCTION

The hydraulics of trapezoidal broad-crested weirs (i.e. with inclined upstream and downstream slopes) is of high engineering relevance. Trapezoidal broad-crested weirs are not only common hydraulic engineering structures (hydropower, discharge measurement, etc.) but topographic features similar to both frontal, side or oblique broad-crested weirs are also observed in diverse flow configurations, such as in case of channel overbanking or when dikes (or levees) are overtopped during flood events (Fig. 1).

Fig. 1. Levee overtopping, to some extent similar to the flow over a broad-crested weir.

The hydraulics of broad-crested weirs was investigated in many experimental studies, such as Felder and Chanson (2012), Goodarzi et al. (2012), Haddadi and Rahimpour (2012), Hager and Schwalt (1994), Madadi, et al. (2013, 2014). Several of these studies highlighted the considerable influence of the weir upstream slope on the discharge coefficient. As summarized in Table 1, existing research covers a range of values of the weir upstream slope. For embankment weirs with equal upstream and downstream slopes of V:H = 1:2, Fritz and Hager (1998) determined the discharge coefficient as a function of the relative crest length, considering multiple crest configurations including the case of the broad-crested weir. Major (2013) evaluated the discharge coefficient for an upstream slope of V:H = 1:1. Sargison and Percy (2009) and Goodarzi et al. (2012) provide discharge coefficient values for smooth trapezoidal broad-crested weirs with various upstream and downstream slopes. Similarly, values of the discharge coefficient derived from extensive research are summarized in the international standard for discharge measurement ISO 4362 (1999). Tokyay and Altan-Sakarya (2011) analyzed the local head loss at positive and negative steps considering either an abrupt step or a V:H = 1:1 slope. They related the local head loss to the Froude number and the relative step height. Madadi et al. (2014) identified increased discharge coefficient up to 10% with decreasing the upstream face slope from 90° to 21°.

Pařílková et al. (2012) investigated experimentally the influence of the weir surface roughness on the discharge coefficient. For vegetated weir surface conventional flow resistance equations may also be used (Gualtieri et al., 2018).

Computational predictions of the flow profiles and discharge coefficient for overflooded obstacles and broad-crested weirs can be obtained using three-dimensional or vertical-two-dimensional models (Velísková et al., 2018). These models are based either on Eulerian methods (Hargreaves et al., 2007; Haun et al., 2011; Kirkgoz et al., 2008; Sarker and Rhodes 2004) or on meshless techniques (Xu and Jin, 2017). Depth-averaged models have also been developed to account for the strong vertical flow contraction at broad-crested weirs and the

Bereitgestellt von University Library Bratislava | Heruntergeladen 31.01.20 12:22 UTC

Table 1. Selected experimental research on flow over broad-crested weirs, with various upstream slopes (V:H = 1:Z_1, see Fig. 2).

Upstream slope Z_1	$Z_1 = 1$	$Z_1 = 2$	$Z_1 = 3$
Fritz and Hager (1998)		✓	
ISO 4362 (1999)	✓	✓	✓
Zerihun and Fenton (2007)		✓	
Sargison and Percy (2009)	✓	✓	
Tokyay and Altan-Sakarya (2011)	✓		
Goodarzi et al. (2012)	✓	✓	
Major (2013)	✓		

resulting non-hydrostatic effects, leading to a good agreement between the numerical results and experimental observations (Darvishi et al., 2017). For a range of research applications, similar models were used successfully for reproducing the hydraulics of embankment breaching (Cantero-Chinchilla et al., 2018; Castro-Orgaz and Hager, 2013).

As shown in Fig. 1, flow conditions similar to flow over broad-crested weirs are also observed in multiple situations, such as in inundation flow, for which standard shallow-water models are routinely applied (Gallegos et al. 2009; Horritt and Bates, 2001). In principle, shallow-water flow models fail to reproduce flow processes at vertical flow contractions, which may lead to errors in the numerical estimation of the overflowing discharge or the upstream head. Nonetheless, no systematic quantification of this error exists so far for various upstream and downstream weir slopes, weir roughness and a broad range of discharges. The objective of the present paper is to fill this gap by assessing systematically the performance of an operational shallow-water flow model applied to the computation of trapezoidal broad-crested weir flow with three different upstream slopes, 8 flow discharges and 3 weir roughness scenarios. The computational results are compared against existing experimental datasets (Fritz and Hager, 1998; Goodarzi et al., 2012; Major, 2013; Sargison and Percy, 2009; Tokyay and Altan-Sakarya, 2011; Zerihun and Fenton, 2007) and standards (ISO 4362, 1999). Madadi et al. (2014) tested different upstream slopes (V:H = 1:0, 1:0.29, 1:0.73, 1:1.19, 1:2.61). Therefore their experimentally determined discharge coefficients were interpolated for the slopes V:H = 1:1 and 1:2 and then compared against numerical results.

METHODS

In total 66 numerical simulations were conducted to compare computed values of the discharge coefficient C_D to existing experimental data and to a standard.

Numerical simulations

We used the numerical model WOLF developed at the University of Liege and routinely applied for research and engineering purposes (e.g., Stilmant et al., 2018). It solves the shallow-water equations, written in conservative form, by means of a finite volume scheme with a flux-vector splitting developed in-house, which is well-balanced with respect to the discretization of the pressure and bottom slope terms (Erpicum et al., 2010). The time integration is performed using a 2-step Runge–Kutta algorithm and a semi-implicit treatment of the bottom friction term is used. The time step is adaptive and computed based on the Courant–Friedrichs–Lewy (CFL) stability criterion, with a CFL number equal to 0.25. It takes values of the order of 10^{-3} s. More details on the model equations and numerical scheme are presented by Erpicum et al. (2010).

The computational domain represents a channel, with a horizontal bottom, in which various trapezoidal broad-crested weir geometries are inserted. It was discretized using a regular grid with spacing $\Delta x = 0.01$ m. Since we consider frontal flow with respect to the weir (no crosswise velocity), the width of the computational domain was limited to a single cell (of width $\Delta y = 0.01$ m); but no lateral friction was imposed. This corresponds to a vertical "slice" in a very wide channel.

The geometry of the trapezoidal broad-crested weir is sketched in Fig. 2. The numerical simulations were performed for an upstream weir height $P = 0.5$ m and a crest width $t = 0.5$ m. The upstream and downstream slopes (1:Z_1 and 1:Z_2) were varied between 1:1 and 1:3. With the considered grid spacing $\Delta x = 0.01$ m, all weir edges were exactly fitting the weir geometry.

The upstream boundary condition for the simulations was a prescribed specific discharge q at the entrance cross-section, distant 8.5 m from the upstream crest edge. The downstream end of the computational domain corresponds to the toe of the downstream slope, where free outflow was prescribed as downstream boundary condition. As the flow regime changes from subcritical to supercritical approximately at the downstream crest edge of the weir, this boundary is not modified when the weir geometry is varied. The side walls were considered as smooth impermeable boundaries.

Computations were performed for both smooth and rough weir surfaces:

- For smooth weirs, a Manning roughness coefficient $n = 0.01$ s/m$^{1/3}$ was applied (this corresponds to a Nikuradse roughness size of $k_s < 0.0002$ m), and the specific discharge was varied in-between $q = 0.02$ m^2/s and $q = 0.15$ m^2/s. The full range of upstream slopes was considered (i.e. 1:Z_1 varying between 1:1 and 1:3).
- The effect of the weir crest roughness on the discharge coefficient was studied for the set of Nikuradse roughness size $k_s = 0.014$, 0.020 and 0.024 m, for specific discharges varying from $q = 0.005$ to $q = 0.25$ m^2/s, and an upstream slope $Z_1 = 2.5$, consistently with the study of Pařílková et al. (2012).

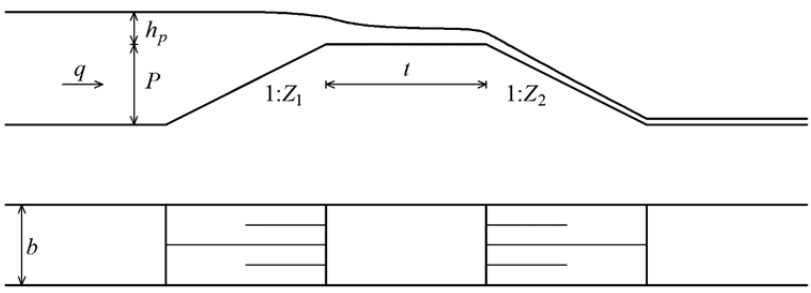

Fig. 2. Sketch of the flow over a trapezoidal broad-crested weir, with main notations.

Bereitgestellt von University Library Bratislava | Heruntergeladen 31.01.20 12:22 UTC

Reference data

Following ISO 4362 (1999), the specific discharge q passing over a frontal trapezoidal broad-crested weir with a rectangular cross-section may be computed based on the following equation:

$$q = \left(\frac{2}{3}\right)^{3/2} C_D C_v \sqrt{g} h_p^{3/2}, \quad (1)$$

where g is the acceleration of gravity and h_p the overflow head (Fig. 2). C_D represents the discharge coefficient and C_v the approach velocity coefficient calculated iteratively from this expression (ISO 4362, 1999):

$$C_v = \left\{1 + \frac{4}{27} C_v^2 \left[C_D \frac{h_p}{(h_p + P)}\right]^2\right\}^{3/2}, \quad (2)$$

where P is the upstream weir height. Dimensional analysis shows that the discharge coefficient C_D depends on seven dimensionless parameters:

$$C_D = f\left(\mathrm{R}, \mathrm{W}, \frac{h_p}{t}, \frac{h_p}{P}, \frac{h_p}{k_s}, \frac{1}{Z_1}, \frac{1}{Z_2}\right), \quad (3)$$

where R is the Reynolds number, W the Weber number, k_s the Nikuradse equivalent roughness size, $1{:}Z_1$ and $1{:}Z_2$ the upstream and downstream slopes, t the crest width (in the streamwise direction).

According to ISO 4362 (1999), the upstream slope $1{:}Z_2$ does not influence the discharge coefficient C_D when the overflow head remains small enough compared to the crest width: $h_p/t \leq 0.5$. Moreover, the influence of R and W vanishes for $h_p \geq 0.05$ m, $P \geq 0.15$ m and channel width $b \geq 0.3$ m. Under such conditions and for a smooth weir surface (C_D is not influenced by h_p/k_s), Eq. (3) reduces to:

$$C_D = f\left(\frac{h_p}{t}, \frac{h_p}{P}, \frac{1}{Z_1}\right), \quad (4)$$

stating that C_D is controlled by the relative crest width (h_p/t), the relative weir height (h_p/P) and the upstream slope ($1{:}Z_1$). ISO 4362 (1999) does not document the influence of varying weir height; therefore, this was also not examined here. ISO 4362 (1999) specifies an accuracy of ±0.5% for the reported values of C_D.

RESULTS AND DISCUSSION

Smooth surface

For each configuration and each prescribed inflow discharge, the hydraulic head upstream of the weir was deduced from the computed water depth in the upstream part of the simulation domain (Table 2). Next, corresponding discharge coefficients were evaluated using Eqs. (1) and (2), in Tables 3 and 4.

Table 2. Computed overflow heads h_p as a function of the specific discharge q and the upstream slope Z_1.

Upstream slope Z_1	Specific discharge q (m²/s)							
	0.02	0.03	0.05	0.07	0.09	0.11	0.13	0.15
1	0.0537	0.0698	0.0972	0.1209	0.1423	0.1622	0.1807	0.1983
2	0.0532	0.0692	0.0965	0.1202	0.1415	0.1613	0.1798	0.1973
3	0.0530	0.0690	0.0962	0.1199	0.1412	0.1610	0.1795	0.1970

Table 3. Computed discharge coefficients C_D for various specific discharges and upstream slopes.

Specific discharge q (m²/s)	Upstream slope $Z_1 = 1$		Upstream slope $Z_1 = 2$		Upstream slope $Z_1 = 3$	
	h_p/t	Computed C_D	h_p/t	Computed C_D	h_p/t	Computed C_D
0.02	0.1074	0.941	0.1064	0.954	0.1060	0.960
0.03	0.1395	0.952	0.1384	0.964	0.1379	0.968
0.05	0.1943	0.963	0.1930	0.973	0.1924	0.977
0.07	0.2418	0.969	0.2403	0.978	0.2397	0.981
0.09	0.2847	0.973	0.2831	0.981	0.2825	0.984
0.11	0.3243	0.975	0.3226	0.983	0.3219	0.986
0.13	0.3614	0.977	0.3596	0.985	0.3589	0.987
0.15	0.3965	0.979	0.3947	0.986	0.3940	0.989

Table 4. Comparison of discharge coefficients C_D for various upstream weir slopes (see Fig. 3).

Upstream slope $Z_1 = 1$			Upstream slope $Z_1 = 2$			Upstream slope $Z_1 = 3$		
C_D from ISO 4362 (1999)	Computed C_D (WOLF)	Relative difference	C_D from ISO 4362 (1999)	Computed C_D (WOLF)	Relative difference	C_D from ISO 4362 (1999)	Computed C_D (WOLF)	Relative difference
0.909	0.941	3.5 %	0.937	0.954	1.8 %	0.947	0.960	1.4 %
0.913	0.952	4.3 %	0.942	0.964	2.3 %	0.952	0.968	1.7 %
0.919	0.963	4.8 %	0.951	0.973	2.3 %	0.962	0.977	1.6 %
0.923	0.969	5.0 %	0.957	0.978	2.2 %	0.967	0.981	1.4 %
0.927	0.973	5.0 %	0.962	0.981	2.0 %	0.972	0.984	1.2 %
0.930	0.975	4.8 %	0.966	0.983	1.8 %	0.976	0.986	1.0 %
0.934	0.977	4.6 %	0.970	0.985	1.5 %	0.980	0.987	0.7 %
0.938	0.979	4.4 %	0.973	0.986	1.3 %	0.983	0.989	0.6 %

Bereitgestellt von University Library Bratislava | Heruntergeladen 31.01.20 12:22 UTC

The numerical simulations confirmed that downstream slope Z_2 has no influence on the overflow head and the discharge coefficient for the broad-crested weir conditions, which agrees with ISO 4362 (1999) and also with data published by Sargison and Percy (2009). Therefore the results of simulations with varying downstream slopes are not further detailed hereafter.

Comparison against ISO 4362 (1999)

In Fig. 3, the computed discharge coefficients C_D are plotted against the values recommended by the standard ISO 4362 (1999) for the range $0.10 \leq h_p/t \leq 0.40$ and for the case of smooth weir surface. Compared to the standard, the numerical predictions systematically overestimate the discharge coefficient, by up to 5%. The deviation between the standard and the numerical predictions is strongly influenced by the weir upstream slope: the steeper the upstream slope, the stronger the deviation. Indeed, the overestimation of C_D is in the ranges 1 to 2%, 1 to 3% and 3 to 6% for upstream slopes of $Z_1 = 3$, $Z_1 = 2$ and $Z_1 = 1$, respectively.

Computed discharge coefficients vs. earlier experimental data

In Figs. 4 to 6, the discharge coefficients evaluated from our simulations are compared not only with the values of the standard ISO 4362 (1999), but also with experimental data from Fritz and Hager (1998), Zerihun and Fenton (2007), Sargison and Percy (2009), Tokyay and Altan-Sakarya (2011), Goodarzi et al. (2012), Major (2013) and Madadi et al. (2014).

The graphs reveal substantial differences between the individual data sources. For instance, Goodarzi et al. (2012) found C_D values more than 10% higher than all other sources. For an upstream slope $Z_1 = 1$, the results by Toykay and Altan-Sakarya (2011), Major (2013) and by Madadi et al. (2014) agree relatively well with the values of ISO 4362 (1999), whereas the discharge coefficients estimated by Sargison and Percy (2009) are by 5 to 7% lower, with a stronger difference for smaller values of h_p/t.

For the slope $Z_1 = 2$ the values of C_D derived by Fritz and Hager (1998) exceed by about 2% the values recommended by ISO 4362 (1999). The only one C_D value published by Zerihun and Fenton (2007) provide only minor difference when compared with ISO 4362 (1999). In contrast, Sargison and Percy (2009) and Madadi et al. (2014) provide discharge coefficients by 4 to 8% smaller than those recommended by ISO 4362 (1999) for the same configuration, better agreement provide data interpolated from Madadi et al. (2014).

In all cases except for data of Goodarzi et al. (2012) the discharge coefficients from numerical simulations exceed the experimental values. The best agreement for the upstream slope $Z_1 = 2$ is obtained with data by Fritz and Hager (1988) and one value of C_D derived by Sargison and Percy (2009) for $h_p/t = 0.13$. The higher discharges coefficients obtained from the simulations may be attributed to limitations inherent to the shallow-water model, namely the assumption of hydrostatic pressure distribution and missing the effect of rapid vertical contractions which may lead to detached flow on the upstream part of the weir crest.

Rough weir crest

In Fig. 7 the results of simulations considering a rough surface for the weir crest are compared with the results of previous measurements (Pařílková et al., 2012).

When a rough surface of the weir crest is taken into account, the shallow-water flow simulations overestimate again C_D compared to experimental observations, particularly for values of h_c/k_s in between 0.5 and 3.5, i.e. for relatively high roughness heights. The differences between computations and observations are in the range of 5% to 8%. When the ratio h_c/k_s is increased, the agreement between simulations and measured values significantly improves, especially for values of h_c/k_s above 5. h_c is critical depth.

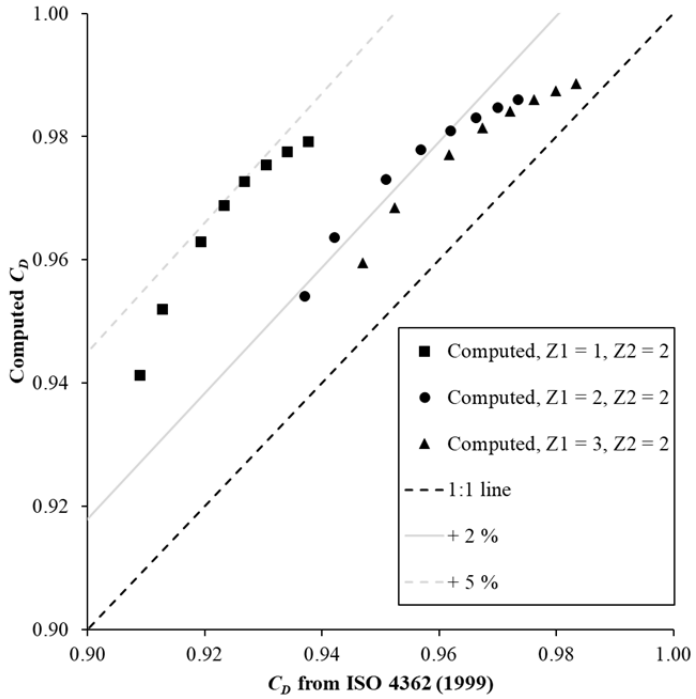

Fig. 3. Discharge coefficients C_D computed with the shallow-water model vs. recommended by ISO 4362 (1999), for various upstream slopes ($1{:}Z_1$) and downstream slopes ($1{:}Z_2$).

Bereitgestellt von University Library Bratislava | Heruntergeladen 31.01.20 12:22 UTC

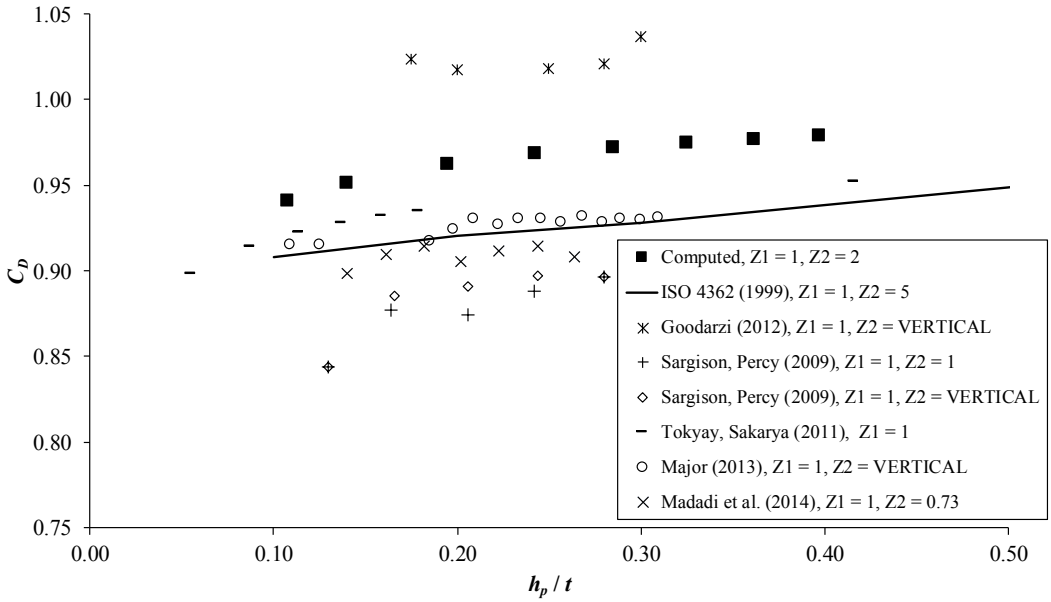

Fig. 4. Comparison between computed discharge coefficients and existing empirical results for upstream slope of $Z_1 = 1$.

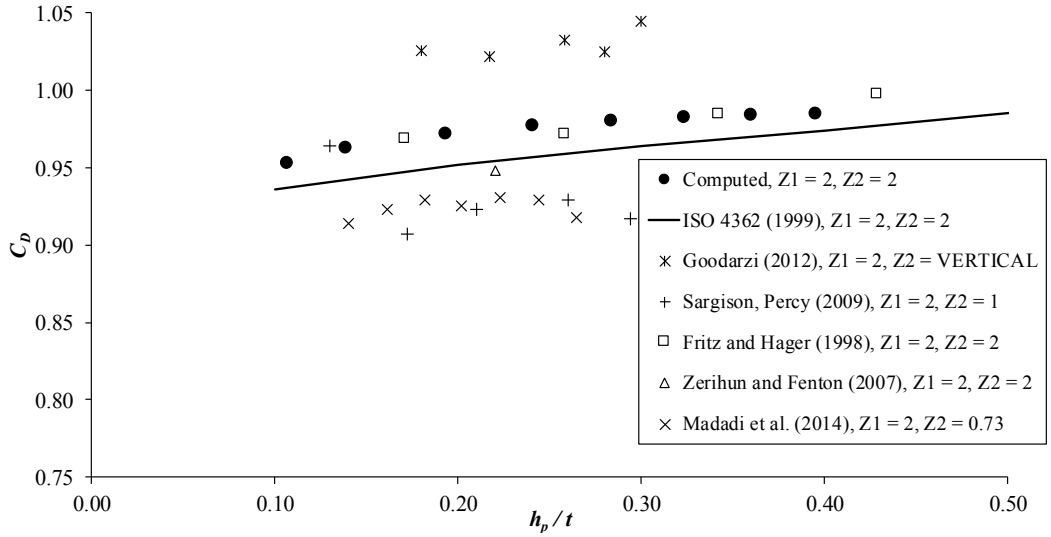

Fig. 5. Comparison between computed discharge coefficients and existing empirical results for upstream slope $Z_1 = 2$.

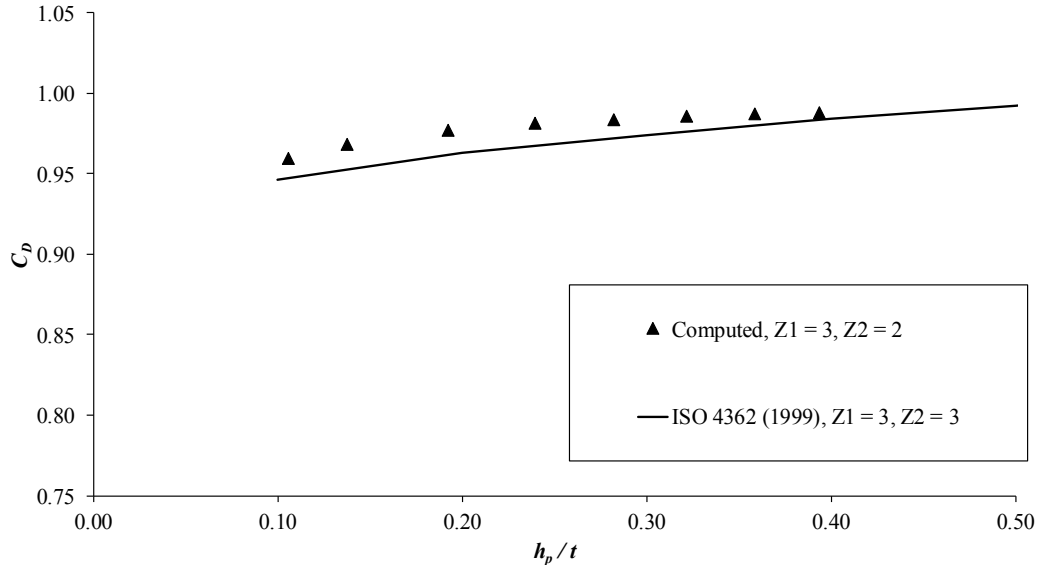

Fig. 6. Comparison between computed discharge coefficients and existing empirical results for upstream slope of $Z_1 = 3$.

Bereitgestellt von University Library Bratislava | Heruntergeladen 31.01.20 12:22 UTC

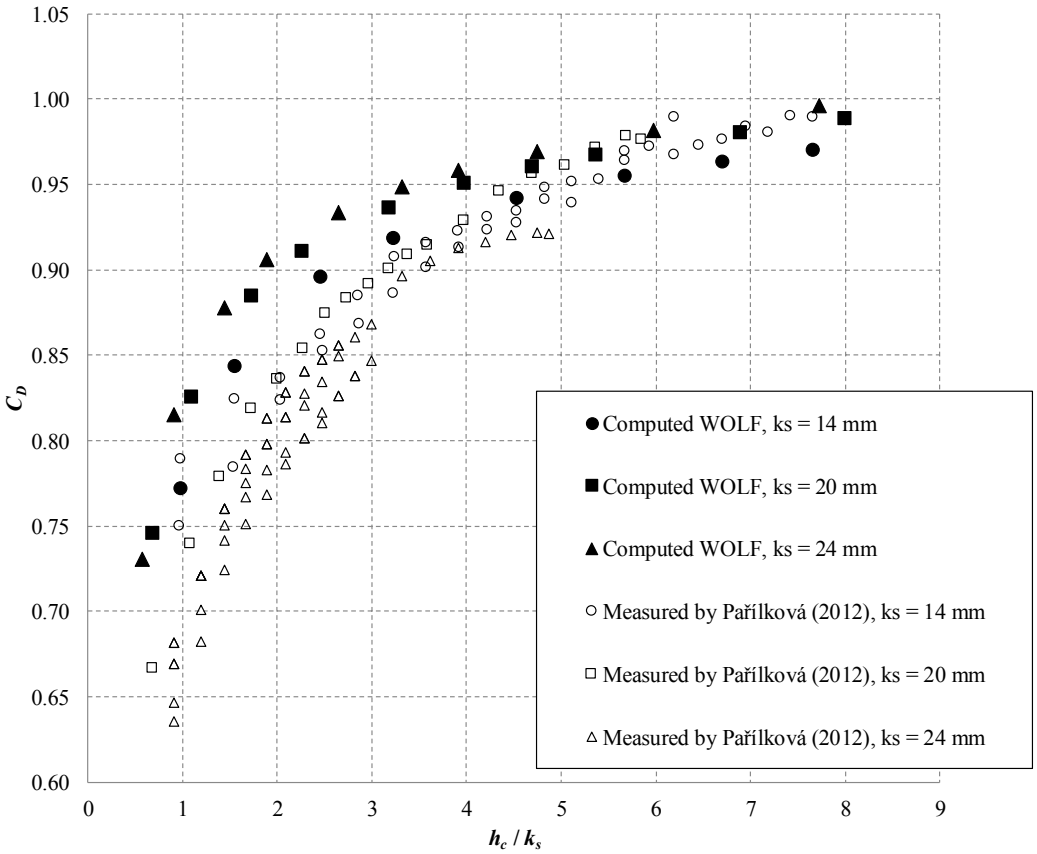

Fig. 7. The comparison of C_D obtained from shallow-water flow simulations (WOLF) and measured values.

CONCLUSIONS

The comparison of results of numerical computations with previously published experimental results was carried out for the evaluation of the discharge coefficient of frontal broad-crested weirs. The analysis was carried out for various weir geometries (upstream slopes), a range of specific discharge and considering both smooth and rough weir crest surface.

The discharge coefficients C_D obtained from numerical simulations were compared with values taken from literature (Fritz and Hager, 1998; Goodarzi et al., 2012; ISO 4362, 1999; Madadi et al., 2014; Major, 2013; Sargison and Percy, 2009; Tokyay and Altan-Sakarya, 2011; Zerihun and Fenton, 2007) and former own laboratory research (Pařílková et al., 2012). For the smooth weir surface, the flow simulations overestimate C_D by 3% to 6%, depending on upstream weir slope and the ratio h_p/t. Numerical simulations showed no effect of the downstream slope of the broad-crested weir, consistently with the experiments. For the rough weir crest, the overestimation of the discharge coefficient drops with an increasing ratio h_c/k_s.

The overestimation of the discharge coefficient in all simulated scenarios may be attributed to nonfulfillment of the assumption of uniform velocity and hydrostatic pressure along the vertical and to "missing" losses due to vertical contraction, which is not incorporated at the standard shallow flow equations (Zerihun and Fenton, 2007).

The results of the study provide practitioners with a quantification of the uncertainties arising when numerical shallow flow models are used at vertical contractions. In case of upstream weir slopes milder than 1:3, the error remains smaller than 2% and the shallow flow model may be used with an accuracy certainly suitable for a broad range of engineering applications. In contrast, in case of slopes steeper than 1:1, the error rapidly increases above 5% and modellers should be careful when simulating flow over steep obstructions, namely when h_p/t is close to 0.2.

Future research will focus on more complex configurations involving e.g. broad-crested side weirs.

Acknowledgements. This paper has been prepared under the projects TH04030087 *Tools for optimization of the management of the levee systems* and LO1408 *AdMaS UP – Advanced Materials, Structures and Technologies*. It was also supported by the University of Liege through a sabbatical leave of Prof. Riha in 2017.

REFERENCES

Cantero-Chinchilla, F.N., Castro-Orgaz, O., Schmocker, L., Hager, W.H., Dey, S., 2018. Depth-averaged modelling of granular dike overtopping. Journal of Hydraulic Research, 56, 4, 537–550. DOI: 10.1080/00221686.2017.1399933.

Castro-Orgaz, O., Hager, W.H., 2013. Unsteady Boussinesq-type flow equations for gradually-eroded beds: Application to dike breaches. Journal of Hydraulic Research, 51, 2, 203–208.

Darvishi, E., Fenton, J.D., Kouchakzadeh, S., 2017. Boussinesq equations for flows over steep slopes and structures. Journal of Hydraulic Research, 55, 3, 324–337.

Erpicum, S., Dewals, B.J., Archambeau, P., Pirotton, M., 2010. Dam break flow computation based on an efficient flux vector splitting. Journal of Computational and Applied Mathematics, 234, 7, 2143–2151.

Felder, S., Chanson, H., 2012. Free-Surface Profiles, Velocity and Pressure Distributions on a Broad-Crested Weir: A Physical Study. Journal of Irrigation and Drainage Engineering, 138, 12,

Bereitgestellt von University Library Bratislava | Heruntergeladen 31.01.20 12:22 UTC

1068–1074.
Fritz, H.M., Hager, W., 1998. Hydraulics of embankment weirs. Journal of Hydraulic Engineering, 124, 9, 963–971.
Gallegos, H.A., Schubert, J.E., Sanders, B.F., 2009. Two-dimensional, high-resolution modeling of urban dam-break flooding: A case study of Baldwin Hills, California. Advances in Water Resources, 32, 8, 1323–1335.
Goodarzi, E., Farhoudi, J., Shokri, N., 2012. Flow characteristics of rectangular broad-crested weirs with sloped upstream face. J. Hydrol. Hydromech., 60, 2, 87–100.
Gualtieri, P., De Felice, S., Pasquino, V., Doria, G.P., 2018. Use of conventional flow resistance equations and a model for the Nikuradse equivalent-sand-grain roughness in vegetated flows at high submergence. J. Hydrol. Hydromech., 66, 1, 107–120.
Haddadi, H., Rahimpour, M., 2012. A discharge coefficient for a trapezoidal broad-crested side weir in subcritical flow. Flow Measurement and Instrumentation, 26, 63–67.
Hager, W.H., Schwalt M., 1994. Broad-crested weir. J. Irrigation and Drainage, 120, 1, 13–26.
Hargreaves, D.M., Morvan, H.P., Wright, N.G., 2007. Validation of the volume of fluid method for free surface calculation: The broad-crested weir. Engineering Applications of Computational Fluid Mechanics, 1, 2, 136–146.
Haun, S., Olsen, N.R.B., Feurich, R., 2011. Numerical modeling of flow over trapezoidal broad-crested weir. Engineering Applications of Computational Fluid Mechanics, 5, 3, 397–405.
Horritt, M.S., Bates, P.D., 2001. Predicting floodplain inundation: Raster-based modelling versus the finite-element approach. Hydrological Processes, 15, 5, 825–842.
ISO 4362, 1999. Hydrometric determinations - Flow measurement in open channels using structures - Trapezoidal broad-crested weirs.
Kirkgoz, M.S., Akoz, M.S., Oner, A.A., 2008. Experimental and theoretical analyses of two-dimensional flows upstream of broad-crested weirs. Canadian Journal of Civil Engineering, 35, 9, 975–986.
Madadi, M.R., Dalir, A.H., Farsadizadeh, D., 2013. Control of undular weir flow by changing of weir geometry. Flow Measurement and Instrumentation, 34, 160–167.
Madadi, M.R., Hosseinzadeh D.A., Farsadizadeh, D., 2014. Investigation of flow characteristics above trapezoidal broad-crested weirs. Flow Measurement and Instrumentation, 38, 139–148.
Major, J., 2013. Influence of upstream face inclination of broad-crested weir on discharge coefficient. BSc diploma thesis, Brno University of Technology, Faculty of Civil Engineering, 58 p.
Pařílková, J., Říha, J., Zachoval, Z., 2012. The influence of roughness on the discharge coefficient of a broad-crested weir. J. Hydrol. Hydromech., 60, 2, 101–114.
Sargison, J.E., Percy, A., 2009. Hydraulics of broad-crested weirs with varying side slopes. Journal of Irrigation and Drainage Engineering, 135, 1, 115–118.
Sarker, M.A., Rhodes, D.G., 2004. Calculation of free-surface profile over a rectangular broad-crested weir. Flow Measurement and Instrumentation, 15, 215–219.
Stilmant, F., Pirotton, M., Archambeau, P., Erpicum, S., Dewals, B., 2018. Hydraulic determination of dam releases to generate warning waves in a mountain stream: Performance of an analytical kinematic wave model. Journal of Hydraulic Engineering, 144, 3, 05017006.
Tokyay, N.D., Altan-Sakarya, A.B., 2011. Local energy losses at positive and negative steps in subcritical open channel flows. Water SA, 37, 2, 237–244.
Velísková, Y., Chára, Z., Schügerl, R., Dulovičová, R., 2018. Velocity profile deformation by flooded obstacle in free surface flow. J. Hydrol. Hydromech., 66, 4, 448–456.
Xu, T., Jin, Y., 2017. Numerical study of the flow over broad-crested weirs by a mesh-free method. Journal of Irrigation and Drainage Engineering, 143, 9, 04017034.
Zerihun, Y.T., Fenton, J.D., 2007. A Boussinesq-type model for flow over trapezoidal profile weirs. Journal of Hydraulic Research, 45, 40, 519–528.

Received 8 January 2019
Accepted 19 March 2019

Bereitgestellt von University Library Bratislava | Heruntergeladen 31.01.20 12:22 UTC

J. Hydrol. Hydromech., 67, 2019, 4, 329–338
DOI: 10.2478/johh-2019-0022

Submergence coefficient of full-width sharp-edged broad-crested rectangular weirs

Zbyněk Zachoval[1*], Jakub Major[1], Ladislav Roušar[2], Ján Rumann[3], Jan Šulc[1], Jan Jandora[1]

[1] Brno University of Technology, Faculty of Civil Engineering, Institute of Water Structures, Veveří 331/95, 602 00 Brno, Czech Republic.
[2] VHRoušar, Radčice 24, 539 73 Skuteč, Czech Republic.
[3] Slovak University of Technology in Bratislava, Faculty of Civil Engineering, Department of Hydraulic Engineering, Radlinského 11, 810 05 Bratislava, Slovak Republic.
[*] Corresponding author. E-mail: zachoval.z@fce.vutbr.cz

Abstract: Full-width sharp-edged broad-crested rectangular weirs in the range $0.1 < h/L \leq 0.3$ situated in rectangular channels are frequently used in submerged flow conditions. To determine the discharge for the submerged flow, submergence coefficient and modular limit shall be known. This article deals with their determination upon a theoretic derivation and experimental research. The equation for modular limit has been determined from energy balance with simplifications. To validate it, extensive experimental research was carried out. However, the derived equation is too complicated for practical use which is why it was approximated by a simple equation applicable for the limited range. The equation for submergence coefficient was derived by modifying Villemonte's application of the principle of superposition and its coefficients were determined using the data from experimental research of many authors. The new system of equations computes the discharge more accurately than other authors' equations, with the error of approximately ±10% in full range of the measured data.

Keywords: Modular limit; Relative weir height; Full-width sharp-edged broad-crested weir; Submergence coefficient.

INTRODUCTION

According to the length of weir in direction of flow, L, weirs of finite-crest width for free flow are classified as (Govinda Rao and Muralidhar, 1963): long-crested weirs $0.0 < h/L \leq 0.1$, broad-crested weirs $0.1 < h/L \leq 0.4$, short-crested weirs $0.4 < h/L \leq 1.5$ to 1.9, and sharp-crested weirs 1.5 to $1.9 < h/L$, where h is the upstream head over the weir crest (Fig. 1). In the text below, broad-crested weirs with sharp (square) upstream and downstream edges, with rectangular longitudinal and cross section profiles in the range $0.1 < h/L \leq 0.3$ are considered. In this range the parallel flow will occur on the weir crest (Bos, 1989) and discharge coefficient for free flow is in effect independent of h/L (Zachoval et al. 2014a). Many authors carried out experimental research with free overflow to determine the discharge coefficient (Azimi et al., 2014; Bazin, 1896; Berezinsky, 1950; Crabbe, 1974; Doeringsfeld and Barker, 1941; Goodarzi et al., 2012; Hager and Schwalt, 1994; Kašpar, 2015; Keutner, 1934; Madadi et al., 2014; Major, 2013; Prentice, 1941 (in Stevens et al., 1941); Rafter, 1900; Sahasrabudhe, 1972; Singer, 1964; Sreetharan, 1983, Tim, 1986; Woodburn, 1932; Zachoval et. al., 2014a) and many authors determine it theoretically (Pavlovsky, 1937; Skogerboe et al., 1967; Tim, 1986).

Sharp-edged broad-crested rectangular weirs are usually designed and operated in submerged flow conditions. One of their biggest advantages compared to other weir types is the high value of modular limit (Bos, 1989), which is the state on the boundary of free and submerged flow. Submerged flow may appear on weirs with little difference between the water levels, especially in extreme discharge conditions. To determine the discharge for submerged flow, submergence coefficient (drowned flow-reduction factor) which corrects the discharge value compared to the free flow shall be known.

In the case of relatively high sharp-edged broad-crested weirs, where the discharge coefficient and the submergence coefficient are basically independent of relative weir height above the channel bed, the information on modular limit and the submergence coefficient are described well (Bos, 1989; Pavlovsky, 1937; USACE, 1977). As for the relatively low weirs, where the modular limit and the submergence coefficient are greatly affected by relative weir height, the information is less detailed and considerably differs. It is one of the reasons why many authors do not recommend measuring of the discharge in submerged flow conditions (Bos, 1984; Hager, 2010; Hager and Schwalt, 1994; Horton, 1907). Due to the above fact, extensive research was carried out focusing on determination of the modular limit and submergence coefficient for a full-width sharp-edged broad-crested rectangular weir in the ranges of $0.1 < h/L \leq 0.3$ and $0.1 < h/P < 3.0$, where P is the weir height.

LITERATURE REVIEW

In the long term, the submerged flow was dealt with by a large number of researchers whose summary is listed e.g. by Horton (1907) and Skogerboe et al. (1967). The studies mostly focused on thin-plate weirs. A substantially lower number of researches concentrated on rectangular short-crested (Azimi et al., 2014) and broad-crested weirs.

For flows over broad-crested weirs, modular limit used to be determined, less often the submergence coefficient. An extensive experimental research on modular limit of round-nosed broad-crested weirs was published by Woodburn (1932). Modular limit and submergence coefficients of various broad-crested weir types were experimentally studied by Berezinskij (1950). Skogerboe et al. (1967) derived an equation for calculation of discharge for submerged flow from the momentum analysis of flow. Harrison (1967) derived modular limit for weirs with round-nosed upstream corner of crest depending on relative weir height above the outflow channel bed. Sahasrabudhe (1972) carried out experimental research on determination of submergence coefficient for round and sharp upstream edge of the weir crest. USACE (1977) recommended graphical de-

Bereitgestellt von University Library Bratislava | Heruntergeladen 31.01.20 12:22 UTC

pendence to determine the submergence coefficient. Nikolov et al. (1978) summed up and particularized recommendations for calculation of submergence coefficient. Bos (1984) recommends determination of modular limit upon mechanical energy analysis. Tim (1986) performed measurements with the stress laid on the effect of the rounding of upstream edge on the submergence coefficient. Hager and Schwalt (1994) determined modular limit through an experiment and expressed the submergence coefficient by means of the index of the tailwater flow depth $\chi = (h_f - h_{f0})/(H - h_{f0})$, where h_f is the submergence head, H is the total head and h_{f0} is the submergence head for modular limit. Bukreev (2001) studied flow over a submerged weir of relatively small height. Wols (2005) carried out experimental research focusing on the measurement of water level and defined the submergence coefficient upon the Villemonte's analysis under submerged flow conditions (Villemonte, 1947). ISO 3846 (2008) recommended determination of modular limit and submergence coefficient solely for the specific weir geometry. Azimi et al. (2014) defined modular limit and submergence coefficient on the basis of their measurements. Geometric parameters and ranges of experimental research of the above listed authors are shown in Table 1. In spite of the rather extensive number of researches into the issue, the results are ambiguous and the values of modular limit and submergence coefficient have not been determined and verified for the entire applicable scope of geometric layouts (h/P), which is the subject of the research carried out by authors of this article.

HEAD-DISCHARGE RELATIONSHIP

Subscripts at quantities in the text below specify affiliation with the U, C, T, E, D profile (Fig. 1) or to a section specified by the profiles. The "0" subscript indicates modular limit conditions.

Full-width sharp-edged broad-crested rectangular weir in a horizontal channel of rectangular cross-section (ISO 3846, 2008) is considered. P_U is the upstream weir height, P_D the downstream weir height and b the weir width. The flow is caused by gravitational acceleration g and is characterised by total head over the weir H in the U profile (Fig. 1)

$$H = h + \frac{\alpha_U \cdot Q^2}{2 \cdot g \cdot b^2 \cdot \left(h + P_U\right)^2} \tag{1}$$

and the submergence total head H_f in the D profile (Fig. 1)

$$H_f = h_f + \frac{\alpha_D \cdot Q^2}{2 \cdot g \cdot b^2 \cdot \left(h_f + P_D\right)^2}, \tag{2}$$

where h is the head over the weir, h_f is the submergence head, α_U and α_D are kinetic energy coefficients (Coriolis coefficient) in profiles U and D and Q is the discharge. The U profile is situated 3h to 4h (ISO 3846, 2008) in front of the upstream face of the weir where the drawdown curve caused by the overflow is negligible. The D profile is located 10h (ISO 3846, 2008) behind the downstream face of the weir where the water level is not affected by the overflow. Measurements show that kinetic energy coefficient varies between $1.02 < \alpha_U < 1.06$ (Zachoval et al., 2012b) and $\alpha_D = 1.11$ (Zubík, 2006).

The equation for Q is derived from Bernoulli's equation for the above profiles and from the continuity equation

$$Q = C_f \cdot C_d \cdot \left(\frac{2}{3}\right)^{3/2} \cdot g^{1/2} \cdot b \cdot H^{3/2}, \tag{3}$$

where C_f is the submergence coefficient and C_d the discharge coefficient. C_f expresses reduction of the flow due to submergence, C_d expresses energy loss for free overflow. As H cannot be directly measured, the following equation is recommended to define Q

$$Q = C_f \cdot C_v \cdot C_d \cdot \left(\frac{2}{3}\right)^{3/2} \cdot g^{1/2} \cdot b \cdot h^{3/2}, \tag{4}$$

where $C_v = (H/h)^{3/2}$ is the approach velocity coefficient to be determined iteratively or read from the relation $C_v = f\{\alpha_U^{1/2} \cdot C_d \cdot h/(h + P_U)\}$ presented by Bos (1989, Figure 1.12).

Modular limit

Modular limit can be expressed by the ratio of h/h_{f0} or H/H_{f0} (Harrison, 1967). The modular limit may be determined experimentally (Azimi et al., 2014; Berezinskij, 1950; Tim, 1986), numerically (Wols, 2005) and analytically. Present analytic derivations are only known for weirs where critical flow

Table 1. Geometry and range of flow parameters.

Author	h (m)	L (m)	P (m)	b (m)	h/L	h/P	h/b
Azimi et al. (2014)	0.030–0.139	0.076–0.304	0.076	0.400	0.11–1.83	0.39–1.83	0.07–0.35
Berezinsky (1950)	0.060–0.101	0.500	0.107	0.900	0.12–0.20	0.56–0.94	0.07–0.11
Hager and Schwalt (1994)	0.030–0.181	0.500	0.401	0.499	0.06–0.37	0.07–0.45	0.06–0.36
Halliwell and Hill (1967) from Markland et al. (1967)	0.040–0.079	0.229–0.457	0.038–0.152	0.284	0.09–0.34	0.27–1.90	0.14–0.28
Sahasrabudhe (1972)	0.060–0.603	0.15–0.30	0.151–0.308	0.460	0.21–3.09	0.21–3.93	0.13–1.31
Tim (1986)	0.031–0.122	0.305	0.102	0.254	0.10–0.40	0.305–1.20	0.12–0.48
Wols (2005)	0.134–0.187	1.00	0.150	0.4	0.134–0.187	0.89–1.25	0.34–0.47

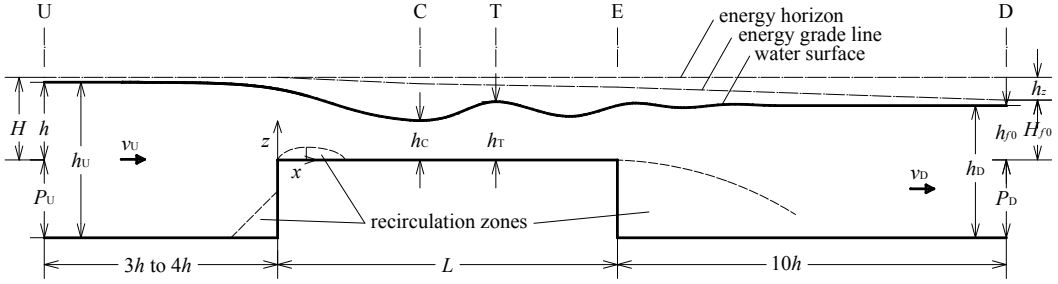

Fig. 1. Longitudinal profile of weir at modular limit.

Bereitgestellt von University Library Bratislava | Heruntergeladen 31.01.20 12:22 UTC

appears along the whole crest length (rounded or bevelled upstream edge) and are based on mechanical energy analysis (Bos, 1984) and momentum analysis (Harrison, 1967). However, flow separation zone (Zachoval et al., 2012a) and undular hydraulic jump (Hager and Schwalt, 1994) form on weir crest, which is why the above analytic derivations are unsuitable and provide incorrect results.

The new analytic derivation respecting the flow separation zone and the hydraulic jump on weir crest is based on energy balance at modular limit (Fig. 1). The derivation neglects the effect of surface tension and effect of friction on side hydraulically smooth walls, which – in the case of free flow – means $h \geq 0.06$ m and $h/b \leq 0.5$ (Zachoval, 2015). To define the specific discharge q, Equation (3) is then applied

$$q = v_i \cdot h_i = \frac{Q}{b} = C_d \cdot \left(\frac{2}{3}\right)^{3/2} \cdot g^{1/2} \cdot H^{3/2}, \quad (5)$$

where v_i and h_i are mean velocity and depth in the profile i = U, C, T, E, D (Fig. 1). Total head loss is calculated as a sum of individual head losses under the presumption they do not affect one another. To determine them, profiles are defined: C which is 2.7H behind the upstream edge of weir crest where flow is contracted (Zachoval et al., 2012a); T at peak of the first wave of undular hydraulic jump; and E at the downstream edge of the weir crest.

Between the U and C profiles, the head loss h_{zUC} appears for free flow. Due to the formation of flow recirculation zone whose height and length partly depends on the H/P_U ratio (Zachoval et al., 2012a), it is to be defined from the depth h_C (in C profile) where the flow is approximately parallel. After Equation (5) is applied, the head loss in free flow conditions is

$$h_{zUC} = H - h_C - \frac{\alpha_C \cdot q^2}{2 \cdot g \cdot h_C^2} = H - h_C - \frac{2^2}{3^3} \cdot \alpha_C \cdot C_d^2 \cdot \left(\frac{H}{h_C}\right)^2 \cdot H, \quad (6)$$

where α_C is kinetic energy coefficient in profile C.

Between the C and E profiles, head loss from undular hydraulic jump, h_{zCT}, and head loss caused by friction on weir crest, h_{zCE}, appear. Expression of the head loss respecting concurrently the friction loss and the hydraulic jump loss for Froude number $Fr_C = v_C/(g \cdot h_C)^{1/2} > 2$ is known and verified (Noor Afzal et al., 2011) but not for the undular hydraulic jump on the crest of broad-crested weir where Froude number varies in the range $1.26 < Fr_C < 1.43$ ($0.1 < h/P_U < 3$). Summary information about undular hydraulic jump is described by Chanson (2009) and Montes and Chanson (1998). Information about wave profile of undular jump on the smooth crest is described by Berezinsky (1950), Bukreev (2001), Hager and Schwalt (1994) and Wols (2005). Due to the difficulty to describe the loss on the crest and the relatively low significance of the total loss (Fig. 6), the assumption of hydrostatic pressure distribution was presumed. Two simplified separate formulas have been used. The head loss caused solely by the hydraulic jump is

$$h_{zCT} = \frac{(h_T - h_C)^3}{4 \cdot h_C \cdot h_T}, \quad (7)$$

where water depth, h_T, is determined from flow momentum analysis. After Equation (5) is applied, the equation for depth is

$$h_T = \frac{h_C}{2} \cdot \left[\left(1 + 8 \cdot \frac{q^2}{h_C^3 \cdot g}\right)^{1/2} - 1\right] = \frac{h_C}{2} \cdot \left\{\left[1 + \frac{2^6}{3^3} \cdot C_d^2 \cdot \left(\frac{H}{h_C}\right)^3\right]^{1/2} - 1\right\}. \quad (8)$$

After Equation (8) is used in Equation (7), head loss caused solely by hydraulic jump can be expressed

$$h_{zCT} = \frac{\left\{\left[1 + \frac{2^6}{3^3} \cdot C_d^2 \cdot \left(\frac{H}{h_C}\right)^3\right]^{1/2} - 3\right\}^3}{2^4 \cdot \left\{\left[1 + \frac{2^6}{3^3} \cdot C_d^2 \cdot \left(\frac{H}{h_C}\right)^3\right]^{1/2} - 1\right\}} \cdot h_C. \quad (9)$$

Head loss by friction on weir crest, h_{zCE}, appears along the $L_{CE} = L - 2.7 \cdot H$ length. In effect, friction does not occur at the distance up to 2.7H, as there is a wake. As one to three waves of hydraulic jump form on the weir crest and the individual loss has rather low significance for the total loss (Fig. 6), mean depth of the flow, h_{CE}, at uniform flow is used for simplified expression of h_{zCE}. After the substitution in Equation (8)

$$h_{CE} = \frac{h_C + h_T}{2} = \frac{1}{2^2} \cdot \left\{\left[1 + \frac{2^6}{3^3} \cdot C_d^2 \cdot \left(\frac{H}{h_C}\right)^3\right]^{1/2} + 1\right\} \cdot h_C. \quad (10)$$

After applying Equation (5), mechanic energy gradient, i_{CE}, for uniform, fully turbulent flow is determined from the equation (García, 2008)

$$i_{CE} = \left(\frac{k_{sCE}}{h_{CE}}\right)^{1/3} \cdot \left(\frac{v_{CE}^2}{C_k^2 \cdot g \cdot h_{CE}}\right) = \left(\frac{k_{sCE}}{h_{CE}}\right)^{1/3} \cdot \left(\frac{q^2}{C_k^2 \cdot g \cdot h_{CE}^3}\right), \quad (11)$$

where k_{sCE} is hydraulic roughness of weir crest surface, v_{CE} the mean velocity and C_k the coefficient of proportionality (Brownlie, 1981). Head loss by friction on weir crest, h_{zCE}, after substitution of Equations (11) and (5) is then

$$h_{zCE} = i_{CE} \cdot L_{CE} = \left(\frac{2}{3}\right)^3 \cdot \left(\frac{C_d}{C_k}\right)^2 \cdot \left(\frac{k_{sCE}}{h_{CE}}\right)^{1/3} \cdot \left(\frac{H}{h_{CE}}\right)^3 \cdot (L - 2.7 \cdot H). \quad (12)$$

In profile E, the head loss is caused by sudden expansion of cross section, h_{zE}, which, assuming an idealised uniform flow in outflow channel and after Equation (5) is applied, results in

$$h_{zE} = \xi_E \cdot \left(\frac{h_D}{h_T} - 1\right)^2 \cdot \frac{q^2}{2 \cdot g \cdot h_D^2} = \frac{2^2}{3^3} \cdot \alpha_D \cdot C_d^2 \cdot \xi_E \cdot \left(\frac{H}{h_D}\right)^2 \cdot \left(\frac{h_D}{h_T} - 1\right)^2 \cdot H, \quad (13)$$

where h_D is the depth in profile D and ξ_E the minor loss coefficient for vertical downstream weir face.

Between profiles E and D, the head loss h_{zED} is caused by friction. Under the presumption of idealised uniform flow in outflow channel and after Equation (5) is applied

$$h_{zED} = \left(\frac{2}{3}\right)^{3/2} \cdot \left(\frac{C_d}{C_k}\right)^2 \cdot \left(\frac{k_{sED}}{h_D}\right)^{1/3} \cdot \left(\frac{H}{h_D}\right)^3 \cdot L_{ED}, \quad (14)$$

Bereitgestellt von University Library Bratislava | Heruntergeladen 31.01.20 12:22 UTC

where L_{ED} is the length of the section between profiles E and D and k_{sED} is hydraulic roughness of outflow channel bed between profiles E and D.

Modular limit expressed by the ratio of H_{f0}/H is then determined from Bernoulli's equation

$$\frac{H_{f0}}{H} = 1 - \frac{h_{zUC}}{H} - \frac{h_{zCT}}{H} - \frac{h_{zCE}}{H} - \frac{h_{zE}}{H} - \frac{h_{zED}}{H} . \quad (15)$$

After Equation (8) is substituted in equations for individual head losses (6), (7), (12), (13) and (14) and after they are substituted in Equation (15), and under the simplifying assumption that $h_D = P_D + h_T$ (idealised flow in outflow channel is uniform and water level upstream and downstream the local loss is identical), equation for direct determination of H_{f0}/H is obtained

$$\frac{H_{f0}}{H} = \frac{h_C}{H} + \frac{2^2}{3^3}\cdot\alpha_C\cdot C_d^2\cdot\left(\frac{H}{h_C}\right)^2 - \frac{1}{2^4}\cdot\frac{\left\{\left[1+\frac{2^6}{3^3}\cdot C_d^2\cdot\left(\frac{H}{h_C}\right)^3\right]^{1/2}-3\right\}^3}{\left[1+\frac{2^6}{3^3}\cdot C_d^2\cdot\left(\frac{H}{h_C}\right)^3\right]^{1/2}-1}\cdot\frac{h_C}{H}$$

$$-\left(\frac{2}{3}\right)^3\cdot\left(\frac{C_d}{C_k}\right)^2\cdot\left(\frac{k_{sCE}}{h_C}\right)^{1/3}\cdot\left(\frac{H}{h_C}\right)^3\cdot\frac{2^{20/3}}{\left\{\left[1+\frac{2^6}{3^3}\cdot C_d^2\cdot\left(\frac{H}{h_C}\right)^3\right]^{1/2}+1\right\}^{10/3}}\cdot\left(\frac{L}{H}-2.7\right)$$

$$-\frac{2^4}{3^3}\cdot\alpha_D\cdot C_d^2\cdot\xi_E\cdot\left(\frac{H}{h_C}\right)^2\cdot\left\{\frac{1}{\left[1+\frac{2^6}{3^3}\cdot C_d^2\cdot\left(\frac{H}{h_C}\right)^3\right]^{1/2}-1}-\frac{1}{2\cdot\frac{P_D}{H}\cdot\frac{H}{h_C}+\left[1+\frac{2^6}{3^3}\cdot C_d^2\cdot\left(\frac{H}{h_C}\right)^3\right]^{1/2}-1}\right\}^2$$

$$-\left(\frac{2}{3}\right)^3\cdot\left(\frac{C_d}{C_k}\right)^2\cdot\frac{1}{\left(\frac{P_D}{k_{sED}}+\frac{h_C}{2\cdot k_{sED}}\cdot\left\{\left[1+\frac{2^6}{3^3}\cdot C_d^2\cdot\left(\frac{H}{h_C}\right)^3\right]^{1/2}-1\right\}\right)^{1/3}}\cdot\frac{1}{\left(\frac{P_D}{H}+\frac{h_C}{2\cdot H}\cdot\left\{\left[1+\frac{2^6}{3^3}\cdot C_d^2\cdot\left(\frac{H}{h_C}\right)^3\right]^{1/2}-1\right\}\right)^3}\cdot\frac{L_{ED}}{H} \quad (16)$$

The equation includes coefficients and ratios that need to be quantified. Measurements show that kinetic energy coefficient in profile C is $\alpha_C = 1.03$ (Hager and Schwalt, 1994), simplified $\alpha_C = 1.0$; in profile D it is $\alpha_D = 1.11$ (Zubík, 2006), simplified $\alpha_D = 1.1$. 10% change in the value of α_D results in the change in H_{f0}/H by maximum 3%. $\xi_E = 1$ applies for vertical downstream weir face (Brater et al., 1996). In the range of $5 < k_s/h < 500$, $C_k = 8.1$ (García, 2008) is considered. Values of k_{sCE} and k_{sED} are determined according to the surface material (Idel´chik, 1966). For smooth surfaces (considered below) and $h \geq 0.06$ m, $k_s = 0.00013$ m is used. For $h \geq 0.06$ m, $0.12 \leq h/L \leq 0.30$ and $h/b \leq 0.5$, C_d is defined from equation (Zachoval, 2015; Zachoval et al., 2014) ($R^2 = 0.98$):

$$\text{for } 0.10 \leq \frac{h}{P_U} < 0.52 \text{ it means } C_d = 0.845 , \quad (17a)$$

$$\text{for } 0.52 \leq \frac{h}{P_U} < 7.0 \text{ it means } C_d = 0.038\cdot\ln\frac{h}{P_U} + 0.87 . \quad (17b)$$

Relation between C_d and h/P_U with values measured by many authors is shown in Fig. 2 (Zachoval et al., 2014a).

Upon the measurement (Zachoval, 2015), the h_C/H ratio for $h \geq 0.06$ m, $0.08 \leq h/L \leq 0.30$ and $h/b \leq 0.5$ ($R^2 = 0.98$) is:

$$\text{for } 0.10 \leq \frac{h}{P_U} < 0.52 \text{ it means } \frac{h_C}{H} = 0.47 , \quad (18a)$$

$$\text{for } 0.52 \leq \frac{h}{P_U} < 2.5 \text{ it means } \frac{h_C}{H} = 0.038\cdot\ln\frac{h}{P_U} + 0.495 . \quad (18b)$$

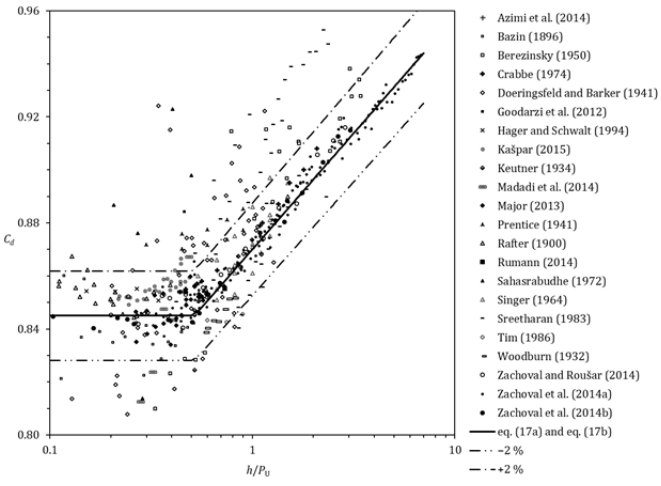

Fig. 2. Relation between C_d and h/P_U for $h \geq 0.06$ m, $0.10 \leq h/L \leq 0.30$, $h/b \leq 0.5$.

Using the above method, modular limit can be determined for any full-width sharp-edged broad-crested rectangular weir in scope of validity of empirical Equations (17) and (18). To verify validity of the above derivation, data acquired through experiments are necessary. As they had not been measured in the required range, experiments were carried out. The experiments are described in section EXPERIMENTS; verification is in section EVALUATION.

Bereitgestellt von University Library Bratislava | Heruntergeladen 31.01.20 12:22 UTC

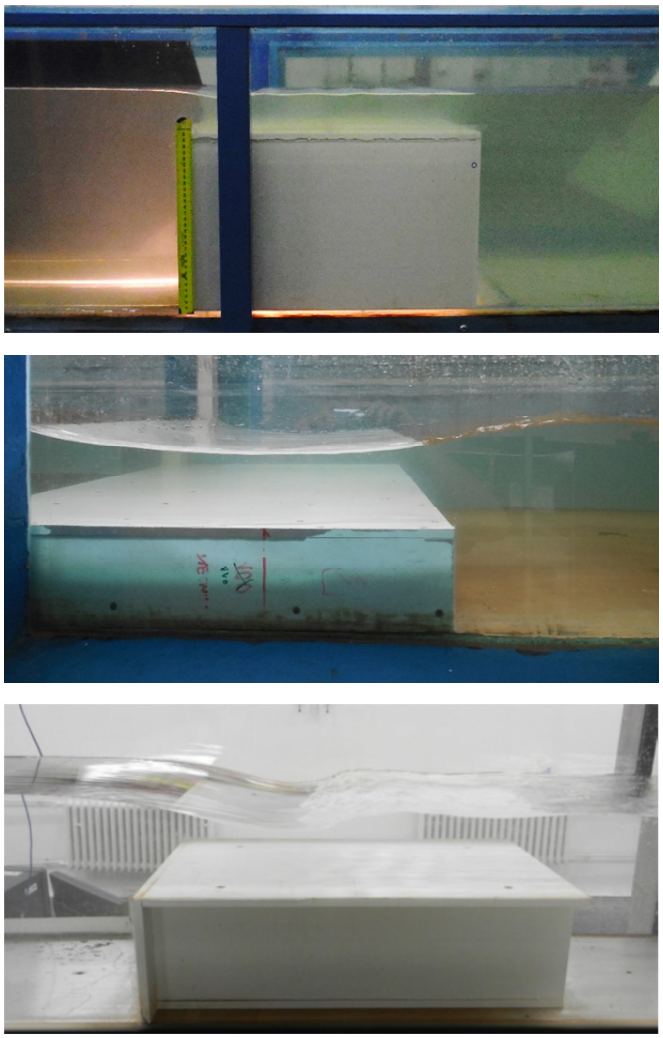

Fig. 3. From the top: channel BUT 0.5 with weir $P = 0.300$ m, channel BUT 1 with weir $P = 0.113$ m, channel SUTB with weir $P = 0.150$ m.

To justify the use of the simplifications described above, the significance of individual head losses on total head loss had to be analysed. The analysis is presented in section EVALUATION.

Submergence coefficient

The submergence coefficient, C_f, is derived by modifying Villemonte's application of the principle of superposition (Villemonte, 1947). The modification consists in relating H and H_f to the total submergence head at modular limit (not to the weir crest level), i.e. to H_{f0}. The discharge given by $H - H_{f0}$ is then

$$Q_u = C_d \cdot \left(\frac{2}{3}\right)^{3/2} \cdot g^{1/2} \cdot b \cdot \left(H - H_{f0}\right)^{3/2} \tag{19}$$

and discharge given by $H_f - H_{f0}$ is

$$Q_d = C_{dd} \cdot \left(\frac{2}{3}\right)^{3/2} \cdot g^{1/2} \cdot b \cdot \left(H_f - H_{f0}\right)^{3/2}, \tag{20}$$

where C_d and C_{dd} are discharge coefficients. C_f is determined by discharge ratio in submerged flow conditions, $Q = Q_u - Q_d$, and discharge in free flow conditions, Q_u; after substitution in Equations (19) and (20)

$$C_f = \frac{Q}{Q_u} = \left(1 - \frac{Q_d}{Q_u}\right)^{C_m} = \left(1 - \frac{C_{dd} \cdot \left(H_f - H_{f0}\right)^{3/2}}{C_d \cdot \left(H - H_{f0}\right)^{3/2}}\right)^{C_m}. \tag{21}$$

Provided that $C_{dd}/C_d = C$, the equation is reduced to

$$C_f = \left[1 - C \cdot \left(\frac{H_f - H_{f0}}{H - H_{f0}}\right)^{3/2}\right]^{C_m}, \tag{22}$$

where C is a proportional coefficient and C_m a power law exponent which need to be determined through an experiment.

EXPERIMENTS

Experiments were carried out in three channels (flumes) (Table 2) with the channel width marked B and active length of the channel marked l. The channels were named according to the institution where they are located: first and second channels in Laboratory of Water Management Research in the Institute of Water Structures at the Faculty of Civil Engineering at the Brno University of Technology (BUT 0.5 and BUT 1), the third one in the Department of Hydraulic Engineering at the Faculty of Civil Engineering at the Slovak University of Technology in Bratislava (SUTB). The channels were provided with transparent side walls made of glass (BUT 1 and SUTB) or polymethylmethacrylate (PMMA) (BUT 0.5). Horizontal channel beds were made of PMMA (BUT 0.5), polished concrete (BUT 1) and stainless steel (SUTB). All channels were equipped with water recirculation.

Full-width sharp-edged broad-crested rectangular weirs (Fig. 3) $B = b$, length L in the direction of flow and height $P = P_U = P_D$ (Table 3) above the channel bed were made of 0.010 m thick polyvinylchloride (PVC) boards with reinforcement ribs (to avoid deformation). The surface was smooth with sharp edges. The weirs in the channels were sealed by silicon sealant. Their position was chosen to ensure sufficiently long approach l_u and outflow l_d channel sections with developed velocity profile (Table 2).

The discharge Q (Table 3) was measured in the supply pipe by flow meters (Table 2); position of water level in outflow channel was set by adjustable tailgates (Table 2). Water level in approach channel in the distance of $3h$ in front of the upstream weir face and water level in outflow channel $10h$ after the downstream weir face (ISO 3846, 2008) were measured by needle gauges (Table 2). Due to the waves formed in the outflow channel, floating board of foam PVC was installed in front of the profile where water level was measured. Water temperature ranged from 18°C to 22°C. Range of measured heads, h, (Table 3) was chosen with respect to the requirements set in the definition of broad-crested weirs not affected by friction and surface tension. Detail information on channels, weirs and measurements can be found in publications listed in Table 3.

Modular limit was determined by means of polynomial approximation curve for $C_f = f\{H_f/H\}$ only in the case of submerged flow ($C_f < 1$). Extrapolation of the approximation curve up to $C_f = 1$ defined the modular limit H_{f0}/H. The method was suitable due to the sufficiently high number of measurements taken under submerged flow conditions.

To verify usability of results for all weirs, values of C_d under free flow conditions were analysed in the ranges of $0.10 \le h/L \le 0.30$, $h \ge 0.06$ m, $h/b \le 0.5$ (Fig. 2). The analysis proved that within the determination uncertainty, values of C_d do not depend on used values of b and L but only on h/P pursuant to the recommendation by Zachoval et al. (2014a).

Bereitgestellt von University Library Bratislava | Heruntergeladen 31.01.20 12:22 UTC

Table 2. Channel parameters.

ID	l (m)	$B = b$ (m)	l_u (m)	l_d (m)	Flow meter, uncertainty at 95% confidence interval	Tailgate	Gauge, resolution (mm)
BUT 0.5	6	0.503	4.0	1.5	electromagnetic, ±0.2%	needle	point, 0.5
BUT 1	12	1.003	8.0	3.4	V-notch weir, ±1.0% to ±1.6%	sluice	point, 0.1
SUTB	7.5	0.409	5.5	1.5	electromagnetic, ±0.2%	flap	point, 0.1

Table 3. Weir parameters and range of measured quantities (N number of measurements).

ID	L (m)	$P = P_U = P_D$ (m)	Q (m³/s)	h (m)	h/L	h/P	h/b	N	Reference
BUT 0.5	0.5	0.051, 0.100, 0.150, 0.200, 0.250, 0.300	0.010–0.065	0.060–0.220	0.11–0.44	0.20–4.14	0.11–0.44	234	Zachoval and Roušar (2014)
BUT 1	0.6	0.052, 0.113, 0.254, 0.603	0.022–0.112	0.061–0.285	0.10–0.48	0.10–4.03	0.06–0.28	193	Zachoval et al. (2014a)
SUTB	0.5	0.150	0.022–0.038	0.109–0.244	0.22–0.49	0.73–1.63	0.27–0.6	14	Rumann (2014)

EVALUATION

Modular limit

Visual observation and photographic documentation of the experiments under modular limit conditions implied that the water level on the weir crest mainly depends on the ratios of h/L and h/P. Undular hydraulic jump appears on the crest. If $h/L = 0.1$, three wave peaks are formed; if $h/L = 0.4$, one peak is formed. Formation of the undular hydraulic jump complies with the observations and measurements by Berezinskij (1950), Hager and Schwalt (1994) and Wols (2005).

Verification of applicability of Equation (16) to determine H_{f0}/H on the basis of the h/P ratio is illustrated in Fig. 4 for smooth surfaces. The graph includes values from the actual experimental research (Rumann (2014) – SUTB; Zachoval and Roušar (2014) – BUT 0.5; Zachoval et al. (2014) – BUT 1) and values defined by other authors (Halliwell and Hill (1967) specified in Markland et al. (1967)) in the ranges of $0.10 \le h/L \le 0.30$, $h \ge 0.06$ m and $h - h_f > 0.01$ m. For comparison purpose, curves defined by calculation from Equation (16) showing the limits of h/L for the approximately medium head over the weir measured in experiments for $h = 0.1$ m are depicted. The graph implies that with respect to measuring uncertainty, Equation (16) provides sufficiently accurate results for majority of the measured data within the entire range, i.e. $0.10 \le h/P \le 3.0$.

It is not possible to verify Equation (16) upon measurements for $P_U \ne P_D$, different relative roughness and different kinetic energy coefficients as there are no measured data. In these cases, the equation is not verified. Provided it could also be used for $P_U \ne P_D$, the effect of certain quantities and ratios may be analysed as shown in Fig. 5. Modular limits are illustrated by 6 curves. The curves for $h/P_U = 0.52$ refer to upper limit of high weirs where the values of C_d and h_C/H are independent of the h/P_U (17a, 18a). Curves for $h/P_U = 2.5$ are limit curves for determination of h_C/H (18b). The values for $h/L = 0.1$ and $h/L = 0.3$ define the range in which the value of C_d is independent of the h/L ratio. To express the scale effect caused by friction and surface tension, minimum head over weir not affected by friction and surface tension was defined to be $h = 0.06$ m (ISO 3846, 2008; Zachoval et al., 2014); maximum value for practical use was set to $h = 10$ m. The graph in Fig. 5 implies that all the above effects in ranges $0 \le h/P_D \le 1$, $0 \le h/P_U \le 2.5$, $0.10 \le h/L \le 0.30$, $h/b \le 0.5$ and for smooth surfaces are negligible, and can be substituted by a single curve. In the case of $h/P_D > 1$, the effects are different and cannot be neglected.

Equation (16) is applicable only to broad-crested weirs in the range of $0.10 \le h/L \le 0.30$. The Equation (16) cannot be used for other ranges, as the flow is not described sufficiently. To justify the use of the adopted simplification when deriving the Equation (16), graph of the relation between the relative individual head loss h_{zi}/h_z and h/P_D for smooth surfaces and for limit cases was elaborated. Two limit cases were specified form Fig. 5 as approximate envelope of all curves in Fig. 5: $h/P_U = 2.5$, $h/L = 0.3$, $h = 10$ m and $h/P_U = 0.52$, $h/L = 0.1$, $h = 0.06$ m. The relation is presented in Fig. 6. The graph shows that when h/P_D increases, the values of h_{zUC}/h_z, h_{zCT}/h_z, h_{zCE}/h_z a h_{zED}/h_z increase but the ratio of h_{zE}/h_z decreases. Within the sum, two individual relative losses, h_{zUC}/h_z and h_{zE}/h_z, are dominant (67% to 98%). The individual significance of other relative losses is relatively small, so the adopted simplifications can be considered acceptable for this case.

Practical use of Equation (16) is difficult, because the formula is very complicated. However, a simple, generally applicable equation with high accuracy cannot be found. Simplification of the equation results in limited applicability range. For a common case of real application: smooth surfaces, $P_U = P_D$, $0.10 \le h/L \le 0.30$, $h/b \le 0.5$ and range $0 \le h/P \le 3.5$, the Equation (16) can be approximated by the following formula

$$\frac{H_{f0}}{H} = 0.71 + 0.18 \cdot \left(\arctan \frac{h}{P} \right)^{0.71}, \tag{23}$$

where the coefficient of determination is $R^2 = 0.94$ for the data measured by us (Table 3). Equation (23) is (if Equation (16) is valid) applicable also for $P_U \ne P_D$ for ranges $0 \le h/P_D \le 1$, $0 \le h/P_U \le 2.5$, $0.10 \le h/L \le 0.30$, $h/b \le 0.5$ and for smooth surfaces (P in the Equation (23) is replaced by P_D). Curve for Equation (23) is shown in both Fig. 4 and Fig. 5 which imply good agreement with Equation (16) as well as the measured data.

Submergence coefficient

The $C_m = 2/5$ and the $C = 1$ were determined by the method of least squares (while respecting uncertainties of measurement) and with use of Equation (23) from all measured data fulfilling the conditions $0.1 \le h/P \le 2.5$, $0.10 \le h/L \le 0.30$, $h/b \le 0.3$, $h \ge 0.06$ m and $h - h_f \ge 0.01$ m. The submergence coefficient, C_f, for $P_U = P_D$ is then

$$C_f = \left[1 - \left(\frac{H_f - H_{f0}}{H - H_{f0}} \right)^{3/2} \right]^{2/5}. \tag{24}$$

Bereitgestellt von University Library Bratislava | Heruntergeladen 31.01.20 12:22 UTC

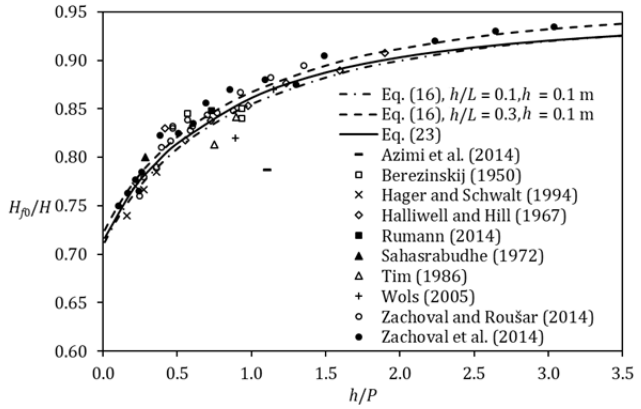

Fig. 4. Dependence of H_{f0}/H and h/P; data complying with requirements on $P_U = P_D$, $h \geq 0.06$ m, $0.10 \leq h/L \leq 0.30$, $h/b \leq 0.5$, $h - h_f > 0.01$ m and smooth surfaces.

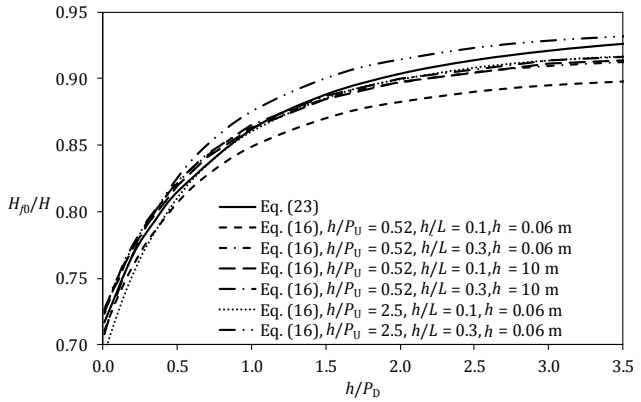

Fig. 5. Dependence of H_{f0}/H and h/P_D for smooth surfaces.

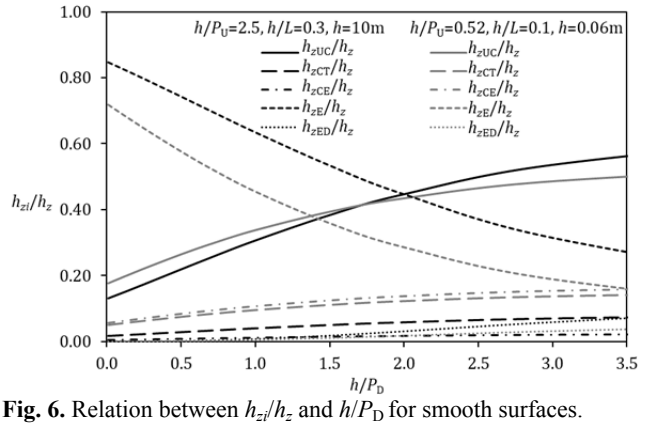

Fig. 6. Relation between h_{zi}/h_z and h/P_D for smooth surfaces.

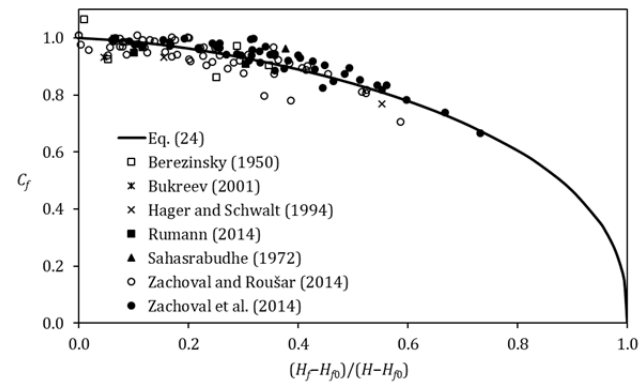

Fig. 7. Dependence of C_f on $(H_f - H_{f0})/(H - H_{f0})$, measured data.

The measured data and Equation (24) were plotted on a graph in Fig. 7. The graph shows good agreement (with respect to uncertainties in measuring small difference $h - h_f$) with the data measured within the range $0 \leq (H_f - H_{f0})/(H - H_{f0}) < 0.7$. For $P_U \neq P_D$, the exponent C_m, and coefficient C could not have been determined due to the lack of measured data.

Comparisons of the calculated coefficients by Equation (24) $C_{f\,\text{Eq. (24)}}$, by Azimi et al. (2014) equation $C_{f\,Azimi\ et\ al.\ (2014)}$, by the Berezinsky (1950) equation $C_{f\,Berezinsky\ (1950)}$, by the Hager and Schwalt (1994) equation $C_{f\,Hager\ and\ Schwalt\ (1994)}$ and computed coefficients from measurement C_f are shown in the Fig. 8 to Fig. 11. The figures imply that the C_f is computed most accurately by Equation (24), Azimi et al. (2014) computed the values inaccurately, Berezinsky (1950) computed the values relatively accurately in the whole range of measured data, and Hager and Schwalt (1994) computed the values relatively accurately in the range of $0.8 < C_f \leq 1.0$. In Fig. 12, comparison of the coefficients calculated by the Villemonte equation with $C = 1.18$ and $C_m = 0.14$ determined by the method of least squares $C_{f\,Villemonte}$ with the C_f is shown. The computed values are relatively accurate only in the range of $0.85 < C_f \leq 1.00$. Consequently, the original formula of Villemonte equation is less suitable for broad-crested weirs.

Method of determining the discharge

Recommended method of determination of the discharge, Q, for an overflow with identical heights of weir faces $P_U = P_D$ and smooth surfaces is:

- Measure the quantities P, h, h_f, L, b and define α_U, α_D (estimate or from measurement). Calculate the ratios h/L, h/P, h/b.
- Verify the applicability of relations for the calculation where $h \geq 0.06$ m, $0.1 \leq h/P \leq 3.0$, $0.10 \leq h/L \leq 0.30$, $h/b \leq 0.33$ must be met and the uncertainty of determining the difference between water levels in profiles U and D must be lower than the maximum permissible uncertainty of Q determination.
- Calculate H_{f0}/H from Equation (23) and C_d from Equations (17). By iteration with use of Equations (1, 2, 3), calculate Q for free flow and then H_f/H. If $H_f/H < H_{f0}/H$, free flow conditions apply and the calculation is completed; if not, the conditions comply with submerged flow and the following step is to be taken.
- Determine Q by iteration with use of Equations (1, 2, 3, 17, 23, 24).

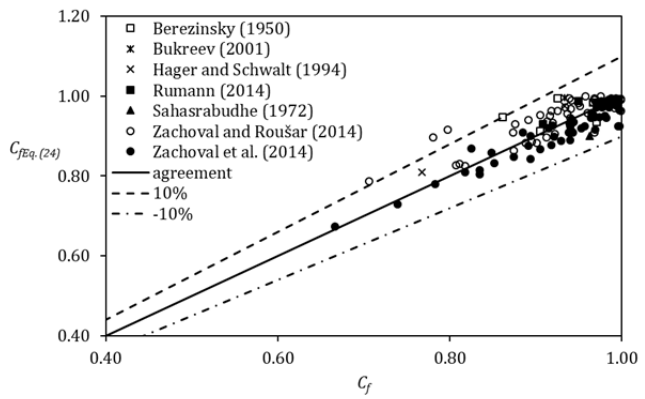

Fig. 8. Graph of agreement between $C_{f\,Eq.\ (24)}$ and C_f.

Bereitgestellt von University Library Bratislava | Heruntergeladen 31.01.20 12:22 UTC

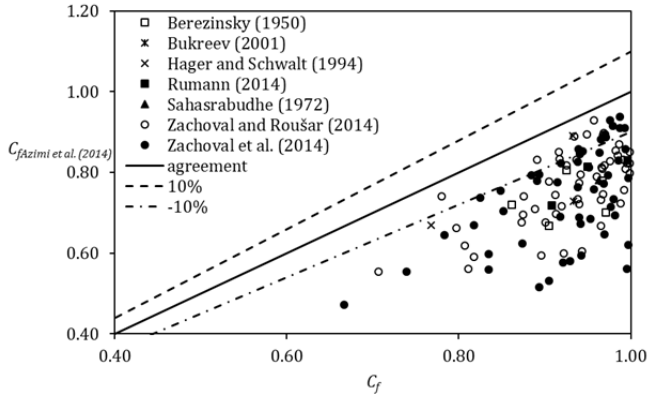

Fig. 9. Graph of agreement between $C_{f\,Azimi\ et\ al.\ (2014)}$ and C_f.

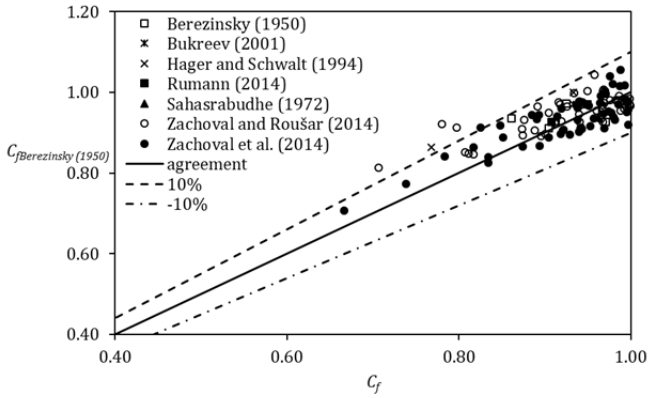

Fig. 10. Graph of agreement between $C_{f\,Berezinsky\ (1950)}$ and C_f.

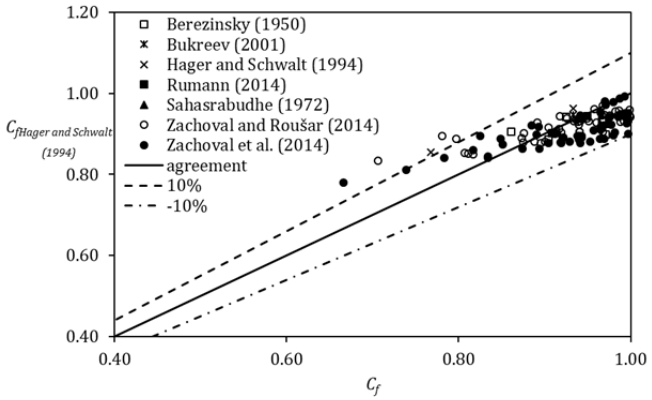

Fig. 11. Graph of agreement between $C_{f\,Hager\ and\ Schwalt\ (1994)}$ and C_f.

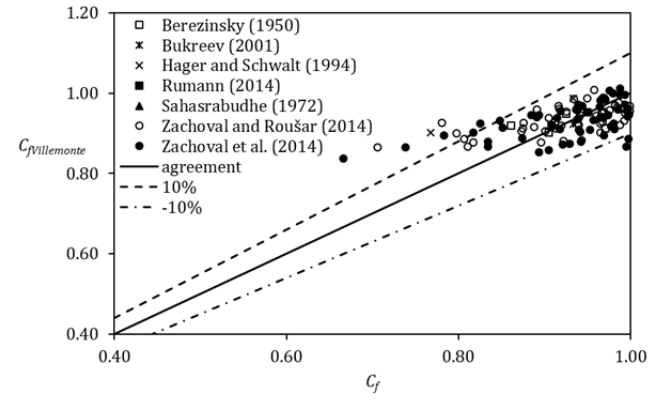

Fig. 12. Graph of agreement between $C_{f\,Villemonte}$ and C_f.

CONCLUSION

The article introduces derivation of the equation to determine modular limit expressed by the H_{f0}/H ratio for full-width sharp-edged broad-crested rectangular weir in the range $0.10 \leq h/L \leq 0.30$ situated in a channel of rectangular cross-section without the effect of friction on side walls and surface tension (16). After analysing the practically applicable ranges and for the case of identical heights of weir faces $P_U = P_D$, the equation was replaced by simple and sufficiently accurate empirical Equation (23) which is, in limited range, also probably applicable (is not verified by measured data) for $P_U \neq P_D$. The article also presents derivation of the equation to determine submergence coefficient, C_f, with empirically defined exponent C_m valid only in the case of $P_U = P_D$. The result is a system of equations describing both free and submerged flow over weir. The described system of equations enables a more accurate calculation of the discharge than those of other above mentioned authors. In the range $0.65 < C_f \leq 1.00$, the error in C_f definition amounts to ±10%.

Considerable extent of the experimental research enabled verification and simplification of the derived equation for modular limit and determination of the exponent for submergence coefficient. Within the experimental research, effort was made to measure the data as accurately as possible for the entire range of broad-crested weirs where the discharge coefficient for free flow is independent of the h/L ratio.

The research implied some important knowledge. Determination of modular limit is dependent on the used method (extrapolation of the approximation curve, agreed value of the change of water surface level in profile U etc.) which affects the evaluation by considerable uncertainty. At modular limit, water level in the outflow channel undulates, which is why mean value shall be considered with respect to both time and area (within the wave length). With the increase in value of the $(H_f - H_{f0})/(H - H_{f0})$ ratio, the uncertainty of determining the difference of water levels at profiles U and D increases; analysis of its effect is therefore recommended for each case.

Acknowledgement. This study was supported by project FAST-S-14-2203 Characteristics of submergence of low rectangular broad-crested weirs and project FAST-S-16-3757 Increasing of safety and reliability of selected hydrotechnical structures.

REFERENCES

Azimi, A.H., Rajaratnam, N., Zhu, D.Z., 2014. Submerged flows over rectangular weirs of finite crest length. J. Irrig. Drain. Eng., 140, 5, 06014001, 1–12.

Bazin, H., 1896. Expériences nouvelles sur l´écoulement en déversoir. 5 article. Annales des ponts et chaussées. Mémoires et documents relatifs à l'art des constructions et au service de l'ingénieur. 2 semestre, Gallica, Paris, pp. 645–731.

Berezinsky, A.P., 1950. Carrying Capacity of the Broad-Crested Weir. Vodgeo, Moscow. (In Russian.)

Bos, M.G., 1984. Long-Throated Flumes and Broad-Crested Weirs. Martinus Nijhoff/Dr W. Junk Publishers, Dordrecht.

Bos, M.G., 1989. Discharge Measurement Structures. Third revised edition. Publication 20. ILRI, Wageningen.

Brater, E.F., King, H.W., Lindell, J.E., Wei, C.Y., 1996. Handbook of Hydraulics. McGraw-Hill, New York.

Brownlie, W.R., 1981. Compilation of alluvial channel data: Laboratory and field. Report No. KH-R-43B. California Institute of Technology, Pasadena.

Bereitgestellt von University Library Bratislava | Heruntergeladen 31.01.20 12:22 UTC

Bukreev, V.I., 2001. Undular jump in open-channel flow over a sill. Journal of Applied Mechanics and Technical Physics, 42, 4, 596–602.

Chanson, H., 2009. Current knowledge in hydraulic jumps and related phenomena. A survey of experimental results. European Journal of Mechanics B/Fluid, 28, 191–210.

Crabbe, A.D., 1974. Some hydraulic features of the square edged broad-crested weir. Water and Water Eng., 78, 10, 354–358.

Doeringsfeld, H.A., Barker, C.L., 1941. Pressure-momentum theory applied to the broad-crested weir. Trans. ASCE, 106, 1, 934–946.

García, M.H., 2008. Sedimentation Engineering: Processes, Measurements, Modelling, and Practice. ASCE, Reston.

Goodarzi, E., Farhoudi, J., Shokri, N., 2012. Flow characteristics of rectangular broad-crested weirs with sloped upstream face. J. Hydrol. Hydromech., 60, 2, 87–100.

Govinda Rao, N.S., Muralidhar, D., 1963. Discharge characteristics of weirs of finite-crest width. La Houille Blanche, 18, 5, 537–545.

Hager, W.H., Schwalt, M., 1994. Broad-crested weir. J. Irrig. Drain. Eng., 120, 1, 13–26.

Hager, W.H., 2010. Wastewater Hydraulics. Springer, Heidelberg.

Harrison, A.J.M., 1967. The streamlined broad-crested weir. Proc. ICE, 38, 4, 657–678.

Horton, R.E., 1907. Weir Experiments, Coefficients, and Formulas. U.S.G.S., Washington.

Idel´chik, J.E., 1966. Handbook of Hydraulic Resistance. Coefficients of Local Resistance and of Friction. Israel Program for Scientific Translations, Jerusalem.

ISO 3846, 2008. Liquid flow measurement in open channels by weirs and flumes. Rectangular broad-crested weirs. IOS, Geneva.

Kašpar, T., 2015. Influence of the weir width on a discharge coefficient of the broad crested weir. Batchelor thesis. Brno University of Technology, Brno, Czech Republic. (In Czech.)

Keutner, C., 1934. Strömungsvorgänge an breitkronigen wehrkörpern und an einlaufbauwerken. Der Bauingenieur, 15, 366–371.

Madadi, M.R., Dalir, A.H., Farsadizadeh, D., 2014. Investigation of flow characteristics above trapezoidal broad-crested weirs. Flow Measurement and Instrumentation, 38, 139–148.

Major, J., 2013. Influence of upstream face inclination of broad-crested weir on discharge coefficient. Bachelor thesis. Brno University of Technology, Brno, Czech Republic. (In Czech.)

Markland, E., Abbott, M.B., Montes, S.S., Allen, J., Smith, C.D., Manning, R., Jaeger, C., Herschy, R.W., Halliwell, A.R. and Hill, J.A., Engel, F.V.A., Williams, J.M., Bunt, E.A., Hall, G.W., 1967. Discussion of the streamlined broad-crested weir. ICE Proc., 38, 657–678.

Montes, J.S., Chanson, H., 1998. Characteristics of undular hydraulic jumps: experiments and analysis. J. Hydr. Eng., 121, 2, 192–205.

Nikolov, N.A., Minkov, I.N., Dimitrov, D.K., Mincheva, S.K., Mirchev M.A., 1978. Hydraulic calculation of a submerged broad-crested weir. Hydrotechnical Construction, 12, 6, 631–634.

Noor Afzal, Bushra, A., Abu Seena, 2011. Analysis of turbulent hydraulic jump over a transitional rough bed of a rectangular channel: universal relations. J. Eng. Mech., 137, 12, 835–845.

Pavlovskij, N.N., 1937. Hydraulic Reference Book. ONTI, Leningrad. (In Russian.)

Rafter, G.W., 1900. On the flow of water over dams. Report on special water-supply investigation. Part II. Appendix No. 16. Transaction of ASCE, 44, 220–398.

Rumann, J., 2014. Submergence characteristic of low rectangular broad-crested weirs – validation measurement. Slovak University of Technology in Bratislava, Bratislava. (In Slovak.)

Sahasrabudhe, S.J., 1972. Discharge characteristics of submerged broad crested weirs. M.E. thesis. University of Rookee, Rookee.

Singer, J., 1964. Square-edged broad-crested weir as a flow measurement device. Water and Water Eng., 28, 820, 229–235.

Skogerboe, G.V., Hyatt, M.L., Austin, L.H., 1967. Design and Calibration of Submerged Open Channel Flow Measurement Structures: Part 4 – Weirs. Utah State University, Logan.

Sreetharan, P.M., 1983. Analytical and experimental investigation of flow measurement by long-based weirs in the rectilinear and curvilinear ranges. PhD thesis. The Hatfield Polytechnic, Hatfield, Hertfordshire, England.

Stevens, J.C., Wilm, H.G., Nelidov, I.M., Hackney, J.W., Prentice, T.H., Bakhmeteff, B.A., Curtis, D.D., Rohwer, C., Hedberg, J., 1941. Discussion of "Doeringsfeld, H.A., Barker, C.L., 1941. Pressure-momentum theory applied to the broad-crested weir". Transactions of the ASCE, 106, 1, 947–967.

Tim, U.S., 1986. Characteristics of some hydraulics structures used for flow control and measurement in open channels. PhD thesis. Concordia University, Montreal.

USACE, 1977. Hydraulic Design Criteria. Low-Monolith Diversion, Discharge Coefficients. USACE, Vicksburg.

Villemonte, J.R., 1947. Submerged-weir discharge studies. Eng. News Record, 867, 54–57.

Wols, B.A., 2005. Undular hydraulic jumps. M.Sc. Thesis. Delft University of Technology, Delft.

Woodburn, J.G., 1932. Tests of broad-crested weirs. Transactions of the American Society of Civil Engineers, 96, 1, 387–416.

Zachoval, Z., 2015. Broad-crested weirs with rectangular control section. Brno University of Technology, Brno.

Zachoval, Z., Mistrová, I., Roušar, L., Šulc, J., Zubík, P., 2012a. Zone of flow separation at the upstream edge of a rectangular broad-crested weir. J. Hydrol. Hydromech., 60, 4, 288–298.

Zachoval, Z., Pařílková, J., Roušar, L., 2012b. Velocity measurements in front of rectangular broad-crested weir. In: Chára, Z., Klaboch, L. (Eds.): Proc. 20th Symposium on Anemometry (Holany-Litice, Czech Republic 2006). Institute of Hydrodynamics ASCR, Prague, pp. 81–86. (In Czech.)

Zachoval, Z., Roušar, L., 2014. Bed load transport over rectangular broad-crested weir. Brno University of Technology, Brno. (In Czech.)

Zachoval, Z., Kněblová, M., Roušar, L., Rumann, J., Šulc, J., 2014a. Discharge coefficient of a rectangular sharp-edged broad-crested weir. J. Hydrol. Hydromech., 62, 2, 145–149.

Zachoval, Z., Roušar, L., Major, J., 2014b. Characteristics of submergence of low rectangular broad-crested weirs. Brno University of Technology, Brno. (In Czech.)

Zubík, P., 2006. PIV and LDA flow parameters measurement in the water channel with high negative step. In: Chára, Z., Klaboch, L. (Eds.): Proc. 20th Symposium on Anemometry (Holany-Litice, Czech Republic 2006). Institute of Hydrodynamics ASCR, Prague, pp. 105–114. (In Czech.)

Received 11 June 2018
Accepted 12 July 2019

NOMENCLATURE

b	weir width (m)
B	channel width (m)
C	proportional coefficient
C_d	discharge coefficient
C_{dd}	discharge coefficient
C_f	submergence coefficient
C_k	coefficient
C_m	power law exponent
C_v	approach velocity coefficient
Fr	Froude number
g	gravitational acceleration (m/s^2)
h	head, depth (m)
h_f	submergence head (m)

Bereitgestellt von University Library Bratislava | Heruntergeladen 31.01.20 12:22 UTC

h_z head loss (m)
H total head (m)
H_f total submergence head (m)
i slope
k_s hydraulic roughness (m)
l length (m)
L weir length in direction of flow (m)
N number of measurements
P weir height (m)
q specific discharge (m^2/s)
Q discharge (m^3/s)
R^2 coefficient of determination
v mean velocity at a cross-section (m/s)
α kinetic energy coefficient
ξ minor loss coefficient

Subscripts:
d downstream
u upstream
0 modular limit
U, C, T, E, D profiles

Bereitgestellt von University Library Bratislava | Heruntergeladen 31.01.20 12:22 UTC

J. Hydrol. Hydromech., 67, 2019, 4, 339–348
DOI: 10.2478/johh-2019-0020

Retarding contaminant migration through porous media using inclined barrier walls

Ayman Allam[1, 2*], Esam Helal[3], Mahmoud Mansour[3]

[1] Civil Engineering Department, Faculty of Engineering, Kafrelsheikh University, Kafrelsheikh, Egypt.
[2] Department of Civil and Environmental Engineering, Tokyo Institute of Technology, Ookayama, Meguro-ku, Tokyo 152-8552, Japan.
[3] Civil Engineering Department, Faculty of Engineering, Menoufia University, Menoufia, Egypt.
E-mails: EsamHelal@sh-eng.menofia.edu.eg, Esameman@yahoo.com (E. Helal), mahmoudmonirmansour@gmail.com (M. Mansour)
[*] Corresponding author. Tel.: +2-010-62056215. E-mails: aymanallam82@eng.kfs.edu.eg, ayman.e.aa@m.titech.ac.jp

Abstract: This study aims to assess the abilities of inclined barrier walls (BWs) to retard the migration of contaminants through porous media. Four cases of BW arrangements were considered, including a single inclined BW (BW_1) and two adjacent BWs (BW_1 and BW_2) with different combinations of inclination ratios (i.e., $I_1 = \theta_1/90°$ and $I_2 = \theta_2/90°$). Furthermore, the effect of the distance (L) between the contamination source and BW_1 on the migration time (T) was evaluated. A numerical model (GeoStudio) containing two modules (SEEP/W and CTRAN/W) was used. The model proved its reliability to simulate contaminant migration through the porous media, where the normalized objective function values between the simulated and analytical results were 0.02 and 0.04 for the discharge of seepage and concentration of contamination, respectively. The results demonstrated that the migration time was strongly influenced by the inclination ratios of the BWs. Three-dimensional regression analysis was applied to demonstrate the combined effect of the inclination ratio, L and BW arrangements on T.

Keywords: Contaminant migration; Advection-diffusion; Inclined barrier walls; Finite element; GeoStudio.

INTRODUCTION

Water scarcity is a widespread problem in many countries around the world, particularly in arid regions (Abdelhaleem and Helal, 2015; Allam et al., 2016). Among them, Egypt faces a particularly great challenge due to its limited access to water resources (Fleifle and Allam, 2016; Sobeih et al., 2017). Moreover, the spread of pollution throughout irrigation and drainage networks threatens the sustainable agricultural use of these limited resources (El Hassan and Allam, 2017). Unfortunately, the surface water (SW) within the Egyptian irrigation and drainage networks receives a large amount of non-point source pollution. Additionally, most of the wastewater generated within Egypt is dumped into its northern lakes without treatment (El-Mezayen et al., 2018). As a widespread alternative, groundwater (GW) represents one of the most promising and economically attractive options to enable access to additional water for different uses (El Hassan and Allam, 2017). However, solid wastes in Egypt are dumped into landfills absent any precautions for the protection of GW and/or SW resources (El-Salam and Abu-Zuid, 2015; Ibrahim and Mohamed, 2016; Ismail and Tawfik, 2015).

The dynamic behaviour of the quality of both GW and SW is commonly viewed as an impediment to the normal operation and performance of irrigation activities in Egypt (Shaban et al., 2010). Obviously, GW and SW pollution are crucial environmental problems that affect not only Egypt but also countries around the world (Barlow and Clarke, 2017). In addition, it is very difficult and expensive to restore polluted aquifers, and the costs required to monitor GW and SW pollution are very high (Strobl and Robillard, 2008). Thus, an efficient tool to protect GW and SW resources from pollution is urgently needed. In this context, the hydraulic control of contaminant migration represents one of the most common tools for the management, planning, and protection of GW and SW resources (Armanyous et al., 2016).

Controlling contaminant pollution involves either containing or redirecting contaminants along a certain direction or to a given location for a defined period. Several physical techniques have been used to control (i.e., restrict, stop, contain, or redirect) the migration of contaminants through porous fields. In this respect, the effects of vertical barrier walls (BWs) and/or extraction wells on the hydraulic control of contaminated GW have been extensively investigated by many researchers (Armanyous et al., 2016; Basha et al., 2012; Eltarabily and Negm, 2015; Guglielmetti and Butler, 1997; Nasr et al., 2003). However, despite the large number of reported studies, the process of hydraulically controlling the migration of contaminants through porous fields is still somewhat immature from an engineering perspective, as most of the abovementioned reports involved laboratory-scale experiments conducted under very limited conditions. In this context, numerical simulations constitute a simple, powerful and economical approach for predicting the migration of pollution through porous media.

Recently, several techniques have been assessed with regard to the numerical simulation of contaminant migration through porous media (Lateb et al., 2016). These methods have all proved their reliability as useful tools for evaluating the efficiency and suitability of physical techniques for controlling contaminant migration through soil (Al-Juboori and Datta, 2017; Eltarabily et al., 2015; Rathod and Sivapullaiah, 2017; Monir et al., 2018). In particular, the finite element method (FEM) represents an accurate and effective numerical technique for simulating the flow field through a porous media. Among the different types of FEM software, GeoStudio has been proven to be flexible and accurate in simulations of the flow field through porous media (Al-Juboori and Datta, 2017; GEOSLOPE International Ltd., 2017; Rathod and Sivapullaiah, 2017).

The effect of the inclination angle of BWs on the migration of contaminants through porous fields is still unclear. Therefore, the objective of this study was to investigate the retarda-

Bereitgestellt von University Library Bratislava | Heruntergeladen 31.01.20 12:22 UTC

tion of contaminant migration through porous media by using inclined BWs. More specifically, the effects of the BW inclination angle and the distance between the source of contamination and the first barrier wall on the rate of contaminant migration were investigated numerically.

MATERIALS AND METHODS

Numerical model

The FEM package GeoStudio 2007 was used to simulate the spread of contaminants in porous media. The GeoStudio package includes four modules that can be employed to simulate the flow of either energy or mass (i.e., the flow modules). Accordingly, the GeoStudio model was used to simulate the effect of using inclined BWs on the retardation of contaminant migration through a porous media. Two modules were used, namely, the flow (SEEP/W) and transport (CTRAN/W) modules. The SEEP/W module is used to simulate the flow of water through saturated porous media. Additionally, the CTRAN/W module is used to simulate solute transfer by advection and diffusion, and it is coupled with SEEP/W to simulate the advection of dissolved solutes through water transfer. Detailed descriptions of the governing equations and processes included in the SEEP/W and CTRAN/W modules are presented in GEOSLPE International Ltd. (2017).

The GeoStudio model was verified in three stages. First, an analytical solution using the fragment method developed by Pavlovsky in 1935 was applied to check the results of the SEEP/W model (Griffiths, 1984). Second, an analytical solution for the one-way migration of contaminants that considers both advection and dispersion was compared with the advection-dispersion analysis of a numerical model using CTRAN/W. Finally, particle tracking analysis (PTA) was performed using a sandbox model to simulate the motion of pollutants through a porous system. A complete description of the verification process is presented in Monir et al. (2018) and Metwally et al. (2018).

The GeoStudio accuracy was evaluated using statistics based on calculations of the root mean square error (RMSE) and normalized objective function (NOF) between the simulated and analytical results as follows:

$$RMSE = \sqrt{\frac{\sum_{i=1}^{N}\left(P_i - C_i\right)^2}{N}} \quad (1)$$

$$NOF = \frac{RMSE}{C_{mean}} \quad (2)$$

where P_i and C_i are the predicted and analytically calculated values, respectively; C_{mean} is the mean of the analytically calculated values; and N is the number of measurements. Model predictions are acceptable for NOF values in the interval from 0.0 to 1.0 (Allam et al., 2015).

Numerical sets

One hundred and twenty numerical runs were performed using inclined and/or vertical BWs. These runs were divided into four sets, as shown in Table 1. In Set I, a single barrier wall (BW_1) with a varying angle of inclination (θ_1) was placed at a distance (L) from a source of pollution. The values of θ_1 were 45°, 60°, 75°, 90°, 105°, 120°, and 135°, and the corresponding values of the dimensionless inclination ratio for BW_1 (I_1) (i.e., θ_1 /90°) were 0.50, 0.67, 0.83, 1.0, 1.17, 1.33 and 1.5, respectively. In sets II, III, and IV, two BWs were used to retard the migration of contaminants, and a second BW (BW_2) was placed in succession at a constant distance (X) downstream of BW_1 (Figure 1).

In Set II, BW_1 was inclined at angles of θ_1 = 45°, 60°, 75°, 105°, 120° and 135° corresponding to I_1 values of 0.50, 0.67, 0.83, 1.17, 1.33 and 1.5, respectively, while the inclination angle of BW_2 (θ_2) was kept constant at 90° corresponding to a dimensionless inclination ratio (I_2) (i.e., θ_2 / 90°) of 1.0.

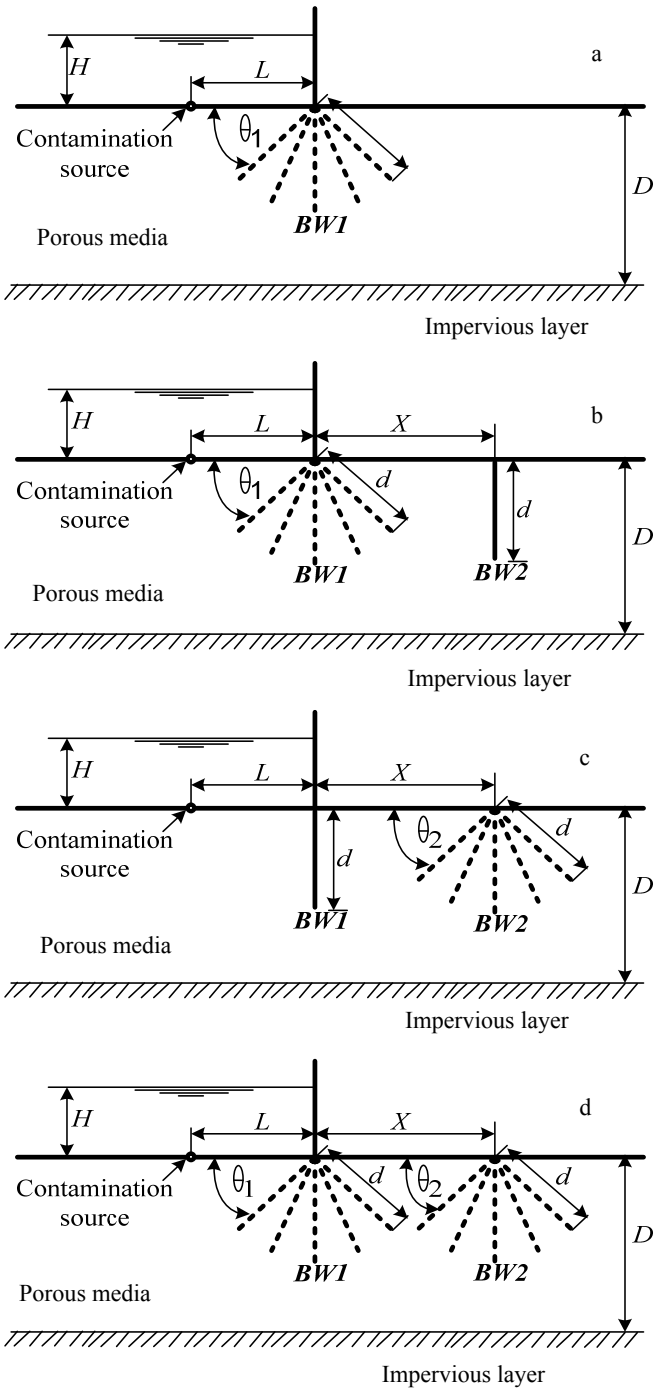

Fig. 1. Barrier walls arrangements for using single inclined barrier wall (BW) with different values of inclination ratio (I_1) (a), case of using two BWs with different values of I_1 and I_2 = one (b), I_1 = 1.0 and different values of I_2 (c), and with different values of I_1 and I_2 (d).

Bereitgestellt von University Library Bratislava | Heruntergeladen 31.01.20 12:22 UTC

Table 1. Conditions of the numerical simulation sets.

Set no.	Definition	Number of Runs	Conditions					
			θ_1	$I_1 = \theta_1/90^o$	θ_2	$I_2 = \theta_2/90^o$	X/D	L/D
Set I	Single barrier wall (BW_1) was placed at distance (L) from a source of pollution with different angles of inclination (θ_1)	35	45°, 60°, 75°, 90°, 105°, 120° and 135°	0.5, 0.67, 0.83, 1.0, 1.17, 1.33 and 1.5	N.A.	N.A.	N.A.	0.05, 0.10, 0.15, 0.20, and 0.25
Set II	The BW_1 was used with different values of θ_1 and subsequent barrier wall (BW_2) was placed at distance (X). The BW_2 was vertical (i.e., $\theta_2 = 90$)	30	45°, 60°, 75°, 105°, 120° and 135°	0.5, 0.67, 0.83, 1.17, 1.33 and 1.5	90°	1	0.6	
Set III	The BW_1 was used with θ_1 = 90° and BW_2 was used with different values of θ_2	30	90°	1	45°, 60°, 75°,105°, 120° and 135°	0.5, 0.67, 0.83, 1.17, 1.33 and 1.5	0.6	
Set IV	The BW_1 and BW_2 were used with different values of θ_1, and θ_2, respectively	25	60° 60° 75° 75° 90°	0.67 0.67 0.83 0.83 1	105° 120° 105° 120° 90°	1.17 1.33 1.17 1.33 1		

N.A. indicates not applicable condition

Table 2. Soil properties for numerical model.

Properties	Value
Porosity (n) %	0.50
Hydraulic conductivity	5×10^{-6} m/s
K_x/K_y	1.0
Longitudinal dispersivity (α_L)	$(0.83\log(F)^{2.41})$*1.2 m (F indicates the flow path length)
Transverse dispersivity (α_T)	$0.1\alpha_L$ m

In Set III, BW_1 was inclined at θ_1 = 90° with an I_1 value of 1.0, while BW_2 was inclined at angles of θ_2 = 45°, 60°, 75°, 105°, 120° and 135° corresponding to I_2 values of 0.50, 0.67, 0.83, 1.17, 1.33 and 1.5, respectively. In Set IV, BW_1 and BW_2 were used with different combinations of θ_1 and θ_2, as shown in Table 1; the values of I_1 were 0.67, 0.83, and 1.0, whereas those of I_2 were 1.17, 1.33, and 1. For all sets, two-dimensional steady-state flow was considered in a homogeneous isotropic porous media with a constant thickness (D) with a hydraulic conductivity (k) of 5×10^{-6} m/s. Longitudinal dispersivity and transverse dispersivity was calculated according to Todd and Mays (2005). The porous media properties for the numerical model are presented in Table 2.

To evaluate the effect of the distance between the pollution source and BW_1 (L) on the contaminant migration time (T), five values of L were considered in the numerical simulations. The effect of L was expressed in terms of the dimensionless distance ratio (L/D), which took values of 0.05, 0.1, 0.15, 0.2, and 0.25.

In the case of a single BW, the time required for 5% of the initial contaminant concentration to arrive at the porous media surface downstream of the BW was determined. In the case of using two successive BWs, the time required for 5% of the initial contaminant concentration to arrive at the porous media surface downstream of BW_2 was determined. The effects of the inclination angles of the *BWs* on the migration time of the contaminants were expressed in terms of the dimensionless time ratio (T/T_0), where T represents the migration time for 5% of the contaminant concentration to reach downstream of the BW under specific conditions, and T_0 is the migration time for 5% of the contaminant concentration to reach downstream of a vertical single BW with L/D = 0.05.

The boundary conditions for the contaminant flow are presented in Figure 1 and Table 2. The governing equations of groundwater motion at hydrodynamic pressure liquid equilibrium, forces that resist seepage flow, gravity acceleration, and flowing acceleration forces are expressed as in Halek and Svec (1979):

$$\begin{cases} \dfrac{1}{mg}\dfrac{\partial V_X}{\partial t}+\dfrac{\partial h}{\partial x}+\dfrac{V_X}{k}=0 \\ \dfrac{1}{mg}\dfrac{\partial V_y}{\partial t}+\dfrac{\partial h}{\partial y}+\dfrac{V_y}{k}=0 \\ \dfrac{1}{mg}\dfrac{\partial V_z}{\partial t}+\dfrac{\partial h}{\partial z}+\dfrac{V_z}{k}=0 \end{cases} \tag{3}$$

where m is the mass, g is gravitational acceleration, V_X, V_y and V_z are velocities components at the x,y,z-directions, respectively, h is head, t is time, and k is the conductivity coefficient.

While, the equation of continuity is expressed as:

$$\frac{\partial V_X}{\partial x}+\frac{\partial V_y}{\partial y}+\frac{\partial V_z}{\partial z}=0 \tag{4}$$

The law of conservation (advective-dispersive equation) for solute migration in saturated media was obtained (Todd and Mays, 2005):

$$\left[\left(D_x\frac{\partial^2 C}{\partial x^2}\right)+\left(D_y\frac{\partial^2 C}{\partial y^2}\right)+\left(D_z\frac{\partial^2 C}{\partial z^2}\right)\right]- \left[\left(\bar{V}_x\frac{\partial c}{\partial x}\right)+\left(\bar{V}_y\frac{\partial c}{\partial y}\right)+\left(\bar{V}_z\frac{\partial c}{\partial z}\right)\right]=\frac{\partial C}{\partial t} \tag{5}$$

Bereitgestellt von University Library Bratislava | Heruntergeladen 31.01.20 12:22 UTC

where C is the contamination concentration and dispersion coefficients D_x, D_y and D_z do not vary through space.

Regression analysis

A three-dimensional regression analysis of the numerical results was performed to assess the impacts of the inclination ratio and the distance to the contamination source on the migration time of the contaminants for different arrangements of BWs. Using the three-dimensional plane function (Eq. 3), a statistical regression of the numerical results for T/T_0 (indicated in Eq. 3 as Z) was considered with two independent variables, namely, L/D (indicated in Eq. 3 as x) and I_1, I_2, or I_1. I_2 (indicated in Eq. 6 as y), as follows:

$$Z = y_0 + a.x + b.y \quad (6)$$

where Z is the dependent variable (T/T_0), and a and b are coefficients that control the plane slope. The model fitness was evaluated using analysis of variance (ANOVA), and significance (p-value) was considered according to a 95% confidence level. The statistical analyses were conducted, and the surface response plots were plotted using SigmaPlot 14.0 software.

RESULTS AND DISCUSSION

Model verification

The simulated seepage discharge of the contaminant calculated using the SEEP/W module and the analytical values of the seepage discharge using the fragment method are presented in Figure S1 (Supplementary). The simulation and analytical results are in good agreement. The value of the NOF was 0.02 for the seepage discharge. The SEEP/W simulations for the seepage discharge of the contaminant were satisfactory, as the value of the NOF was close to 0.0. Based on these results, the SEEP/W module can be applied to effectively simulate the migration of contaminants through porous media and around BWs.

The analytical solution of the one-way migration of contamination in consideration of both advection and dispersion was compared with the advection-dispersion analysis by using the CTRAN/W module, as shown in Figure S2. The values of the NOF were 0.015 and 0.004 for pollutant concentrations at discharge times of T = 0.315 and 0.95 years, respectively. The CTRAN/W module verification for the simulated contaminant migration was satisfactory, as the value of the NOF was close to 0. Based on these results, the CTRAN/W module can be applied to effectively simulate the migration of contaminants through porous media.

Furthermore, an experimental simulation of the arrival time of contaminants migrating through porous media using a sandbox model was compared with the numerical PTA in consideration of different values of L/D (Figure S3), and the NOF between the experimental and numerical results of the arrival time was 0.04. Consequently, the SEEP/W and CTRAN modules can be applied to effectively simulate the migration of contaminants through porous media.

The flow field of contaminants through porous media and around different arrangements of barrier walls

Single inclined barrier wall

The effects of using a single inclined barrier wall (i.e., BW_I) with different values of the inclination ratio (I_1) (i.e., $I_1 = \theta_1/90°$) on the dimensionless ratio of the contaminant migration time (T/T_o) at different values of the dimensionless distance ratio (L/D) are presented in Figure 2a. Most values of T/T_o were greater than one, which means that an inclined BW constitutes an effective mechanism for retarding contaminant migration. For L/D = 0.15, 0.20, and 0.25, T/T_o exhibited an increase with an increase in I_1. For L/D = 0.05 and 0.10, T/T_o slightly increased with an increasing inclination ratio for the BW up to I_1 = 1.0 (i.e., θ_1 = 90°), whereas there was no clear effect as I_1 exceeded a value of one. At L/D = 0.25, the value of T/T_o using a single inclined BW with I_1 = 1.5 increased by 12%, 28%, 33%, 43%, 49%, and 54% corresponding to I_1 = 1.33, 1.17, 1, 0.83, 0.67 and 0.5, respectively. This could be due to an increase in the flow line length of contaminants needed to reach the porous media surface downstream of the inclined BW, as described in Table S1. The results show that at L/D = 0.25, the value of L_p/D for I_1 = 1.5 increased by 7%, 15%, 17%, 21%, 28% and 44% compared with its values at I_1 = 1.33, 1.17, 1, 0.83, 0.67 and 0.5, respectively.

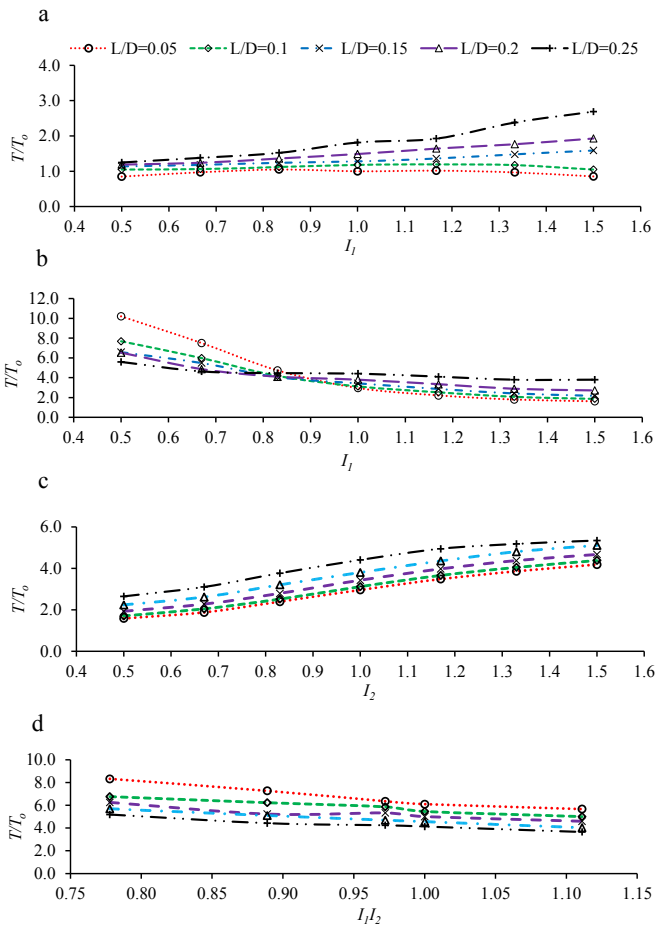

Fig. 2. The travel time dimensionless ratios at different values of L/D in case of using single inclined barrier wall (BW) with different values of inclination ratio (I_1) (a), two BWs with different values of I_1 and I_2 = 1.0 (b), two BWs with I_1 = 1.0 and different values of I_2 (c), and two BWs with different values of I_1 and I_2 (d).

Similarly, the T/T_o values changed as L/D increased for all values of I_1. For example, the values of T/T_o using a single inclined BW with I_1 = 1.5 and L/D = 0.25 increased by 2.6%, 3%, 3.6%, and 4.3% compared with its values at L/D = 0.20, 0.15, 0.10 and 0.05, respectively. Hence, the effect of I on T/T_o is more obvious for higher values of L/D than for lower values. The minimum and maximum values of T/T_o were obtained at I_1

Bereitgestellt von University Library Bratislava | Heruntergeladen 31.01.20 12:22 UTC

= 1.5 with L/D = 0.05 and 0.25, respectively, which Could be due to an increase in the flow line length with increases in both the inclination angle and the distance between the barrier wall and the pollution source **.** In summary, the best value of I_1 for locating a single inclined BW to retard the downstream migration of contaminants is I_1 = 1.5, and the BW should be as far from the contamination source as possible. The contamination flow field through porous media using a single inclined barrier wall with I_1 = 0.83 at different times, the shapes of the flow lines, and the equipotential lines are presented in Figure 3. The results show that the time required for 5% of the initial contaminant concentration to arrive at the porous media surface downstream of the BW was 12.7 years with I_1 = 0.83 and L/D = 0.15.

An inclined barrier wall followed by a vertical barrier wall

The effects of using an inclined BW with different inclination angle ratios followed by a vertical BW on the values of T/T_o at different L/D ratios are presented in Figure 2b. For all tested flow conditions, all values of T/T_o were greater than one. For all values of L/D, T/T_o decreased with an increase in I_1. For instance, the value of T/T_o at I_1 = 0.5 and L/D = 0.05 increased by 26%, 54%, 71%, 78%, 82% and 84% relative to its values at I_1 = 0.67, 0.83, 1, 1.17, 1.33 and 1.5, respectively. In addition, the value of T/T_o at I_1 = 0.5 and L/D= 0.25 increased by 17%, 20%, 21%, 27%, 32% and 39% compared with its values at I_1 = 0.67, 0.83, 1, 1.17, 1.33 and 1.5, respectively. These results prove that the effect of an increase in I_1 on T/T_o decreases with an increase in L/D, which conforms with the percolation line

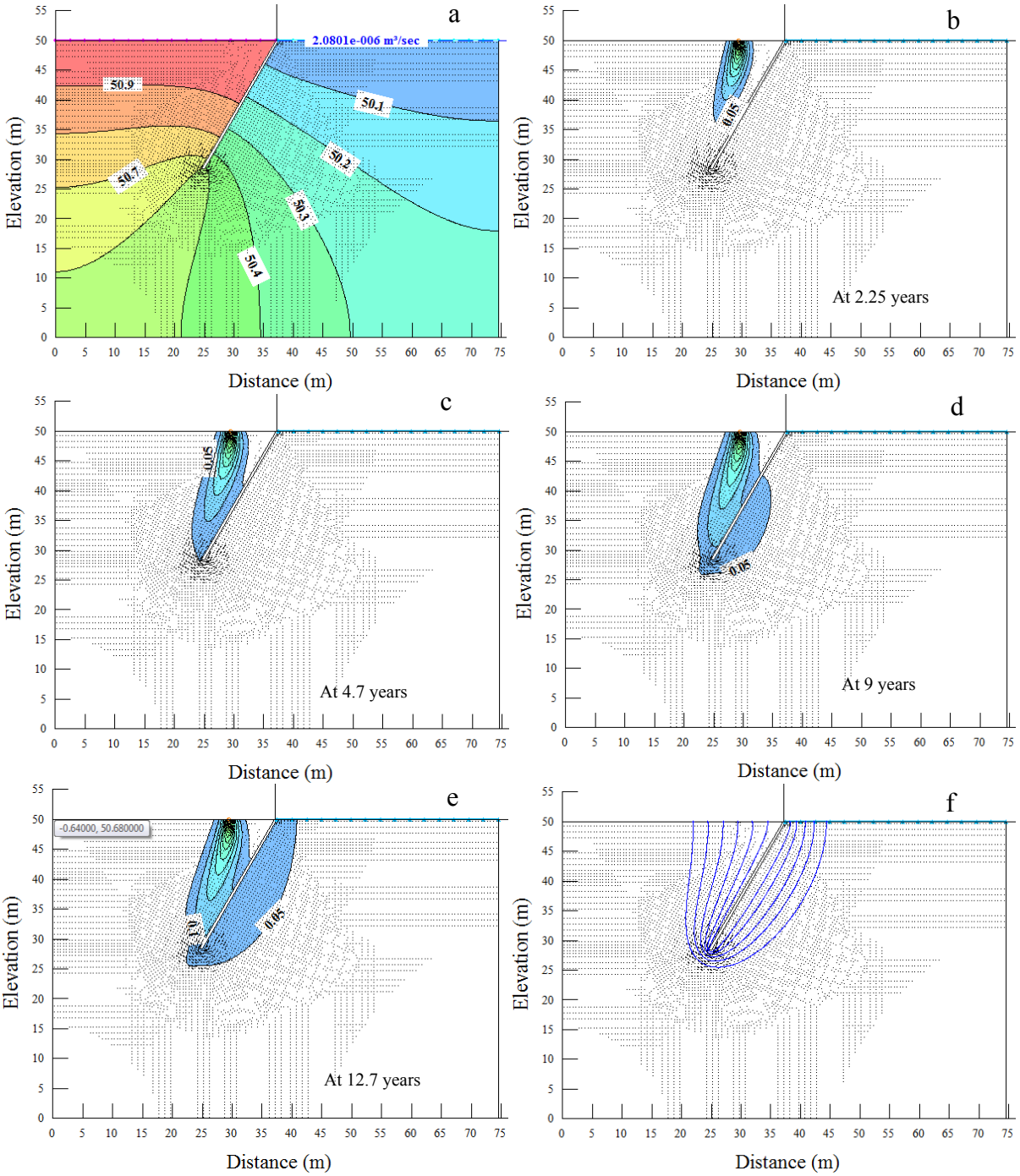

Fig. 3. Equipotential lines (a), flow filed of contaminant through soil after different times (b, c, d, e), flow lines (f) in case of using single inclined barrier wall with I_1 = 0.83, and L/D = 0.15.

Bereitgestellt von University Library Bratislava | Heruntergeladen 31.01.20 12:22 UTC

results described in Table 1S. These results show that the best arrangement for using BW_1 with different values of θ_1 and a vertical BW_2 is the use of BW_1 with I_1 = 0.5 (i.e., θ_1 = 45°) at L/D = 0.05. In contrast, using an inclined BW followed by a vertical BW gives higher values of T/T_o than those obtained with a single inclined BW, especially for I_1 < 0.90.

Vertical barrier wall followed by an inclined barrier wall

The effects of using a vertical BW followed by an inclined BW with different inclination ratios on T/T_o at different values of L/D are presented in Figure 2c. For all values of L/D, T/T_o displayed a significant increase with an increment in I_2. At L/D = 0.05 and I_2 = 1.5, T/T_o increased by 62%, 55%, 43%, 29%, 17% and 8% relative to its values at I_2 = 0.5, 0.67, 0.83, 1, 1.17, and 1.33, respectively. In contrast, at L/D = 0.25 and I_2 = 1.5, T/T_o increased by 50%, 42%, 29%, 17%, 7% and 3% compared with its values at I_2 = 0.5, 0.67, 0.83, 1, 1.17, and 1.33, respectively. These results are also in accordance with the percolation line results shown in Table 1S. In summary, the best arrangement for a vertical BW followed by an inclined BW with different inclination ratios is the use of BW_2 with I_2 = 1.5 at L/D = 0.25. Under these circumstances, the longest flow line and the corresponding longest migration time can be attained.

Figures 2b and 2c clarifies that the use of an inclined BW followed by a vertical BW gives higher values of T/T_o for I_1 values that are lower than 1.0. However, using a vertical BW followed by an inclined BW gives higher values of T/T_o for I_2 values exceeding 1.0.

Using two successive inclined barrier walls

The effects of using two successive inclined BWs with different inclination ratios on T/T_o at different values of L/D are presented in Figure 2d. The two inclination ratios (i.e., I_1 and I_2) were multiplied together to express the combined effect ($I_1.I_2$) of the inclination ratios of both walls on the contaminant migration time. For all values of L/D, T/T_o showed a significant decrease with an increment in $I_1.I_2$. The values of T/T_o with two inclined BWs at I_1 = 0.67 and I_2 = 1.17 ($I_1.I_2$ = 0.78) increased by 32%, 26%, 27%, 29% and 30% for L/D= 0.05, 0.1, 0.15, 0.2, and 0.25, respectively, compared with its values at I_1 = 0.83 and I_2 = 1.33 ($I_1.I_2$ = 1.11). In contrast, the values of T/T_o with two inclined BWs at I_1 = 0.67 and I_2 = 1.33 ($I_1.I_2$ = 0.89) increased by 16%, 12%, 4%, 11% and 7% for L/D = 0.05, 0.1, 0.15, 0.2, and 0.25, respectively, compared with its values at I_1 = 1.0 and I_2 = 1.0 ($I_1.I_2$ = 1.0). These results show that the effects of I_1 and I_2 on T/T_o decrease with an increase in the value of L/D. In summary, the use of two successive inclined BWs gives higher values of T/T_o, especially for higher values of I_1 and I_2. The flow field of contamination through porous media with two successive inclined BWs at I_1 = 0.83 and I_2 = 1.16 at different times, the shapes of the flow lines, and the equipotential lines are all presented in Figure 4.

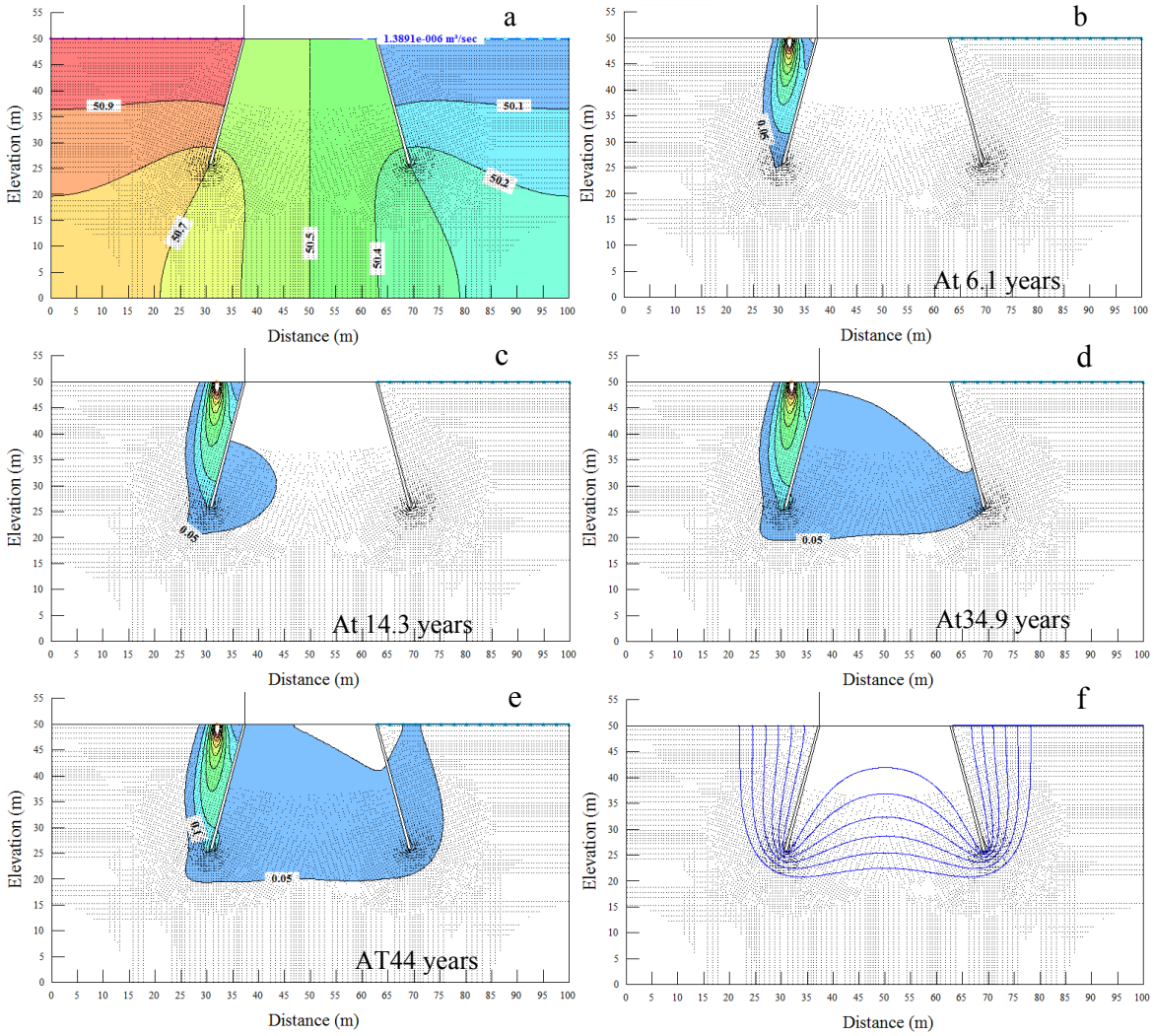

Fig. 4. Equipotential lines (a), flow filed of contaminant through soil after different times (b, c, d, e), flow lines (f) in case of using two inclined barrier walls with I_1 = 0.83, I_2 = 1.16 and L/D = 0.1.

Bereitgestellt von University Library Bratislava | Heruntergeladen 31.01.20 12:22 UTC

Comparison between different barrier wall arrangements

A comparison among different barrier arrangements, namely, the single vertical barrier arrangement examined by Basha et al. (2012), the two equal barriers with solid floors evaluated by Metwally et al. (2018), and the arrangements examined in the present study (Set I, Set II, Set III, and Set IV), is presented in Figure 5. This comparison shows that the value of T/T_0 with a single inclined BW increases relative to its value with the single vertical barrier of Basha et al. (2012) by a value ranging from 19.5% to 32.5%. In contrast, the values of T/T_0 with the inclined BWs in Set II, Set III, and Set IV increased by values ranging from 27% to 244%, from 21% to 41%, and from 18% to 181%, respectively, relative to the corresponding values for two equal barriers with solid floors as suggested by Metwally et al. (2018). Furthermore, the values of T/T_0 for Set II, Set IV and Set III increased compared with its values for the single vertical barrier of Basha et al. (2012) by values ranging from 209% to 920%, from 194% to 318%, and from 185% to 732%, respectively. These results prove the effectiveness of using inclined BW as opposed to vertical BW for retarding the migration of contaminants.

Three-dimensional regression analysis of the contaminant migration time

The three-dimensional plane equation (Eq. 6) was applied for the three-dimensional regression analysis of the numerical results. The combined effect of L/D (x) with I_1, I_2, or $I_1.I_2$ (y) on the migration time (T/T_0) was extensively assessed. Accordingly, the following equations were obtained as functions of the independent variables (x and y) to fit the observed data (Eqs. 7–10):

$$\frac{T}{T_0} = 0.246 + 3.711(x) + 0.511(y) \quad (7)$$

$$\frac{T}{T_0} = 7.692 + 1.512(x) - 3.848(y) \quad (8)$$

$$\frac{T}{T_0} = -0.402 + 6.501(x) + 2.879(y) \quad (9)$$

$$\frac{T}{T_0} = 12.481 - 11.764(x) - 5.591(y) \quad (10)$$

where Eqs. (7), (8), (9), and (10) represent T/T_0 for a single BW, two BWs where BW_1 is inclined, two BWs where BW_2 is inclined, and two inclined BWs, respectively. The predicted values of T/T_0 were statistically compared with the simulated values using ANOVA, as shown in Table 3.

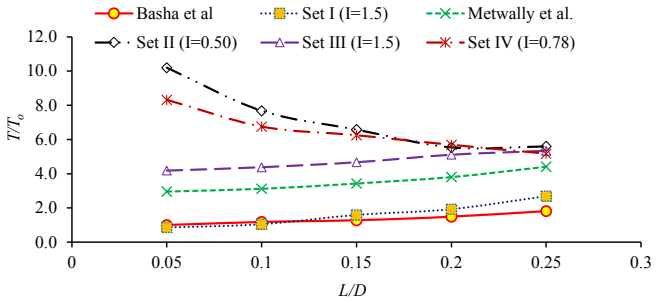

Fig. 5. Comparison between different barriers arrangements (I indicates the inclination ratio of barrier wall).

Table 3. Statistical analysis of ANOVA and 3D regression (plane) coefficients.

Single BW		Degree of freedom	Sum of squares	Mean square	F-value	P-value
	Regression	3	63.7509	21.2503	36.7157	<0.0001
	Residual		1.4901	0.0466		
	Total	35	65.241	1.864		
	R	R^2	Adjusted R^2	Standard error of estimate		
	0.8346	0.6965	0.6775	0.2158		
		Coefficient	Standard error	t-value		
	y_0	0.2459	0.1389	1.7706	0.0862	
	a	3.706	0.5158	7.1845	<0.0001	
	b	0.5111	0.1094	4.6706	<0.0001	
Two BW and the 1st one is inclined		Degree of freedom	Sum of squares	Mean square	F-value	P-value
	Regression	3	637.9384	212.6461	97.6634	<0.0001
	Residual	32	9.4998	0.2969		
	Total	35	647.4382	18.4982		
	R	R^2	Adjusted R^2	Standard error of estimate		
	0.9269	0.8592	0.8504	0.5449		
		Coefficient	Standard error	t-value	P-value	
	y_0	7.6919	0.3507	21.9331	<0.0001	
	a	1.5125	1.3025	1.1613	0.2541	
	b	–3.8481	0.2763	–13.9276	<0.0001	
Two BW and the 2nd one is inclined		Degree of freedom	Sum of squares	Mean square		
	Regression	3	456.6856	152.2285		
	Residual	32	0.7331	0.0229		
	Total	35	457.4187	13.0691		
	R	R^2	Adjusted R^2	Standard error of estimate		
	0.9909	0.9818	0.9807	0.1514		
		Coefficient	Standard error	t-value	P-value	
	y_0	–0.4021	0.0975	–4.124	0.0002	
	a	6.5	0.3618	17.9654	<0.0001	
	b	2.8794	0.0769	37.4637	<0.0001	
Two BW and both are rotating		Degree of freedom	Sum of squares	Mean square		
	Regression	3	757.3452	252.4484		
	Residual	22	1.3968	0.0635		
	Total	25	758.742	30.3497		
	R	R^2	Adjusted R^2	Standard error of estimate		
	0.9749	0.9505	0.946	0.252		
		Coefficient	Standard error	t-value	P-value	
	y_0	12.4815	0.4493	27.7821	<0.0001	
	a	–11.764	0.7127	–16.5065	<0.0001	
	b	–5.5908	0.4563	–12.2538	<0.0001	

Bereitgestellt von University Library Bratislava | Heruntergeladen 31.01.20 12:22 UTC

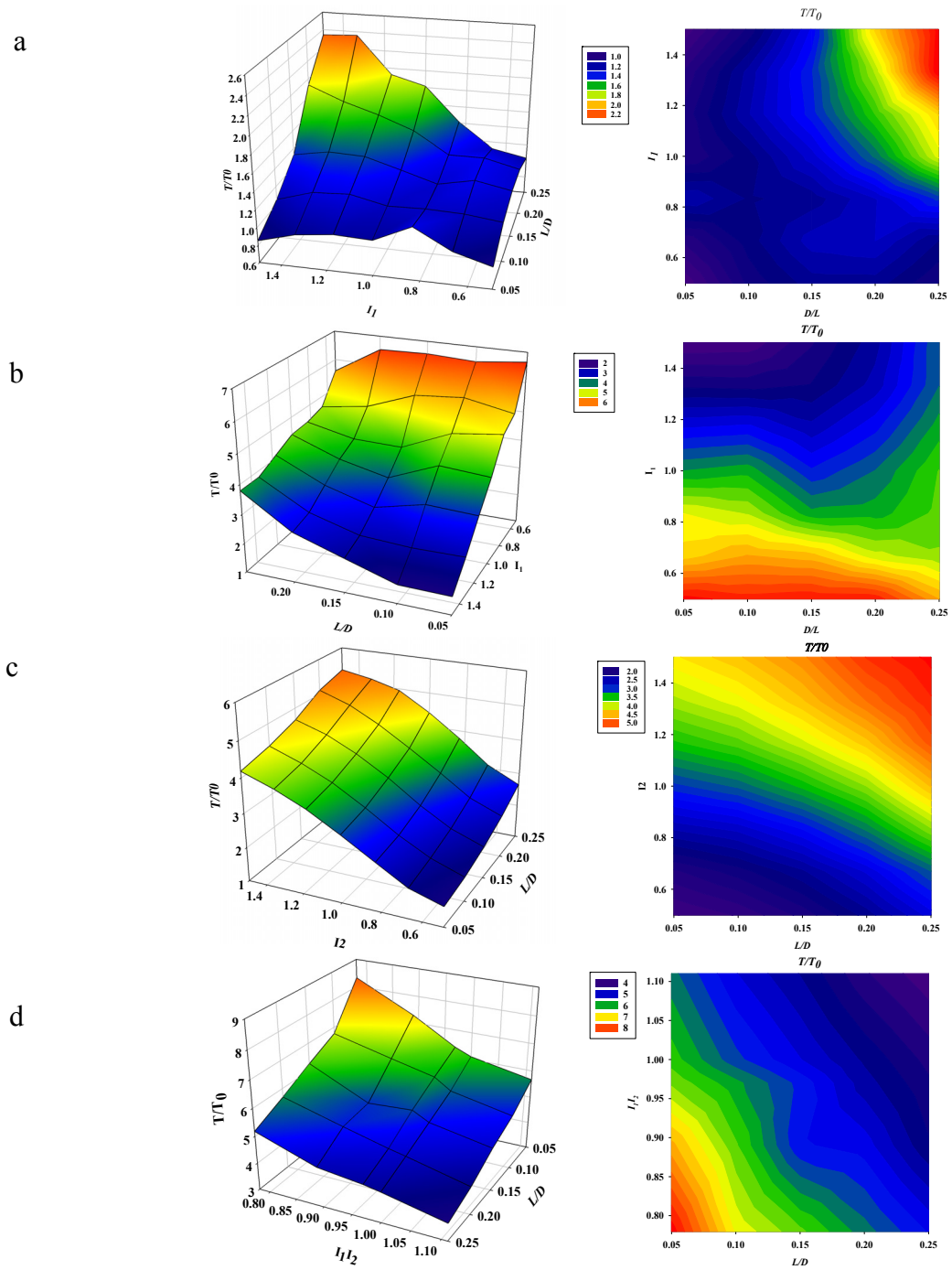

Fig. 6. Three-dimensional and contour plots of the representing the combination of L/D and I_1, or I_2, or $I_1.I_2$ and the resulted transport time (T/T_0) for single inclined barrier wall (a), two barrier walls and the 1st one is inclined (b), two barrier walls and the 2nd one is inclined (c), and using two inclined barrier walls (d).

The results reveal that the R^2 values of the four models statistically fitted to the simulated data ranged from 0.69 to 0.98. The F-values were higher than the p-values (low probability), indicating that the predicted results are significant. The three-dimensional plots for T/T_0 as functions of L/D and I_1, I_2, or $I_1.I_2$ are also shown in Figure 6. In this analysis, a peak value for T/T_0 was clearly detected; therefore, the maximum T/T_0 value can be recorded under the conditions used herein.

CONCLUSIONS

The effects of using inclined barrier walls (BWs) on the contaminant migration time (T/T_o) through porous media was evaluated. A numerical model (GeoStudio) with two modules (SEEP/W and CTRAN/W) was used to simulate groundwater (GW) flow and solute migration through porous media. Four cases of BW arrangements were considered, including a single BW (BW_1) and two successive BWs (BW_1 and BW_2) with different combinations of inclination angles (i.e., θ_1 and θ_2 for BW_1 and BW_2, respectively). The model accuracy was evaluated using statistics based on calculations of the normalized objective function (NOF) between the simulated and analytical results. The values of the NOF were 0.02 and 0.04 for the discharge of seepage and concentration of contamination, respectively. Accordingly, the model proved its reliability to simulate contaminant migration through porous media, as the NOF val-

Bereitgestellt von University Library Bratislava | Heruntergeladen 31.01.20 12:22 UTC

ues were close to zero. For a single BW, T/T_o increased with an increase in I_1. Moreover, the effect of an increase in I_1 on T/T_o decreased with an increase in L/D. The best I_1 value for a single inclined BW to retard the downstream migration of contaminants is $I_1 = 1.5$, and the BW should be located as far from the contamination source as possible.

In the case with an inclined BW followed by a vertical BW, for all values of L/D, T/T_o decreased with an increase in I_1. Additionally, the effect of an increase in I_1 on T/T_o decreased with an increase in L/D. In the case with a vertical BW followed by an inclined BW, for all values of L/D, T/T_o significantly increased with an increment in I_2; for all values of L/D, T/T_o significantly decreased with an increment in $I_1.I_2$. Moreover, the effects of the inclination ratios I_1 and I_2 on T/T_o decreased with an increase in L/D. In summary, the migration time was strongly influenced by the inclination angles of the BWs; for all tested conditions, $T/T_o > 1$, indicating that inclined BWs have a significant ability to retard contaminant migration. Three-dimensional regression analysis was applied to examine the combined effect of the BW inclination angles, the distance to the source of contamination and the arrangements of BWs on the contaminant migration time. These three-dimensional models could be effectively used to quantify the effects of inclined BW on the hydraulic retardation of contaminant flow fields through porous media.

Acknowledgements. The authors would like to thank the staff of the Irrigation and Hydraulics Laboratory, Civil Engineering Department, Faculty of Engineering, Menoufia University, Egypt, for their valuable support during the experimental work of this study.

REFERENCES

Abdelhaleem, F.S., Helal, E.Y., 2015. Impacts of Grand Ethiopian Renaissance Dam on different water usages in upper Egypt. Br. J. Appl. Sci. Technol., 8, 5, 461–483.

Al-Juboori, M., Datta, B., 2017. Influence of hydraulic conductivity and its anisotropy ratio on the optimum hydraulic design of water retaining structures founded on permeable soils. In: 13th Hydraulics in Water Engineering Conference (p. 220). Engineers Australia.

Allam, A., Tawfik, A., Yoshimura, C., Fleifle, A., 2016. Multi-objective models of waste load allocation toward a sustainable reuse of drainage water in irrigation. Environ. Sci. Pollut. Res., 23, 12, 11823–11834.

Allam, A., Fleifle, A., Tawfik, A., Yoshimura, C., El-Saadi, A., 2015. A simulation-based suitability index of the quality and quantity of agricultural drainage water for reuse in irrigation. Sci. Total Environ., 536, 79–90.

Armanyous, A.M., Ghoraba, S.M., Rashwan, I.M.H., Dapaon, M.A., 2016. A study on control of contaminant transport through the soil using equal double sheet piles. Ain Shams Eng. J., 7, 1, 21–29.

Basha, A.M.A, Al Nimr, A., Rashwan, I.M.H., Gabr, A.M., 2012. Use of sheet piles to control contaminant transport through the soil. J. Am. Sci., 8, 12, 568–573. (ISSN: 1545-1003). http://www.jofamericanscience.org.

Barlow, M., Clarke, T., 2017. Blue Gold: The Battle against Corporate Theft of the World's Water. The New Press, Routledge.

El Hassan, W., Allam, A., 2017. Management of the integration between irrigation and drainage water in the Nile Delta. In: Barceló, D., Kostianoy, A.G. (Eds.): The Handbook of Environmental Chemistry. Springer, Berlin, Heidelberg, pp. 1–8.

Eltarabily, M.G.A., Negm, A.M., 2015. Numerical simulation of fertilizers movement in sand and controlling transport process via vertical barriers. Int. J. Environ. Sci. Dev., 6, 8, 559–568.

Eltarabily, M., Negm, A.M., Valeriano, O.C.S., 2015. Protection of irrigation water from phosphate transport through the layered soil by using vertical barriers walls. In: Eighteenth International Water Technology Conference, IWTC18, Sharm ElSheikh, pp. 12–14.

El-Salam, M.M.A., Abu-Zuid, G.I., 2015. Impact of landfill leachate on the groundwater quality: A case study in Egypt. J. Adv. Res., 6, 4, 579–586.

El-Mezayen, M.M., Rueda-Roa, D.T., Essa, M.A., Muller-Karger, F.E., Elghobashy, A.E., 2018. Water quality observations in the marine aquaculture complex of the Deeba Triangle, Lake Manzala, Egyptian Mediterranean coast. Environ. Monit. Assess., 190, 7, 436–445.

Fleifle, A., Allam, A., 2016. Remediation of Agricultural Drainage Water for Sustainable Reuse. In: The Nile Delta. Springer, Cham, pp. 297–324.

GEOSLOPE International Ltd., 2017. Heat and Mass Transfer Modeling with GeoStudio 2018. 2nd Ed. Calgary, Alberta, Canada.

Griffiths, D.V., 1984. Rationalized charts for the method of fragments applied to confined seepage. Géotechnique, 34, 2, 229–238.

Guglielmetti, J.L., Butler, P.B., 1997. Use of a geomembrane steel sheet pile verticle barrier to curtail organic seepage. No. CONF-970208--PROC.

Halek, V., Svec, J., 1979. Groundwater Hydraulics. Elsevier Scientific Publishing Company, New York, pp. 19–50.

Ibrahim, M.I.M., Mohamed, N.A.E.M., 2016. Towards sustainable management of solid waste in Egypt. Procedia Environ. Sci., 34, 336–347.

Ismail, S., Tawfik, A., 2015. Treatment of hazardous landfill leachate using Fenton process followed by a combined (UASB/DHS) system. Water Sci. Technol., 1700–1708.

Lateb, M., Meroney, R.N., Yataghene, M., Fellouah, H., Saleh, F., Boufadel, M.C., 2016. On the use of numerical modelling for near-field pollutant dispersion in urban environments − A review. Environ. Pollut., 208, 271–283.

Metwally, N., Sobieh, M., Rashwan I., Helal, E., 2018. Control of contaminant transport using equal double sheet piles with impervious floor. M.Sc. Thesis. Civil Engineering Department, Menoufia University, Egypt.

Monir, M.M., Ellayn, F., Rashwan, I., Sobieh, M., Helal, E., 2018. Delaying solute transport through the soil using unequal double sheet piles with a surface floor. Ain Shams Engineering Journal, 9, 4, 3399–3409.

Nasr, R., Zeydan, B., Ghoraba, S.M., 2003. Three-dimensional finite element analysis of seepage around heading up structures. Mansoura Eng. J., 28, 1, 68–92.

Rathod, D., Sivapullaiah, P.V., 2017. Migration of Sulphate Under Different Conditions: Electro-Kinetic Remediation Technique. Indian Geotechnical Journal, 47, 4, 485–494.

Shaban, M., Urban, B., El Saadi, A., Faisal, M., 2010. Detection and mapping of water pollution variation in the Nile Delta using multivariate clustering and GIS techniques. J. Environ. Eng., 91, 1785–1793.

Sobeih, M.M., Arabi, N.E., Helal, E., Awad, B.S., 2017. Management of water resources to control groundwater levels in the southern area of the western Nile delta, Egypt. Water Science, 31, 2, 137–150.

Strobl, R.O., Robillard, P.D., 2008. Network design for water quality monitoring of surface freshwaters: A review. J. Environ. Manage., 87, 4, 639–648.

Todd, D.K., Mays, L.W., 2005. Groundwater Hydrology. 3rd Ed. Wiley.

Received 3 December 2018
Accepted 19 March 2019

NOMENCLATURE

BW_1	First barrier wall	–
BW_2	Second barrier wall	–
C	Contaminant concentration	ML^{-3}
C_s	Contaminant concentration at source	ML^{-3}
d	Depth of barrier walls	L
D	Soil layer thickness (i.e., effective depth of aquifer in meters)	L
H	Head difference between upstream and downstream (m)	L
k	Hydraulic conductivity (m/s)	$L^{-1}T^{-1}$

Bereitgestellt von University Library Bratislava | Heruntergeladen 31.01.20 12:22 UTC

L	Distance between the contamination source and the 1st barrier wall (m)	L
L_p	Flow path length (m)	L
Q	Seepage discharge (m^3/s)	L^3T^{-1}
T	Arrival time of 5% of the contaminant concentration downstream	T
T_o	Arrival time of 5% of the contaminant concentration using a single vertical barrier wall downstream for $L/D = 0.05$ and $I_1 = 1$	T
X	Distance between two adjacent barrier walls in meters (i.e., the length of the solid floor between the barrier walls)	L
i	Dimensional form factor in the i[th] fragment	–
θ_1	Inclination angle of the first barrier wall with the horizontal direction upstream	–
θ_2	Inclination angle of the second barrier wall with the horizontal direction upstream	–

SUPLEMENTARY

Table S1. Flow path lengths for different barrier wall arrangements.

Set No.	Flow path length (m)						
	I_1	I_2	L/D= 0.05	L/D= 0.10	L/D= 0.15	L/D= 0.20	L/D= 0.25
Set I	0.50	N.A.	47.3	47.3	47.4	47.5	48.8
	0.67		51.0	52.4	55.0	58.6	62.9
	0.83		52.1	54.9	58.6	63.2	68.4
	1.00		52.6	56.4	61.1	66.4	72.2
	1.17		51.9	56.7	62.1	67.9	74.1
	1.33		51.9	56.7	62.1	67.9	74.1
	1.5		49.8	55.3	61.3	67.6	73.9
Set II	0.50	1.00	116.0	108.0	103.0	98.9	95.9
	0.67		105.0	101.4	95.7	93.8	94.6
	0.83		97.0	91.3	89.6	91.2	94.9
	1.17		76.1	78.7	83.8	89.8	96.2
	1.33		70.3	76.3	83.0	89.8	96.7
	1.50		68.6	75.7	82.9	90.0	97.1
Set III	1.00	0.5	63.9	67.1	71.7	77.2	83.4
		0.67	68.5	70.6	75.2	80.8	87.0
		0.83	76.6	76.8	80.3	85.4	91.3
		1.17	92.8	89.6	90.8	94.4	99.3
		1.33	97.4	93.7	94.2	97.3	101.8
		1.5	99.1	95.5	95.8	98.5	102.7
Set IV	0.67	1.17	106.8	101.4	98.8	99.3	101.9
	0.83	1.17	103.3	97.4	95.1	96.1	99.1
	0.67	1.33	111.0	109.3	104.5	102.1	102.2
	0.83	1.33	113.5	106.6	101.3	98.9	99.3
	1.00	1	85.5	83.5	85.8	90.1	95.6

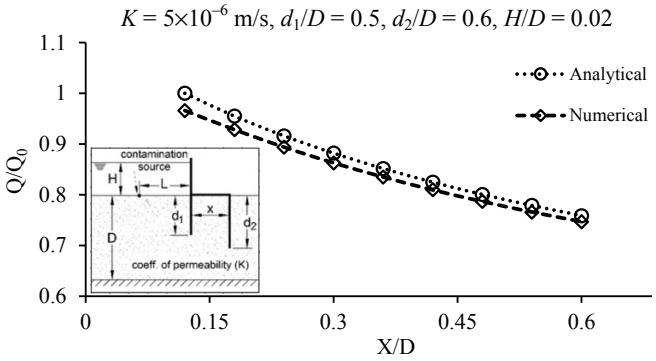

Fig. S1. The seepage discharge of contaminant by using fragments method (analytical) and SEEP/W model (numerical) at different values of X/D after Monir et al. (2018).

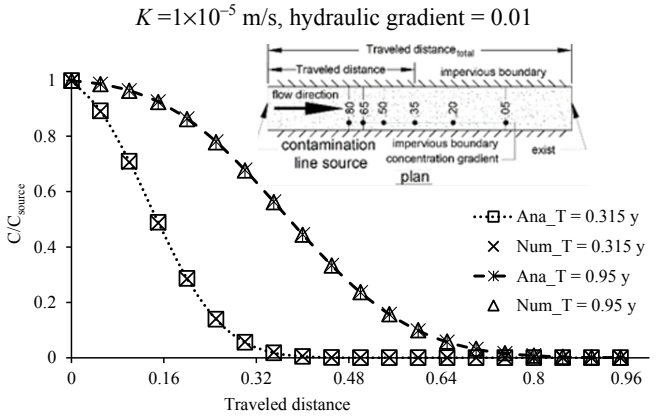

Fig. S2. The distance from the contamination source and contamination concentration for analytical and numerical solutions at two different periods after Monir et al. (2018).

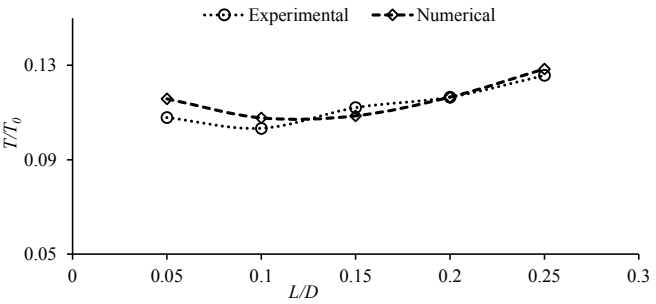

Fig. S3. The arrival time of contaminant by using experimental and numerical particle tracking analysis after Monir et al. (2018).

Bereitgestellt von University Library Bratislava | Heruntergeladen 31.01.20 12:22 UTC

J. Hydrol. Hydromech., 67, 2019, 4, 349–358
DOI: 10.2478/johh-2019-0016

The seepage transport of heavy metal Pb^{2+} through sand column in the presence of silicon powders

Bing Bai*, Zhenqian Zhai, Dengyu Rao

School of Civil Engineering, Beijing Jiaotong University, Beijing, 100044, P R China.
* Corresponding author. Tel.: +86 010 51684815. E-mail: bbai@bjtu.edu.cn

Abstract: The coupled transport of heavy metals with suspended particles has been a topic of growing interest. The main purpose of this study is to experimentally investigate the seepage transport of heavy metal Pb^{2+} in the presence of silicon powders (SPs) through a sand column under different seepage velocities (v = 0.087–0.260 cm/s), injection Pb^{2+} concentrations (C_P = 0–800 μg/ml) and SP sizes (D_{50} = 2.8–25.5 μm), which were likely to be encountered in practical engineering. The sand column was installed in a cylindrical chamber of 300 mm in length and 80 mm in internal diameter. The results clearly show that the increase in acidity results in a reduction of the repulsive interactions between SPs and the matrix, and consequently a decrease in the peak values in breakthrough curves (BTCs), especially for larger-sized SPs. The peak values and recovery rate of Pb^{2+} are obviously increased and an earlier breakthrough can be observed, due to the higher capacity of SPs with negative charge to adsorb heavy metal pollutants such as Pb^{2+} with positive charge. The adsorption of Pb^{2+} on SPs can reduce the repulsive forces between SPs and the matrix, thus resulting in the increase of the deposition possibility of SPs and the decrease of peak value and recovery rate.

Keywords: Seepage transport; Silicon powder; Heavy metal; Coupled effect; Sand column.

INTRODUCTION

The coupled transport of contaminants such as heavy metals, organic matters and radioactive materials with solid particles has been a topic of growing interest in a wide variety of fields, such as the filtration of colloidal particles, microbial pathogen-induced groundwater pollution, and bioremediation of contaminated groundwater aquifers in porous media (Chrysikopoulos et al., 2017; Porubcan and Xu, 2011; Sen and Khilar, 2006). Silicon powders (SPs) play an important role in soil and aquifer contamination and those SPs transported easily in the water flow can act as carriers of contaminants (Haliena et al., 2016; Kim and Walker, 2009). Oxides, clay minerals and colloidal organic particles that exist ubiquitously in the subsurface environment may make that the otherwise low mobile contaminants can more rapidly be transported towards greater depths and into ground and surface waters bodies due to their large specific surface area and high sensitivity to the physical and chemical environment (Sen and Khilar, 2006).

Contaminants in porous medium can be roughly classified into three types, including contaminants adsorbed on immobile solid particles, contaminants dissolved in water, and contaminants adsorbed on the surface of solid particles that move with water flow (Chrysikopoulos et al., 2017; Sen and Khilar, 2006). However, SPs can also be a barrier to the migration of contaminants if their presence clogs the porous medium (Bennacer et al., 2017; Li and Zhou, 2010; Natarajan and Kumar, 2011). Puls and Powell (1992) showed that the transport rate of colloid-associated arsenate (As) was more than 21-times that of dissolved As. Kersting et al. (1999) found that the radionuclides in the aquifers at the Nevada test site, where hundreds of underground nuclear tests were conducted, were associated with the colloidal component of the groundwater, and mobile colloids had the potential to enhance the transport of non-soluble contaminants due to the adsorption effect. Karathanasis (1999) also showed that the presence of colloids obviously enhanced metal (Cu and Zn) transport by 5- to 50-fold over that without colloids, with Zn being consistently more mobile than Cu. Yin et al. (2010) investigated colloid-facilitated Pb transport in shooting range soils, and showed that there was a significant correlation between colloids and Pb in the leachates, and both the decrease in ionic strength and the increase in flow rate contributed to the release of colloids and Pb.

Generally, colloids provide a carrier for the rapid transport of heavy metals like Pb (Grolimund et al., 1996). Pang et al. (2005) studied the transport of bacteria-facilitated cadmium (Cd) by column experiments in a gravel aquifer, and discovered that the adsorption of Cd onto bacteria was positively related to solution pH, bacterial concentration and negative surface charge, but inversely related to Cd concentration. Missana et al. (2008) investigated the effect of the presence of bentonite colloids on the seepage migration of europium (Eu) and plutonium (Pu) in a granite environment, and found that the seepage migration of these radionuclides was mostly colloid driven. Wang et al. (2015) showed that illite colloids (<0.1 μm in size) did not influence As transport in sand columns due to their relatively low affinity for As, and humic acid substantially increased As transport because of the competition of humic acid against As for adsorptive sites on humic acid and potential formation of non-adsorbing aqueous phase As-humic acid complexes. Thus, clay-mineral colloids may not have a large potential to increase As transport. Ma et al. (2016) investigated the co-transport of soil colloids (<1.2 μm in size) and As at different pH and ionic strength in sand columns, and the results showed that the strong repulsion between the porous media and the soil colloids promoted As transport by blocking the adsorption of As onto the porous media, and the colloids acted not only as a carrier in facilitating solute transport but also as a barrier in the course of solute adsorption. Zhou et al. (2016) studied the co-transport of a single layer of graphene oxide (GO) particles and Cu^{2+} in granular natural sand columns, and concluded that GO had fairly high mobility and could serve as an effective carrier of Cu^{2+}.

Some mathematical models have been proposed to characterize the colloid-facilitated transport of contaminants in the dissolved phase (Sen and Khilar, 2006), which generally com-

Bereitgestellt von University Library Bratislava | Heruntergeladen 31.01.20 12:23 UTC

prise the mass balance equations for solid particles and contaminants and the reaction processes among the constituents. Bekhit et al. (2009) studied the combined effect of colloids and bacteria on the contaminant transport and proposed a conceptual model considering multiple reactions, which was suitable for the case of three mobile constituents and a fixed solid matrix. Katzourakis and Chrysikopoulos (2014) also developed a mathematical model for the simultaneous transport of viruses and colloids in homogeneous porous media with uniform flow. Certainly, the feasibility of these mathematical models relies heavily on a good understanding of the coupled transport of multiple mobile and immobile species in aqueous phase. Overall, there is limited knowledge about the coupled transport of multiple components in porous media due to their complex physicochemical coupling behaviors.

Despite the recognized importance of the coupled transport of contaminants with solid particles like colloids due to their abundance in groundwater and particular physical properties such as large specific surface area and high adsorption capacity (Bai et al., 2017; Bekhit et al., 2009), surprisingly little is known about the coupled transport of contaminants with relatively larger solid particles with a median diameter of >1 μm.

The main objective of this research is to investigate the coupled transport of Pb^{2+} and SPs under different seepage velocities, injection Pb^{2+} concentrations and SP sizes in a porous medium consisting of sand columns. The variation of transport parameters such as the longitudinal dispersivity and deposition coefficient of SPs and the recovery rate of Pb^{2+} and SPs with the injected concentration of Pb^{2+} are discussed based on experimental results, and the coupled transport processes are analyzed using analytical solutions accounting for the release effect of the hydrodynamic deposition.

EXPERIMENTAL APPROACHES

Column setup

The sand column was installed in a cylindrical toughened Plexiglas chamber of 300 mm in length and 80 mm in internal diameter filled with quartz sands. Nylon membranes were placed at both ends of the sand column to obtain uniform seepage water and particle flow. A water tank was used to supply deionized seepage water. A peristaltic pump (LongerPump BT600-2J, Baoding, China; control range: 120–1200 ml/min) was used to provide constant water flow rates (i.e., 0.087, 0.173, and 0.260 cm/s). Flow water was pumped downwards through the vertical sand column, and the flow velocity was measured by a flow meter installed at the column inlet. The SP suspension with a given concentration of Pb^{2+} was injected using a 60-ml syringe at the column inlet.

Characteristics of the materials

Quartz sands (median diameter: d_g = 2.2 mm; size range: 0.5–3.5 mm) were used as the porous material, in which the particles of 0.5–1 mm, 1–2 mm and 2–3.5 mm accounted for about 2.3%, 36.1% and 61.6%, respectively. These particles were pretreated with 0.01 mol/l of NaOH solution and 0.01 mol/l of HNO_3 solution in sequence to remove impurities, rinsed several times with deionized water, and oven-dried for 48 h at 105 °C prior to the experiments. The saturated sand column was packed in 3-cm increments with quartz sands mixed with deionized water to avoid air entrapment, and then vibrated cautiously by hand to ensure uniform packing. The water level was maintained a few centimeters above the sand surface. The measured density of the solid matrix was ρ_s = 2.65 ± 0.05 g/cm^3, and the porosity, which was defined as the ratio of the pore volume to the total column volume, was controlled in n = 41.7% when preparing a sample layer by layer. Four types of artificial spherical SPs (mainly composed of SiO_2) with a median diameter of D_{50} = 2.8, 10.9, 18.7 and 25.5 μm (i.e., dimensionless ratios D_{50}/d_g = 0.0013–0.0116) and a density of ρ_s = 2.20 g/cm^3 were selected as injected particles. These particles had an unimodal particle size distribution (PSD), and the particle-size distribution was in the range of 1–80 μm measured by laser diffraction (LA-950 Mode, Horiba, Japan).

Operating procedure and measurement

The SP suspension with different particle (C_{inj} = 1, 2, 4 and 8 mg/ml) and Pb^{2+} (C_P = 0–800 μg/ml) concentrations was injected at Darcy velocities, v, of 0.087, 0.173, and 0.260 cm/s. The Reynolds numbers varied between 1.12 and 3.34, confirming that the experiments were conducted under laminar flow conditions (Alem et al., 2013; Bennacer et al., 2017). In each experiment, V_{inj} = 30 ml of SP suspension was injected in a pulse-injection fashion over a period of t_{inj} = 2 s. The turbidity level in the effluent was measured three times and the means were used to minimize errors. All experiments were performed at room temperature of 22–24°C.

The transport process of SP suspension is complex (Tusara et al., 2015; Walshe et al., 2010; Xue et al., 2016) due to the mixed injection of contaminants like Pb^{2+} with SPs and the environmental change of seepage water (e.g., the variation of pH and Pb^{2+} concentration). Heavy metal Pb^{2+} ions exist generally under acidic conditions (e.g., pH = 5.5), and thus there is a need to investigate the effect of acidity on the coupled transport of SPs and Pb^{2+}. Two SP suspensions with different pH values were considered in this study. One suspension was neutral (pH = 7) and the other suspension was adjusted to pH = 5.5 by adding 0.01 mol/l of nitric acid (HNO_3) solution. The pH value of seepage water in the tank was the same as that of the injected suspension (pH = 7 or 5.5).

Various concentrations of Pb^{2+} solutions were prepared with powdered $Pb(NO_3)_2$ and deionized water, and the pH was adjusted to pH = 5.5 with 0.01 mol/l of NaOH solution. To estimate the effect of ionic strength (Na^+) caused by sample preparation, the transport processes of three concentrations of Pb^{2+} (C_P = 100, 300 and 500 μg/ml) were investigated. The pH of the seepage water was the same as that of the injected solutions (pH = 5.5). The results show that a trace amount of Na^+ ions in Pb^{2+} solution has almost a negligible effect on the transport of Pb^{2+}.

The turbidity in the effluent was measured using a turbidity meter (2100N, HACH Co., USA; measurement range: 0–4000 Nephelometric Turbidity Units (NTU)) and then converted to particle concentration. The results show that there is a consistent relationship between particle concentration C [ML^{-3}] and turbidity N [NTU] for pH = 5.5 to 7, and thus the Pb^{2+} concentration of less than 800 μg/ml is used in this study. The concentration of Pb^{2+} dissolved in the solution was measured using an atomic absorption spectrophotometer (TAS-990G, Puxi Co., China; wavelength range: 190–900 nm). The Pb^{2+} absorbed on the surface of SPs in the effluent was extracted by adding 0.1 mol/l of EDTA (ethylenediaminetetraacetic acid disodium) in a constant temperature incubator (HZQ-F160, Baidian Co., China) and then centrifuged (Sigma 3K15, Minsks Co., Germany). The extraction efficiency of this method can be higher than 90 % (Fangueiro et al., 2002; Nedwed and Clifford, 2000).

Bereitgestellt von University Library Bratislava | Heruntergeladen 31.01.20 12:23 UTC

Transport theory and parameters

A solution accounting for the release effect of the hydrodynamic deposition for variable concentration injection is used to simulate the experimental breakthrough curves (BTCs), and the outlet of SPs (or soluble heavy metals) in a uniform one-dimensional flow is analyzed by the following convection-dispersion partial differential equation (CDE) and deposition equation, respectively (Katzourakis and Chrysikopoulos, 2014; Simunek and van Genuchten, 2008):

$$\frac{\partial C(z,t)}{\partial t} = D\frac{\partial^2 C(z,t)}{\partial z^2} - u\frac{\partial C(z,t)}{\partial z} - \frac{\rho_s}{n}\frac{\partial \sigma(z,t)}{\partial t} \quad (1)$$

$$\frac{\rho_s}{n}\frac{\partial \sigma(z,t)}{\partial t} = k_d \cdot C(z,t) - k_r \cdot \frac{\rho_s}{n}\sigma(z,t) \quad (2)$$

where z is the coordinate [L], n is the porosity of the porous medium, D is the hydrodynamic dispersion coefficient [$L^2 T^{-1}$], u is the average interstitial particle velocity [LT^{-1}], t is the time [T], σ is the concentration of particles deposited onto the solid matrix [MM^{-1}], k_d is the deposition coefficient [T^{-1}], and k_r is the release coefficient [T^{-1}].

The initial and boundary conditions are set as follows: $C(z,0) = 0$, $\sigma(z,0) = 0$, $C(0,t) = g(t)$, and $C(+\infty,t) = 0$. The particle concentration can be obtained from Eqs. (1) and (2) by the Laplace transform and the Laplace transform inversion (Bai et al., 2017):

$$C(z,t) = \exp(\frac{uz}{2D}) \cdot \int_0^t g(\tau) \cdot \left[k_r \cdot W(z,t-\tau) + \frac{\partial W(z,t-\tau)}{\partial t} \right] d\tau \quad (3)$$

where τ is a dummy integration variable.

$$W(z,t) = \exp(-k_r t)\int_0^t I_0[2(\alpha\eta(t-\eta))^{1/2}] \cdot \frac{z}{2\eta\sqrt{\pi D\eta}} \cdot \exp\left[-\frac{z^2}{4D\eta} - \frac{u^2\eta}{4D} + (k_r - k_d)\eta \right] d\eta \quad (4)$$

$$\frac{\partial W(z,t)}{\partial t} = \exp(-k_r t)\int_0^t \left\{ \begin{matrix} (\frac{\alpha\eta}{t-\eta})^{1/2} I_1[2(\alpha\eta(t-\eta))^{1/2}] - \\ k_r I_0[2(\alpha\eta(t-\eta))^{1/2}] \end{matrix} \right\} \cdot \frac{z}{2\eta\sqrt{\pi D\eta}} \cdot \exp\left[-\frac{z^2}{4D\eta} - \frac{u^2\eta}{4D} + (k_r - k_d)\eta \right] d\eta + \exp(-k_r t) \cdot \frac{z}{2t\sqrt{\pi Dt}} \cdot \exp\left[-\frac{z^2}{4Dt} - \frac{u^2 t}{4D} + (k_r - k_d)t \right] \quad (5)$$

where α is an arbitrary constant, and I_0 and I_1 are the modified Bessel function of the first-kind of order zero and one, respectively.

For an instantaneous plane source with a particle concentration of $g(t)$ [ML^{-3}], one has:

$$g(t) = I \cdot \delta(t - t') \quad (6)$$

where $I = m/Q = m/(vA)$ is the strength of the plane source [MTL^{-3}], with m, Q and A being the mass of injected particles [M], the flow rate [L^3T^{-1}], and the column cross-sectional area [L^2], respectively; $\delta(\cdot)$ is the Dirac delta function; and t' is the moment of particle injection [T].

Note that $\int_\alpha^\beta f(t)\delta(t-\xi)\mathrm{d}t = f(\xi)$ ($\alpha \le \xi \le \beta$), the substitution of Eq. (6) into Eq. (3) yields:

$$C(z,t-t') = \frac{I}{2\sqrt{\pi D}} \cdot A_1(z,t-t') \cdot \left\{ \int_0^{t-t'} A_2(t-t') \cdot A_3(z,\eta) \cdot A_4(z,\eta) d\eta + A_3(z,t-t') \cdot A_4(z,t-t') \right\} \quad (7)$$

where $A_1(z,t) = \exp(\frac{uz}{2D} - k_r t)$, $A_2(t) = (\frac{\alpha\eta}{t-\eta})^{1/2} \cdot I_1[2(\alpha\eta(t-\eta))^{1/2}]$, $A_3(z,t) = \frac{z}{t^{3/2}}$, and $A_4(z,t) = \exp[-\frac{z^2}{4Dt} - \frac{u^2 t}{4D} + (k_r - k_d)t]$.

Eq. (7) can be used to simulate the BTCs of SPs for pulse injection, where the injection duration is sufficiently short to be considered instantaneous (Bennacer et al., 2017). Eq. (7) can be degenerated to the classical solution based on the convection–dispersion model by letting $k_r = 0$ and $t' = 0$. The simulated BTCs are obtained from Eq. (7) using Mathematica 9 (Wolfram Research). Here, the concept of dimensionless pore volume (PV) is introduced to describe the time process, which refers to the ratio of the total volume of water flowing through the sand column to the pore volume of the sand column. The dispersivity is defined as $\alpha_d = D/u_0$, where u_0 is the average interstitial fluid velocity ($u_0 = v/n$) (Bai et al., 2017). The recovery rate is defined by integrating simulated BTCs area:

$$R_e = \int_0^\infty Q\, C_{out}(t)\mathrm{d}t / m \quad (8)$$

where R_e is the recovery rate (%).

Four parameters (particle velocity u, dispersivity α_d, deposition coefficient k_d, and release coefficient k_r) can be fitted using Eq. (7). However, it would be very difficult to estimate more than three parameters simultaneously. In order to circumvent this problem, it is assumed that $k_r = 0.1k_d$ (Bekhit et al., 2009; Katzourakis and Chrysikopoulos, 2014) because the release coefficient k_r is small as compared to the deposition coefficient k_d, such that only three parameters need to be identified. Overall, k_r has a nearly linear effect on R_e in a large range of k_r/k_d ratios (e.g., $k_r/k_d = 0.01–0.2$). For example, when $C_{inj} = 4$ mg/ml, $u_0 = 0.2$ cm/s, $u/u_0 = 0.8$, $\alpha_d = 0.3$ cm and $k_d = 0.04$ s^{-1}, R_e is increased from 49.6 % to 55.0% and then to 62.5 % as the k_r/k_d increases from 0.01 to 0.1 and then to 0.2.

RESULTS AND DISCUSSION

The effect of acidity on the transport of SPs

The relationships between the relative concentration C_R and PV for different injected concentrations of SPs (C_{inj}) are given in Figs. 1 and 2, where $v = 0.087$ cm/s and $v = 0.260$ cm/s. C_R is defined as $C_R = (C_{out} \cdot V_p)/m = (C_{out} \cdot V_p)/(C_{inj} \cdot V_{inj})$, where C_{out} and V_p are the particle concentration at the outlet and the pore volume of the entire soil column, respectively (Ahfir et al., 2009; Bai et al., 2017).

Obviously, the decline of pH (pH = 7→5.5) results in more pronounced sorption deposition due to the increase of positive charge H^+ with the addition of HNO_3. Actually, the pH of the suspension can have a significant effect on the surface charge properties of SPs and the matrix according to the Derjaguin-Landau-Verwey-Overbeek (DLVO) theory (Bennacer et al.,

Bereitgestellt von University Library Bratislava | Heruntergeladen 31.01.20 12:23 UTC

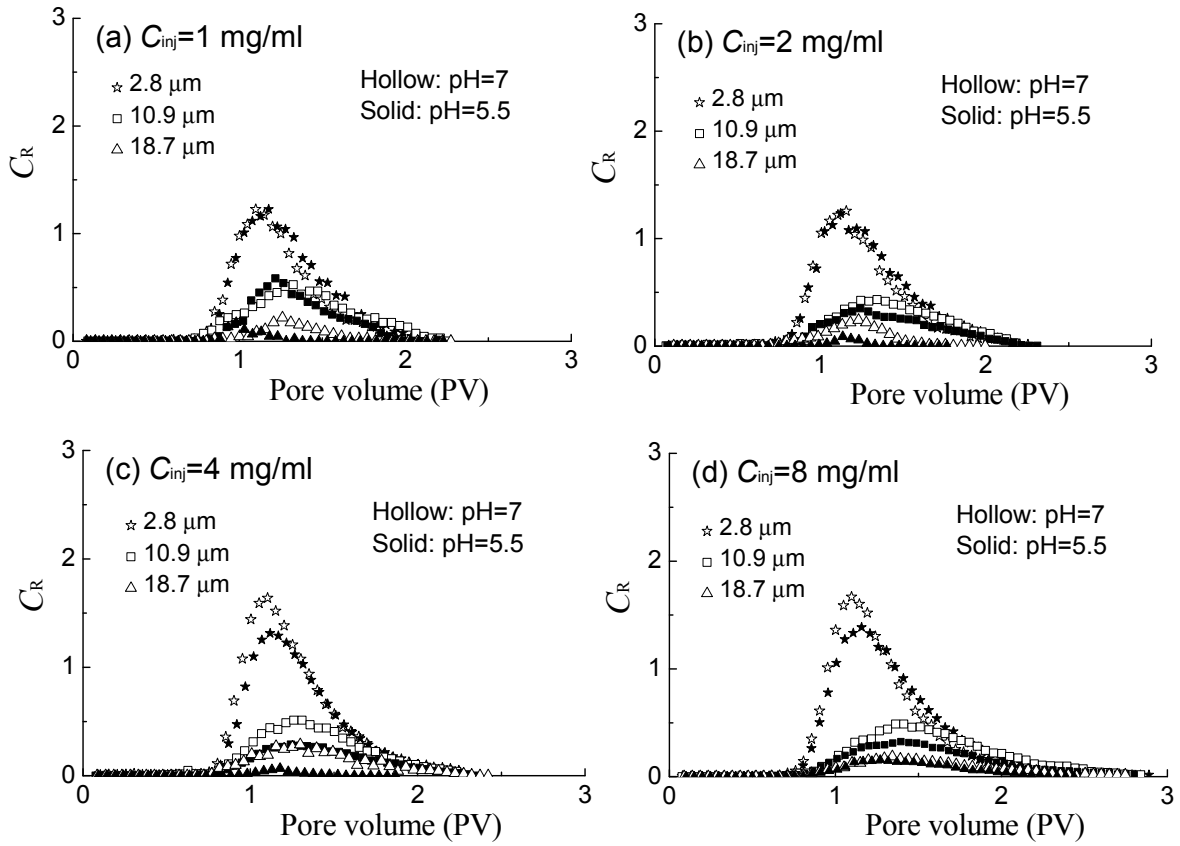

Fig. 1. BTCs of SPs at v = 0.087 cm/s for different SP sizes and acidity levels: (a) C_{inj} = 1 mg/ml, (b) C_{inj} = 2 mg/ml, (c) C_{inj} = 4 mg/ml, and (d) C_{inj} = 8 mg/ml.

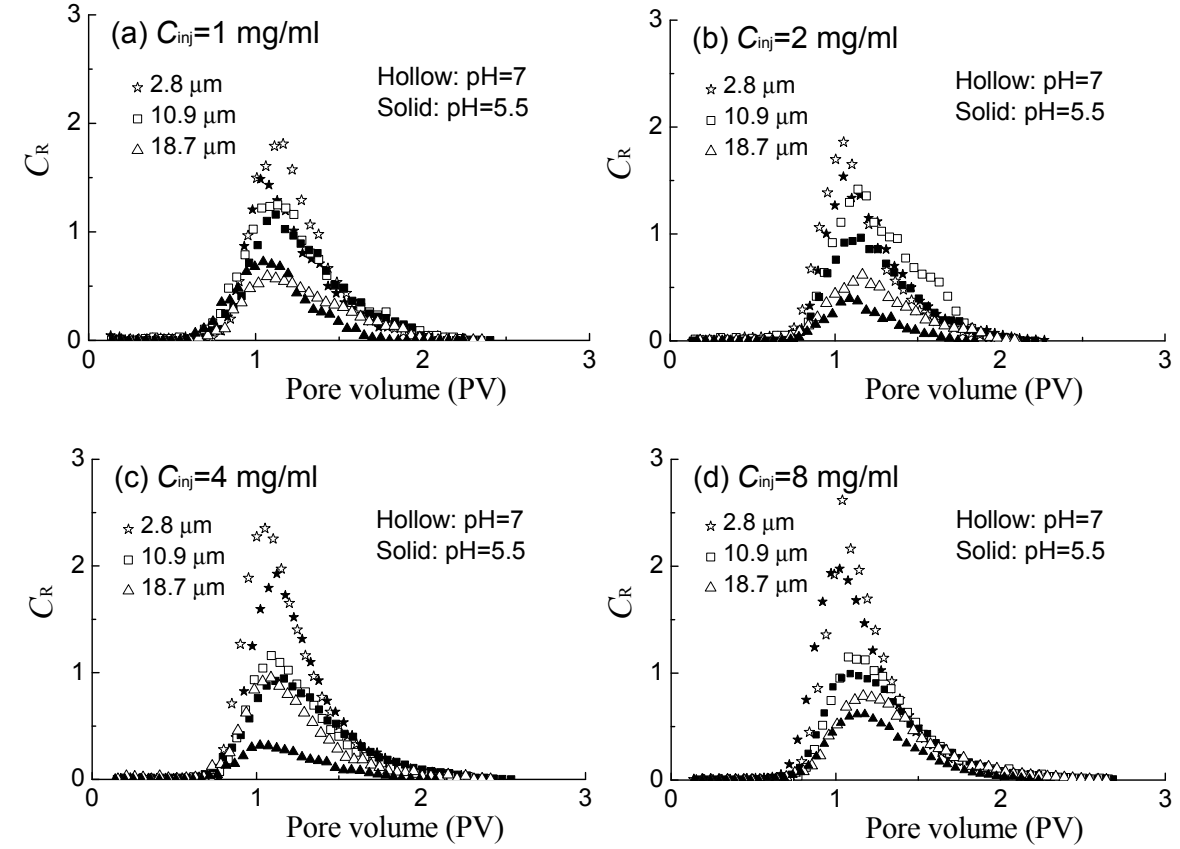

Fig. 2. BTCs of SPs at v = 0.260 cm/s for different SP sizes and acidity levels: (a) C_{inj} = 1 mg/ml, (b) C_{inj} = 2 mg/ml, (c) C_{inj} = 4 mg/ml, and (d) C_{inj} = 8 mg/ml

Bereitgestellt von University Library Bratislava | Heruntergeladen 31.01.20 12:23 UTC

2017; Johnson et al., 2010; Tusara et al., 2015), and thus the deposition of SPs. Also, the increase of acidity (pH = 7→5.5) results in a reduction in the repulsive interactions between SPs and the matrix, and thus a decrease in peak value especially for SPs with a large size. For example, when D_{50} = 2.8, 10.9 and 18.7 (Fig. 1(c), C_{inj} = 4 mg/ml and v = 0.087 cm/s, the peak values are C_R = 1.64, 0.51 and 0.29 for pH = 7, and C_R = 1.31, 0.29 and 0.07 for pH = 5.5, respectively. Similar trends can be observed for different SP concentrations (C_{inj} = 1, 2, 4 and 8 mg/ml) and flow velocities (v = 0.087, 0.173 and 0.260 cm/s), which is also in good agreement with previous studies (e.g., Chrysikopoulos et al., 2017; Tusara et al., 2015). For example, Tusara et al. (2015) showed that decreasing the pH of the brine from 8 to 5.5 resulted in an increase in the deposition of suspended particles throughout the porous column and consequently a lower permeability along the porous column. Chrysikopoulos et al. (2017) found that the decrease of pH from 7 to 4 yielded smaller absolute zeta potentials and consequently smaller repulsion forces between SPs (e.g., graphene oxide nanoparticles and kaolinite particles) and the matrix (e.g., spherical glass beads and quartz sands).

The peak values decrease and the corresponding PVs increase slightly with increasing particles size (D_{50} = 2.8→10.9→18.7 μm; see Figs. 1 and 2) at the same flow velocity. As discussed in detail elsewhere (e.g., Ahfir et al., 2009; Bradford et al., 2009), the number of the matrix pores larger than the particles decreases with increasing particle size, resulting in an increase in the number of particles captured by throat pores and a decrease of the peak values in the effluent.

The seepage transport of Pb^{2+}

Fig. 3 shows the penetration processes of Pb^{2+} ions under different concentrations and flow velocities. It shows that the peak values of Pb^{2+} increase with increasing concentration of Pb^{2+} (C_P = 100→200→300→500 μg/ml), but the corresponding PVs remain largely unchanged (PV = 1.04–1.08). It seems that unlike SPs, the peak occurrence of the BTCs of Pb^{2+} is independent of flow velocity. In fact, picometer-scale Pb^{2+} ions are completely soluble in water and move almost simultaneously with the water flow, which is mainly affected by the dispersivity and deposition effect. The so-called size exclusion effect makes the SP plume to have a lower effective dispersion coefficient than soluble Pb^{2+} due to the preferential advection of particles along the central streamline (Ahfir et al., 2009; Bennacer et al., 2017). Moreover, the hydrodynamic force on the SPs increases with increasing water flow velocity, thus resulting in a decrease of deposition, and consequently an increase of the number of SPs at the outlet and the increase of peak values.

The transport processes of the heavy metal Pb^{2+} are also described using Eqs. (1) and (2). Fig. 4 gives the transport parameters of Pb^{2+} as a function of injection concentration obtained by fitting Eq. (7). All curves fit well with the experimental results (R^2>0.92) with only a few exceptions (e.g., see Fig. 3(a) and Fig. 3(b)). Fig. 4 shows that the moving velocity of Pb^{2+} (u/u_0 = 0.71–0.84; Fig. 4(a)) is always lower than the water flow velocity (u/u_0 = 1), and even lower than that (u/u_0 = 0.85–0.90) of two natural SiO_2 particles with D_{50} = 25 and 47 μm at a similar flow velocity of v = 0.066–0.199 cm/s in a previous study of Bai et al. (2017). Here, u/u_0 is defined as the ratio of the interstitial Pb^{2+} (or SPs) velocity u to the interstitial water velocity u_0. In this sense, the moving velocity of Pb^{2+} is similar to that of a dissolved tracer (i.e., fluorescein) obtained by Bai et al. (2017), which is also in good agreement with many previous studies (Ahfir et al., 2009; Chrysikopoulos et al., 2017). This can be attributed to the tortuous transport paths of Pb^{2+} induced by its dispersivity and the obvious deposition of Pb^{2+} caused by high adsorption ability with the matrix. Fig. 4

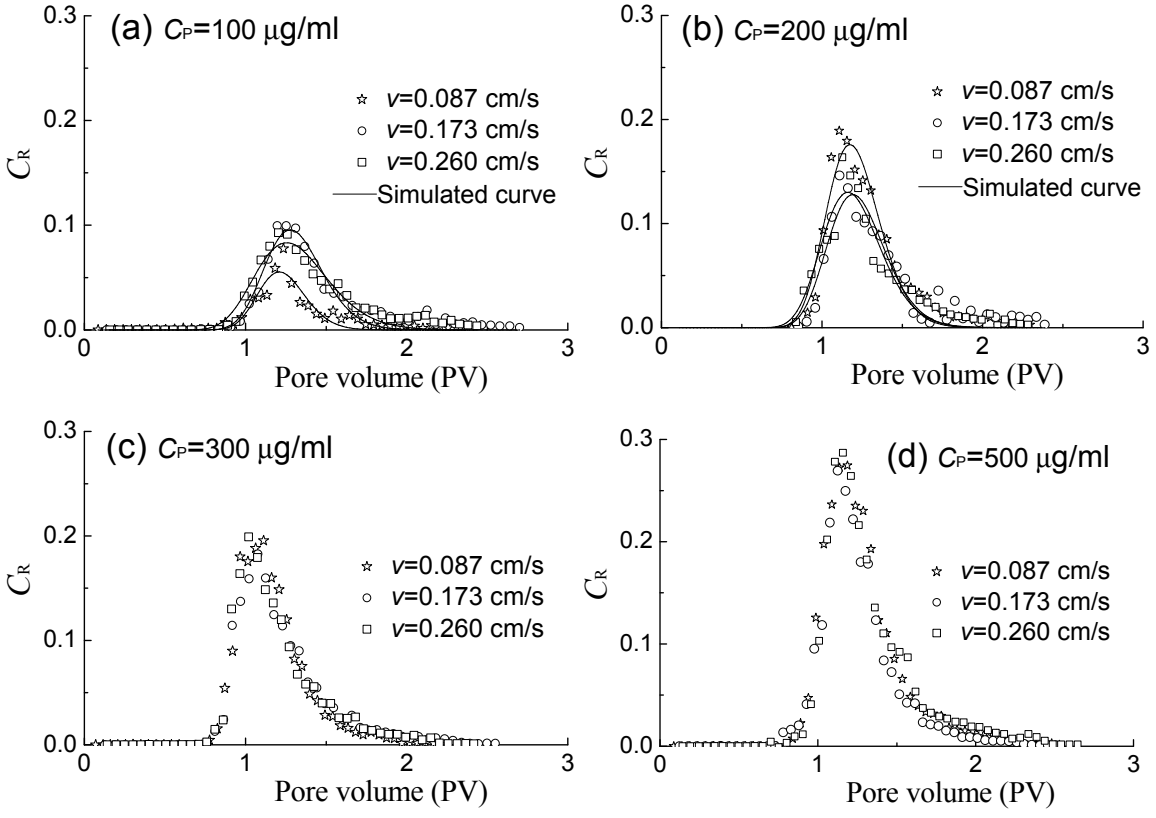

Fig. 3. BTCs of Pb^{2+} for various flow velocities: (a) C_P = 100 μg/ml, (b) C_P = 200 μg/ml, (c) C_P = 300 μg/ml, and (d) C_P = 500 μg/ml.

Bereitgestellt von University Library Bratislava | Heruntergeladen 31.01.20 12:23 UTC

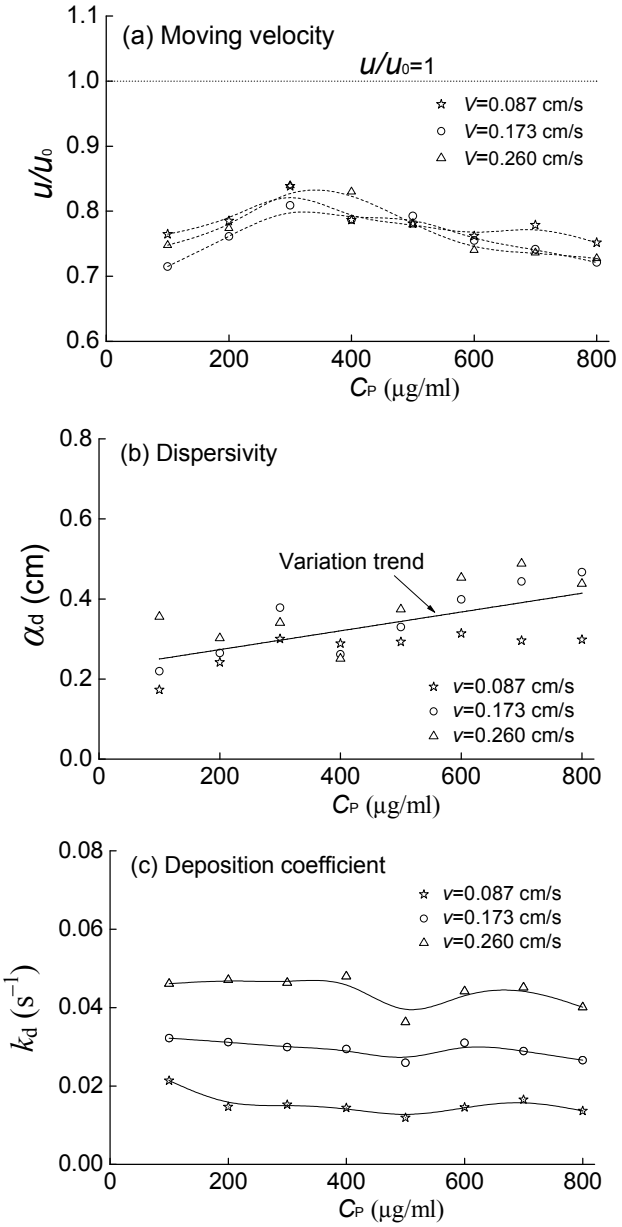

Fig. 4. The transport parameters of Pb^{2+} as a function of injection concentration: (a) moving velocity, (b) dispersivity, and (c) deposition coefficient.

also gives the experimental results and the variation of dispersivity α_d and deposition coefficient k_d with the Pb^{2+} concentration in the range of C_P = 0–800 μg/ml. It is evident that the dispersivity α_d is linearly related to the Pb^{2+} concentration (Fig. 4(b); R^2 = 0.77), regardless of the flow velocity due to its negligible effect. The dispersivity increases with the increase of C_P, resulting in a decrease in the moving velocity of Pb^{2+} to u/u_0 = 0.72 at a high concentration of e.g., C_P = 800 μg/ml (Fig. 4(a)). However, the deposition coefficients decrease slightly with the increase of C_P (Fig. 4(c)), but increase with the increase of flow velocity. Actually, the existence of positive charge (i.e., H^+ and Pb^{2+}) in the solution makes the repulsive interactions between Pb^{2+} and the matrix to decrease with the decrease of the total interaction energy (i.e., the repulsive electrical double layer forces) by the DLVO theory (Porubcan and Xu, 2011). As a result, the decrease of the moving velocity of Pb^{2+} (u) and the increase of dispersivity (Fig. 4(b)) together induces apparent deposition (Fig.4(c)), and the deposition coefficient is increased by almost two times from k_d = 0.014–0.021 s^{-1} to k_d = 0.036–0.048 s^{-1} with the increase of the Darcy velocity from v = 0.087 cm/s to v = 0.260 cm/s.

The coupled transport of Pb^{2+} and SPs

The mixed suspension of Pb^{2+} and SPs are prepared following the same procedure as that of Pb^{2+} solution. Fig. 5 shows the transport of Pb^{2+} under three flow velocities (v = 0.087, 0.173 and 0.260 cm/s) and four SP sizes (D_{50} = 2.8, 10.9, 18.7 and D_{50} = 25.5 μm) in the presence of SPs (called "coupled transport", solid marks) or the absence of SPs (called "single transport", hollow marks) at pH = 5.5, C_P = 500 μg/ml and C_{inj} = 2 mg/ml, respectively. It can be seen from Fig. 5(a) that the peak values of Pb^{2+} are obviously increased due to the presence of SPs, and an earlier transport of Pb^{2+} with smaller PVs corresponding to peak values is observed, which can be attributed to the promotion effect of SPs on the transport of Pb^{2+}. It is well known that SPs with negative charge on their surfaces have a high capacity to adsorb heavy metal pollutants such as Pb^{2+} with positive charge. The SPs move with water flow (Li and Zhou, 2010; Natarajan and Kumar, 2011) and act as a third phase (mobile solid phase) in addition to the immobile solid phase of the porous media. Thus, Pb^{2+} can be adsorbed to SPs in a similar fashion as they do to the immobile solid matrix and can migrate in subsurface media at a rate similar to, or even greater than, that in the mobile aqueous phase due to the so-called size exclusion effect (Alem et al., 2013; Bai et al., 2017). Moreover, the penetration processes and the peak values also have nothing to do with flow velocity. Fig. 5 indicates that the peak values are C_R = 0.40, 0.51, 0.44 and 0.36 in the presence of SPs for D_{50} = 2.8, 10.9, 18.7 and 25.5 μm, respectively; but C_R = 0.28 on average in the absence of SPs. Here, the peak values are the mean values for the three velocities (v = 0.087, 0.173 and 0.260 cm/s).

The so-called promotion effect was previously observed in the coupled transport of colloids of < 1 μm in size with various contaminants such as alkali and alkaline earth cations (Cs^+ and Sr^{2+}), transition metals (Ni^{2+}, Co^{2+}, Cu^{2+} and Pb^{2+}), oxyanions (arsenic and iodate), and organic compounds (Bekhit et al., 2009; Chrysikopoulos et al., 2017; Katzourakis and Chrysikopoulos, 2014). The promotion or retardation of SPs on contaminants has been shown to depend on their coupled effect, the migration characteristics of SPs themselves, the hydrodynamic force, the physicochemical environment of suspension, etc. (Bekhit et al., 2009; Sen and Khilar, 2006). The existence of SPs with an appropriate size range (e.g., D_{50} = 2.8–10.9 μm; Fig. 5(a) and Fig. 5(b)) can significantly accelerate the transport of Pb^{2+} due to the size exclusion effect. However, those SPs whose sizes exceed a limit (e.g., D_{50} = 18.7 μm, D_{50}/d_g = 0.0085; see the comparison of Fig. 5(b) and Fig. 5(c)) have only a small promotion effect or even an inhibition effect on the migration of Pb^{2+} due to the decrease of the permeability of porous medium caused by the plugging effect. For example, when D_{50} = 25.5 μm (D_{50}/d_g = 0.0116; Fig. 5(d)), the peak values of Pb^{2+} for C_R = 0.36 are only slightly higher than that for C_R = 0.28 in the absence of SPs, which is due to the remarkable deposition of large SPs onto the matrix (see Fig. 5(d)) despite the obvious absorption of Pb^{2+} on the SP surface. The plugging effect refers to the trapping of SPs in small pore throats that are too small to allow particle passage. Some researches indicated that this effect is mainly related to a threshold of D_{50}/d_g which is about in the range of D_{50}/d_g = 0.0016–0.027 (Alem et al., 2013; Bradford et al., 2009; Porubcan and Xu, 2011; Shen et al., 2008),

Bereitgestellt von University Library Bratislava | Heruntergeladen 31.01.20 12:23 UTC

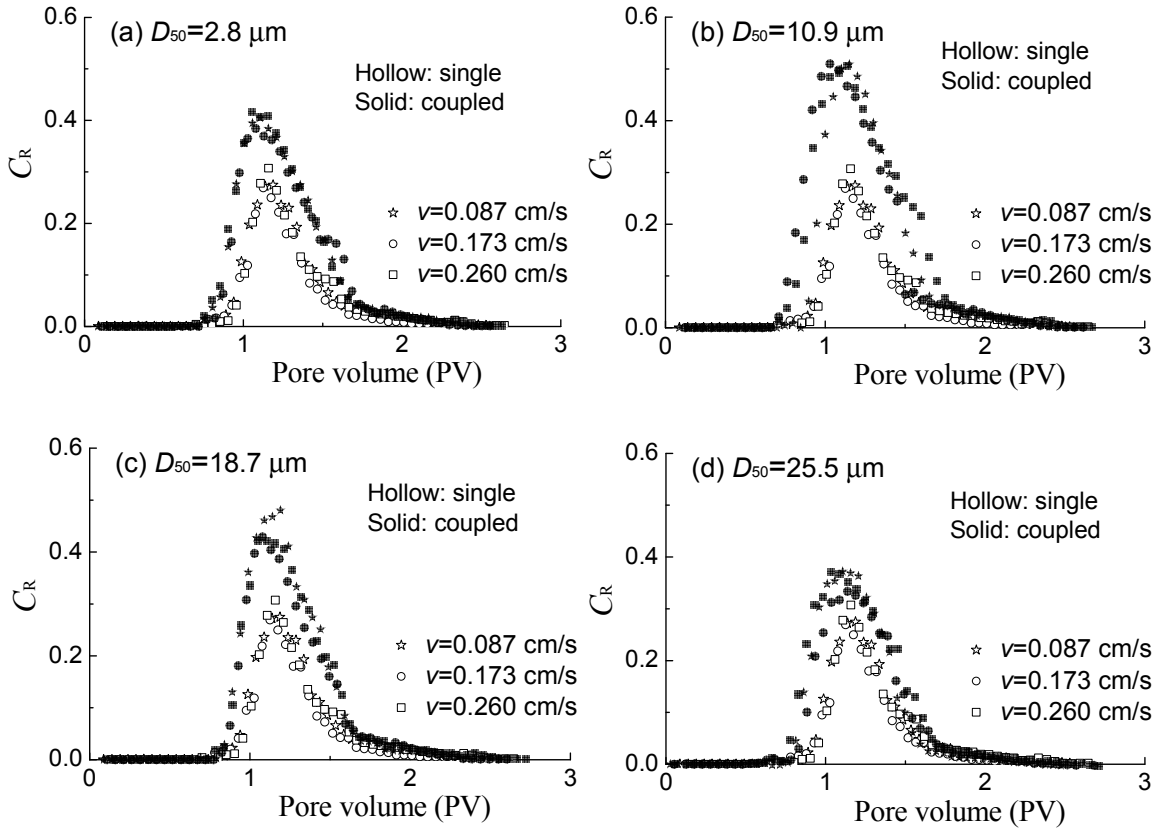

Fig. 5. BTCs of Pb^{2+} during the coupled transport with SPs: (a) D_{50} = 2.8 μm, (b) D_{50} = 10.9 μm, (c) D_{50} = 18.7 μm, and (d) D_{50} = 25.5 μm.

beyond which SPs will have a retardation effect on the transport of contaminants. The plugging effect is also related to the physical properties and particle-size distribution of SPs, the shape and surface roughness of the solid matrix, pore-scale hydrodynamics, the solution chemistry, etc.

Fig. 6 gives the BTCs for the coupled or single transport of SPs with different sizes at pH = 5.5, C_P = 500 μg/ml and C_{inj} = 2 mg/ml. Certainly, the peak values of SPs are decreased in the presence of Pb^{2+}, which seems to become more obvious at lower velocities (e.g., v = 0.087 cm/s), especially for larger SP sizes (e.g., D_{50} = 18.7 μm; Fig. 6(c)). For example, when D_{50} = 2.8 μm (Fig. 6(a)), the peak values are C_R = 1.08, 0.89 and 0.51 in the presence of Pb^{2+} and C_R = 1.54, 1.42 and 1.23 in the absence of Pb^{2+} for v = 0.087, 0.173 and 0.260 cm/s, respectively. The existence of Pb^{2+} absorbed on SPs can reduce the repulsive force between SPs and the matrix by the DLVO theory due to the change of surface charge properties of SPs and the matrix (i.e., the decrease of the absolute zeta potentials in theory) (Johnson et al., 2010; Tusara et al., 2015), and then enhance the deposition possibility of SPs onto the matrix. Hence, the coupled effect of Pb^{2+} with strong charge on SPs cannot be neglected, which is attributed to the decrease of the double electric layer on the SP surface (i.e., the decrease of surface potential energy).

There is an increasing interest in the effects of suspended particles like colloids and SPs on the seepage migration of contaminates like Pb^{2+}. However, the adsorption of contaminants on solid particles has attracted less attention, probably due to that the mass of contaminants adsorbed onto the solid particles can be negligible compared with the mass of solid particles. Actually, the participation of some specific contaminants will have an obvious effect on the transport of solid particles due to the change of their surface charge properties but cause no dramatic change in their mass. Unlike weak polar or neutral contaminants, special attention should be given to the coupled effect on the transport of solid particles with heavy metal ions like Pb^{2+} with strong electric polarity. In essence, the influence of Pb^{2+} on the transport of solid particles is mainly determined by the change of the physicochemical environment of suspensions.

The effect of coupled process on transport parameters

Fig. 7 gives the values of particle velocity, dispersivity, deposition coefficient obtained by fitting Eq. (7) to observed BTCs (e.g., see Fig. 6(a) and Fig. 6(b)) and recovery rate of SPs using Eq. (8) under different flow velocities (v = 0.087 and 0.260 cm/s) and SP sizes (D_{50} = 2.8, 10.9 and 18.7 μm) when the concentration of SPs is C_{inj} = 2 mg/ml. C_P = 0 in Fig. 7 indicates the absence of Pb^{2+}. The coefficients of determination are R^2 > 0.95 except for few curves, and the variation trends in B-spline curves are also given. As mentioned before, the velocities of SPs (u/u_0 = 0.80–1.00) are generally higher than those of Pb^{2+} (u/u_0 = 0.71–0.84; see Fig. 4(a)), especially for those large-sized SPs (e.g., D_{50} = 18.7 μm) due to the size exclusion effect, indicating the earlier appearance of peak values (see Fig. 6). Moreover, the particle velocity slightly increases with the increase of Pb^{2+}concentration, which is partially caused by the enhancement of deposition due to the coupled action of Pb^{2+} (Fig. 6). The dispersivity of SPs decreases with the concentration of Pb^{2+} (C_P = 0→500 μg/ml; Fig. 7(b)) and the SP size in the range of D_{50} = 2.8–18.7 μm, but increases with flow velocity (v = 0.087 cm/s→0.260 cm/s).

The deposition coefficient of SPs increases with increasing flow velocity (v = 0.087→0.260 cm/s) and SP size (D_{50} = 2.8→10.9→18.7 μm; Fig. 7(c)), which is in line with previous studies (Bai et. al., 2017; Bennacer et. al., 2017). More importantly, the deposition coefficient of SPs generally increases

Bereitgestellt von University Library Bratislava | Heruntergeladen 31.01.20 12:23 UTC

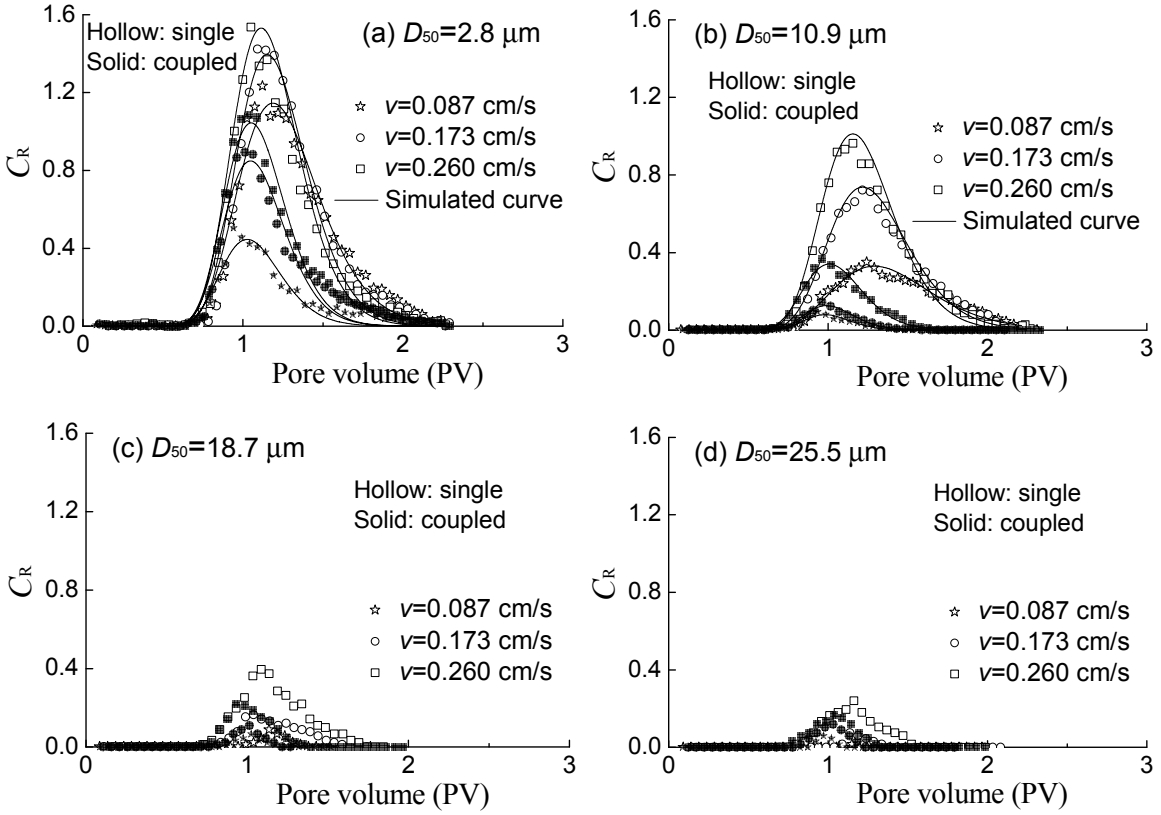

Fig. 6. BTCs of SPs during the coupled transport: (a) D_{50} = 2.8 μm, (b) D_{50} = 10.9 μm, (c) D_{50} = 18.7 μm, and (d) D_{50} = 25.5 μm.

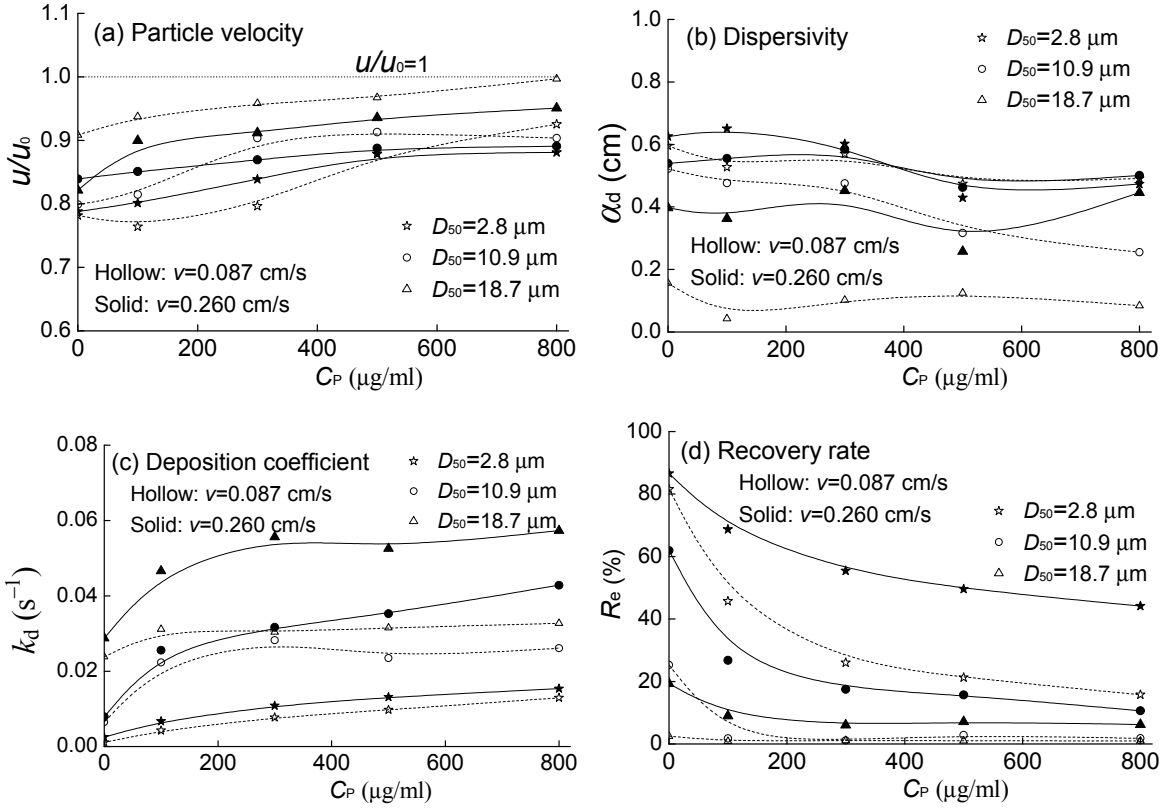

Fig. 7. The transport parameters of SPs during the coupled transport: (a) particle velocity, (b) dispersivity, (c) deposition coefficient, and (d) recovery rate.

with the injected concentration of Pb^{2+} and then remains almost constant, which is caused by the enhancement of the coupled effect (mutual adsorption) between SPs and Pb^{2+} and the obvious adsorption onto the surface of the matrix. As a result, the recovery rate of SPs at the outlet decreases with the injected Pb^{2+} concentration and finally tends to be constant (Fig. 7(d)), indicating that caution must be taken when using single-transport parameters to predict the co-transport of SPs in the

Bereitgestellt von University Library Bratislava | Heruntergeladen 31.01.20 12:23 UTC

presence of multiple components. Certainly, the recovery rate of SPs increases with the increase of flow velocity (v = 0.087→0.260 cm/s; see Fig. 7(d)). When v = 0.260 cm/s, the recovery rates are to 44.1%, 10.6% and 6.2% for C_P = 500 μg/ml, and 86.6%, 61.9% and 19.3% for C_P = 0 when D_{50} = 2.8, 10.9, 18.7 μm, respectively.

By contrast, the recovery rate of Pb^{2+} is obviously increased from R_e = 2.0–11.8% in the absence of SPs (hollow marks) to R_e = 18.2–28.9% in the presence of SPs (solid marks; Fig. 8(a)) in the range of C_P = 100–800 μg/ml when D_{50} = 2.8 μm. However, the recovery rate of Pb^{2+} is independent of the flow velocity especially when D_{50} = 2.8 μm and 18.7 μm. Moreover, the recovery rate slightly increases with the injected concentration of Pb^{2+} and finally tends to be a steady value. However, it is noted that the steady state for SPs with a larger size can be achieved at a smaller C_P. For example, the steady values are approximately C_P = 500 and 300 μg/ ml for D_{50} = 10.9 and 18.7 μm, respectively (Fig. 8(b) and Fig. 8(c)).

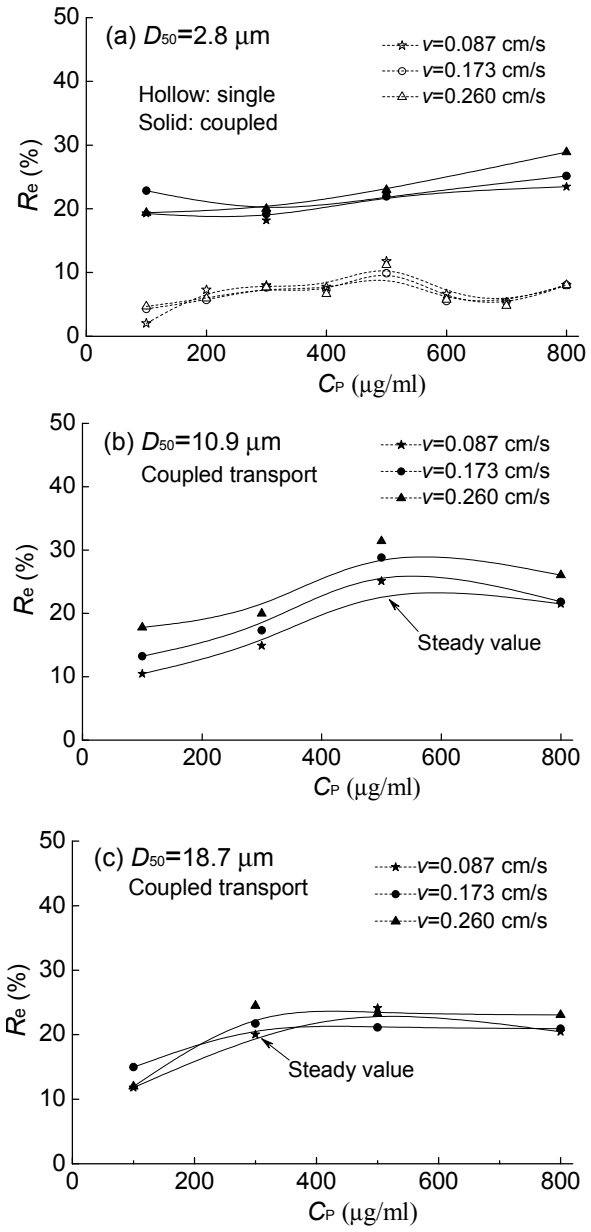

Fig. 8. Recovery rate of Pb^{2+} as a function of the injection concentration during the coupled transport with SPs: (a) D_{50} = 2.8 μm, (b) D_{50} = 10.9 μm, and (c) D_{50} = 18.7 μm.

CONCLUSIONS

The increase in acidity from pH = 7 to pH = 5.5 results in more pronounced sorption deposition due to the increase of positive charge H^+ with the addition of HNO_3. Thus, the increase in acidity can reduce the repulsive interactions between SPs and the matrix, resulting in a decrease of the peak values in BTCs, especially for SPs with a large size.

For heavy metal ions such as Pb^{2+}, the peak values of BTCs increase with the increase of the injected Pb^{2+} concentration and are not related to flow velocity. With the increase of the injected concentration, the dispersivity increases and the deposition coefficient decreases slightly. The peak value and recovery rate of Pb^{2+} are obviously increased and an earlier breakthrough can be observed, due to the high capacity of SPs with negative charge to adsorb heavy metal pollutants such as Pb^{2+} with positive charge. The promotion or retardation of SPs on Pb^{2+} is closely related to the D_{50}/d_g value, which depends mainly on the coupled effect of Pb^{2+} and SPs, the transport characteristics of SPs themselves, the hydrodynamic force, the physicochemical environment of suspension, etc.

The adsorption of Pb^{2+} on SPs can reduce the repulsive forces between SPs and the matrix, thus resulting in the increase of the deposition possibility of SPs and the decrease of peak value and recovery rate.

Acknowledgements. This research was funded by the National Natural Science Foundation of China (51678043; 51878035) and National Key Basic Research Program of China (2015CB057800). The authors would like to thank Dr. Horst H. Gerke of Leibniz Centre for Agricultural Landscape Research for his constructive suggestions.

REFERENCES

Ahfir, N.D., Benamar, A, Alem, A, Wang, H.Q., 2009. Influence of internal structure and medium length on transport and deposition of suspended particles: a laboratory study. Transport in Porous Media, 76, 2, 289–307.

Alem, A, Elkawafi, A, Ahfir, N.D., Wang, H.Q., 2013. Filtration of kaolinite particles in a saturated porous medium: hydrodynamic effects. Hydrogeology Journal, 21, 573–586.

Bai, B., Long, F., Rao, D.Y., Xu, T., 2017. The effect of temperature on the seepage transport of suspended particles in a porous medium. Hydrological Processes, 31, 2, 382–393.

Bekhit, H.M., EI-Kordy, M.A., Hassan, A.E., 2009. Contaminant transport in groundwater in the presence of colloids and bacteria: model development and verification. Journal of Contaminant Hydrology, 108, 152–167.

Bennacer, L., Ahfir, N.D., Bouanani, A., Alem, A., Wang, H.Q., 2017. Coupled effects of ionic strength, particle size, and flow velocity on transport and deposition of suspended particles in saturated porous media. Transport in Porous Media, 118, 2, 251–269.

Bradford, S.A., Kim, H.N., Haznedaroglu, B.Z., Torkzaban, S., Walker, S.L., 2009. Coupled factors influencing concentration-dependent colloid transport and retention in saturated porous media. Environmental Science and Technology, 43, 18, 6996–7002.

Chrysikopoulos, C.V., Sotirelis, N.P., Kallithrakas-Kontos, N.G., 2017. Cotransport of graphene oxide nanoparticles and kaolinite colloids in porous media. Transport in Porous Media, 119: 181–204.

Fangueiro, D., Bermond, A., Santos, E., Carapuca, H., Duarte, A., 2002. Heavy metal mobility assessment in sediments based on a kinetic approach of the EDTA extraction: search for optimal experimental conditions. Analytica Chimica Acta, 459, 2,

Bereitgestellt von University Library Bratislava | Heruntergeladen 31.01.20 12:23 UTC

245–256.
Grolimund, D., Borkovec, M., Barmettler, K., Sticher, H., 1996. Colloid-facilitated transport of strongly sorbing contaminants in natural porous media: a laboratory column study. Environmental Science and Technology, 30, 10, 3118–3123.
Haliena, B., Zheng, H., Melson, N., Kaplan, D.I., Barnett, M.O., 2016. Decreased salinity and actinide mobility: colloid-facilitated transport or pH change. Environmental Science and Technology, 50, 625−632.
Johnson, W.P., Pazmino, E., Ma, H., 2010. Direct observations of colloid retention in granular media in the presence of energy barriers, and implications for inferred mechanisms from indirect observations. Water Research, 44, 1158–1169.
Karathanasis, A.D., 1999. Subsurface migration of copper and zinc mediated by soil colloids. Soil Science Society of America Journal, 63, 830–838.
Katzourakis, V.E., Chrysikopoulos, C.V., 2014. Mathematical modeling of colloid and virus cotransport in porous media: application to experimental data. Advances in Water Resources, 68, 62–73.
Kersting, A.B., Efurd, D.W., Finnegan, D.L., Rokop, D.J., Smith, D.K., Thompson, J.L., 1999. Migration of plutonium in ground water at the Nevada Test Site. Nature, 397, 56–59.
Kim, H.N., Walker, S.L., 2009. Escherichia coli transport in porous media: influence of cell strain, solution chemistry, and temperature. Colloids and Surfaces B: Biointerfaces, 71, 1, 160–167.
Li, Z.L., Zhou, L.X., 2010. Cadmium transport mediated by soil colloid and dissolved organic matter: a field study. Journal of Environmental Sciences, 22, 1, 106–115.
Ma, J., Guo, H., Lei, M., Wan, X., Zhang, H., Feng, X., Wei, R., Tian, L., Han, X., 2016. Blocking effect of colloids on arsenate adsorption during co-transport through saturated sand columns. Environmental Pollution, 213, 638–647.
Missana, T., Alonso, U., Garcia-Gutierrez, M., 2008. Role of bentonite colloids on europium and plutonium migration in a granite fracture. Applied Geochemistry, 23, 6, 1484–1497.
Natarajan, N., Kumar, G.S., 2011. Spatial moment analysis of colloid facilitated radionuclide transport in a coupled fracture-matrix system. International Journal of Energy and Environment, 2, 3, 491–504.
Nedwed, T., Clifford, D.A., 2000. Feasibility of extracting lead from lead battery recycling site soil using high-concentration chloride solutions. Environmental Progress and Sustainable Energy, 19, 3, 197–206.
Pang, L., Close, M.E., Noonan, M., Flintoft, M., van den Brink, P., 2005. A laboratory study of bacteria-facilitated cadmium transport in alluvial gravel aquifer media. Journal of Environmental Quality, 34, 1, 237–247.
Porubcan, A.A., Xu, S., 2011. Colloid straining within saturated heterogeneous porous media. Water Research, 45, 1796–1806.
Puls, R.W., Powell, R.M., 1992. Transport of inorganic colloids through natural aquifer material: implications for contaminant transport. Environmental Science and Technology, 26, 3, 614–621.
Sen, T.K., Khilar, K.C., 2006. Review on subsurface colloid and colloid-associated contaminant transport in saturated porous media. Advances in Colloid and Interface Science, 119, 2–3, 71–96.
Shen, C., Huang, Y., Li, B., Jin, Y., 2008. Effects of solution chemistry on straining of colloids in porous media under unfavorable conditions. Water Resources Research, 44, 5, 335–342.
Simunek, J., van Genuchten, M.T., 2008. Modeling nonequilibrium flow and transport processes using HYDRUS. Vadose Zone Journal, 7, 2, 782–797.
Tusara, L., Itoi, R., Yamashiro, R., Fukuda, D., Kawahara, Y., 2015. Effects of suspended material and solution pH on solid deposition in porous media. Journal of the Geothermal Research Society of Japan, 37, 4, 143–152.
Walshe, G.E., Pang, L.P., Flury, M., Close, M.E., Flintoft, M., 2010. Effects of pH, ionic strength, dissolved organic matter, and flow rate on the co-transport of MS2 bacteriophages with kaolinite in gravel aquifer media. Water Research, 44, 4, 1255–1269.
Wang, Q., Cheng, T., Wu, Y., 2015. Distinct roles of illite colloid and humic acid in mediating Arsenate transport in water-saturated sand columns. Water Air and Soil Pollution, 226, 5, 1–15.
Xue, S., Kong, X., Zhu, F., Hartley, W., Li, X., Li, Y., 2016. Proposal for management and alkalinity transformation of bauxite residue in China. Environmental Science and Pollution Research, 23, 13, 12822–12834.
Yin, X., Gao, B., Lena, Q., Ma, L.Q., Saha, U.K., Sun, H., Wang, G., 2010. Colloid-facilitated Pb transport in two shooting-range soils in Florida. Journal of Hazardous Materials, 177, 620–625.
Zhou, D.D., Jiang, X.H., Lu, Y., Fan, W., Hou, M.X., Crittenden, J.C., 2016. Cotransport of graphene oxide and Cu(II) through saturated porous media. Science of the Total Environment, 550, 717–726.

NOMENCLATURE

C	particle concentration
N	turbidity level
d_g	median diameter of porous materials
ρ_s	density of solid matrix or particles
n	porosity of porous materials
D_{50}	median diameter
C_{inj}	concentration of particle suspension
C_P	concentration of Pb^{2+} in particle suspension
v	Darcy velocity
V_{inj}	volume of suspended particle suspension in each injection
t_{inj}	sustained time of particle injection
z	coordinate
D	hydrodynamic dispersion coefficient
u	average interstitial particle velocity
t	time
σ	concentration of particles deposited onto the solid matrix
k_d	deposition coefficient
k_r	release coefficient
τ	dummy integration variable
α	arbitrary constant
I_0, I_1	modified Bessel function of the first kind of order zero and one
I	strength of the plane source
m	mass of particles injected
Q	water flow rate
A	cross-sectional area of column
$\delta(\cdot)$	Dirac delta function
ξ	dummy time
t'	particle injection moment
α_d	longitudinal dispersivity
u_0	average interstitial fluid velocity
PV	pore volume
R_e	recovery rate
C_R	relative concentration
C_{out}	particle concentration at the outlet
V_p	pore volume of the entire soil column
R^2	coefficient of determination

Received 14 March 2018
Accepted 9 October 2018

Bereitgestellt von University Library Bratislava | Heruntergeladen 31.01.20 12:23 UTC

J. Hydrol. Hydromech., 67, 2019, 4, 359–371
DOI: 10.2478/johh-2019-0015

Extension of the Gardner exponential equation to represent the hydraulic conductivity curve

Theophilo B. Ottoni Filho[1], Marlon G. Lopes Alvarez[2], Marta V. Ottoni[3*], Arthur Bernardo Barbosa Dib Amorim[1]

[1] Department of Water Resources and Environment, Politechnical School, Federal Univ. of Rio de Janeiro (CT/UFRJ), Ilha do Fundão, Rio de Janeiro, RJ, Brazil. CEP: 21941-909
[2] State Environmental Institute (INEA), Av. Venezuela 110, Saúde, Rio de Janeiro, RJ, Brazil. CEP: 20081-312.
[3] Department of Hydrology, Geological Survey of Brazil (CPRM), Av. Pasteur, 404, Urca, Rio de Janeiro, RJ, Brazil. CEP: 22290-240
[*] Corresponding author. Tel.: +55 21 2546 0352. E-mail: marta.ottoni@cprm.gov.br

Abstract: The relative hydraulic conductivity curve $K_r(h) = K/K_s$ is a key variable in soil modeling. This study proposes a model to represent $K_r(h)$, the so-called Gardner dual (GD) model, which extends the classical Gardner exponential model to h values greater than h_o, the suction value at the inflection point of the $K_r(h)$ curve in the log-log scale. The goodness of fit of GD using experimental data from UNSODA was compared to that of the MVG [two-parameter (K_{ro}, L) Mualem-van Genuchten] model and a corresponding modified MVG model (MVGm). In 77 soils without evidence of macropore flow, GD reduced the RMSE errors by 64% (0.525 to 0.191) and 29% (0.269 to 0.193) in relation to MVG and MVGm, respectively. In the remaining 76 soils, GD generally was less accurate than MVG and MVGm, since most of these soils presented evidence of macropore flow (dual permeability). GD has three parameters and two degrees of freedom, like MVG. Two of them allow the calculation of the macroscopic capillary length, a parameter from the infiltration literature. The three parameters are highly dependent on the $K_r(h)$ data measurement in a short wet suction range around h_o, which is an experimental advantage.

Keywords: Hydraulic conductivity curve; Gardner exponential model; Mualem-van Genuchten model.

INTRODUCTION

The unsaturated hydraulic conductivity curve is a key soil hydrodynamic function in water and solute transfer in the vadose zone. Variations in the $K(h)$ curve are highly non-linear with suction h ($h > 0$) at the same time that they may reach values of various orders of magnitude. This requires a reliable mathematical model of representation of this curve for the proper description of hydraulic flows. In this study, we will assume the saturated hydraulic conductivity (K_s) to be a pre-established parameter and therefore it is sufficient to consider the relative hydraulic conductivity $K_r = K/K_s$.

Thus, the choice of a mathematical model to represent the K_r vs. h data is crucial (in this study we will not use the $K_r(\theta)$ models, where θ is the volumetric water content; the suction is expressed in cm). The $K_r(h)$ curve is usually given graphically in the log-log scale (Figure 1), where log = $\log_{10}$. Figure 1 shows a typical graph with the log K_r vs. log h data plot tending to the origin (h tending to 1.0 cm and K_r tending to 1.0) in a convex curve asymptotic to the horizontal axis log h. Above certain h_o suction values, there is a general tendency to an inflection of the experimental plot and to its curvature to become concave or quasi-linear (as in Figures 2 and 3 in Peters and Durner (2008), for example). Other graphs like this one will be shown along the study. According to Peters and Durner (2008) this inflection might be caused by film flow effects which would be relevant to define $K_r(h)$ in higher suction ranges ($h > h_o$), but irrelevant and largely dominated by capillary bundle flow effects in wetter moisture ranges ($h < h_o$). Various strictly empirical equations were proposed to represent K_r vs. h data between the 1950s and 1970s, as reported by Raats and Gardner (1971), Vereecken et al. (1990) and Leij et al. (1997). The most

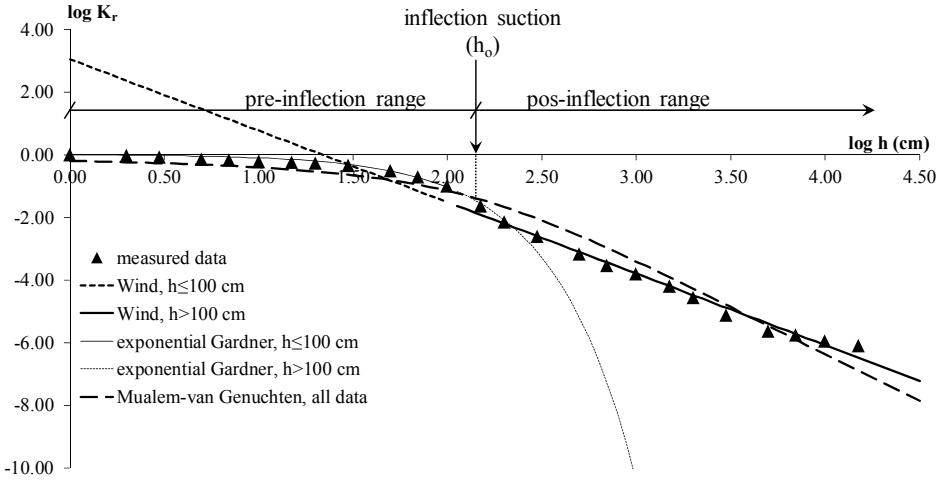

Fig. 1. Typical example [soil 4670 from the UNSODA database (Leij et al., 1996)] of representation of data of the relative conductivity curve $K_r = K/K_s$; a curve inflection tendency can be observed around suction h_o. The Wind and Gardner exponential equations were adjusted only for the measured data set with $h \geq 100$ cm or $h \leq 100$ cm, respectively. The Mualem-van Genuchten equation was adjusted for the complete data set.

Bereitgestellt von University Library Bratislava | Heruntergeladen 31.01.20 12:23 UTC

commonly used, according to Vereecken et al. (1990), are those where suction appears in a power or exponential function, as shown below.

One of the pioneer and frequently used empirical equations is the Wind power equation (Wind, 1955), also called the Brooks and Corey (Leij et al., 1997) hydraulic conductivity equation, or the Campbell (Wösten et al., 2001) equation.

$$K_r = ah^{-b}, \qquad a \text{ and } b > 0. \tag{1}$$

This equation fits the log K_r vs. log h data to a straight line. It is valid only for suction values greater than a minimum value (Campbell (1974) and Poulsen et al. (1999) propose minimal values of 100 cm and 20 cm, respectively). Therefore, the model is inadequate to fit the $K_r(h)$ curve at suction ranges close to saturation, as shown in Figure 1. Outside the convex range of the data plot, some soils tend to linearity, as shown in Figure 1, which justifies using Equation (1). As the Wind equation does not apply to low suction values, it is not recommended to describe ponding or low tension infiltration flows.

The most used empirical $K_r(h)$ equation in the literature on infiltration is the Gardner one-parameter exponential model (Gardner, 1958):

$$K_r = e^{-h/\lambda}. \tag{2}$$

Parameter $\lambda > 0$, called the macroscopic capillary length (White and Sully, 1987), is expressed in cm in this paper. The sorptive number, $\alpha = 1/\lambda$ (White and Sully, 1987), is often used instead of λ. An acknowledged inconvenience of this equation is that it fits the K_r vs. h data properly generally only in a limited suction range close to saturation (Communar and Friedman, 2014; Gardner, 1958; Jarvis and Messing, 1995; Russo, 1988), as shown in the example in Figure 1, where it is inappropriate for h >100 cm, in contrast to that observed for the Wind equation. Figure 1 makes it clear that the convex part of the experimental data plot is well represented by the Gardner exponential model. Beyond inflection point h_o = 130 cm, the model results are greatly different from the experimental data.

Equation (2) is largely used because it allows linearizing the Richards equation in cases of steady (Wooding, 1968) and unsteady flows (Philip, 1969; Warrick, 1974). Based on this linearization, various analytical solutions related to infiltration have been developed for both surface and sub-surface water application methods. These solutions underlie many infiltration test methods for in-field determination of saturated hydraulic conductivity and macroscopic capillary length. The most popular tests use the steady flow condition and their most popular devices are: the ring infiltrometers (Reynolds, 2008a; Reynolds and Elrick, 1990), disk (or tension) infiltrometers (Clothier and Scotter, 2002; Reynolds, 2008b), and constant head well permeameters (Reynolds et al., 1985; Reynolds, 2008c). Analytical solutions based on Equation (2) for transient infiltration flows with various water application devices are also common in the literature (Philip, 1986; Reynolds, 2011; Vandervaere, 2002, among others), including solutions related to drip irrigation engineering (Communar and Friedman, 2014). Inversion of the Richards equation for infiltration flows using numerical methods to determine K_s and λ is also made easy by the use of Equation (2), because in this case the $K(h)$ curve requires only these two parameters, which is advantageous since the corresponding numerical scheme usually provides a single solution with efficiency and convergence (Lazarovitch et al., 2007). The great acceptability of Equation (2) to handle infiltration flows results from its generally good representation of K_r vs. h data at low suction ranges, which are the suction ranges most representative of usual infiltration processes. Another advantage of Equation (2) is that its shape parameter (λ) is a strictly hydraulic-structural soil variable, such as the saturated hydraulic conductivity (K_s), because, according to the infiltration theory by disk infiltrometers at zero suction on the imbibition surface (Vandervaere, 2002; White and Sully, 1987):

$$\lambda K_s = S_p^2 0.55/(\theta_s - \theta_i), \tag{3}$$

where θ_s and θ_i are the volumetric water content at saturation and at initial conditions before wetting, respectively, and S_p is the soil sorptivity, defined as

$$S_p = \lim_{t \to 0} \mathrm{d}I/\mathrm{d}\sqrt{t}, \tag{4}$$

where I is the cumulative infiltration (infiltration volume divided by the disk area) and t is the infiltration time. Soil sorptivity (at zero suction on the imbibition surface) depends on θ_s minus θ_i and is a measure of the capacity of the soil to absorb infiltration water strictly due to soil pressure gradients (capillarity).

The last strictly empirical equation we refer to is the Gardner power equation (Gardner, 1958):

$$K_r = (1 + ch^d)^{-1}, \qquad c \text{ and } d > 0. \tag{5}$$

As demonstrated in Figure 3 from Raats and Gardner (1971), in a log-log graph and at low suction values, Equation (5) expresses $K_r(h)$ as a convex curve asymptotic to the horizontal axis (h) and which tends to a straight line with the increase in h, that is, Equation (5) simultaneously incorporates the qualities of the Wind and Gardner exponential equations (Figure 1). In principle, this must reflect on a better fit of Equation (5) in relation to the fit of the other two equations for wider suction ranges, from saturation to high tensions. This superiority of Equation (5) was demonstrated by Vereecken et al. (1990) using a database with 45 soils. The Mualem-van Genuchten (MVG) model will be discussed next. However, in a log-log scale, similarly to the Gardner power model, it also gives a convex curve at low suctions and fits to a straight line at higher tensions (Figure 1; Figure 2 in van Genuchten, 1980). In fact, the literature confirms that at wide suction ranges Equation (5) in general has experimental data fit errors comparable to those of the MVG model (Schaap and Leij, 1998; Vereecken et al., 2010; Weynants et al., 2009).

Instead of strictly empirical relations, another tendency is to determine the $K_r(h)$ curve from the water retention curve, $\theta(h)$, as its data are more easily obtained than those of the former. For this reason, hydraulic models are recurrent in the literature dedicated to the determination of K_r based on the calculation of the porous space distribution. The abovementioned MVG model is one of such models, where:

$$K_r = S^L \left[1 - \left(1 - S^{n/(n-1)}\right)^{1-1/n}\right]^2, \tag{6}$$

$$S = S(h) = \left[1 + (\alpha h)^n\right]^{-(1-1/n)}, \tag{7}$$

$$S = \frac{\theta(h) - \theta_r}{\theta_s - \theta_r}. \tag{8}$$

Equation 6 represents the Mualem (1976) hydraulic conductivity model which can be applied to the van Genuchten expression, Equation (7) (van Genuchten, 1980), which in turn allows using suction h to calculate the soil effective saturation, S,

Bereitgestellt von University Library Bratislava | Heruntergeladen 31.01.20 12:23 UTC

defined in Equation (8). In fact, Equations (7) and (8) model the water retention curve. In the MVG model, parameters θ_s (saturated water content), θ_r (residual water content), and the two shape parameters, α (cm^{-1}) and n (dimensionless), can be considered water retention curve data fitting parameters, while parameter L (pore connectivity, dimensionless) can be considered a hydraulic conductivity curve data fitting parameter (Vereecken et al., 2010). The four water retention curve parameters are positive, except θ_r, which can also be null (rarely has it been fitted with a negative value, according to Vereecken et al., 2010), and $n > 1$. Parameter L can be positive, null or negative (Schaap and Leij, 2000). MVG (Equations 6–8) is the most popular hydraulic conductivity model based on the water retention curve, among the various equivalent models that have been proposed (Kosugi et al., 2002; Leij et al., 1997). It also is the most used representation of the $K_r(h)$ curve in the mathematical simulation of flows and transport in the vadose zone (Vereecken et al., 2010). The MVG model was conceived to fit $K_r(h)$ in a wide suction range, generally from saturation to the "wilting point" [$\theta(h$ = 15000 cm)]. Its most used version is the one which does not require any K_r vs. h experimental data. In this case, the default value of L = 0.5 is used (Mualem, 1976; van Genuchten, 1980) and the $K_r(h)$ curve can be obtained simply from the parameterization of the $\theta(h)$ curve. However, the default L = 0.5 must be considered cautiously, since in the study by Schaap and Leij (2000) of 235 soils from the UNSODA database (Leij et al., 1996), L = –1 resulted in a decrease in the mean fitting error of $K_r(h)$ by 43% (1.31 for L = 0.5 to 0.75 for L = –1).

The flexibilization of the MVG model considers a multiplicative factor ($K_{ro} \leq 1$) in Equation (6):

$$K_r = K_{ro} S^L \left[1 - \left(1 - S^{n/(n-1)}\right)^{1-1/n}\right]^2 . \quad (9)$$

This new parameterization of the MVG model (Equations (7–9)) requires two fitting parameters for the $K_r(h)$ curve, K_{ro} and L, which makes the MVG model more accurate (Veerecken et al., 2010). In fact, in the study by Schaap and Leij (2000), parameterization of Equations (7–9) applied to the authors' database led to a significant decrease in the fitting mean error of $Kr(h)$, 69%, (1.31 for L = 0.5, K_{ro} = 1, in contrast to 0.41 for flexible L and K_{ro}), in relation to the most common parameterization with default L = 0.5. As the focus of our study is the accuracy of the mathematical representation of the hydraulic conductivity curve in the soil moisture range from saturation to the "wilting point", the MVG model parameterized with Equations (7–9) will be adopted here as a reference, also due to its great acceptability. An inconvenience of this reference model is that with Equation (9), $K_r(h = 0) = K_{ro} \leq 1.0$, that is, generally $K(h = 0) \neq K_s$, which is an inconsistency. In spite of this, another argument for the use of Equations (7–9) in this study as a reference is that certain soils can present a dual permeability field close to saturation (suction range from zero to a few centimeters): the first permeability field takes up a greater soil volume, is relatively macroscopically homogeneous and has a slower flow, usually called matrix flow; and the second, of smaller volume than the first one, is much more heterogeneous within the soil volume and has a faster flow, called macropore or fast flow. The latter field, formed by large and clearly individualized pores or cracks, and/or large spaces between soil peds, is well described in the literature (Beven and Germann, 1982; Jarvis, 2007; Lassabatere et al., 2014; Perret et al., 1999) and its hydraulic behavior has been modeled (Jarvis, 2008; Larsbo and Jarvis, 2006; Lassabatere et al., 2014). In porous structures where this double permeability close to saturation clearly occurs, the macropore flow is commonly a major component of the total flow. As a result, the saturated and unsaturated hydraulic conductivity (in the very wet range) can be strongly influenced by the macropore flow. Outside the narrow suction range where both flows occur interactively, the macropore flow becomes null and the unsaturated hydraulic conductivity is determined by only the matrix flow. Due to the narrow suction range (approximately 0–10 cm, as proposed by Jarvis, 2007) where the macropore flows occur, various authors (Schaap and van Genuchten, 2006; van Genuchten and Nielsen, 1985; Vereecken et al., 2010) admit that the strictly empirical equations and the usual models of representation of $K_r(h)$, such as Equations (7–9), can represent only the matrix flows. For this reason, Equation (9) is used here as a reference in the representation of the $K_r(h)$ curve, despite the fact that K_{ro} in Equation (9) can be smaller than 1 (sometimes by various orders of magnitude) in soils that present macropore flow. Schaap and Leij (2000) determined an approximate mean value of K_{ro} = 0.1 for their database, which indicates that soils with macropore flow were frequent. In the MVG parametrization of the soil in Figure 1, K_{ro} = 0.81 and there is no marked tendency to dual permeability, since the data plot in the very wet range (0–10 cm suction) clearly tended to the origin of the axes smoothly and asymptotically to the log h-axes. We can see that the MVG model (Equations (7–9)) represented the data for this soil relatively well across the whole suction range.

Schaap and van Genuchten (2006) introduced a modification suggested by Vogel et al. (2001) into the MVG model (Equations (7–9)) in an attempt to improve its efficiency, mainly in the suction range close to saturation. Additionally, they also included the macropore flow effects. The final product, the modified MVG model (MVGm), was tested with the same previously mentioned database (Schaap and Leij, 2000). The representation of the $K_r(h)$ curve improved significantly (37%) in relation to Equations (7–9) (error of 0.41 in contrast to 0.26 with the MVGm model). Although this result is promising, the MVGm model has not been widely used.

Assuming that the Gardner exponential model (Equation (2)) can be satisfactorily applied in a limited suction range close to saturation, the main objective of this study was to modify this model to extend it to suction values greater than a certain transition suction value, h_o. The extended model has been labeled Gardner dual model (GD). Another objective was to describe the GD model behavior and its parameters. The proposed model will be tested with practically the same database as that used by Schaap and Leij (2000) and its performance will be compared mainly to that of the Mualem-van Genuchten (MVG) model (Equations (7–9)), but also to that of the modified MVG model (MVGm). The measured suction of the samples varied from minimum values from 1 cm to 40 cm to maximum that rarely exceeded 15000 cm.

MODEL DEVELOPMENT AND DESCRIPTION

The GD model assumes that for $h \leq h_o$, the transition suction, the depletion of K_r is exponential to the increase in h, as predicted by Equation (2). The exponential depletion will be extended to $h \geq h_o$, but on the log scales of K_r and h (h expressed in cm), that is, for $h \geq h_o$:

$$\log K_r = a + b e^{-\log h/\beta} , \quad (10)$$

where $\beta > 0$, the conductive depletion coefficient (dimensionless), is a parameter of the GD model. Constants a and b will be

Bereitgestellt von University Library Bratislava | Heruntergeladen 31.01.20 12:23 UTC

calculated so that $K_r(h)$ is continuous and smooth (with continuous derivative) at $h = h_o$. Making $X = \log h$, $X_o = \log h_o$, $Y = \log K_r$, $Y_o = Y(X_o) = \log K_{ro}$ (different from K_{ro} in Equation (9), despite the same notation), which from Equation (2) is:

$$Y_o = -(\log e)h_o/\lambda, \quad (11)$$

where λ is the macroscopic capillary length and e is the Neper constant, thus:

$$a = -\frac{h_o}{\lambda}(\log e + \beta); b = \frac{h_o\beta}{\lambda} e^{\log h_o/\beta}.$$

Using Equations (2) and (11) and applying the two expressions above to Equation (10), the GD model becomes:

$$Y = Y(X) = (-\log e/\lambda)h,\ 0 \le h \le h_o, \quad (12a)$$

$$Y_o - Y = \frac{h_o\beta}{\lambda}\left[1 - e^{-(X-X_o)/\beta}\right],\ h \ge h_o. \quad (12b)$$

The derivatives of Y are:

$$dY/dX = -h/\lambda,\ 0 \le h \le h_o, \quad (13a)$$

$$dY/dX = (Y_o/\log e)e^{-(X-X_o)/\beta},\ h \ge h_o. \quad (13b)$$

$$d^2Y/dX^2 = -\frac{h}{(\log e)\lambda} < 0,\ 0 \le h < h_o, \quad (14a)$$

$$d^2Y/dX^2 = \frac{-Y_o}{(\log e)\beta} e^{-(X-X_o)/\beta} > 0,\ h > h_o. \quad (14b)$$

Analyzing the behavior of the $Y(X)$ curve at X_o, Equations (11) to (13) confirm that it is continuous and smooth, with:

$$dY/dX\left(X \to X_{o-}\right) = -h_o/\lambda = dY/dX\left(X \to X_{o+}\right) = Y_o/\log e. \quad (15)$$

X_o is a point of inflection of the $Y(X)$ curve, since Equation (14) indicates that the signal of d^2Y/dX^2 changes at X_o (and also d^2Y/dX^2 is discontinuous), and the $Y(X)$ curvature changes from convex ($d^2Y/dX^2 < 0$, $h < h_o$) to concave ($d^2Y/dX^2 > 0$, $h > h_o$), as shown in Figure 2. Equations (14b) and (15) also show that:

$$\beta = -\frac{dY/dX(X_o)}{d^2Y/dX^2(X \to X_{o+})}, \quad (16)$$

which confirms that the three model parameters (h_o, λ, β) are entirely determined by the $Y(X)$ curve behavior at the $X = X_o$ inflection point.

Using the GD model, we next define a soil structural index related to the $Y(X)$ curve, similar to the S structural index in Dexter (2004) related the water retention curve, $w(\log h)$ (w is the gravimetric water content), defined as $S = -dw/d(\ln h)$ ($h = h_o$), where h_o is the $w(\log h)$ curve inflection point and ln is the natural logarithm. This new parameter will be labeled conductive depletion index (dimensionless) and represented as the S_k index, defined as:

$$S_k = -dY/d(\ln h)\ (h = h_o). \quad (17)$$

As $dY/d(\ln h) = dY/dX \log e$, by Equations (15), (17) and (11):

$$S_k = -Y_o = -\log K_{ro} = (\log e)h_o/\lambda. \quad (18)$$

Figure 2 shows an example of fit of the $Y(X)$ curve based on the GD model; the (X_o, Y_o) inflection point and its tangent straight line are indicated, including the graphic representation of the derivative, which, according to Equations (15) and (18), is:

$$|dY/dX(X_o)| = T = \mathrm{tg}(\gamma) = S_k/\log e. \quad (19)$$

The dual model (Equation (12)) can also be calculated from Equation (20) using variable $g = h/h_o$ and the S_k index (Equation (18)):

$$-Y(g) = \log(K_r^{-1}) = S_k\, d_\beta(g), \quad (20a)$$

$$d_\beta(g) = g,\ 0 \le g \le 1, \quad (20b)$$

$$d_\beta(g) = 1 + (\beta/\log e)\left[1 - g^{-(\log e/\beta)}\right],\ g \ge 1. \quad (20c)$$

Function $d_\beta(g)$ varies as a power function, is smooth at $g = 1$ and depends only on parameter β. Its curve in Figure 3 (g is in log scale and d_β is in decimal scale) has the same shape (inverted) as that of $Y(X)$ (Figure 2), since $\log g = X - X_o$, and, from Equations (18) and (20a):

$$d_\beta = Y/Y_o = \log K_r/\log K_{ro}. \quad (21)$$

Due to Equation (21), $d_\beta(g)$ can be considered a normalized relative hydraulic conductivity curve. Thus, from Equation (20a), the parameter S_k is a multiplicative structural index of unsaturated hydraulic conductivity and the hydraulic conductivity, K_o, corresponding to Y_o:

$$K_o = K(h = h_o) = K_{ref} = K_s/(10^{Sk}), \quad (22)$$

can be considered a reference unsaturated hydraulic conductivity or a soil physical quality parameter.

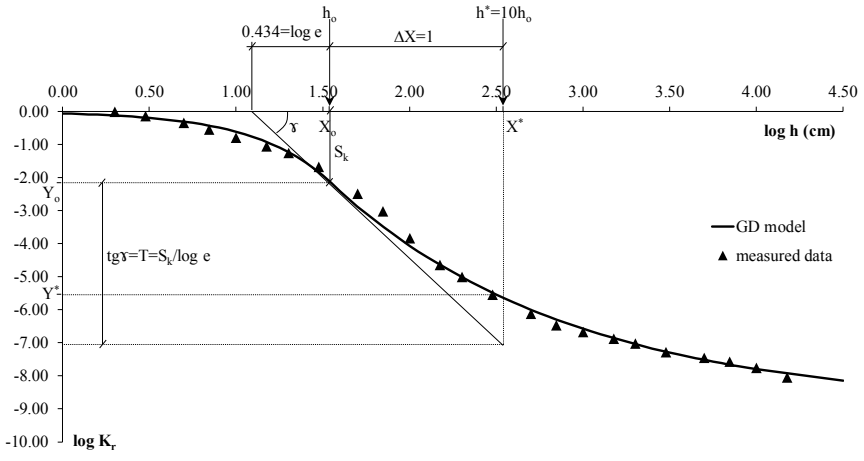

Fig. 2. Example (UNSODA database soil 4661) of fit of the experimental data to the $Y(X)$ curve calculated with the GD model; curve inflection point at h_o = 35 cm indicated. S_k index = 2.14 and the absolute value of the derivative [tg(γ)] at the curve inflection are also indicated. From Equation (18), λ = 7.09 cm. From Equation (16), the curvature of the concave part of the curve ($X > X_o$) close to its inflection depends on parameter β = 1.38.

Bereitgestellt von University Library Bratislava | Heruntergeladen 31.01.20 12:23 UTC

In order to characterize the influence of parameter β on the shape of $d_\beta(g)$ curves, we defined the positive fraction F_g based on a given $g>1$ ($h> h_o$) value:

$$F_g = |(Y - Y_o)|/ [T (X - X_o)] = (Y - Y_o)/ [-T (X - X_o)], \quad (23)$$

where T is the same as in Equation (19). From Equations (18), (20a) and (20c):

$$F_g = F_g(\beta) = (\beta/\log g)(1 - g^{-\log e/\beta}) = (\beta/\log g)(1 - e^{-\log g/\beta}) \quad (24)$$

From the equation above, $\lim_{\beta \to 0} F_g = 0$, from which Equation (23) shows that Y tends to Y_o when β tends to 0, which, according to Equation (21), implies that $d_o(g) = 1$, as in Figure 3 ($g>1$). When β tends to infinite, according to Equation (14b), d^2Y/dX^2 tends to 0 and the $Y(X)$ curve tends to the straight line below:

$$Y - Y_o = -T (X - X_o), (X > X_o, \beta \to \infty). \quad (25)$$

Applying Equation (25) to Equation (23), $\lim_{\beta \to \infty} F_g = 1$ and, from Equations (18), (19), (20a) and (25):

$$d_\infty(g) = 1 + (\log g/\log e), \quad (26)$$

the same as in Figure 3, where $d_\infty(g)$ is linear ($g > 1$). Equation (25) implies that the Wind equation (Equation (1)) is a particular case of the GD model, when $h > h_o$ and β tends to infinite (or $\beta > 100$, as shown in Figure 3). In this case, power b in the Wind model is the value of $T = S_k/\log e$.

When β does not tend to zero or infinite, its influence on the shape of the $d_\beta(g)$ curves, $g > 1$, [or on the shape of $Y(X)$, $X > X_o$], is better characterized considering the particular case of fraction F_g (Equation (24)) when $g = 10$, that is:

$$F_{10} = f(\beta) = \beta [1 - e^{-(1/\beta)}]. \quad (27)$$

The $f(\beta)$ value, labeled linearization fraction, is a much more adequate parameter to describe the shape of the $Y(X)$ curve, for $X > X_o$, than parameter β. The values of $f(\beta)$ [$0 < f(\beta) < 1$] are shown in Figure 4. For $f(\beta) > 0.90$ ($\beta > 5$ approximately), Figure 3 indicates that $Y(X)$ is nearly linear; for $\beta > 100$ [$f(\beta) > 0.995$], $Y(X)$ is practically linear and invariant for β. When $f(\beta) < 0.90$ ($\beta < 5$ approximately), the linearity of $Y(X)$, $X > X_o$, can be questioned, and its curvature at X_o increases with the decrease in β, as shown in Figure 3. Therefore, the GD model flexibilizes the convex-linear shape (described in the Introduction) of the $Y(X)$ curves generated by the Gardner power and Mualem-van Genuchten models for the entire suction range, from saturation to $h > h_o$.

When the coordinates (X_o, Y_o) of the inflection point of $Y(X)$ are known, parameter β can be estimated from a single measurement of the hydraulic conductivity at a suction greater than h_o, that is, for a known value (X^*,Y^*) of pair (X,Y), $X^*>X_o$. In this case, fraction F_{g*} can be calculated (Equations (18), (19) and (23)), and, as function $F_g(\beta)$ is invertible for any $g>1$ (since $dF_g/d\beta > 0$):

$$\beta = F_{g*}^{-1}[F_{g*}(\beta)] = F_{g*}^{-1}\left[(\log e/Y_o)(Y^* - Y_o)/(X^* - X_o)\right]. \quad (28)$$

Applying the equation above to the example in Figure 2, where $X_o = \log 35$, $X^* = \log 350$, $Y_o = -2.14$, $Y_o^* \approx -5.7$ (graphically), then $g^* = 10$, $F_{g*} = f(\beta)$, and $\beta = f^{-1}(F_{g*} = 0.72) = 1.4$ (Figure 4).

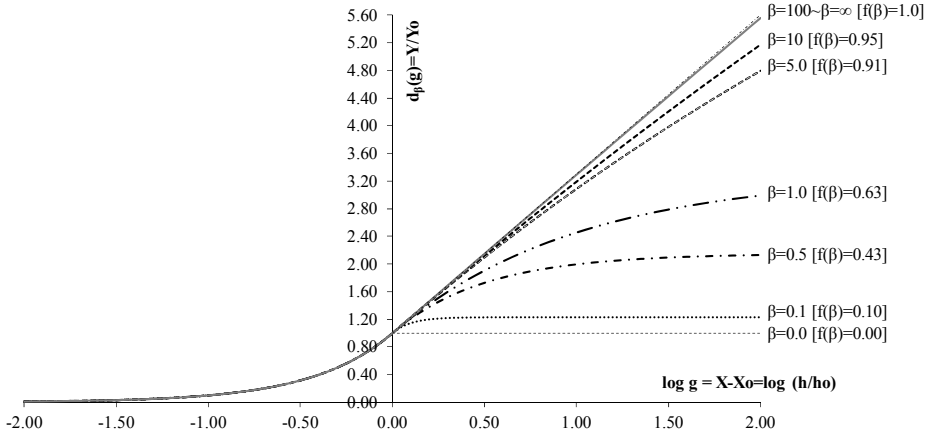

Fig. 3. Normalized relative hydraulic conductivity curve (d_β function) and its variations with parameter β, including the two limiting curves with β tending to zero and infinite. The infinite-β curve practically coincides with that of $\beta = 100$.

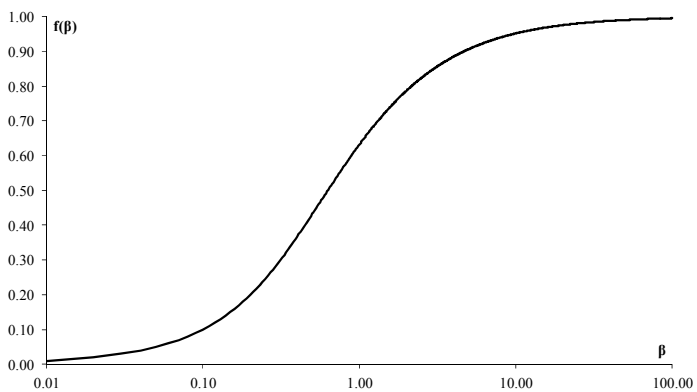

Fig. 4. Relationship between the linearization fraction, $f(\beta)$, and the conductive depletion coefficient, β.

Bereitgestellt von University Library Bratislava | Heruntergeladen 31.01.20 12:23 UTC

SOIL DATABASE

Hydraulic and textural data were taken from the database in Schaap and Leij (2000), who selected 235 soil samples from the UNSODA international database (Leij et al, 1996; Nemes et al., 2001). The water retention curve data [with at least six pairs (θ, h)] and hydraulic conductivity data [with at least five pairs (K,h)] for the 235 samples were determined, as well as the saturated hydraulic conductivity values, K_s. Other information from this database, including the methods of determination of the variables, the specification and definition of the textural classes, as well the sample distribution per textural class groups, are described by Leij et al. (1996), Schaap and Leij (2000), and Nemes et al. (2001). From the 235 samples, 82 were excluded for introducing uncertainty in the optimization of the parameters of the model proposed. The most frequent source of uncertainty was the indirect determination of K_s using pedotransfer functions for 60 samples. For the other samples, K_s was determined by direct measurement. Another 17 samples were excluded because their K was measured only in a limited suction range, either under 100 cm or over 40 cm. Five more samples were omitted due to inconsistent (K, h) pair measurement close to saturation. Therefore, the database of this study contained 153 samples. The measured suction with any tested soil varied from a minimum from 1 cm to 40 cm to a maximum that rarely exceeded 15000 cm.

PARAMETER OPTIMIZATION

Let be a set of N ($N \geq 3$) data pairs of the relative hydraulic conductivity data of a sample, forming two sequences: $\{h_i,\ h_i \geq 1\ \text{cm}\}$ (increasing sequence) and $\{Y_{mi} = \log K_{rm}(h_i)\}$, $i = 1,..., N$, where subscript m indicates the measured value. The minimum limits of $h_1 = 1$ cm and $N = 3$ are arbitrary. Let $h_{\min}$ be the smallest suction value h_i such that $K_{rm}(h_i) < 1$ ($Y_{mi} < 0$) and let $h_{\max} = h_N$. For lack of data, the optimization algorithm will not work if $h_{\max} \leq 100$ cm and $h_{\min} > 40$ cm. The latter restriction results from the fact that the transition suction, h_o, cannot be optimized if $h_o < h_{\min}$ (because in this case there would not be any data to characterize the K_r depletion of Equation (2)). Therefore, so as not to jeopardize the optimization of the GD model parameters, an appropriate number of measurements at low suction range ($h_i < h_o$) is desirable. If the optimized h_o is equal to $h_{\max}$, the algorithm considers the GD model to be the Gardner exponential model.

Using Equation (12) to represent the GD model, the objective function to optimize its three parameters (h_o, λ, β) was to minimize the sum of the square errors (SSE):

$$\text{SSE} = \sum_{i=1}^{N} (Y(h_i) - Y_{mi})^2 \tag{29}$$

A Visual Basic computer program was written to interface with Microsoft Excel spreadsheets for the calculation of the algorithm of determination of the three parameters. Additionally, the program also calculates the error evaluation statistics described next. The suction and hydraulic conductivity data are inputted in the main window of the program, which also contains the routine execution buttons. The program is available from the corresponding author upon request. The alternative model parameters, S_k and $f(\beta)$, are calculated from h_o, λ and β with Equations (18) and (27), respectively.

MODEL EVALUATION

The model was evaluated based on the two indicators described below which were calculated for each soil sample: Root Mean Square Error (RMSE) and Mean Error (ME_j) for each j suction interval.

RMSE (dimensionless) is a measure of the global mean error of fitting to N pairs of sample data [(h_i, Y_{mi})], given by:

$$\text{RMSE} = \sqrt{\text{SSE}/(N-2)}\ , \tag{30}$$

where SSE is given by Equation (29) and Y by Equation (12) for the optimized model parameters. Although the GD model has three parameters, it has only two degrees of freedom as Equation (12) is defined by parts ($h < h_o$ and $h > h_o$), each part containing only one parameter (λ or β, respectively), which makes the denominator of Equation (30) equal to $(N-2)$, instead of $(N-3)$.

ME (dimensionless) complements the RMSE measure by calculating the fitting error in each of the following nine suction intervals, represented by the limits: 1.0, 3.2, 10, 32, 100, 320, 1000, 3200, 10000, 32000 cm. The value of ME_j for each j value ($1 \leq j \leq 9$) is given by:

$$ME_j = \frac{1}{N_j} \sum_{i=1}^{N_j} \left[Y(h_{ji}) - \log K_{rm}(h_{ji}) \right], \tag{31}$$

where N_j is the total number of measurement pairs [h_{ji}, $K_{rm}(h_{ji})$] in suction interval j and Y is calculated with Equation (12) using the optimized parameters. Thus, a positive or negative ME_j value indicates that the model respectively either overestimates or underestimates the K_r values in interval j.

For a sample set, the goodness of fit of the model is given by the arithmetic mean of the RMSE values of the samples, and for each j value, $j = 1,\ldots,9$, by the weighted mean of the ME_j values of the samples (with the weight equal to the number of measurements of the respective sample within interval j).

Comparison with the Mualem-van Genuchten models

The method of evaluation described above is identical to that used by Schaap and van Genuchten (2006) to evaluate the fitting errors of models MVG and MVGm, with, roughly speaking, the same database used in our study (in fact they used the 235 samples from the UNSODA database, as already mentioned, rather than the 153 samples of this study). Both models also have two degrees of freedom. All this makes the comparison of the Gardner dual model to these two models easier. The authors also kindly granted us access to their full database (personal communication). We will use the same four soil sets that they used to compare the performance of the models according to textural class groups, namely Sands, Loams, Silts and Clays.

Table 1 and Figure 5 show, respectively, the RMSE mean values and the probability distributions of the RMSE values, for models GD, MVG and MVGm. Considering the complete database (Figure 5a), we observe that model GD in general calculates the K_r curve data with intermediate accuracy in relation to the two other models, with a mean RMSE of 0.378 for GD, and 0.468 and 0.280 for the MVG and MVGm models, respectively. The goodness of fit of the GD model improves substantially when only the model's 77 best fitting soils (50% percentile) are considered, giving an RMSE < 0.32 (Figure 5a). These soils make up database A in Table 1. In this case, according to Table 1, the GD model mean error was confirmed to be 64% smaller than that of the MVG model (0.191 in contrast to

Bereitgestellt von University Library Bratislava | Heruntergeladen 31.01.20 12:23 UTC

Table 1. RMSE values for the complete database and for four subsets of its soils taking into account models GD, MVG and MVGm.

Database	Number of Soils	Mean RMSE		
		GD model	MVG model	MVGm model
Complete	153	0.378	0.468	0.280
* A	77	0.191	0.525	0.269
** B	76	0.569	0.410	0.291
*** A'	55	0.236	0.558	0.278
**** B'	50	0.554	0.386	0.250

* soils with $RMSE_{GD} < 0.32$; ** soils with $RMSE_{GD} \geq 0.32$; *** soils with K_r measurements in range $h \leq 10$ cm; all K_r values > 0.10 in this suction range; **** soils with K_r measurements in range $h \leq 10$ cm; at least one K_r value ≤ 0.10 in this suction range.

0.525) and 29% smaller than that of the MVGm model (0.191 in contrast to 0.269), which indicates the superiority of the model proposed regarding the goodness of fit for A, as also shown in Figure 5b.

However, the goodness of fit of the GD model was much poorer when only soils in database B (76 soils) were considered; database B complements database A in relation to the complete database, that is, it comprises samples with $RMSE_{GD} \geq 0.32$. According to Table 1, the $RMSE_{GD}$ in this group of soils increased to 0.569, a value significantly higher than the corresponding MVG and MVGm errors (0.410 and 0.291). The differences between the $K_r(h)$ experimental data plots of databases A and B reveal that the data plots of A (Figure 6, soils 4650 and 4673 from UNSODA) tend to converge to the origin of the Cartesian axes [$K_r(h = 1) = 1$] asymptotically to the log h-axes, while those of B (Figure 7, soils 4092 and 4111) clearly do not. These four soils are common and consistent examples of the differences mentioned between the log-log graphs of the $K_r(h)$ data of databases A and B. The GD model requires that the Gardner exponential model be valid close to saturation, which it is not consistent with the plot of the experimental pairs (log h, log K_r) of B close to saturation. This has a significant negative impact on the fitting of GD for these soils. For MVG, this impact is weakened by its multiplicative parameter, K_{ro} (Equation (9)), which generally induces a better fitting of the MVG curves to the database B data in relation to the GD fitting, as shown in Figure 7. What can justify the abrupt variation of hydraulic conductivity close to saturation in soils from database B is the macropore flow phenomenon, which applies, as we have seen, only to a very limited suction range, in the order of 0–10 cm. Another reason might be experimental inconsistencies involving saturated and unsaturated hydraulic conductivity measurements very close to saturation. However, our analysis does not require the characterization of the cause of this distinct behavior of $K_r(h)$ close to saturation. For this reason, and to simplify the text, from this point on we assume that the abrupt depletion of conductivity close to K_s is due only to macropore flow.

To better support the interpretation that the main cause of the poorer goodness of fit of the GD model is the abrupt variation of the $K_r(h)$ curve measures close to saturation, we excluded the soils without K_r measures in the range $h \leq 10$ cm (48 samples) from the complete database. Two subsets were taken from the remaining database (105 samples): subset A' (55 samples), with K_r data greater than 0.10 (K "close" to K_s) in the range $h \leq 10$ cm, and subset B' (50 samples), the complement of A' in relation to the 105 soils. In this way, subset A' has only samples that did not present a marked tendency of abrupt depletion of K_r data close to saturation, while subset B' may have this tendency. A more objective criterion is thus established than that used in the previous paragraph to justify the worse performance of the GD model with database B. In fact, we observed that 85% of the samples in A' and B' belong to databases A and B, respectively. That is, the goodness of fit of the GD model was adequate (RMSE < 0.32) for most of the samples where the $K_r(h)$ data plot seems to converge asymptotically to the saturation data (Figure 5c). When the asymptotic convergence is dubious (case of B'), the GD model was normally not accurate (RMSE ≥ 0.32). Soil 4070 (Figure 8) was an exception, as the convergence was asymptotic and the GD model was not accurate (RMSE = 0.520). This sample was a peculiar case in the database, with an indication of only existing matrix flow in the whole suction range (without relevant macropore flow) and the proposed model did not fit its data accurately. The other sample in Figure 8 (soil 4670, the soil in Figure 1) is a more common example of A', which also had an indication of only matrix flow and the GD model was accurate (RMSE = 0.103). Table 1 compares the RMSE values of A' and B' for models GD, MVG and MVGm.

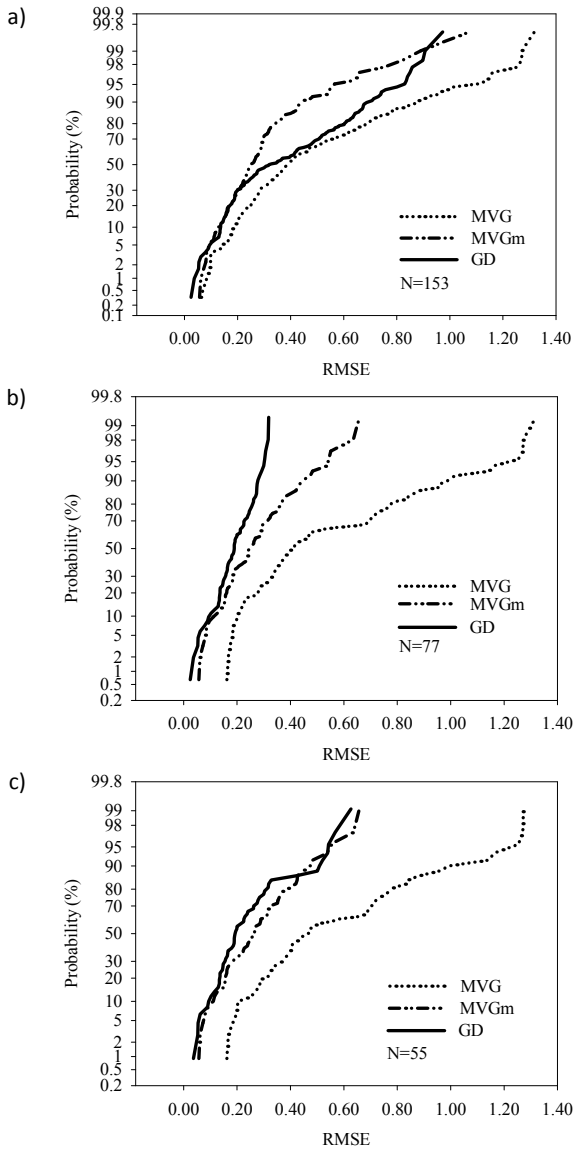

Fig. 5. Probability distribution of the RMSE values of the samples taking into account models GD, MVG and MVGm. (a) Complete soil database; (b) Soil database A ($RMSE_{GD} < 0.32$); (c) Soil database A' (soils with K_r measures in range $h \leq 10$ cm, with all K_r measures greater than 0.10 in this range).

Bereitgestellt von University Library Bratislava | Heruntergeladen 31.01.20 12:23 UTC

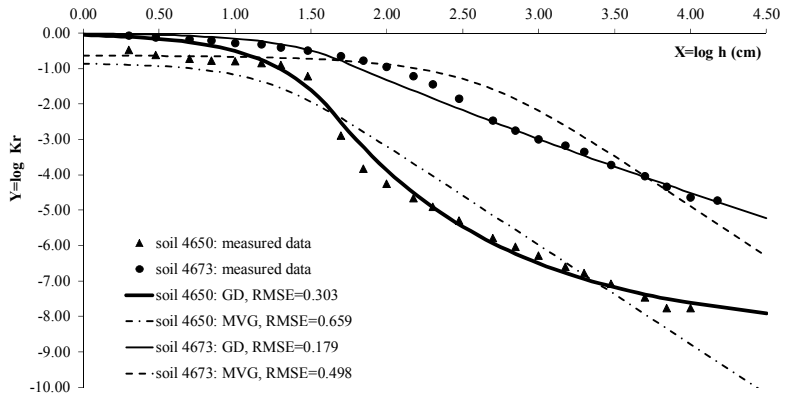

Fig. 6. Experimental data of the K_r curve and GD and MVG fits for two soils from database A, where the GD model has a good quality of fit (RMSE < 0.32).

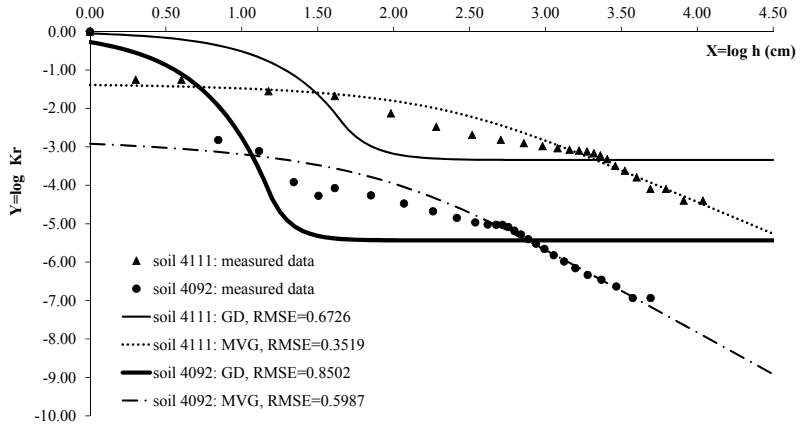

Fig. 7. Experimental data of the K_r curve and GD and MVG fits for two soils from database B, where in general the GD model does not have a good quality of fit (RMSE ≥ 0.32).

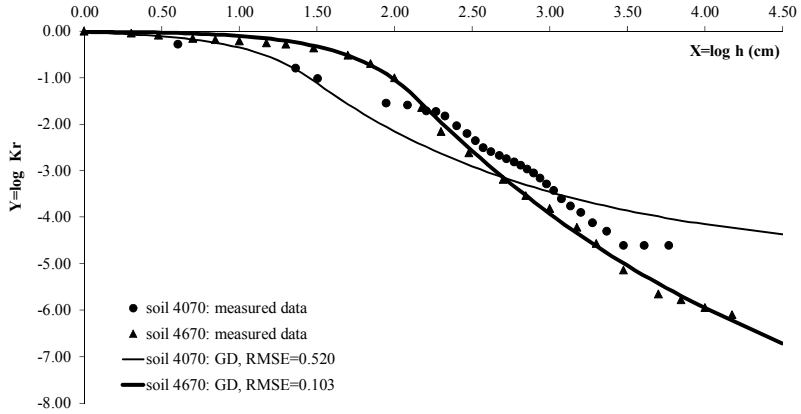

Fig. 8. Two examples of fitting of the GD model for database A', for which only matrix flow is expected to occur over the entire suction range. Soil 4670 is the most common example of GD model fitting when macropore flow is not relevant, for which GD performed well. Soil 4070 is an exception in database A', as the GD model was not efficient.

Figure 9 shows the probability distributions of the reciprocal of parameter K_{ro} of model MVG (Equation 9) for the complete database and for the 15 soils (10% of the complete database) with the worst performance for GD or MVG. In general, the more parameter $1/K_{ro}$ is different from 1, the greater the tendency of macropore flow. Figure 9 confirms the tendency of the soils with the worst performance with the GD model to have macropore flow, which does not happen in the soils with the worst performance for MVG, for which $K_{ro} = 1$ predominates. In this last case, 11 of the 15 soils are from database A ($RMSE_{GD} < 0.32$), that is, they present only matrix flow in the whole suction range, without signs of relevant macropore flow. This indicates a difficulty for the model MVG to represent hydraulic conductivity data in the matrix flow condition, which has already been shown in the literature (Schaap and Leij, 2000; Schaap and van Genuchten, 2006; van Genuchten and Nielsen, 1985; Vogel et al., 2001), and, in fact led to the development of model MVGm. Also, because MVG imposes a linear representation to the log K_r vs. log h graph at great suction ranges, in contrast to the GD model, the MVG model is unable to give a good fitting for soils that have a curved log K_r vs. log h data plot at those suction ranges. This is the case of soils 4650 (Figure 6) and 4661 (Figure 2), with $RMSE_{MVG}$ values of 0.659 and 0.581, respectively, in contrast to the corresponding $RMSE_{GD}$ values of 0.303 and 0.164. In agreement, Table 2 confirms the best performance of the GD model in comparison to the MVG and MVGm models with all textural class groups when there is only the matrix flow (with an insignificant exception for Loams). The performance of the GD model with the full database was intermediate to those of the two other models with all groups.

Figure 10 shows the calculations of the ME errors for models GD and MVG in the nine suction intervals mentioned in the beginning of this section, considering the complete database of

Bereitgestellt von University Library Bratislava | Heruntergeladen 31.01.20 12:23 UTC

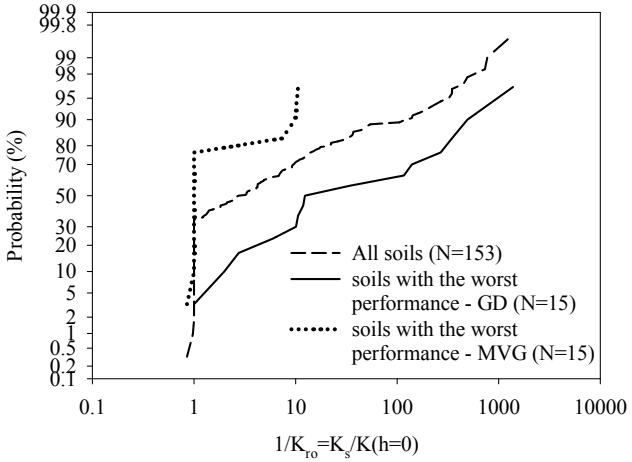

Fig. 9. Probability distribution of parameter $1/K_{ro}$ of model MVG (Equation (9)) for the complete database and the 15 soils with the worst performance with models GD and MVG.

Table 2. RMSE values per textural class for the complete database and the database of the soils that only presented matrix flow in the whole suction range (without relevant macropore flow).

	Summarized classes	Number of Soils	Mean RMSE		
			GD model	MVG model	MVGm model
Complete Database	Sands	68	0.360	0.473	0.321
	Loams	27	0.373	0.497	0.225
	Silts	40	0.431	0.444	0.263
	Clays	18	0.338	0.459	0.244
	All	153	0.378	0.468	0.280
Database A ($RMSE_{GD} < 0.32$)	Sands	37	0.203	0.465	0.286
	Loams	15	0.179	0.599	0.171
	Silts	15	0.187	0.498	0.316
	Clays	10	0.167	0.679	0.281
	All	77	0.191	0.525	0.269

our study (model GD) or that of Schaap and van Genuchten (2006) (model MVG), both with approximately the same number of samples (153 and 235 samples, as described previously). We can see that the GD errors were generally smaller or greater (in absolute value) than the MVG errors in suction intervals 1–32 cm and 32–15000 cm, respectively. When only soils without relevant macropore flow were considered (database A), the ME errors of GD were nearly null, that is, the model proposed determined the $K_r(h)$ curve without a marked bias over the whole suction range.

Evaluation of the model constants

In this subsection we considered the parameters and indexes previously described concerning the model GD in relation to the 77 soils in database A ($RMSE_{GD} < 0.32$), as these constants for database B ($RMSE_{GD} \geq 0.32$) usually refer to a poor model optimization quality and, therefore, have an inaccurate meaning. We will describe and comment how these parameters and indexes vary in A and in the four textural class groups of A (Table 3 and Figure 11, respectively). We acknowledge that this is a preliminary statistical analysis due to the reduced number of samples. Table 3 presents the soil constants in increasing order of their coefficients of variation (CV). Coefficient β was not included in Figure 11 for lack of interest for analysis.

Table 3 indicates that there are four levels of variability of soil constants in A: $f(\beta)$ and S_k (CV ≅ 37%), h_o and λ (CV ≅ 115%), K_s and K_o (CV ≅ 235%), β (CV = 319%). As already mentioned, parameter $f(\beta)$ describes the shape of the $h > h_o$ branch of the $K_r(h)$ curve better than parameter β does. The fact that β is more variable than $f(\beta)$ by approximately one order of magnitude (according to Figure 4, this occurs mainly because $f(\beta)$ is little sensitive to variations of β when $f(\beta)$ tends to 1) is another advantage to use $f(\beta)$ rather than β as a curve shape parameter. We can see in Figure 11a that the mean linearization fractions varied little in the four textural class groups, around 0.67, which indicates a little dependence of $f(\beta)$ from the soil granulometry. The $f(\beta)$ maxima tended to 1, in agreement with the situations for which the Wind model ($h > h_o$) was particularized. Very small $f(\beta)$ [$f(\beta) < 0.3$] values generally corresponded to samples with K_r measures in a very limited suction range.

Table 3. Means and coefficients of variation of the GD model soil constants for database A (77 soils), where: $f(\beta)$ is the linearization fraction, S_k - conductive depletion index, h_o - transition suction, λ - macroscopic capillary length, K_s - saturated hydraulic conductivity, K_o - reference unsaturated hydraulic conductivity, and β - conductive depletion coefficient.

	$f(\beta)$	S_k	h_o (cm)	λ (cm)	K_s (cm/d)	K_o (cm/d)	β
mean	0.672	1.59	52.8	14.5	184	6.20	20.9
CV (%)	36.1	37.8	113	116	225	243	319

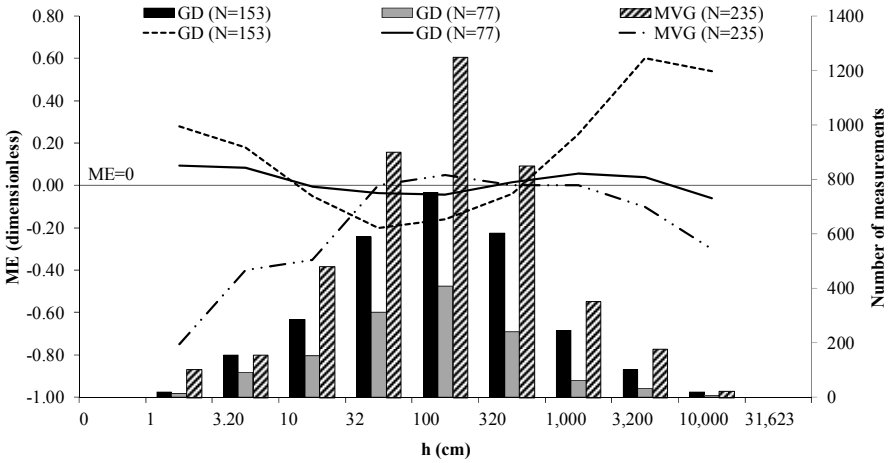

Fig. 10. Mean errors (ME) of models GD and MVG in the nine suction intervals considered (lines) and number of measurements (bars) in each interval. For MVG, we considered the Schaap and van Genuchten (2006) database, with 235 soils (results taken from the authors' Figure 4). For GD, we considered the complete database of our study (153 soils), as well as database A (77 soils) with only the soils without signs of relevant macropore flow.

Bereitgestellt von University Library Bratislava | Heruntergeladen 31.01.20 12:23 UTC

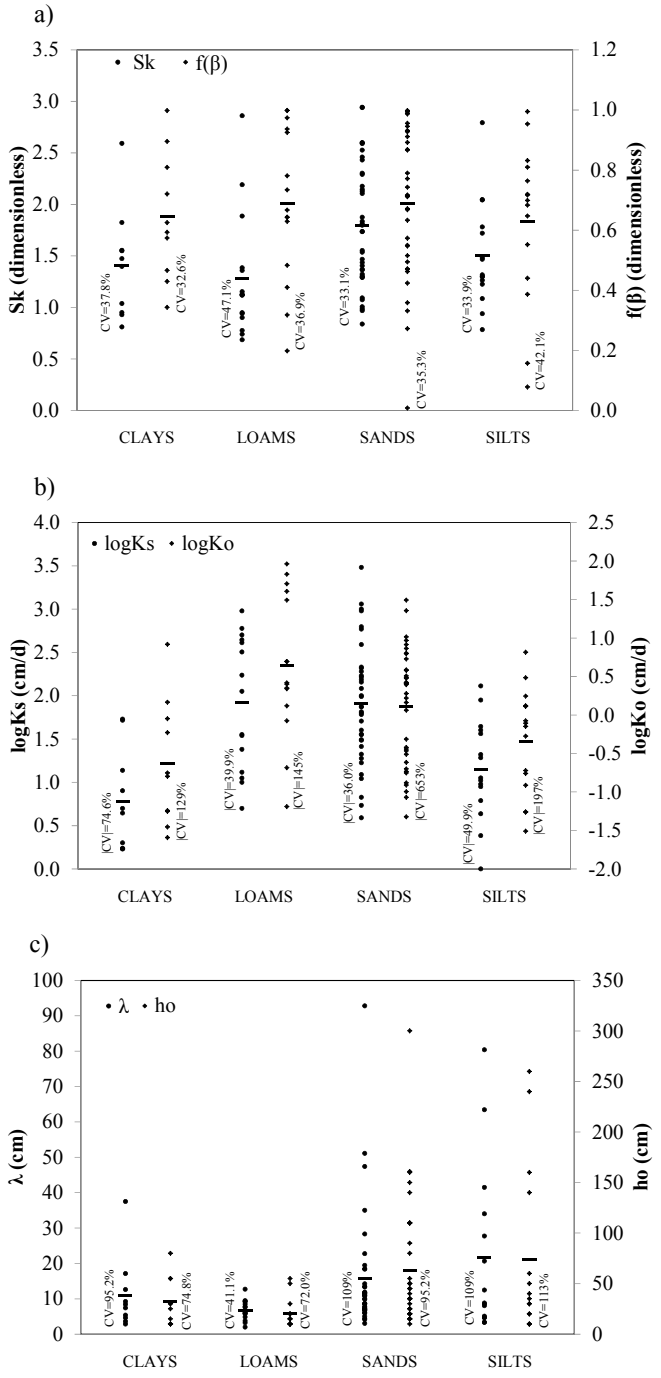

Fig. 11. Means, coefficients of variation (CV) and values of the GD model soil constants for the four textural class groups in database A: Clays - 10 soils, Loams -15 soils, Sands -37 soils, Silts - 15 soils. (a) $f(\beta)$, S_k; (b) log K_s (cm/d), log K_o (cm/d) (means and CVs of the logarithmic values); (c) h_o (cm), λ (cm).

Soils 4650 and 4673 in Figure 6 are examples of mean and high values, [$f(\beta)$ = 0.67] and [$f(\beta)$ = 0.95], respectively, of the linearization fraction, which indicates that the situation of the curvilinear shape of the $Y(X)$ (for $h > h_o$) curve of the first soil is frequent in database A. Examples of more extreme situations of the parameter are shown in Figure 12: soil 2561 [$f(\beta)$ = 0.996] and soil 2743 [$f(\beta)$ = 0.48]. Soils 4673 (Figure 6) and 2561 (Figure 12) illustrate the quasi-linear and linear branches $h > h_o$ of $Y(X)$, respectively.

The S_k index is the GD model constant better related to the global depletion capacity of the hydraulic conductivity curve, as it is a multiplicative value of $Y = \log K_r$ in the entire suction range, according to Equation (20). Another constant directly related to the depletion potential of the $K_r(h)$ curve is $f(\beta)$, but concerning only its $h > h_o$ branch. That is, the greater the S_k and $f(\beta)$ values are, the greater the depletion capacity of $K_r(h)$. Index S_k is also proportional to the absolute value of the dY/dX slope at the $Y(X)$ inflection point (Equation (19); Figures 2 and 12), at the same time that it is the absolute value of Y at this point (Equation (18); Figures 2 and 12), thus being a soil structural hydraulic parameter. As seen, another parameter with this nature is the macroscopic capillary length, λ, related to S_k by Equation (18). However, λ relates only to the branch $h < h_o$ of $Y(X)$ and its use with the GD model is unnecessary when the values of S_k and h_o are known (Equation (20)). In Figure 11a, the mean value of S_k varied between the textural class groups, indicating a certain dependence from the soil granulometry: samples in the Sands group (sand, loamy sand, sandy loam, sandy clay loam) tended to present values (S_k = 1.79) greater than those of the other groups. This confirms the general notion that in unsaturated conditions (but not very close to saturation), sandy soils tend to be less permeable than the others (Hillel, 1998). S_k had the smallest mean value in the Loams (loam and clay loam) group (S_k = 1.28). The maxima and minima for the four textural class groups were approximately 2.8 and 0.75, respectively. Figure 12 presents examples of $Y(X)$ curves for low (S_k = 0.90, soil 2743), medium (S_k = 1.45, soil 4670) and high (S_k = 2.13, soil 2561) depletion index conditions. Soil 2561 is a sand with a high depletion potential for the $K_r(h)$ curve; K decreases by eight orders of magnitude between saturation and the suction value of 350 cm. In addition to S_k, its $f(\beta)$ parameter is also high [$f(\beta)$ = 0.996], which contributes to an increase in the conductive depletion. Sample 2743 is an opposite example: a clay loam with a low depletion potential. In this case, for the suction value of 160 cm, the K value decreased by only two orders of magnitude in relation to the saturation. Extrapolating the GD model to this soil at suctions greater than 160 cm, with both small S_k and $f(\beta)$ values, the conductive depletion must remain very low, as indicated in Figure 12. Soil 4670 is an intermediate example of the depletion potential of the $Y(X)$ curve in relation to the other two soils.

The reference unsaturated hydraulic conductivity, $K_o = K(h_o)$, was calculated with Equation (22). It is a soil physical quality parameter, as it depends exclusively on the saturated hydraulic conductivity (K_s) and the S_k index. In the three soil examples above, the respective K_s and K_o of 2561 (sand), 2743 (clay loam) and 4670 (silt) are (in cm/d): (3020, 23), (320, 40), (89, 3.0), which indicates a distinct level and ordination of reference unsaturated hydraulic conductivity values in relation to the saturated values. Figure 11b illustrates the distributions of the log K_s and log K_o values for the four textural class groups. The geometric mean value (4.40 cm/d) of K_o of the Loams group was approximately three times larger than the geometric mean (1.30 cm/d) of the Sands group and one order of magnitude greater than those of the other two groups. As the transition suction (h_o) normally corresponded to a wet soil situation (mean h_o = 52.8 cm, Table 3), we conclude that in the wet range (but not very close to saturation) of database A, the soils from the Loams group tend to have a greater hydraulic conductivity in comparison to the other soils.

Among the three parameters, h_o, λ and S_k, only two are needed for the calculation of $K_r(h)$, because of Equation (18). Figure 11c shows the distribution of the h_o and λ values in the four textural class groups, which shows that with only one exception (λ in the Loams group), these parameters were much more variable than the third parameter; their coefficients of variation

Bereitgestellt von University Library Bratislava | Heruntergeladen 31.01.20 12:23 UTC

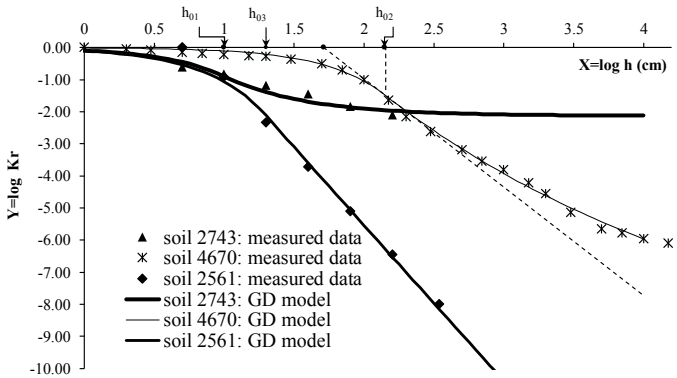

Fig. 12. Three examples of GD model fitting involving soils with low (S_{k1} = 0.90, soil 2743), mean (S_{k2} = 1.45, soil 4670) and high (S_{k3} = 2.13, soil 2561) S_k indexes from database A. The other parameters are: soil 2743 (h_{o1} = 10 cm, λ_1 = 4.8 cm, $f_1(\beta)$ = 0.48), soil 4670 (h_{o2} = 140 cm, λ_2 = 41.5 cm, $f_2(\beta)$ = 0.83), soil 2561 (h_{o3} = 20 cm, λ_3 = 4.1 cm, $f_3(\beta)$ = 0.996). The transition suction values of the three curves are indicated. The tangent at the inflection of the $Y(X)$ curve is shown only for soil 4670.

in general were at least twice as great as those of S_k. This might indicate a greater difficulty in the indirect estimation of h_o and λ using pedofunctions rather than in the estimate of S_k. The h_o and λ mean values also seem to vary with soil granulometry. They were greater in groups Sands and Silts, smaller in the other two groups and maximum in the Silts group (h_o = 74 cm, λ = 21.8 cm). The transition suction value was limited to the 10–300 cm range, showing that the experimental determination of the X_o, Y_o coordinates of the inflection point of $Y(X)$, of great relevance in the characterization of the GD model parameters, must be restricted to the wet range of the hydraulic conductivity curve (where suction can be monitored by tensiometry), which is greatly advantageous. This h_o range is consistent with the suction values at the inflection points of the (log K_r) vs (log h) curves of Figures 2 and 3 in Peters and Durner (2008). Parameter λ was within range 2.0–93 cm, with mean value of 14.5 cm, which is consistent with the literature (Communar and Friedman, 2014; Reynolds, 2016; White and Sully, 1987). This parameter is commonly considered a measure of the soil dynamic capillarity. Usually, medium and fine textured soils are considered to have greater λ values, and coarser soils, smaller values (Communar and Friedmand, 2014, Reynolds, 2016). However, in database A, Sands tended to have a greater λ than Clays and Loams (Figure 11c). Yet, White and Sully (1987) admitted that soil granulometry should not influence this parameter markedly. On the other hand, the small number of samples in database A makes a more judicious analysis difficult. It is also commonly accepted that soils with greater λ values (more "capillary") are less depletive in terms of $K_r(h)$ than those with smaller λ values. This holds only in the suction range to which the Gardner exponential model applies. In wider suction ranges, according to Equation (18), the depletion potential of $K_r(h)$ (S_k index) also depends on the value of h_o, when compared to λ. This is the case of sand 2561 in Figure 12, which is much more depletive than clay loam 2743, despite their very close λ values, what is justified by their very distinct h_o values, in a relative comparison (h_o = 20 cm and 10 cm, respectively). This is also the case of silt 4670 in Figure 12, globally more depletive than soil 2743, despite its far greater "dynamic capillarity" (λ = 41.5 cm and 4.8 cm, respectively).

CONCLUSION

The model proposed, called the Gardner dual model (GD model) is, in fact, a natural extension of the Gardner exponential model of hydraulic conductivity (Equation 2), since the extension equation (Equation 10), for $h > h_o$, expresses the same law of exponential decay of hydraulic conductivity with suction, only changing the decimal scales of h and K_r (Equation 2) by the corresponding logarithmic scales (Equation 10). The transition suction from the decimal to the logarithmic law, h_o, might result from a change of soil hydraulic behavior as the porous space becomes drier, as suggested by Peters and Durner (2008). The GD model was more accurate than the two-parameter (K_{ro} and L) Mualem-van Genuchten model (MVG model) and the corresponding modified MVG model (MVGm model) in the representation of the $K_r(h)$ curve in 77 soils that did not present relevant macropore flow. In this case, the mean RMSE of the model proposed was 64% smaller (0.191 to 0.525) and 29% smaller (0.191 to 0.269) than those of the MVG and MVGm models, respectively; the GD model also calculated $K_r(h)$ more efficiently than the MVG model in all suction ranges. The remaining 76 soils generally presented signs of relevant macropore flow, which tended to lead to poorer performance of the GD model in all suction ranges and to a generally lower accuracy than those of the other two models. We conclude that the mathematical representation of the GD model was more adequate than those of the MVG and MVGm in soils with only matrix flow in the whole suction range. On the other hand, the GD model is not recommended for soils with dual permeability close to saturation. Therefore, modifying the GD model to include the effects of macropore flow is an interesting possibility. Another issue that deserves investigation is the determination of the suction upper limit beyond which the GD model is not valid. In this paper the model was evaluated for suctions smaller than 15000 cm.

Like models MVG and MVGm, the proposed model has two degrees of freedom, although it requires three parameters for its calculations. One of the parameters is the conductive depletion coefficient, (β), or, alternatively, the linearization fraction [$f(\beta)$], which are dimensionless shape parameters of the hydraulic conductivity curve, as shown in Figure 3. The other two model parameters depend strictly on the coordinates X_o, Y_o of the inflection point of the $Y(X)$ curve, where X = log h, Y = log K_r. They are the transition suction, h_o (cm), and the conductive depletion index, S_k (dimensionless). The first is the suction at the inflection of the $Y(X)$ curve, the limit suction value of the range in which the classic Gardner exponential model is applicable. The second parameter, S_k, is the absolute value of log K_r at h_o, with the definition of S_k similar to that of the S index of the water retention curve. The macroscopic capillarity length λ (cm), a physical parameter known in the infiltration literature, can be calculated from h_o and S_k. Thus, this study has demonstrated that the determination of the GD model parameters is highly dependent on the measurement of the $Y(X)$ curve at suction values close to its inflection (see also Equation (28)), which is an experimental advantage, since the transition suction, h_o, has been demonstrated to be within a wet range (h_o = 10 to 300 cm). This must favor the estimation of the hydraulic conductivity in a wide suction range after the optimization of the GD model parameters using only the experimental data in the wet range with suction values around h_o.

Bereitgestellt von University Library Bratislava | Heruntergeladen 31.01.20 12:23 UTC

REFERENCES

Beven, K., Germann, P., 1982. Macropores and water flow in soils. Water Resour. Res., 18, 1311–1325.

Campbell, G.S., 1974. A simple method for determining unsaturated conductivity from moisture retention data. Soil Sci., 17, 311–314.

Clothier, B., Scotter, D., 2002. Unsaturated water transmission parameters obtained from infiltration. In: Dane, J.H., Topp, G.C. (Eds.): Methods of Soil Analysis, Part 1. SSSA Book Ser. 4, SSSA, Madison, WI, pp. 879–889.

Communar, G., Friedman, S.P., 2014. Determination of soil hydraulic parameters with cyclic irrigation tests. Vadose Zone J., 13, 4, 12 p, DOI: 10.2136/vzj2013.09.0168.

Dexter, A.R., 2004. Soil physical quality. Part I. Theory, effects of soil texture, density, and organic matter, and effects on root growth. Geoderma, 120, 201–214.

Gardner, W.R., 1958. Some steady-state solutions of the unsaturated moisture flow equation with application to evaporation from a water table. Soil Sci., 85, 228–232.

Jarvis, N.J., 2007. A review of non-equilibrium water flow and solute transport in soil macropores: principles, controlling factors and consequences for water quality. European Journal of Soil Science, 58, 523–546.

Jarvis, N.J., 2008. Near-saturated hydraulic properties of macroporous soils. Vadose Zone J., 7, 1302–1310.

Jarvis, N.J., Messing, I., 1995. Near-saturated hydraulic conductivity in soils of contrasting texture as measured by tension infiltrometers. Soil Sci. Soc. Am. J., 59, 27–34.

Kosugi, K.I., Hopmans, J.W., Dane, J.H., 2002. Water retention and storage: Parametric models. In: Dane, J.H., Topp, G.C. (Eds.): Methods of Soil Analysis, Part 1. SSSA Book Ser. 4, Madison, WI, pp. 739–757.

Lassabatere, L., Yilmaz, D., Peyrard, X., Peyneau, P.E., Lenoir, T., Simunek, J., Angulo-Jaramillo, R., 2014. New analytical model for cumulative infiltration into dual-permeability soils. Vadose Zone J., 13, 15pp. DOI: 10.2136/vzj2013.10.0181.

Larsbo, M., Jarvis, N., 2006. Information content of measurements from tracer microlysimeter experiments designed for parameter identification in dual-permeability models. J. Hydrol., 325, 273–287.

Lazarovitch, N., Ben-Gal, A., Simunek, J., Shani, U., 2007. Uniqueness of soil hydraulic parameters determined by a combined Wooding inverse approach. Soil Sci. Soc. Am. J., 71, 860–865.

Leij, F.J., Alves, W.J., van Genuchten, M.Th, Williams, J.P., 1996. The UNSODA unsaturated soil hydraulic database, version 1.0, EPA report EPA/600/R-96/095, EPA National Risk Management Laboratory, G-72, Cincinnati, OH.

Leij, F.J., Russel, W.B., Lesch, S.M., 1997. Closed-form expressions for water retention and conductivity data. Ground Water, 35, 5, 848–858.

Mualem, Y., 1976. New model for predicting hydraulic conductivity of unsaturated porous media. Water Resour. Res., 12, 513–522.

Nemes, A., Schaap, M.G., Leij, F.J., Wosten, J.H.M., 2001. Description of the unsaturated soil hydraulic database UNSODA version 2.0, J. Hydrol., 251, 151–162.

Perret, J., Prasher, S.O., Kantzas, A., Langford, C., 1999. Three-dimensional quantification of macropore networks in undisturbed soil cores. Soil Sci. Soc. Am. J., 63, 1530–1543.

Peters, A., Durner, W., 2008. A simple model for describing hydraulic conductivity in unsaturated porous media accounting for film and capillary flow. Water Resour. Res., 44, W11417. DOI: 10.1029/2008WR007136.

Philip, J.R., 1969. Theory of infiltration. Adv. Hydrosci., 5, 215–296. DOI: 10.1016/B978-1-4831-9936-8.50010-6.

Philip, J.R., 1986. Linearized unsteady multidimensional infiltration. Water Resour. Res., 22, 1717–1727.

Poulsen, T.G., Moldrop, P., Yamaguchi, T., Jacobsen, O.H., 1999. Predicting saturated and unsaturated hydraulic conductivity in undisturbed soils from soil water characteristics. Soil Sci., 164, 877–887.

Raats, P.A.C., Gardner, W.R., 1971. Comparison of empirical relationships between pressure head and hydraulic conductivity and some observations on radially symmetric flow. Water Resour. Res., 7, 921–928.

Russo, D., 1988. Determining soil hydraulic properties by parameter estimation: On the selection of a model for the hydraulic properties. Water Resour. Res., 24, 453–459.

Reynolds, W.D., Elrick, D.E., Clothier, B.E., 1985. The constant head well permeameter: Effect of unsaturated flow. Soil Sci., 139, 172–180. DOI: 10.1097/00010694-198502000-00011.

Reynolds, W.D., Elrick, D.E., 1990. Ponded infiltration from a single ring: I. Analysis of steady flow. Soil Sci. Soc. Am. J., 54, 1233–1241.

Reynolds, W.D., 2008a. Saturated hydraulic properties: Ring infiltrometer. In: Carter M.R., Gregorich E.G. (Eds.): Soil Sampling and Methods of Analysis. 2nd ed. CRC Press, Boca Raton, FL, pp. 1043–1056.

Reynolds, W.D., 2008b. Unsaturated hydraulic properties: Field tension infiltrometer. In: Carter, M.R., Gregorich, E.G. (Eds.): Soil Sampling and Methods of Analysis. 2nd ed., CRC Press, Boca Raton, FL, pp. 1107–1127.

Reynolds, W.D., 2008c. Saturate4d hydraulic properties: Well permeameter, In: Carter, M.R., Gregorich, E.G. (Eds.): Soil Sampling and Methods of Analysis. 2nd ed., CRC Press, Boca Raton, FL, pp. 1025–1042.

Reynolds, W.D., 2011. Measuring soil hydraulic properties using a cased borehole permeameter: Falling-head analysis. Vadose Zone J., 10, 999–1015. DOI: 10.2136/vzj2010.0145.

Reynolds, W.D., 2016. A unified Perc Test-well permeameter methodology for absorption field investigations. Geoderma, 264, 160–170. http://dx.doi.org/10.1016/j.geoderma.2015.10.015

Schaap, M.G., Leij, F.J., 1998. Using neural networks to predict soil water retention and soil hydraulic conductivity. Soil & Tillage Research, 47, 37–42.

Schaap, M.G., Leij, F.J., 2000. Improved prediction of unsaturated hydraulic conductivity with the Mualem-van Genuchten model. Soil Sci. Soc. Am. J., 64, 843–851.

Schaap, M.G., van Genuchten, M.Th., 2006. A modified Mualem-van Genuchten formulation for improved description of the hydraulic conductivity near saturation. Vadose Zone J., 5, 27–34.

van Genuchten, M.Th., 1980. A closed-form equation for predicting the hydraulic conductivity in unsaturated soils. Soil Sci. Soc. Am. J., 44, 892–898.

van Genuchten, M.Th., Nielsen, D.R., 1985. On describing and predicting the hydraulic properties of unsaturated soils. Annales Geophysicae, 3, 615–628.

Vandervaere, J.-P., 2002. Unsaturated water transmission parameters obtained from infiltration: Three-dimensional infiltration using disk permeameters: Early-time observations, In: Dane, J.H., Topp G.C. (Eds.): Methods of Soil Analysis, Part 1, SSSA Book Ser. 4, Madison, WI.

Vogel, T., van Genuchten, M.Th., Cislerova, M., 2001. Effect of the shape of the soil hydraulic functions near saturation on variably-saturated flow predictions. Advances in Water Resources, 24, 133–144.

Vereecken, H.J., Maes, Feyen, J., 1990. Estimating unsaturated hydraulic conductivity from easily measured soil properties. Soil Sci., 149, 1–12.

Vereecken, H., Weynants, M., Javaux, M., Pachepsky, Y., Schaap, M.G., van Genuchten, M.Th., 2010. Using pedotransfer functions to estimate the van Genuchten-Mualem soil hydraulic properties: A review. Vadose Zone J., 9, 1–26.

Bereitgestellt von University Library Bratislava | Heruntergeladen 31.01.20 12:23 UTC

Warrick, A.W., 1974. Time-dependent linearized infiltration. I. Point sources. Soil Sci. Soc. Am. Proc., 38, 383–386. DOI: 10.2136/sssaj1974.03615995003800030008x.

Weynants, M., Vereecken, H., Javaux, M., 2009. Revisiting Vereecken pedotransfer functions: Introducing a closed-form hydraulic model. Vadose Zone J., 8, 86–95. DOI: 10.2136/vzj2008.0062.

White, I., Sully, M.J., 1987. Macroscopic and microscopic capillary length and time scales from field infiltration. Water Resour. Res., 23, 1514–1522.

Wind, G.P., 1955. Field experiment concerning capillary rise of moisture in heavy clay soil. Neth. J. Agric. Sci., 3, 60–69.

Wooding, R.A., 1968. Steady infiltration from a shallow circular pond. Water Resour. Res., 4, 1259–1273.

Wösten, J.H.M., Pachepsky, Y.A., Rawls, W.J., 2001. Pedotransfer functions: Bridging the gap between available basic soil data and missing soil hydraulic characteristics. J. Hydrol., 251, 123–150.

Received 7 December 2018
Accepted 27 March 2019

Bereitgestellt von University Library Bratislava | Heruntergeladen 31.01.20 12:23 UTC

J. Hydrol. Hydromech., 67, 2019, 4, 372–383
DOI: 10.2478/johh-2019-0009

Computational and experimental pore-scale studies of a carbonate rock sample

William Godoy[1*], Elizabeth M. Pontedeiro[1, 2], Fernanda Hoerlle[1], Amir Raoof[2], Martinus Th. van Genuchten[2, 3], José Santiago[1], Paulo Couto[1]

[1] Civil Engineering Program – PEC/COPPE – LRAP, Federal University of Rio de Janeiro, Rio de Janeiro, Brazil.
[2] Department of Earth Sciences, Utrecht University, Utrecht, The Netherlands.
[3] Center for Environmental Studies, CEA, São Paulo University, UNESP, Rio Claro, SP, Brazil.
[*] Corresponding author. E-mail: wmgodoy@petroleo.ufrj.br

Abstract: Carbonate rocks host several large water and hydrocarbon reservoirs worldwide, some of them highly heterogeneous involving complex pore systems. Pre-salt reservoirs in the Santos Basin off the south-east coast of Brazil, are an example of such rocks, with much attention focused on proper characterization of their petrophysical and multiphase flow properties. Since it is very difficult to obtain rock samples (coquinas) from these very deep reservoirs, analogues from north-eastern Brazil are often used because of very similar geological age and petrophysical properties. We used a coquina plug from an outcrop in a quarry in northeast Brazil to perform a comprehensive set of analyses. They included Scanning Electron Microscopy (SEM), Energy-Dispersive X-ray Spectroscopy (EDS), X-ray Diffraction (XRD), and micro-computed tomography (μCT) image acquisition using a series of pixel sizes, as well as direct permeability/porosity measurements. Some of the experimental data were collected from the plug itself, and some from a small sample of the rock slab, including thin sections. Results included the carbonate rock composition and the pore system at different scales, thus allowing us to reconstruct and model the porosity and absolute permeability of the coquina using 3D digital imaging and numerical simulations with pore network models (PNMs). The experimental and numerical data provided critical information about the well-connected pore network of the coquina, thereby facilitating improved predictions of fluid flow through the sample, with as ultimate objective to improve hydrocarbon recovery procedures.

Keywords: Pore network modeling; Carbonate rock; Coquina; Absolute permeability; μCT.

INTRODUCTION

Carbonate rocks host about 50% of worldwide hydrocarbon reserves (Vik et al., 2013). In Brazil, the pre-salt carbonate reservoirs accounted for 50% of total national oil production in 2018 (ANP, 2018). Although the annual production from the pre-salt reservoirs is increasing constantly, there are several challenges regarding their geological and petrophysical characterization (Corbett et al., 2017; Luna et al., 2016), as well as quantifying multiphase flow in their pore systems (Corbett et al., 2016). This because of the extremely heterogeneous nature of many carbonate rocks. One challenge of the pre-salt reservoirs is the difficulty to obtain samples for purposes of geological, sedimentological and petrophysical characterization. An alternative is to use analogue samples that are geologically similar to the pre-salt reservoir rocks (Corbett et al., 2016). For this many have used carbonate rocks samples from an outcrop in the northeast region of Brazil (Azambuja Filho et al., 1998), mostly to study their porosity and permeability properties. These samples, called coquinas (Tavares et al., 2015), contain large amounts of shells and as such exhibit considerable heterogeneity and anisotropy.

In order to study the petrophysical properties of carbonate rocks, with special focus on their pore networks, non-destructive visualization techniques such as X-ray computed microtomography, μCT (Blunt, 2001; Bultreys et al., 2015; Cnudde and Boone, 2013; Dal Ferro et al., 2013; Wildenschild and Sheppard, 2013) and scanning electron microscopy, SEM (de Boever et al., 2015; Fäy-Gomord et al., 2017; Hemes et al., 2015), have been widely used. Energy-dispersive X-ray spectroscopy (EDS) is also used often for qualitative (Goldstein et al., 2003) and even quantitative (Newbury and Ritchie, 2013) analyses of the composition of different rocks and soils. Although destructive, energy-dispersive X-ray diffraction (XRD) techniques are similarly important for qualitative/quantitative analyses (Hillier, 1994).

In our work we used μCT as an excellent non-invasive method for characterizing and quantifying rock structures and studying dynamic pore-scale processes. Digital reconstructions of image stacks are then used to represent the internal structure of a coquina sample, thereby providing connections between the different pores (i.e., pore bodies and throats) in a pore network, leading to a quantitative understanding of fluid behavior in the sample. An extremely important step after acquiring μCT images is the processing of generated data. This processing step can be done using one or more filters (e.g., anisotropic diffusion and/or non-local means filters) to correct and enhance the quality of the images. Non-local means filters (Buades et al., 2005) are especially popular when working with images of heterogeneous carbonate rocks (e.g., Shah et al., 2015).

Subsequent to treatment of the images using one or more filters, a segmentation step is needed to isolate the pore system from the rock matrix, thus allowing their digital reconstruction. Segmentation can be done using different algorithms (automated methods) or by direct analysis using optical microscopy or SEM (manual procedures), thus allowing one to separate between the pore spaces and the solid rock matrix (Al-Raoush and Willson, 2005; Wildenschild et al., 2002). The use of thin sections impregnated with blue epoxy resin helps to more accurately identify pore spaces, especially for detecting the intraparticle porosity of coquina samples. Although the use of visual segmentation methods requires some experience, they often improve the selection of regions where meso- and macro-pores are dominant, among other applications. The use of SEM as an auxiliary tool also guarantees the possibility of visualizing, with high resolution, regions that may become indistinct in μCT images generated with larger pixel sizes (Blunt et al., 2013; Bultreys et al., 2016). Several automated methods for segmen-

Bereitgestellt von University Library Bratislava | Heruntergeladen 31.01.20 12:23 UTC

tation are now available for different types of images (Andrä et al., 2013; Iassonov et al., 2009; Sezgin and Sankur, 2004).

After segmentation and subsequent skeletonization to define the pore structure in terms of pore bodies and pore throats, various approaches can be used for modeling the absolute permeability and related pore-scale transport processes. These include methods for solving the Navier–Stokes equations (or simplifications thereof), including Lattice Boltzmann methods (Jafari et al., 2011; Ramstad et al., 2010), traditional mesh-based computational fluid dynamics approaches (e.g., finite difference, finite volume and finite element methods) as described by Thijssen (2007) among others, as wll as pore network modeling (PNM) and related techniques (Blunt et al., 2013; Bultreys et al., 2015; Joekar-Niasar and Hassanizadeh, 2012; Raoof et al., 2013).

Several alternative approaches are available to estimate the absolute permeability from pore space characteristics, such as effective-medium approximations, EMAs (Doyen, 1988; Ghanbarian et al., 2018) and critical path analyses, CPAs (Ghanbarian et al., 2016; Katz and Thompson, 1986) techniques. The main difference between EMA and CPA techniques refers to the pore-throat size distribution: EMA approaches are better suited for media having relatively narrow pore-throat size distributions, while CPA techniques are best used for more heterogeneous media having broader pore-throat distributions (e.g., Ghanbarian et al., 2018).

Specific objectives of this study were to generate and study the pore-scale network of a real coquina plug using experimental and digital data, and to perform numerical fluid flow simulations based on porous networks based on 3D X-ray microtomography images obtained using different pixel sizes. Experimental data obtained for the plug and rock slab (taken from the same plug) using different techniques (permeameter/porosimeter, SEM-EDS and XRD measurements) were analyzed to improve identification of the pore system and the composition of the rock material. Our main objective was to construct the pore structure of a real coquina sample that serves as a geologically analogue of a Brazilian pre-salt reservoir rock, using experimental data, geological information, 3D modeling, and numerical simulation to identify and understand the main parameters that influence reconstruction of the pore system, which will allow us to simulate fluid flow and transport within the medium with good correlation with real data.

MATERIALS AND METHODS

In this section we provide a geologic description of the area where the carbonate rock sample for our study was taken, as well as its characterization regarding the pore system and mineralogical composition. Based on this information, we provide details about the digital reconstruction of its pore system and a brief description of the pore-scale network modeling approach used to estimate absolute permeability values.

Carbonate rock sample description and preparation

The carbonate rock sample selected for our study was taken from an outcrop of the Morro do Chaves Formation in the Sergipe-Alagoas Basin in north-east Brazil. The coquina samples from this site are close analogues in terms of porosity and permeability of coquinas taken from the pre-salt hydrocarbon reservoirs off the coast of south-east Brazil, such as the presence of well-connected meso- and macro-pores ranging from few micrometers up to several millimeters. The Sergipe-Alagoas Basin is located in the Brazilian states of Sergipe and Alagoas, and with a small portion in the state of Pernambuco Brazil (Fig. 1). Although the basins of Sergipe and Alagoas exhibit important differences in terms of their structure and stratigraphy (Thompson et al., 2015), it is possible to define the Sergipe-Alagoas Basin as a single entity (Campos Neto et al., 2007). The basin is known in that its outcrops include all sections of the Brazilian continental margin, with a total estimated area of over 44,000 km². According to Campos Neto et al. (2007), the evolution of this basin is related to the separation of the Gondwana continent, with its subsidence occurring in the Rifte phase. At this stage the first tectonic pulse occurred, which commenced a sedimentary sequence during which the Morro do Chaves Formation was generated.

The Morro do Chaves Formation is defined by Azambuja Filho et al. (1998) as a carbonate succession that is interspersed with siliciclastic rocks of the Coqueiro Seco and Rio Pitanga formations. Located in the municipality of São Miguel dos Campos, in the state of Alagoas, the Morro do Chaves Formation currently corresponds to a quarry (mine) called Mina São Sebastião (Fig 1). The coquinas were formed by bivalves and non-marine ostracodes with varying percentages of terrigenous deposits. As detailed by Tavares et al. (2015), shells have different sizes and degrees of fragmentation, with facies in some cases containing bivalves in living or articulated positions. They noted that coquinas from Morro do Chaves have calcite as the main mineralogical component, while containing mostly mollusc shells. The rock matrix is composed of clay, siliciclastic sand (mainly quartz), as well as some lithoclasts of igneous, sedimentary and metamorphic rocks. According Tavares et al. (2015), six lithofacies can be identified in the

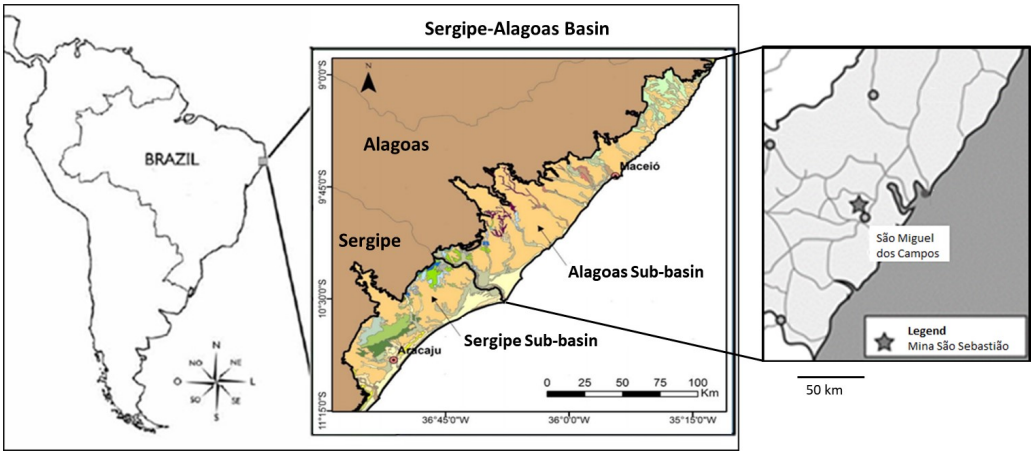

Fig. 1. Location of the Sergipe-Alagoas Basin, in the northeast region of Brazil, identifying the constituent sub-basins and the location of the quarry called Mina São Sebastião (in the city of São Miguel dos Campos), where the Morro do Chaves Formation is located.

Bereitgestellt von University Library Bratislava | Heruntergeladen 31.01.20 12:23 UTC

Morro do Chaves Formation, using both taphonomic (for shell fragmentation) and compositional (for the presence of micrite and siliciclastic sand) criteria.

A well-studied layer (Corbett et al., 2016; Luna et al., 2016) in the Morro do Chaves Formation (Fig. 2a), called Bed 2B (Fig. 2b) was selected. Corbett et al. (2016) pointed out that it is possible to use cross-stratification as evidence that the coquinas in this layer were deposited lakewards or lagoonwards as accreting bioclastic bars. A plug from that layer (Fig. 2b), designated as plug 1-34A (Fig. 2c), was selected for our study. The plug was prepared, flattened (top and bottom), cleaned with methanol and toluene, and placed in an oven at 60°C for 24 hours. The cleaning and drying processes were the same as adopted by Corbett et al. (2017), without needing a humidity-controlled drying environment since the carbonate sample did not contain gypsum or solid hydrocarbon-like gilsonite or pyrobitumen. After preparation and cleaning, the plug was approximately 35 mm in diameter and 35 mm in length. Porosity and absolute permeability measurements were performed in the laboratory using a Wheaterford DV-4000® gas porosimeter/permeater, while the porosity was measured using Helium (He) gas and the absolute permeability using Nitrogen gas (N_2). The equipment had a reliable range between 0.001 mD and 40,000 mD for absolute permeability measurements. We also measured the pore volume, grain density, mass, length and the actual diameter.

A 30-μm thick thin section having dimensions of 70 mm × 45 mm (Fig. 2d) was prepared, as well as a rock slab (Fig. 2e), from the cuts (top and bottom) of plug 1-34A after flattening of the surface of the sample. During preparation of the rock slab, a region of 10 mm × 10 mm and 5 mm thickness (red region in Fig. 2e) was selected, cut, and then used to obtain various data. We used SEM to characterize the surface and to visualize the chosen pore spaces, and EDS for qualitative analysis and identification of the main elements composing the surface. SEM was performed in a Hitachi TM3030® Plus low vacuum atmosphere and an acceleration voltage of 1.5 kV, and EDS using a Bruker XFlash® MIN SVE detector. The same region (shown in red in Fig. 2e) was used to acquire μCT images using smaller pixel sizes (of 6.77 and 9.97μm).

The remaining material after preparing the rock slab was powdered and taken for analysis using XRD techniques. Pulverization was carried out in an agate grinding mill followed by micronization in a McCrone mill. The powdered material weighted around 2.0 grams. XRD analyses were performed in a Bruker D8® Advanced diffractometer using the following test conditions: Cu tube, 40 kV nominal voltage and 40 mA current, Soller slit 2.5°, primary slit 0.6 mm, secondary slit 5mm, LINXEYE® linear detector with opening of 189 channels, Ni of 0.02mm, step size of 0.02 and speed of 1.1° / min. Qualitative mineralogical analyses were done with Jade 9 software (with PDF-2 database). Quantitative analyses were carried out using the Rietveld Method within the TOPAS software.

X-ray computed microtomography

We used a Bruker X-ray computed microtomography Skyscan® model 1173 with a sealed X-ray source, tungsten target and a flat panel detector. The X-ray tube with tungsten filaments (Hamammatsu, model L9181) operates effectively between 40 and 130 kV voltages with a maximum current of 200 μA, reaching a maximum power of 8 W and a maximum focal size of 5 μm (Machado et al., 2016). The detection system (Hamammatsu model C7942SK-05) consisted of a flat-panel sensor, operated with a maximum pixel array of 2240 x 2240, and with its recording carried out by an array of photodiodes forming electrical and digital signals.

Because of the large size of the plug, the size of the obtained pixel was approximately 9.97 μm. This value is the maximum supported by the equipment given the dimensions of the entire plug to perform the acquisition and reconstruction at feasible times (approximately 360 min for acquisition and 420 min for reconstruction of the 9.97 μm pixel size μCT images involving a stack of images with 3,749 slices). For our study we obtained several μCT images with pixel sizes of 9.97 μm, 18.17 μm, and 24.95 μm. The rock slab X-ray microtomography provided

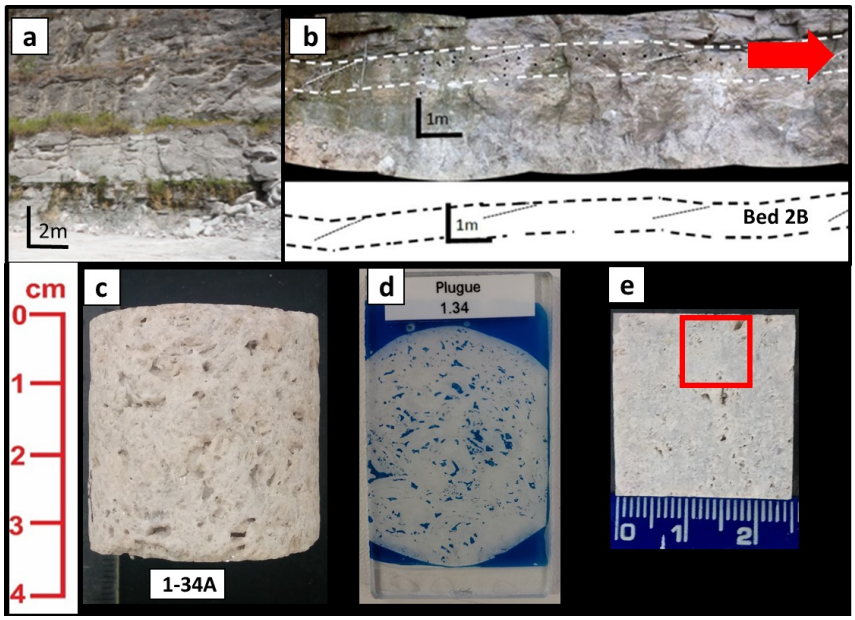

Fig. 2. (a) Image of the Morro do Chaves Formation in the Mina São Sebastião quarry of the city of São Miguel dos Campos; (b) identification of a layer (called Bed 2B) highlighted by the red arrow, from which the sample (named 1-34A) was taken; (c) image of the plug showing some vugular porosity in the sample; (d) thin section obtained from the cut of one end of the sample during flattening; and (e) rock slab prepared from the thin section, with the red square showing the region that was analyzed using SEM-EDS, XRD, and μCT with higher resolution.

Bereitgestellt von University Library Bratislava | Heruntergeladen 31.01.20 12:23 UTC

images with 6.77 µm pixel size, close to the maximum limit supported by the equipment, and 9.97 µm pixel size images. The selection of 9.97 µm was deliberate since this value represents the smallest pixel size when using the whole plug. The acquisition parameters for the plug and the rock slab, with the different pixel sizes, are listed in Table 1.

After the data acquisition step, it was necessary to use a specific software from the equipment manufacturer, capable of converting information from the detector (based on an analysis of the attenuation suffered by a beam of incident radiation passing through, in this case, a carbonate rock) into data that is interpreted as digital images that can be loaded and interpreted by other software. We used for this purpose the Bruker NRecon® (v.1.6.9.4) and InstaRecon® (v 1.3.9.2) softwares, which allowed us to correct and treat the main image artefacts generated during acquisition, such as beam hardening and the presence of ring artefacts (Table 1). We further used a workstation with 2 Intel® Xeon® E5-2640 v3 processors, 256 Gb RAM, and a NVIDIA® Quadro® M4000 (8 GB RAM) GPU for µCT image acquisition and reconstruction.

Digital reconstruction, image post-processing and segmentation

A first step after µCT image acquisition is the application of specific filters to reduce noise from the images and to sharpen them. We used the Avizo® 9.5 software to pass the non-local means filter (Fig. 3b) and to reconstruct the 3D model of the rock, as well as to segment the image, by means of the *Interactive Thresholding* function (Fig. 3c) after definition of the threshold value.

We next used an algorithm to detect the grey-level value that corresponds to the threshold value based on the selected Kittler and Illingworth (1986) segmentation method. The selected value was supported by analyses of SEM images and the grey-level histogram obtained from the µCT images. Verification of the pore systems impregnated with blue epoxy resin on the thin section was performed using a Zeiss Imager M2m® optical microscope with an increase of 2.5 times. Scanning was done by capturing images in mosaics, which were automatically joined by the microscope itself, resulting in a panoramic image of the entire thin section. Finally, we followed the methodology of Kaczmarczyk et al. (2011) for analysis of the grey value histograms using the Fytik® 0.9.8 software (Wojdyr, 2010) to generate Gaussian curves that represented the population of the pore system and the rock matrix itself. This to verify and evaluate the results by Kittler and Illingworth (1986) based on visual methods. The procedure was repeated for each image stack generated with different pixel sizes. The overlapping pixels were considered as part of the pore system. Imaging, 3D reconstruction, modeling and numerical simulations were carried out using a workstation with 2 Intel® Xeon® E5-2640 v4 processors, 512 Gb RAM, and a NVIDIA® Quadro® P6000 (24 GB RAM) GPU.

Pore network modeling

After reconstruction of the 3D pore system, based on selection of the appropriate threshold value, the connected networks were analyzed to simulate fluid flow using an in-house code based in part on previous work by Raoof et al. (2013). We selected networks based on the size of the clusters (voxel count), since the numerical simulations were carried out assuming connectivity between the top and bottom of the sample (the *z*-axis), being the direction of the experiments with this plug. We kept the same procedure for the rock slab models (reconstructed from different pixel size µCT images). The Avizo® 9.5 software was used to separate the larger networks and to generate topology information for subsequent reconstruction of the PNM. The pore domains were generated based on topology information provided by the software.

Pore bodies of the pore network were identified as the largest elements present in the network, with spherical geometry, while pore throats were identified and calculated based on

Table 1. µCT acquisition and reconstruction parameters.

Image pixel size (µm)	Source voltage (kV)	Current (µA)	Smoothing factor	Ring artefact correction factor	Filter: Al / Cu (mm/mm)
6.77 (rock slab)	70	114	5	5	0.5 / 0.5
9.97 (rock slab)	70	114	6	6	0.5 / 0.5
9.97 (plug)	130	61	5	1	0.5 / 0.5
18.17 (plug)	130	61	3	5	0.5 / 0.5
24.95 (plug)	130	61	7	5	0.5 / 0.5

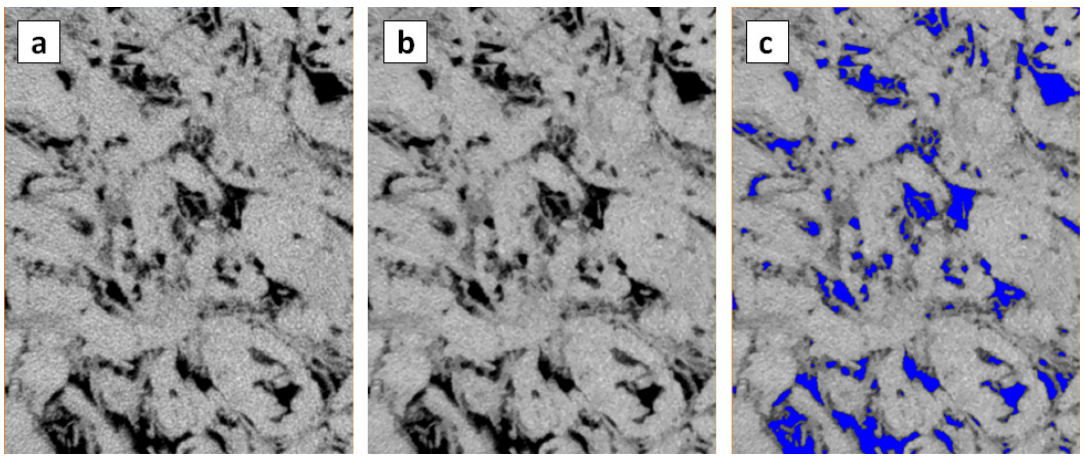

Fig. 3. Main steps related to treatment of (a) an original µCT image using (b) a non-local filter, and (c) interactive thresholding for segmentation purposes from Avizo® 9.5.

Bereitgestellt von University Library Bratislava | Heruntergeladen 31.01.20 12:23 UTC

being smaller spherical elements, depending upon their size and topology, as discussed by Fouard et al. (2006). The length of the pore throats was defined by the distance between two connected pore bodies, while their radii were calculated as a function of the mean radii of the spherical elements along the path between the two pore bodies. We calculated the radii of the pore throats using three different averaging methods: harmonic, geometric, and arithmetic. Absolute permeabilities were calculated using the generated pore structure, while saturated fluid flow within the network domain was simulated using a PNM algorithm.

Since extensive reviews of PNM techniques can be found in the literature (de Vries et al., 2017; Raoof and Hassanizadeh, 2010, 2012; Raoof et al., 2010, 2013), we present here only the main equations. The approach assumes laminar flow within the porous media, using Poiseuille's formula to obtain the volumetric flow rate within each pore:

$$q_{ij} = \frac{\pi}{8\mu} r_{ij}^4 \frac{p_i - p_j}{l_{ij}} \tag{1}$$

where q_{ij} is the discharge through the pore throat between pore bodies i and j; p_i and p_j are pressures of the two adjacent pore bodies; r_{ij} is the pore throat radius; l_{ij} is the throat length, and μ is the fluid dynamic viscosity.

Considering incompressible flow, the volume balance for each pore body i requires:

$$\sum_j^{N_i} q_{ij} = \frac{\pi}{8\mu} \sum_j^{N_i} r_{ij}^4 \frac{p_i - p_j}{l_{ij}} = 0 \tag{2}$$

where N_i is the pore coordination number of pore i. Applying this equation to each pore body results in a linear system of equations with a sparse, symmetric and positive-definite coefficient matrix, which is to be solved for the pore body pressures.

Next, considering the sample as a representative elementary volume (REV), the average pore water velocity, $\bar{v}$, can be calculated as (Raoof et al., 2013):

$$\bar{v} = \frac{Q_{tot} L}{V_f} \tag{3}$$

where Q_{tot} is the total discharge rate through the pore network, L is the length of the pore network, and V_f is the total volume of the fluid phase within the pore network. The total discharge rate can be calculated at the inlet or outlet of the pore network as the sum of all fluxes. Finally, the intrinsic permeability, k, of the sample can be determined using Darcy's law using the results from (3):

$$k = \frac{\mu Q_{tot} L}{A \Delta P} = \frac{\mu \bar{v} V_f}{A \Delta P} \tag{4}$$

where μ is the fluid dynamic viscosity, ΔP is the pressure difference between the inlet and outlet pores, and A is the cross-sectional area of the pore network.

For our study we imposed a pressure differential of 5.0×10^{-3} Pa between the upper and lower boundaries of the PNM along the z-axis. This small differential was adopted to guarantee laminar flow (low Reynolds number), an important assumption to solve Eqs. (1) to (4).

RESULTS AND DISCUSSION

Before presenting results of the various pore network calculations for the entire coquina plug, we first summarize data from the experimental tests, as well as results from the rock slab pore network numerical simulations.

Experimental data

The first results for the plug were obtained using the DV-4000® equipment, after the cutting, flattening and cleaning procedures. The measured values were used for comparison with estimates obtained digitally and numerically for the porosity and absolute permeability, respectively. Table 2 presents the main experimental results for plug 1-34A. The data are indicative of groundwater reservoirs, which generally have a relatively high porosity (15–20%) and an intermediate permeability (150–650 mD), with relatively good connectivity between the various pores.

After this step we analyzed images of the thin section for the purpose of characterizing and identifying the coquina pore system. Fig. 4 shows images obtained with optical microscopy. The images show that the rock is formed by fragments of robust shells (Fig 4b), with the bioclast fragments varying in size from 1 to 8 mm. The bioclasts are oriented moderately, with little fragmentation and only slight abrasion. A very few (about 2%) siliciclastic grains were observed, sub-rounded, spherical and with an average size of 0.5 mm.

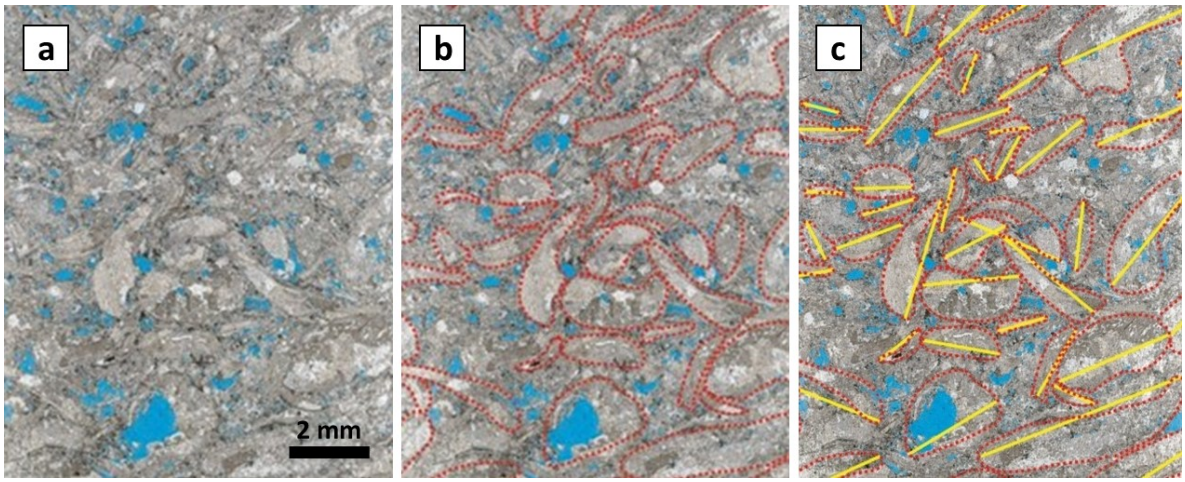

Fig. 4. Scanned images obtained with optical microscopy showing (a) blue epoxy resin filling the pores of the thin section, (b) highlighted in red the contours of bivalve shells, and (c) highlighted in yellow the size of the bivalve shells.

Bereitgestellt von University Library Bratislava | Heruntergeladen 31.01.20 12:23 UTC

Several dissolution phases generated the current porosity of the selected sample. The types of porosity present are intraparticle, interparticle, vugular and intercrystalline, with a predominance of interparticle and vugular porosities, and lower intraparticle porosities. The measured porosity and absolute permeability indicate good connectivity between the meso- and macro-pores. This information is important not only to aid in the segmentation step, but also to predict the absolute permeability through numerical simulations. The results suggest that fluid will flow preferably through pore spaces that can be reconstructed digitally, disregarding sub-resolution porosity that is identified using high-resolution images from very small sample volumes. Rabbani et al. (2017) recently estimated the absolute permeability from an analysis of thin sections, but their approach could not predict the behavior of carbonate rock samples having absolute permeabilities above 200 mD. For this reason we did not predict the permeability of our coquina based on an analysis of thin sections since the permeability was more than 600 mD.

SEM was used next to analyze the surface of the selected cut of the rock slab (red region in Fig. 2e) in order to evaluate the characteristics and dimensions of different pore structures. We selected a central area of the cut, which constituted the inner part of a bivalve shell. The images in Fig. 5 show a gradual zoom of this region, with increases of 50, 150, 300, 800, 1200 and 2000 times the original size. Fig. 5a shows the presence of several large pores in the order of a few millimeters, externally to the center of the bivalve, while the largest zoom shows pores larger than 30 µm (Fig. 5f). These observations suggest that optical microscope analyses of the thin section were consistent since they showed the same patterns: predominance of interparticle and vugular porosities in different regions. These results are important to understand the main aspects related to the pore size distribution and the connectivity of these pore systems.

Several regions were particularly challenging for analyzing the pore system and the rock composition. We selected a southern region from the cut rock slab to perform an EDS analysis. The analysis helped us to evaluate dubious regions, which could be interpreted visually as pores or as material with a lower attenuation coefficient in the µCT images, as well as providing a qualitative indication of the elements presented in the sample. Fig. 6a shows three well-identified regions (represented by the letters A, B and C above the arrows, in the image). The yellow arrow (A) indicates a pore that is a few mm wide, while the red arrow (B) points to a well-defined pore (in the center) surrounded by a region that is more poorly defined. That region has a grey-level quite similar to that of the area in blue (C), which clearly does not correspond to a pore. The EDS allowed us to identify the latter region (C) as being composed of siliciclastic material (Fig. 6d), which was already identified in the thin section.

Fig. 6b provides a qualitative analysis using different colors indicating the main components of the sample: a blue area in the center and a predominantly pink region throughout the remaining area. A more refined analysis revealed the presence of calcium (Fig. 6c), silicon (Fig. 6d), oxygen (Fig. 6e) and carbon (Fig. 6f). Results suggest that the studied rock is composed mainly of calcium, oxygen and carbon (most likely $CaCO_3$), indicating that the coquina was probably formed by calcite as previously shown by Tavares et al. (2015) from evaluations of coquinas from the same Morro do Chaves formation.

In order to confirm the results above, an XRD-based qualitative and quantitative mineralogical analysis of the rock slab was performed using the Jade 9 software (with the PDF-2 database), and also with the Rietveld Method of the TOPAS software, respectively. The composition was defined as 99.8% calcite ($CaCO_3$), thus corroborating the EDS results. Another important result of the XRD analysis was that the grey-level regions associated with the siliciclastic materials were not significant in size, and not representative, thus reducing uncertainties in the automated segmentation procedure. These evaluations are important to verify possible grey level regions where the pore system may be interpreted erroneously during segmentation.

Coquina rock slab modeling

Based on insight from the experimental data, we proceeded with modeling the selected rock slab region. The µCT images of the thin section showed the presence of clear vugular porosity, as well as some intraparticle porosity. Fig. 7a shows the selected region (red square) that was used for the SEM, EDS and µCT images using two different pixel sizes, whose 3D reconstruction can be observed in Fig. 7b. The 3D reconstructions of the pore systems from the 6.77 µm (Fig. 7c) and

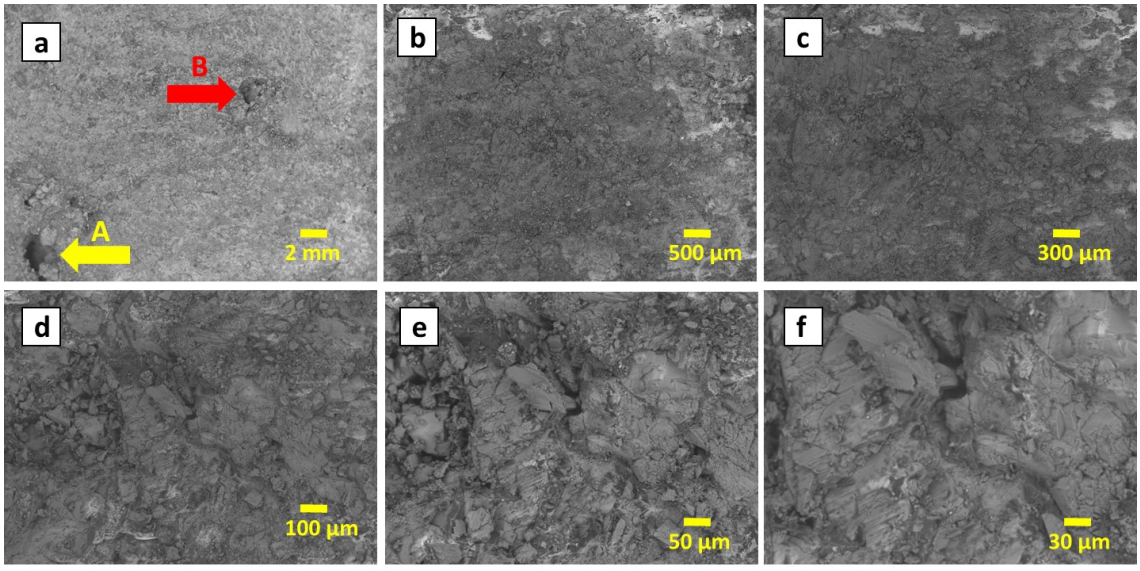

Fig. 5. SEM images obtained with an increase of (a) 50; (b) 150; (c) 300; (d) 800; (e) 1200, and (f) 2000 times the selected region of the rock slab. Fig. 5a shows the presence of two large pores of a few millimeter each (A and B).

Bereitgestellt von University Library Bratislava | Heruntergeladen 31.01.20 12:23 UTC

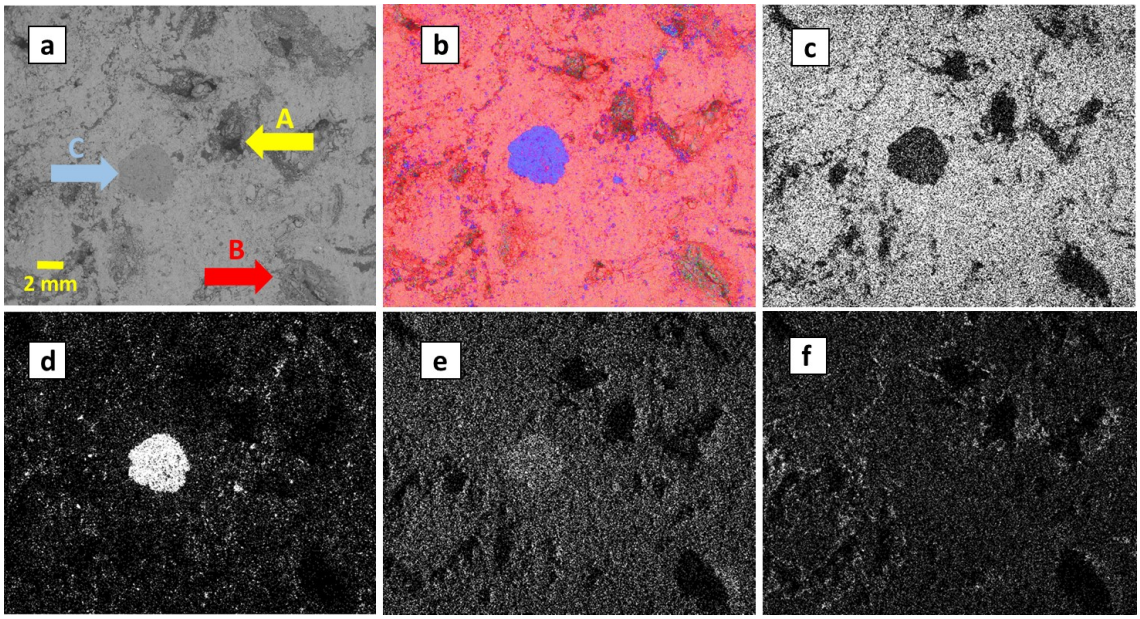

Fig. 6. (a) EDS image of the analyzed area, identifying three well-defined regions (A, a well-defined pore, B, a pore-centered region with dark grey level around it, and C, a dark grey level region similar to B but with no obvious pore boundary), (b) visual evaluation (colors) of the different components of the sample; (c) abundant presence of calcium, (d) presence of silicon in a small region (white dots), (e) oxygen, and (f) carbon distributed around the sample.

9.97 μm (Fig. 7d) pixel size μCT images showed that the vug was part of the largest pore system within the rock slab, and close to a region whose contours delimited a bivalve shell. This region showed very little porosity, regardless of the pixel size used for μCT imaging. Digital porosities obtained with the two different pixel sizes are shown in Table 3.

Next, we performed PNM simulations for laminar fluid flow in two digitally reconstructed rock slabs, to obtain the absolute permeability. As shown in Table 3, estimated values were much higher than the measured value of 639 mD data for the entire plug (Table 2). The higher calculated values were to be expected because of the very small rock slab volume used in the μCT analysis. The volume presumably was much smaller than the minimum representative elementary volume (REV) needed for scale-independent permeability measurements (or calculations in this case). By comparison, the rock slab was large enough for the porosity calculations and measurements. We hence emphasize here that the PNM-based permeability estimates we obtained for the modeled rock slabs do not have an immediate direct relationship with the permeability measured using the entire coquina plug. To properly compare the measured absolute permeability of the plug, the PNM model should be applied to the entire plug.

We selected the largest pore systems from each reconstructed model, which are visualized in Fig. 7e (from the 6.77 μm pixel size μCT images) and Fig. 7f (from the 9.97 μm pixel size μCT images). The number of voxel-based clusters in Fig. 6e was higher than that found when we analyzed Fig. 7f, indicating that small clusters (represented by different colors) are only generated from higher-resolution images. Figs. 7g and 7h show the PNMs of the regions discussed previously. A first direct observation refers to the amount of pore bodies and pore throats generated for the construction of the PNMs. For construction of the model imaged with 9.97 μm pixel size, we generated a much smaller number of points (Figs. 8a and 8b), although the topology of the system was maintained.

Some important conclusions can be drawn from the PNM simulations based on different pixel size μCT images. Most important, the results for porosity and absolute permeability were larger for the reconstructed model using higher resolution μCT images (6.77 μm), thus suggesting that some pore bodies and pore throats were not included in the lower resolution μCT images (9.97 μm), which must have influenced the numerical estimates. Differences between the absolute permeability values varied between 11.8% and 22.2%, considering the different averages for pore-throat construction in each model. The pore throat radii based on harmonic means of the spherical elements that composed them were physically coherent, since they accounted for regions of constriction prior to modeling the pore throats using the PNM.

Table 2. Experimental results from plug 1-34A.

Sample	Pore Volume (cc)	Porosity He (%)	Permeability N_2 (mD)	Grain Density (g/cc)	Diameter (cm)	Length (cm)	Mass (g)
1-34A	5.74	16.30	639.08	2.69	3.60	3.53	79.3

Table 3. Porosity (ϕ) and absolute permeability (k_{abs}) estimated from the reconstructed coquina rock slab obtained with two different pixel sizes.

PNM – μCT Pixel size images (μm)	ϕ (%)	k_{abs} (mD)		
		Harmonic	Geometric	Arithmetic
6.77	8.43	2,568	2,755	2,984
9.97	7.72	2,137	2,422	2,746
Difference (%)	8.4	16.8	12.1	8.0

Bereitgestellt von University Library Bratislava | Heruntergeladen 31.01.20 12:23 UTC

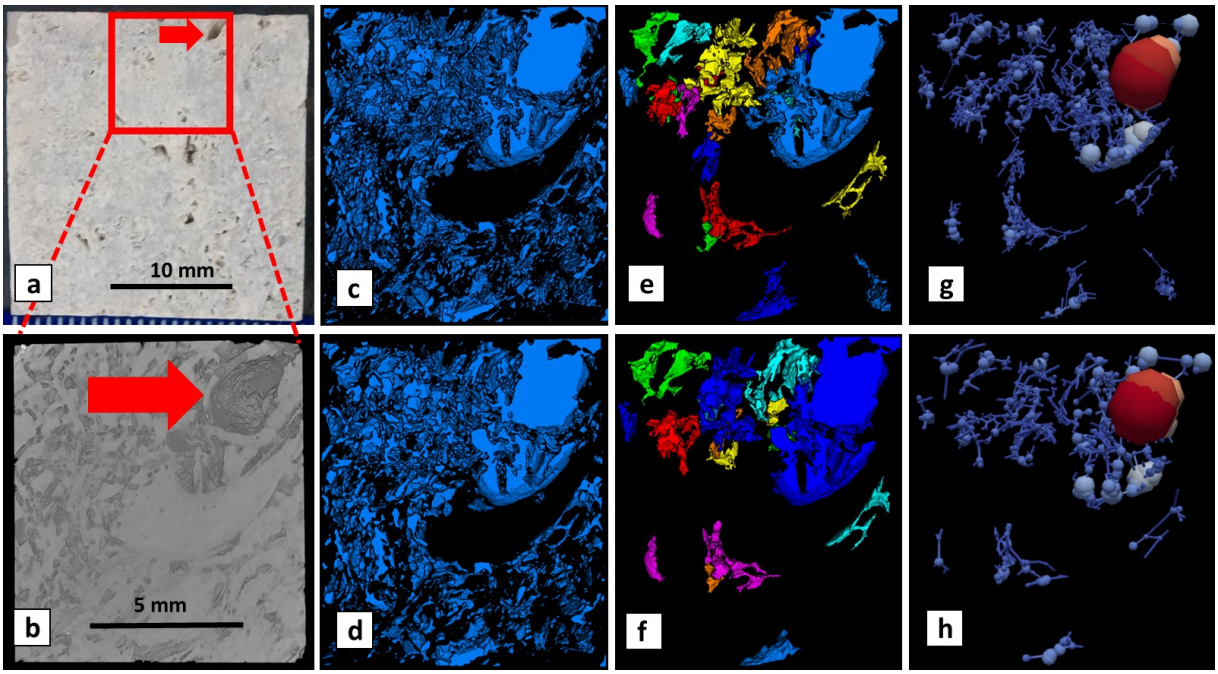

Fig. 7. (a) Image of the selected area for µCT, indicating with a red arrow the presence of vugular porosity; (b) 3D volume reconstruction of the region using 6.77 µm pixel size µCT images, with the red arrow highlighting the same vug as in Fig.6a; (c) 3D segmentation and reconstruction of the pore region of the sample, with the right upper extremity being the assimilated vug and a central region with lower porosity showing well-defined bivalve contours from the 6.77 µm pixel size µCT images; (d) same from the 9.97 µm images (e) selection of the largest pores from the 6.77 µm µCT images; (f) same from the 9.97 µm images; (g) PNM generated with the largest pores from the 6.77 µm pixel size µCT images; and (h) same from the 9.97 µm images.

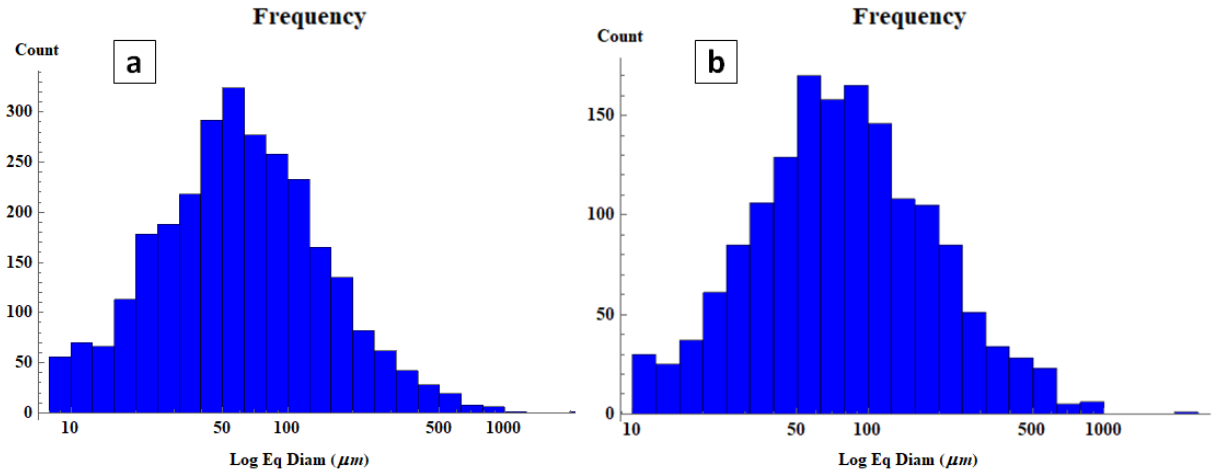

Fig. 8. Pore size frequency distributions (equivalent diameters) of the digital pore system of the rock slab obtained using (a) 6.77 µm and (b) from 9.97 µm µCT images. Notice a much larger number of spherical elements in the reconstructed model using the higher resolution.

An analysis of the region with the greatest pressure differential, which was responsible for most of the fluid flow, is shown in Fig. 9. The plots visualize the length of the pore throats and the radii of the pore bodies for the slab reconstructed PNM using 6.77 µm (Fig. 9a) and 9.97 µm (Fig. 9b) pixel size µCT images as obtained with the Paraview® software (Ayachit, 2015). A larger number of pore bodies and pore throats are apparent when using higher resolution µCT images, which leads to higher absolute permeability values. The images in Fig. 8 were generated from the models whose pore throats were calculated using harmonic means of their constituent spherical elements. The smaller pore throat diameters for both models can be seen in Fig. 9c and Fig. 9d, as well as the pressure (ranging from 0 to 5.0×10^{-3} Pa) in each pore body of this region. The simulation results indicate that fluid in this rock slab flows preferably through the mesopores and macropores.

Coquina plug modeling

After analysis of the rock slab, we similarly performed an analysis of the coquina plug in its entirety. Our objective was to estimate its petrophysical properties as well as to study PNM performance for a heterogeneous and complex pore system involving a large number of mesopores and macropores. We selected for this purpose the µCT images generated using three different pixel sizes of 9.97, 18.17, and 24.95 µm, thus testing the effects of resolution on the calculated parameters. Table 4 presents results of the 3D modeling scenarios and the experimental data of the selected petrophysical properties. Regarding porosity, the pore network reconstructed with higher resolution µCT images clearly presented better results when comparing the digital estimates to the measured data in Table 1. The same is true for the absolute permeability estimates using PNM.

Bereitgestellt von University Library Bratislava | Heruntergeladen 31.01.20 12:23 UTC

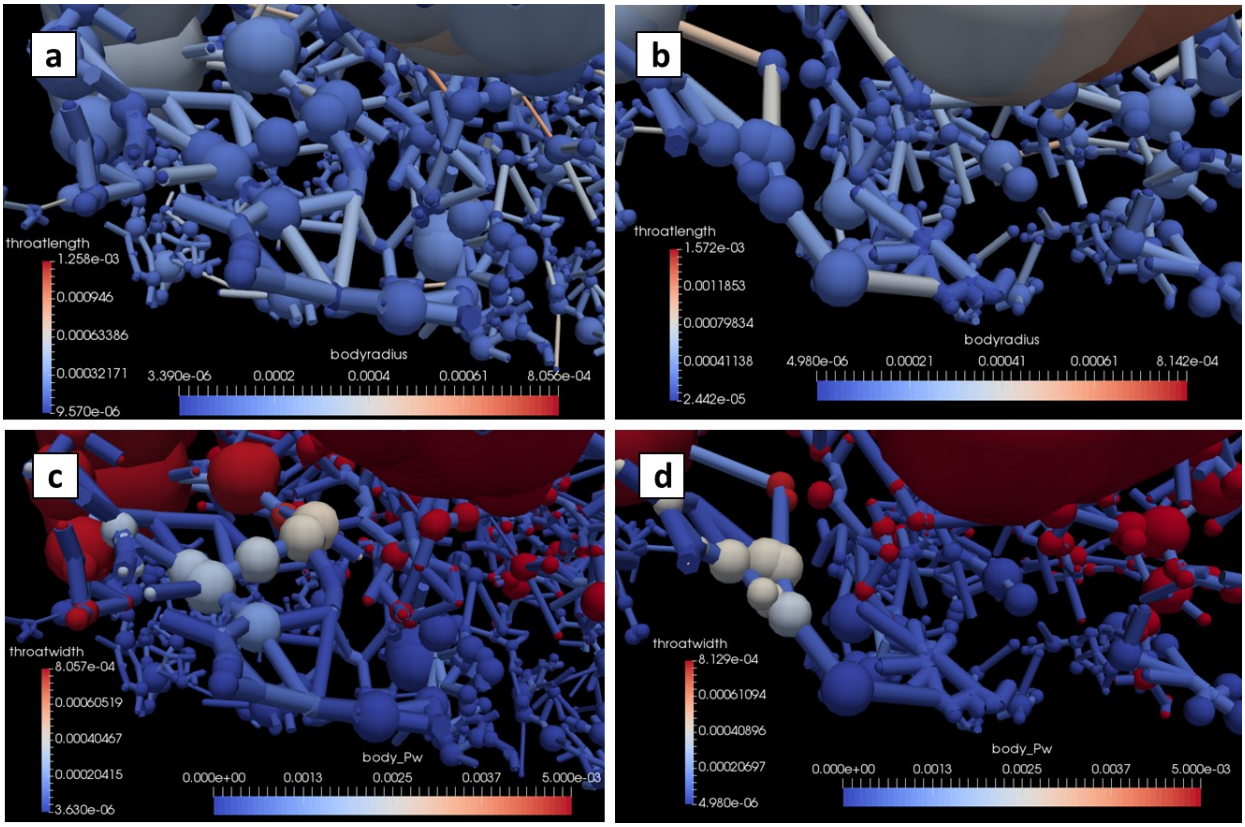

Fig. 9. PNMs of the reconstructed slab (a) from the 6.77 μm pixel size μCT images, and (b) from the 9.97 μm images, showing the distributions of pore radii and pore lengths. PNMs of the regions with greater pressure differentials between pore bodies following numerical simulation of fluid flow, as well as of the diameters of the pore throats in these regions, using (c) 6.77 μm pixel size μCT images and (d) 9.97 μm images. The length and pressure units are m and Pa, respectively.

Table 4. Porosity (ϕ) and absolute permeability (k_{abs}) of the reconstructed coquina plug using PNM.

PNM – μCT Pixel size images (μm)	ϕ (%)	k_{abs} (mD)		
		Harmonic	Geometric	Arithmetic
9.97	12.4	548.3	953.9	1,236.9
18.17	11.3	480.5	911.5	1,419.0
24.95	10.0	464.9	848.4	1,283.9
Experimental	16.3	639.1		

Another important point refers to the average used to calculate the pore throats, based on the spherical elements that do not represent pore bodies on the models. Harmonic averaging gave the best results compared to the measured data, presenting a percentual difference of 14.2%, 24.8%, and 27.3% for the PNM based results using μCT images with 9.97μm, 18.17μm, and 24.95 μm pixel size, respectively. We note here that the comparison between the PNM and the measured data for the entire plug does not require some REV verification since the experimental results were measured also on the entire plug.

Fig. 10 shows frequency distributions of the generated pore throats and pore bodies. The results indicate that the total number of pore bodies and pore throats for the model using higher resolution μCT images is more than 60 times larger than obtained with the lower resolution μCT images. This impressive increase relates to the capacity to recreate pore bodies and pore throats that are not detectable from lower resolution μCT images, as can be seen in Fig. 10d, 10e, and 10f, which presents the range of pore throat radii (in m) for the models based on μCT images with 9.97 μm, 18.17 μm, and 24.95 μm, respectively.

We next present PNM results for plug I-34A obtained with the intermediate resolution (18.17 μm pixel size μCT images) and assuming the harmonic averages of the pore throats as shown in Fig. 11. The input and output boundaries were implemented based on the selection of 2% of the plug length, which leads to a well-defined layer for fluid entrance. As expected, some overlap occurred of the distributions of the pore bodies and pore throats, but with the largest pore throats being linked to the largest pore bodies, thus indicating good results regarding the PNM generation methodology. A selected few pore throats were several mm wide, which created regions for considerable fluid flow between the two linked pore bodies. However, the majority of pore throats remained within the μm range. The larger pore throats were important to preserve connections between vugs, thus creating preferential paths for fluid flow.

We also compared PNM results (all using harmonic averages of the pore throat radii) obtained with the different resolutions. Fig. 12 shows the final generated pore network and the calculated pressure fields. Results indicated that part of the well-connected network could not be generated using lower resolution μCT images. Still, in terms of fluid flow, the PNM captured important connections between mesopores and macropores since the calculated absolute permeabilities values (as shown in Table 4) were close to the measured value. The three PNM simulations showed specific regions with higher pressure drops, which were preferably accessed by fluid during the flow experiment. Fig. 12 further shows that the number of pore bodies and pore throats increases immensely as the μCT images resolution increased.

Another important result relates to the possibility to conduct numerical experiments using relatively large sample volumes.

Bereitgestellt von University Library Bratislava | Heruntergeladen 31.01.20 12:23 UTC

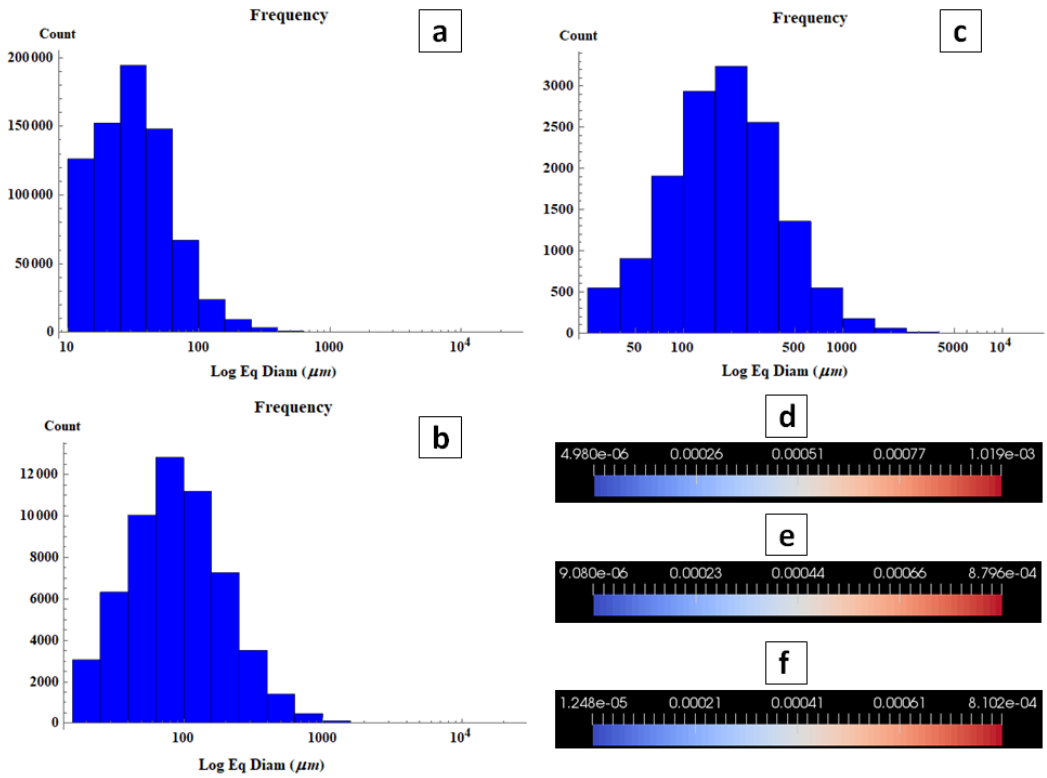

Fig. 10. Pore size frequency distributions (equivalent diameters) of the digital pore system of the plug obtained using (a) 9.97 µm, (b) 18.17 µm, and (c) 24.95 µm µCT images; and the range of pore throat radii (scale in m) found with the models generated using (d) 9.97 µm, (e) 18.17 µm, and (f) 24.95 µm µCT images.

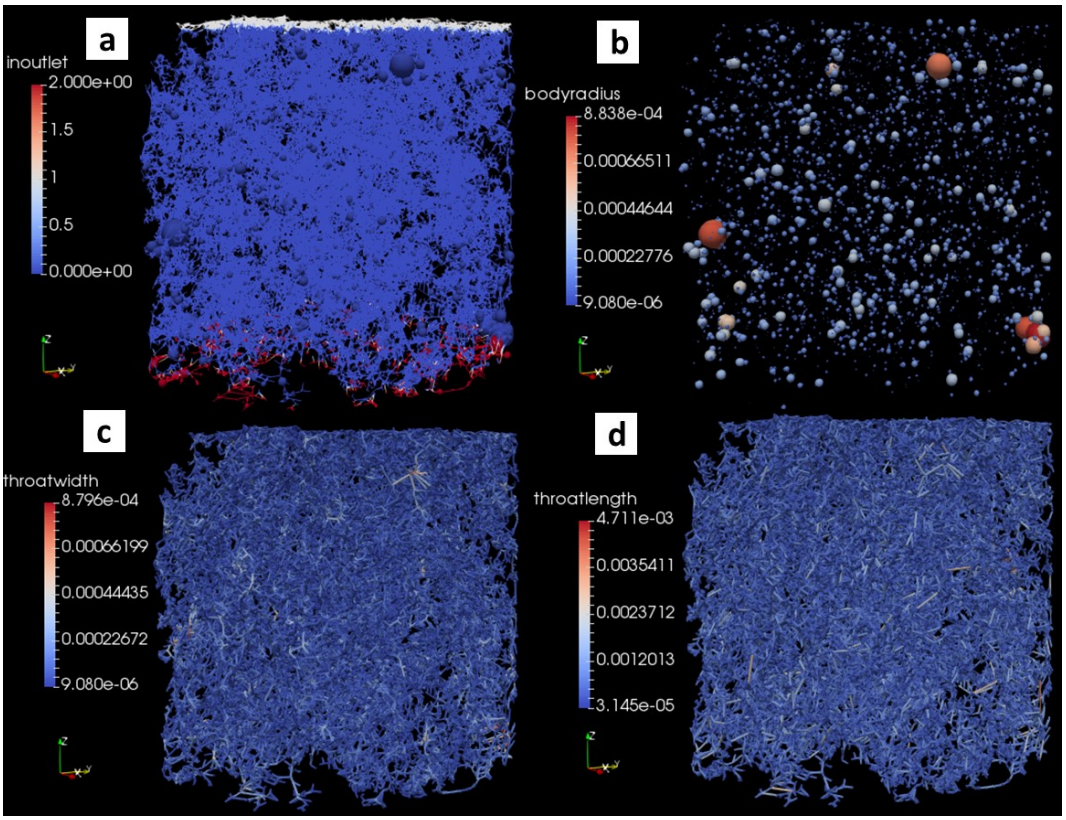

Fig. 11. PNM results for plug 1-34A based on 18.17 µm µCT images presenting: (a) input (white region) and output (red region) boundaries for the fluid flow numerical simulations, and ranges of (b) pore body radii, (c) pore throat radii, and (d) pore throat lengths (scales are in m).

We showed that this is feasible despite the computational demand. The use of relatively large plugs avoids non-representative results, especially for the absolute permeability in view of the required REV. This characteristic is crucial when upscaling results from plugs to cores and beyond.

Bereitgestellt von University Library Bratislava | Heruntergeladen 31.01.20 12:23 UTC

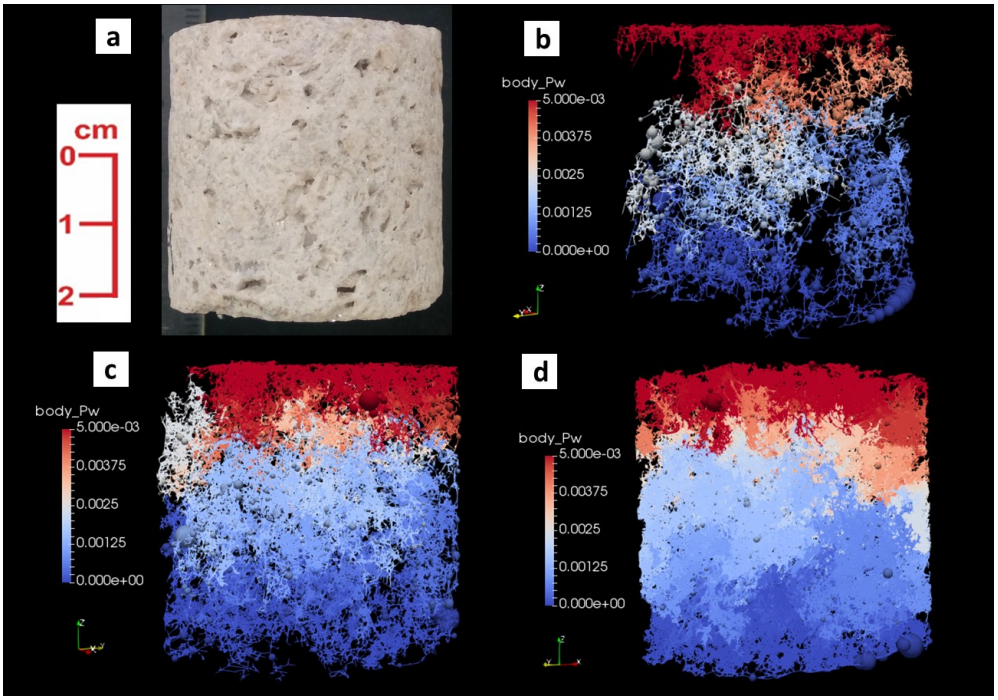

Fig. 12. (a) Image of plug 1-34A, and PNM results of the pressure field based on (b) 24.95 μm, (c) 18.17 μm, and (d) 9.97 μm pixel size μCT images (pressure scales are in Pa).

CONCLUSIONS

This study investigated experimentally and numerically several aspects of a coquina carbonate rock sample, a very close analogue to important pre-salt hydrocarbon reservoir rocks of Santos Basin (Brazil). A series of analyses were carried out on a thin section using optical microscopy, on a rock slab taken from a plug using SEM, EDS, XRD and μCT, and on a larger plug using both μCT images and direct measurements. These analyses together with 3D imaging was used to examine the rock matrix composition and to verify and digitally reconstruct the pore systems, which provided much insight about the matrix and macropore fluid flow processes in the naturally very heterogeneous rock sample. Using PNM numerical simulations, we could estimate the absolute permeability of the rock slab and the entire plug, which presented a properly REV relative to the measured value. The experimental results were important to stablish significant correlations for the entire plug, mostly to obtain reliable information about the pore structure required in the modeling step. In our study we could detect bivalve and ostracode shells within the coquina sample and identify mesopores and macropores providing the main pathways for fluid flow inside the almost pure calcite rock sample. Digital reconstruction of the pore system, along with detailed experimental analyses, allowed us to construct and use the PNM models with confidence. The models were also used to verify the main aspects related to fluid flow modeling: (*i*) rock slab models provided less accurate permeability values compared to the entire plug due to their volumes below the REV; (*ii*) pore throat radii calculated with harmonic averages gave the best results for the absolute permeability; and (*iii*) higher μCT resolution images provided the best result for the permeability according to the experimental data for the entire plug. In order to generate more realistic pore systems for the coquinas, we intend to use additional experimental techniques like nuclear magnetic resonance to verify prevailing pore distributions, and to further improve the segmentation procedures for additional PNM studies, especially for multiphase flow conditions.

Acknowledgements. This research was carried out in association with ongoing R&D projects registered as ANP 19027-2, “Desenvolvimento de infraestrutura para pesquisa e desenvolvimento em recuperação avançada de óleo – EOR no Brasil” (UFRJ/Shell Brasil/ANP) for setting-up an advanced EOR Lab facility for R&D in Brazil, and ANP 20163-2, “Análise experimental da recuperação de petróleo para as rochas carbonáticas do pré-sal brasileiro através da injeção alternada de CO2 e água”, both sponsored by Shell Brasil under the ANP R&D levy as “Compromisso de Investimentos com Pesquisa e Desenvolvimento”. This study was financed in part by the Coordenação de Aperfeiçoamento de Pessoal de Nível Superior-Brasil (CAPES) - Finance Code 001. We acknowledge Professor Ricardo Tadeu, Olga Oliveira and Alessandra Machado from LIN/UFRJ for using their μCT equipment and their technical support with image acquisitions. We also acknowledge Professor Leonardo Borghi and the LAGESED/UFRJ team for geological discussions, Adão Gonçalves from LIAP/UFRJ for the SEM-EDS analysis, Petrobras Research Center (CENPES) for the XRD analyses, and the LRAP/UFRJ team for sample preparation and petrophysical measurements.

REFERENCES

Al-Raoush, R.I., Willson, C.S., 2005. A pore-scale investigation of a multiphase porous media system. Journal of Contaminant Hydrology, 77, 67–89.

Andrä, H., Combaret, N., Dvorkin, J., Glatt, E., Han, J., Kabel, M., Zhan, X., 2013. Digital rock physics benchmarks – part I: Imaging and segmentation. Comput. Geosci., 50, 25–32.

ANP – Agência Nacional do Petróleo, Gás Natural e Biocombustíveis. 2018. Anuário estatístico brasileiro do petróleo, gás natural e biocombustíveis: 2018. Available at www.anp.gov.br/publicacoes/anuario-estatistico/anuario-estatistico-2018.

Ayachit, U., 2015. The ParaView Guide: A Parallel Visualization Application, Kitware. ISBN 978-1930934306

Azambuja Filho, N.C., Arienti, L.M., Cruz, F.E.G., 1998. Guidebook to the rift-drift Sergipe-Alagoas passive margin basin, Brazil. In: AAPG International Conference & Exhibition, 1998, Rio de Janeiro, Brazil, AAPG/PETROBRAS.

Bereitgestellt von University Library Bratislava | Heruntergeladen 31.01.20 12:23 UTC

Blunt, M.J. 2001. Flow in porous media – pore-network models and multiphase flow. Current Opinion in Colloid & Interface Science, 6, 3, 197–207.

Blunt, M.J., Bijeljic, B., Dong, H., Gharbi, O., Iglauer, S., Mostaghimi, P., Paluszny, A., Pentland, C., 2013. Pore-scale imaging and modelling. Adv. Water Resour., 51, 197–216.

Buades, A., Coll, B., Morel, J.L., 2005. A non local algorithm for image denoising. IEEE Int. Conf. Computer Vision and Pattern Recognition, CVPR 2005, 2, 60–65.

Bultreys, T., Van Hoorebeke, L., Cnudde, V., 2015. Multi-scale, micro-computed tomography-based pore network models to simulate drainage in heterogeneous rocks. Adv. Water Resour., 78, 36–49.

Bultreys, T., De Boever, W., Cnudde, V., 2016. Imaging and image-based fluid transport modeling at the pore scale in geological materials: A practical introduction to the current state-of-the-art. Earth-Sci. Rev., 155, 93–128.

Cnudde, V., Boone, M.N., 2013. High-resolution X-ray computed tomography in geosciences: A review of the current technology and applications. Earth-Sci. Rev., 123, 1–17.

Campos Neto, O.D.A., Lima, W.S, Cruz, F.G., 2007. Bacia de Sergipe-Alagoas. Boletim de Geociencias da Petrobras, 15, 2, 405–415.

Corbett, P.W., Estrella, R., Rodriguez, A.M., Shoeir, A., Borghi, L., Tavares, A.C., 2016. Integration of cretaceous Morro do Chaves rock properties (NE Brazil) with the Holocene Hamelin Coquina architecture (Shark Bay, Western Australia) to model effective permeability. Petrol. Geosci., 22, 2, 105–122.

Corbett, P.W.M., Wang, H., Câmara, R.N., Tavares, A.C., Borghi de Almeida, L.F., Perosi, F., Bagueira, R., 2017. Using the porosity exponent (m) and pore-scale resistivity modelling to understand pore fabric types in Coquinas (Barremian-Aptian) of the Morro do Chaves Formation, NE Brazil. Marine and Petroleum Geology, 88, 628–647.

Dal Ferro, N., Charrier, P., Morari, F., 2013. Dual-scale μCT assessment of soil structure in a long-term fertilization experiment. Geoderma, 204, 84–93.

De Boever, W., Derluyn, H., Van Loo, D., Van Hoorebeke, L., Cnudde, V., 2015. Data-fusion of high resolution X-ray CT, SEM and EDS for 3D and pseudo-3D chemical and structural characterization of sandstone. Micron, 74, 15–21.

de Vries, E.T., Raoof, A., van Genuchten, M.T., 2017. Multiscale modelling of dual-porosity media: a computational pore-scale study flow and solute transport. Adv. Water Resour., 105, 82–95.

Doyen, P.M., 1988. Permeability, conductivity, and pore geometry of sandstone. J. Geophys. Res.: Solid Earth, 93, B7, 7729–7740.

Fäy-Gomord, O., Soete, J., Davy, C.A., Janssens, N., Troadec, D., Cazaux, F., Caline, B., Swennen, R., 2017. Tight chalk: Characterization of the 3D pore network by FIB-SEM, towards the understanding of fluid transport. J. Petrol. Sci. Eng., 156, 67–74.

Fouard, C., Malandain, G., Prohaska, S., Westerhoff, M., 2006. Blockwise processing applied to brain micro-vascular network study. IEEE Trans. Medical Imaging, 25, 10, 1319.

Ghanbarian, B., Torres-Verdín, C., Skaggs, T.H., 2016. Quantifying tight-gas sandstone permeability via critical path analysis. Adv. Water Res., 92, 316–322.

Ghanbarian, B., Torres-Verdín, C., Lake, L.W., Marder, M., 2018. Gas permeability in unconventional tight sandstones: Scaling up from pore to core. J. Petrol. Sci. Eng., 173, 1163–1172.

Goldstein, J.I., Newbury, D.E., Joy, D.C, Lyman, C.E., Echlin, P., Lifshin, E., Sawyer, L., Michael, J., 2003. Scanning Electron Microscopy and X-Ray Microanalysis. 3rd ed. Springer, New York. ISBN 978-1-4615-0215-9

Hemes, S., Desbois, G., Urai, J.L., Schröppel, B., Schwarz, J.O., 2015. Multi-scale characterization of porosity in Boom Clay (HADES-level, Mol, Belgium) using a combination of X-ray μ-CT, 2D BIB-SEM and FIB-SEM tomography. Micropor. Mesopor. Mat., 208, 1–20.

Hillier, S., 1994. Pore-lining chlorites in siliciclastic reservoir sandstones: electron microprobe, SEM and XRD data, and implications for their origin. Clay Miner., 29, 665–679.

Iassonov, P., Gebrenegus, T., Tuller, M., 2009. Segmentation of X-ray computed tomography images of porous materials: A crucial step for characterization and quantitative analysis of pore structures. Water Resour. Res., 45, 9–20.

Jafari, S., Yamamoto, R., Rahnama, M., 2011. Lattice-Boltzmann method combined with smoothed-profile method for particulate suspensions. Phys. Rev. E., 83, 2, 026702.

Joekar-Niasar, V., Hassanizadeh, S.M., 2012. Analysis of fundamentals of two-phase flow in porous media using dynamic pore-network models: a review. Crit. Rev. Environ. Sci. Technol., 42, 1895–1976.

Katz, A.J., Thompson, A.H., 1986. Quantitative prediction of permeability in porous rock. Physical Rev. B, 34, 11, 8179.

Kaczmarczyk, J., Dohnalik M., Zalewska, J., 2011. Evaluation of Carbonate Rock Permeability, with the Use of X-ray Computed Microtomography. Nafta-Gaz Rok, 67, 4, 233–239.

Kittler, J., Illingworth, J., 1986. Minimum error thresholding: Pattern recognition, 19, 1, 41–47. https://doi.org/10.1016/0031-3203(86)90030-0

Luna, J, Perosi, F.A., Dos Santos Ribeiro, M.G., Souza, A., Boyd, A., De Almeida, L.F.B, Corbett, P.W.M., 2016. Petrophysical rock typing of Coquinas from the Morro do Chaves Formation, Sergipe-Alagoas Basin (Northeast Brazil). Braz. J. Geophys., 34, 4, 509–521.

Machado, A.C., Teles, A.P., Pepin, A., Bize-Forest, N., Lima, I., Lopes, R.T., 2016. Porous media investigation before and after hydrochloric acid injection on a pre-salt carbonate coquinas sample. Applied Radiation and Isotopes, 110,160–163.

Newbury, E.D., Ritchie, N.W.M., 2013. Is scanning electron microscopy/energy dispersive X-ray spectrometry (SEM/EDS) quantitative? Scanning, 35, 141–168.

Rabbani, A., Assadi, A., Kharrat, R., Dashti, N., Ayatollahi, S., 2017. Estimation of carbonates permeability using pore network parameters extracted from thin section images and comparison with experimental data. J. Nat. Gas Sci. Eng., 42, 85–98.

Ramstad, T., Øren, P.E., Bakke, S., 2010. Simulation of two-phase flow in reservoir rocks using a lattice Boltzmann method. Soc. Pet. Eng. J., 15, 917–927.

Raoof, A., Hassanizadeh, S.M., 2010. A new method for generating pore-network models of porous media. Transp. Porous Media, 81, 3, 391–407.

Raoof, A., Hassanizadeh, S.M., Leijnse, A., 2010. Upscaling transport of adsorbing solutes in porous media: pore-network modeling. Vadose Zone J., 9, 3, 624–636.

Raoof, A., Hassanizadeh, S.M., 2012. A new formulation for pore-network modeling of two-phase flow. Water Resour. Res., 48, 1.

Raoof, A., Nick, H.M., Hassanizadeh, S.M., Spiers, C.J., 2013. PoreFlow: A complex pore-network model for simulation of reactive transport in variably saturated porous media. Comp. Geosci., 61,160–174.

Sezgin, M., Sankur, B., 2004. Survey over image thresholding techniques and quantitative performance evaluation. J. Electron. Imaging, 13, 1, 146–165.

Shah, S.M., Gray, F., Crawshaw, J.P., Boek, E.S., 2015. Micro-computed tomography porescale study of flow in porous media: effect of voxel resolution. Adv. Water Resour., 95, 276–287.

Tavares, A.C., Borghi, L., Corbett, P., Nobre-Lopes, J., Câmara, R., 2015. Facies and depositional environments for the coquinas of the Morro do Chaves Formation, Sergipe-Alagoas Basin, defined by taphonomic and compositional criteria. Braz. J. Geol., 45, 3, 415–429.

Thijssen, J., 2007. Computational Physics. Cambridge University Press, Cambridge. ISBN 9781139171397. https://doi.org/10.1017/CBO9781139171397

Thompson, D.L., Stilwell, J.D., Hall, M., 2015. Lacustrine carbonate reservoirs from Early Cretaceous rift lakes of Western Gondwana: Pre-Salt coquinas of Brazil and West Africa. Gondwana Res., 28, 26–51.

Vik, B., Bastesen, E., Skauge, A., 2013. Evaluation of representative elementary volume for a vuggy carbonate rock – Part I: Porosity, permeability, and dispersivity. J. Petrol. Sci. Eng., 112, 36–47.

Wildenschild, D., Vaz, C.M.P, Rivers, M.L., Rikard, D., Christensen, B.S.B., 2002. Using X-ray Computed Tomography in Hydrology: Systems, Resolutions, and Limitations. J. Hydrol., 267, 3, 285–297.

Wildenschild, D., Sheppard, A.P., 2013. X-ray imaging and analysis techniques for quantifying pore-scale structure and processes in subsurface porous medium systems. Adv. Water Resour., 50, 217–246.

Wojdyr, M., 2010. Fityk: a general-purpose peak fitting program. J. Appl. Crystall., 43, 5, 1126–1128.

Zhang, D., Zhang, R., Chen, S., Soll, W.E., 2010. Pore scale study of flow in porous media: Scale dependency, REV, and statistical REV. Geophys. Res. Lett., 27, 8, 1195–1198.

Received 13 March 2019
Accepted 16 April 2019

Bereitgestellt von University Library Bratislava | Heruntergeladen 31.01.20 12:23 UTC

J. Hydrol. Hydromech., 67, 2019, 4, 384–392
DOI: 10.2478/johh-2019-0017

Predicting impacts of climate change on evapotranspiration and soil moisture for a site with subhumid climate

András Herceg[1*], Reinhard Nolz[2], Péter Kalicz[1], Zoltán Gribovszki[1]

[1] University of Sopron, Institute of Geomatics and Civil Engineering, Bajcsy-Zsilinszky s. 4, Sopron H-9400, Hungary.
[2] University of Natural Resources and Life Sciences, Vienna, Institute of Hydraulics and Rural Water Management, Muthgasse 18, 1190 Wien, Austria.
[*] Corresponding author. Tel.: +36 30 719 4527. E-mail: herceg.andras88@gmail.com

Abstract: The current and ongoing climate change over Europe can be characterized by statistically significant warming trend in all seasons. Warming has also an effect on the hydrological cycle through the precipitation intensity. Consequently, the supposed changes in the distribution and amount of precipitation with the continuously increasing temperature may induce a higher rate in water consumption of the plants, thus the adaptation of the plants to the climate change can be critical. The hydrological impact of climate change was studied based on typical environmental conditions of a specific agricultural area in Austria. For this purpose, (1) a monthly step, Thornthwaite-type water balance model was established and (2) the components of the water balance were projected for the 21st century, both (a) with a basic rooting depth condition (present state) and (b) with a (hypothetically) extended rooting depth (in order to evaluate potential adaption strategies of the plants to the warming). To achieve the main objectives, focus was set on calibrating and validating the model using local reference data. A key parameter of the applied model was the water storage capacity of the soil ($SOIL_{MAX}$), represented in terms of a maximum rooting depth. The latter was assessed and modified considering available data of evapotranspiration and soil physical properties. The adapted model was utilized for projections on the basis of four bias corrected Regional Climate Models. An extended rooting depth as a potential adaptation strategy for effects of climate change was also simulated by increasing $SOIL_{MAX}$. The basic simulation results indicated increasing evapotranspiration and soil moisture annual mean values, but decreasing minimum soil moisture for the 21st century. Seasonal examination, however, revealed that a decrease in soil moisture may occur in the growing season towards to the end of the 21st century. The simulations suggest that the vegetation of the chosen agricultural field may successfully adapt to the water scarcity by growing their roots to the possibly maximum.

Keywords: Water balance; Plant available water; Weighing lysimeter; Regional Climate Model.

INTRODUCTION

Climate change is mainly characterized by a global rise of average temperatures (global warming) and its subsequent impacts on the hydrological cycle. The average temperature already increased by 0.6°C during the 20th century, and is predicted to further increase during upcoming decades (IPCC, 2014). Baseline scenarios of global warming – such that do not consider mitigation effects – predict an increase of 3.7°C to 4.8°C by 2100 compared to pre-industrial levels. As increased temperatures also reflect a higher energy potential in the atmosphere, the resulting intensification of driving forces will influence the hydrological cycle. Expected effects include alteration of precipitation patterns and evapotranspiration processes at multiple scales (Sun et al., 2010). Consequently, extreme events in terms of thunderstorms as well as droughts are supposed to occur more often (IPCC, 2014). It is widely accepted that such massive impacts will considerably affect ecosystems and the services they provide for human well-being as, for example, food production. Against this background, it is necessary to evaluate impacts of climate change on the components of the water cycle (IPCC, 2007). According to the impact analysis studies of water balance models (e.g., Keables and Mehta, 2010; Lutz et al., 2010; Mohammed et al., 2012; Remrová and Císleřová, 2010), Zamfir (2014) demonstrated that the evapotranspiration may increase, but the soil water content may decrease in the future due to the presumably increasing temperature and the decreasing precipitation. Consequently, the occurrence of water scarcity may become more common towards the end of the 21st century.

The "Marchfeld" in the eastern part of Austria is one of the major field crop production area (covering about 1000 km^2 dominated by agricultural production), and nevertheless one of the driest region in Austria (Eitzinger et al., 2013). The region is characterized by a subhumid climate with a mean annual temperature and precipitation of approximately 10°C and 550 mm, respectively (Götz et al., 2000). Typical summers are hot and dry; winters are mainly cold with severe frost and limited snow cover (Götz et al., 2000). A typical soil type is Chernozem, a black-colored fertile soil (Götz et al., 2000). Despite the generally favorable environmental conditions, the region is prone to water deficit stress. Calculated reference evapotranspiration was on average 830 mm per year in the period 1990–2013 (after personal communication with Reinhard Nolz). Hence, irrigating agricultural fields has a long tradition to balance water deficit and ensure proper soil water conditions for crop production. For the future, irrigation is expected to become even more important for agricultural production in the "Marchfeld" because of climate change effects (Nachtnebel et al., 2014).

The researches on Marchfeld in context of water stress focus mainly on crop simulations (basically on winter wheat), e.g., Eitzinger et al. (2003, 2013), Strauss et al. (2012) and Thaler et al. (2012). However, some part of Marchfeld is grassland, and as we know none of the study has analyzed the effect of climate change on that grass covered surfaces until now. Therefore, the open question of this study was: How the water balance of grass covered areas may change in the future?

Bereitgestellt von University Library Bratislava | Heruntergeladen 31.01.20 12:23 UTC

The main objective of this study was to upgrade and adjust the well-known water balance model after Thornthwaite to compute evapotranspiration and soil moisture based on simple and easily obtainable weather data (Dingman, 2002; Thornthwaite and Mather, 1955), and using high precision weighing lysimeter data (Nolz et al., 2016) for calibration and validation for local environmental conditions. Such an adjusted Thornthwaite-type water balance model was previously tested for a forest stand and for a mixed surface cover using MODIS data as calibration, for which it delivered proper results (Herceg et al., 2016). This study was also initiated to estimate future evapotranspiration and soil moisture under environmental conditions considered representative for the "Marchfeld".

The projection phase required weather data that were extracted from Regional Climate Models (RCMs) that were downscaled from Global Climate Models (GCMs). The dataset covered three periods in the 21st century (2015–2045; 2045–2075; 2070–2100). Considering predicted rainfall and evapotranspiration, soil moisture could be calculated based on a simple water balance. In doing so, two specific aspects were considered: In order to address the uncertainty of predictions (i.e., variations between different climate databases), the required model input was chosen from four different RCMs. The other aspect referred to plant water uptake and water deficit stress. For the simulations, two basic conditions were distinguished with respect to the rooting zone depth. The first run was based on a rooting depth corresponding to the rooting depht of the plants in the lysimeter during the calibration period (basic rooting depth of the plants). The second assumption was that plants were able to adapt to water stress conditions by increasing their rooting depth in order to suffice their needs taking advantage of a larger soil water reservoir (extended rooting depth of the plants).

In such a way, potential stress conditions were determined for both basic and extended rooting depth. Differences arising from varying soil characteristics as well as the changes of aboveground biomass were not considered in this study.

The new aspect of the study was on one hand the two-stage evapotranspiration calibration process (calibration of potential, and the calibration of the actual evapotranspiration separately), on second hand, the adaption of the broken-line regression method in the calibration of the potential evapotranspiration.

The main advantage of this model is the low amount of input data requirement (precipitation and temperature); therefore it could easily be extended to larger regional scale. The simplicity of this water-balance model ensures fast impact analysis of climate change on evapotranspiration and soil water storage, and requires a significant lower amount of work for input data' preprocessing for baseline investigations than more complex models. Nevertheless, the use of only two input parameters enables a much easier uncertainty analysis of the applied model.

MATERIALS AND METHODS

Study site and data base

Basic data for this study were obtained at the experimental farm of the University of Natural Resources and Life Sciences, Vienna (BOKU), in Groß-Enzersdorf (48°12'N, 16°34'E; 157 m). The location is regarded representative for the Marchfeld with respect to the climatic conditions. The experimental farm hosts a reference weather station of the Austrian "Zentralanstalt für Meteorologie und Geodynamik (ZAMG)" at which meteorological quantities were monitored according to the standard of the World Meteorological Organization (WMO). Data included air temperature, precipitation, relative humidity, global radiation, and wind velocity measured in 10 m height (Nolz et al., 2016).

Soil water balance components were determined using a single weighing lysimeter. It was installed at the experimental farm together with a second lysimeter in 1983 to study evapotranspiration at the surface, water content in the soil profile, and water drainage at the bottom outlet of the lysimeters (Neuwirth and Mottl, 1983). Its cylindrical vessel has an inner diameter of 1.9 m, a resulting surface area of 2.85 m^2, and a hemispherical bottom with a maximum depth of 2.5 m. During installation, a typical soil profile was created by re-packing soil in layers as follows:

- sandy loam soil (0–140 cm) (30% sand, 50% silt, 20% clay; porosity: 43%),
- gravel (140–250 cm) (mainly large pore sizes with negligible water holding capacity).

The soil characteristics and the consequent hydraulic properties were taken as basis for the simulations.

The lysimeter and the surrounding area of approximately 50 m x 50 m were permanently covered by grass. The grass was cut about twice a month during the vegetation period and irrigated about twice a week during summer, but shorter or longer non-irrigated and rainless periods can also be found (for three weeks in the growing season). Therefore there were basically well watered conditions in the growing season due to the irrigation, but periods with water scarcity (non-reference conditions) can also be found. In the dormant season there were even longer periods without irrigation. Maintenance also included manual clearing from weed and fertilization with long-term compound fertilizer for lawns.

Evapotranspiration (ETO_{lys}) was determined by considering soil water within the lysimeter (W_{lys}) and fluxes across its boundaries such as drainage (W_{drain}), evapotranspiration (ETO_{lys}), and precipitation (P_{lys}) and irrigation (I_{lys}).

To determine W_{lys}, nominal lysimeter weight was measured using a weighing facility. A mechanical system transformed the weight to an electronic load cell with an accuracy of ±0.2 kg (Nolz et al., 2013a). The analog output signal was amplified, converted to digital units, averaged and stored on a local server. Logging intervals were 15 and 10 minutes from 2004 to 2009 and from 2009 to 2011, respectively. The raw values (digital units) were converted into nominal mass (kg) using a calibration factor (Nolz et al., 2013a). It has to be noted that the calibrated weighing data represent relative lysimeter mass in kg, defined as current mass minus an unknown reference mass. Hence, only mass changes were determined. Dividing the nominal mass by the surface area (m^2) resulted in soil water equivalent (W_{lys} / mm). Drainage water was measured at the bottom outlet of the lysimeter using a tipping bucket. Tipping and weighing data were logged at the same time intervals. Counts of tipping were converted into outflow data using a calibration factor (Nolz et al., 2013a). Dividing by the surface area resulted in drainage water (W_{drain}/mm). Soil water and drainage water were linked to a nominal time series ($W_{lys} + W_{drain}$), which was smoothed using a specific procedure (Nolz et al., 2013b; Nolz et al., 2014).

Equation (1) illustrates the relation between measured ($W_{lys} + W_{drain}$) and unknown (P_{lys}, I_{lys}, ETO_{lys}) water balance components.

$$\Delta(W_{lys} + W_{drain}) = (P_{lys} + I_{lys}) - ETO_{lys} \quad (1)$$

Therein $\Delta(W_{lys} + W_{drain})$ represents changes in soil water due to boundary fluxes (evapotranspiration ETO_{lys}, and precipitation P_{lys} plus irrigation I_{lys}).

Bereitgestellt von University Library Bratislava | Heruntergeladen 31.01.20 12:23 UTC

Accordingly, negative values of $\Delta(W_{lys} + W_{drain})$ – referring to a time interval of 10 or 15 minutes – were attributed to evapotranspiration under reference conditions (Nolz et al., 2014). Evaporation and interception losses were not considered. ETO_{lys} was then processed to a daily time series (ETO_{lys} / mm d^{-1}), with each day lasting from 7 a.m. to 7 a.m. of the following day. Finally, evapotranspiration as well as weather and data covering the years 2004 to 2011 were processed as monthly sums.

Model description

The Thornthwaite-type water balance model represents a 1-D system, considering only vertical fluxes. Input values are monthly precipitation (*PM*) (mm $month^{-1}$) and mean monthly temperature (*TM*) (°C) according to Thornthwaite (1955). Dingman (2002) slightly modified the original model, which has been applied as a basis. All input data (monthly sums from 2004 to 2011) originate from the experimental site in Groß-Enzersdorf; irrigation amounts of the lysimeter were added to precipitation.

The first step in setting up the model was the calculation of the potential evapotranspiration (*PET*). A temperature-based PET-model after Hamon (1964) was applied (Eq. 2):

$$PET_H = 29.8D\frac{e^*}{T_D + 273.2} \tag{2}$$

with

$$e^* = 0.611\exp\left(\frac{17.3T_D}{T_D + 237.3}\right) \tag{3}$$

where D is the daylight hours (h day^{-1}), T_D is the daily average temperature (°C), e^* is saturation vapor pressure (kPa).

PET_H from daily time-step was aggregated to monthly sum, noted PET_{MH} (mm $month^{-1}$).

The following Equations (4–10) of this sub-chapter originated from Dingman (2002): When monthly precipitation (P_M) exceeds PET_{MH}, soil water storage is assumed to sufficiently provide vegetation with water and therefore *ET* is at its potential rate (Eq. 4):

$$\text{If } P_M \geq PET_{MH} \tag{4}$$

$$\text{then } ET_M = PET_{MH} \tag{5}$$

$$SOIL_M = \min\left\{\left[\left(P_M - ET_M\right) + SOIL_{M-1}\right],\ SOIL_{MAX}\right\} \tag{6}$$

where ET_M (mm $month^{-1}$) is the monthly actual evapotranspiration, and $SOIL_M$ (mm $month^{-1}$) is the monthly soil moisture representing the amount of soil water that is available for the vegetation (not the total amount of soil water). $SOIL_{MAX}$ (mm $month^{-1}$) was introduced by considering unsaturated hydraulic parameters of the lysimeter soil type and rooting depth:

$$SOIL_{MAX} = \left(\theta_{fc} - \theta_{pwp}\right)z_{rz} \tag{7}$$

where: θ_{fc} is the water content at field capacity [m^3/m^3], θ_{pwp} is the water content at permanent wilting point [m^3/m^3] and z_{rz} is the rooting depth (vertical extent of rooting zone in mm), the standard value is 1000 mm.

Both ET_M and $SOIL_M$ denote the result parameters of the presented study.

For the simulation procedure, the first $SOIL_{M-1}$ value was set to a maximum value that corresponded with the soil-water storage capacity ($SOIL_{MAX}$). The basic assumption was that soil water storage is completely filled at the beginning of each vegetation period.

Values for θ_{fc} and θ_{pwp} were estimated based on the texture of the soil in the lysimeter using a pedotransfer function according to Baumer (1992). Input values are soil particle fractions (sand, silt, clay), bulk density (1.5 g cm^{-3} in our case), and humus content (1% in this study).

The soil water was considered as storage reservoir used for evapotranspiration under condition of

$$P_M < PET_{MH} \tag{8}$$

$$\text{then: } ET_M = P_M + \Delta SOIL \tag{9}$$

$$\text{where: } \Delta SOIL = SOIL_{M-1} - SOIL_M = SOIL_{M-1}*\left(1 - \exp\left(-\frac{PET_{MH} - P_M}{SOIL_{MAX}}\right)\right) \tag{10}$$

with $\Delta SOIL$, the difference in the soil water storage (mm $month^{-1}$).

Model calibration and validation

Evapotranspiration data of the grass-covered lysimeter served as basis for calibration and validation. It is important to note that the model was not calibrated for drainage. However, drainage term can be calculated with the help of the model results.

In case of the lysimeter, runoff is not likely, thus only the recharge remains according to the following equation:

$$R = P_M - ET_M - \Delta SOIL \tag{11}$$

This equation is for the average monthly "water surplus" (i.e., the available water for recharge and runoff) (Dingman, 2002 pp. 316).

The available time series (2004–2011) was divided into two parts, whereof the first (2004–2008) was used for calibration and the second (2009–2011) for validation.

The first step of calibration considered potential evapotranspiration for actual land cover (i.e. periods when potential evapotranspiration values were close to actual evapotranspiration) using ETO_{lys}-values at well-watered (relative high soil moisture) conditions. The latter were assumed to occur when precipitation (P_M) exceeded potential evapotranspiration (PET_{MH}) or actual evapotranspiration (ETO_{lys}) exceeded potential evapotranspiration (PET_{MH}).

The ETO_{lys}-values selected in such a way are denoted $PETO_{lys}$. Measured $PETO_{lys}$ values (response variable) were correlated with calculated PET_{MH} values (explanatory variable).

The regression line demonstrates the correlation between PET_{MH} and $PETO_{lys}$ and with the slopes of a broken-line regression - as a calibration parameter - we can determine the calibrated Hamon type potential evapotranspiration (PET_M) (Figure 2). It is important to note that PET_{MH} is the Hamon type, globally calibrated, calculated, while PET_M is the locally calibrated potential evapotranspiration (for the study area). Due to the various state of the vegetation, *PET* of the dormant and the growing seasons are not the same, therefore different relationships had to be established for both parts (Rao et al., 2011). For this purpose, a software package named 'segmented' in the 'R' software environment was applied (R Core Team, 2012). The broken-line or segmented models create a piecewise linear relationship between the response and one or more of the ex-

Bereitgestellt von University Library Bratislava | Heruntergeladen 31.01.20 12:23 UTC

planatory variables. This linear relationship is represented by two or more straight lines connected at unknown values called breakpoints (Muggeo, 2008). The basic principle was that when PET_{MH} is equal to 0, then $PETO_{LYS}$ is 0 as well. The correlation between PET_{MH} and $PETO_{LYS}$ cannot be described with a simple regression line, since the large lack of fit, and we did not want to use more complicated function. Consequently, broken-line regression was chosen.

The second step of the calibration is the estimation of the calibrated $SOIL_{MAX}$ parameter using ETO_{LYS} data for the same (2004–2008) period. In this case, the initially estimated $SOIL_{MAX}$ parameter adjusted in order to reach minimum root mean square error between ETO_{lys} and ET_M by using the 'optim' function of 'R' software. (The range of this adjustment was from 10 mm to 1000 mm). Based on the value of $SOIL_{MAX}$ after the calibration, the vertical extent of the rooting zone (plant water uptake) was inversely estimated using soil texture data. The details of this estimation can be found in the Model Adjustment chapter.

Parameters of the calibration were considered for running the model with data of the validation period (2009–2011).

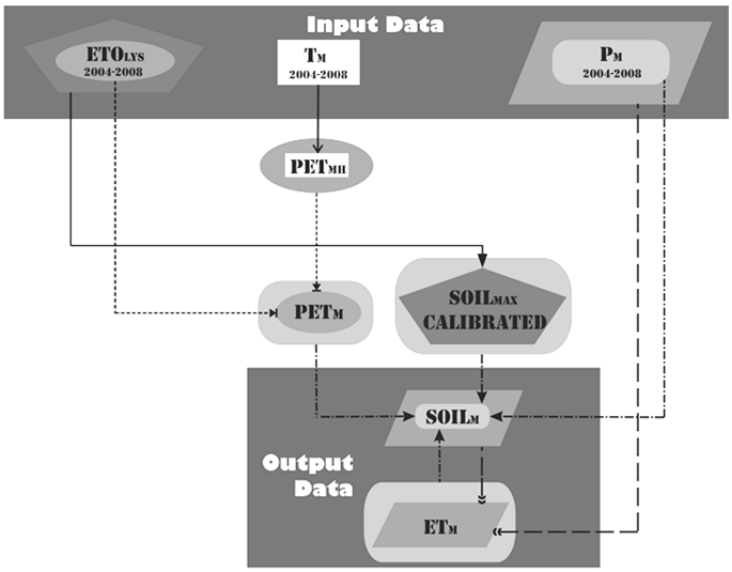

Fig. 1. Schematic representation of workflow of the modelling process including the relationships between input data, calculated and calibrated parameters, and output data. Parameters: ETO_{LYS} is the measured actual evapotranspiration; PET_{MH} is the Hamon type potential evapotranspiration; PET_M is the calibrated potential evapotranspiration; ET_M is the actual evapotranspiration, $SOIL_{MAX}$ *CALIBRATED* is the calibrated soil water storage-capacity of the soil, and $SOIL_M$ is the soil moisture. The different shapes with the different type of arrows illustrate the connections amongst the used parameters during the model workflow.

Evaluating model performance

Model performance was evaluated using the Nash-Sutcliffe criterion, which is typical for calibrating and validating hydrologic models. In particular, it is suitable for models that simulate continuous time series of different time-period (Dingman, 2002). A proper model performance is presumed when the Nash-Sutcliffe coefficient, *NSE*, calculated according to Eq. 12, returns a value between 0.8 and 1.0:

$$NSE = 1 - \frac{\sum_{i=1}^{N}(ETO_{LYS\_i} - ET_{M\_i})^2}{\sum_{i=1}^{N}(ETO_{LYS\_i} - m_{ETO\_LYS})^2} \quad (12)$$

ETO_{LYS_i} is the time series of measured values, ET_{M_i} is the time series of simulated values and m_{ET_LYS}: average value of ETO_{LYS} for the period being measured.

Projection procedure

Regional climate models (RCMs)

The validation of the model required the partition of the available dataset (2004–2011) into calibration (2004–2008) and validation periods (2009–2011). The original period of calibration however; was too short for the basis of the projection procedure, therefore we re-run the model using all available data. This re-run consequently means recalibration, therefore it delivered new and more reliable calibration parameters as well (Table 5). Here as much data as possible was assumed to deliver the best possible calibration relation. Nevertheless, there was small amount of data in the dormant season of the calibration (Figure 2).

Inputs for predicting future developments of ET_M and $SOIL_M$ were the equation of the broken line regression, the calibrated $SOIL_{MAX}$ value, and predicted temperature and precipitation values. The latter originate from four grid-based, bias-corrected regional climate models (RCMs). Data were extracted from the nearest pixel to the experimental sites coordinates. The main properties of the RCMs can be found in Table 1. The underlying database called "FORESEE" contains daily meteorological data (min./max. temperature, and precipitation) based on ten RCMs for 2015–2100, and observation based data for the period 1951–2009, interpolated to 1/6×1/6 degree spatial resolution grid. The bias correction of the RCMs was done by a cumulative distribution functions fitting technique. This method corrected systematic errors in the RCM results. In case of precipitation, the intensity as well as the frequency of precipitation was corrected (Dobor et al., 2013).

In the following, each model is referred to as their model ID (first column of Table 1)

The RCMs time scale covers a range from 2015 to 2100. Each of them contains temperature and precipitation data in monthly time intervals. To evaluate the results for the 21st century, four main investigational periods were established: 1985–2015, 2015–2045, 2045–2075, and 2070–2100. With the data at hand, these 30-years-blocks with a 5-years overlap in the last two periods seemed the best partitioning. The overlap in the last part of the 21st century was necessary, because only 25 years of data were available.

Table 1. The applied RCMs (Linden van der and Mitchell, 2009).

Model ID	Research Institute	Regional climate model	Driving general circulation model	Emission scenario	Spatial resolution
1	Max-Planck-Institute for Meteorology (MPI)*	REMO	ECHAM5	A1B	25km
2	Sweden's Meteorological and Hydrological Institute (SMHI)**	RCA	ECHAM5-r3	A1B	25km
3	Danish Meteorological Institute (DMI)***	HIRHAM5	ECHAM5	A1B	25km
4	Royal Netherlands Meteorological Institute (KNMI)****	RACMO2	ECHAM5-r3	A1B	25km

*: Jacob (2001); **: Jones et al. (2004); ***: Christensen et al. (1996); ****: Lenderink et al. (2007)

Bereitgestellt von University Library Bratislava | Heruntergeladen 31.01.20 12:23 UTC

Table 2. Annual mean values of temperature and precipitation derived from the regional climate models from 1985 to 2100 with standard deviations in parentheses In the first investigation period (1985–2015), the observation based averaged values (with standard deviations in parentheses) can be found.

Model ID	Parameter	1985/2015	2015/2045	2045/2075	2070/2100
1	T [°C]	–	11.0 (0.92)	12.4 (0.89)	13.3 (0.88)
	P [mm]	–	653 (128)	635 (99)	692 (127)
2	T [°C]	–	10.9 (0.84)	12.1 (0.63)	13.0 (0.73)
	P [mm]	–	664 (106)	743 (116)	752 (122)
3	T [°C]	–	11.1 (0.78)	11.9 (0.87)	12.6 (0.73)
	P [mm]	–	587 (102)	634 (122)	653 (146)
4	T [°C]	–	11.3 (0.69)	12.3 (0.73)	13.2 (0.84)
	P [mm]	–	543 (127)	585 (126)	611 (115)
Average	T [°C]	11.1 (0.76)	11.1 (0.81)	12.2 (0.78)	13.0 (0.79)
	P [mm]	606 (98)	612 (116)	649 (116)	677 (127)

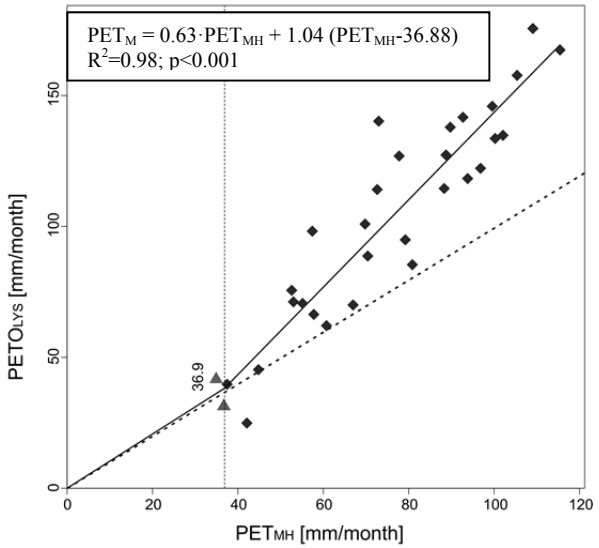

Fig. 2. Relationship between $PETO_{lys}$ and PET_{MH} in dormant (to the left of the dotted vertical line) and growing season, with trend lines (solid) and 1:1 line (dashed).

The annual mean of temperature as well as precipitation showed an increasing tendency (+15% for T; +12% for P) at the end of the 21st century (Table 2). '1' had the highest, while '3' had the lowest value of temperature at the end of the investigation period. In the case of precipitation, '2' had the highest, but '4' had the lowest values. The values of '2' show the smallest deviation from the mean of the four RCMs in the context of temperature, while values of "3" demonstrate it in context of precipitation. However, '1' in general gives most representative values for Middle-Europe according to Dobor et al. (2013). Basic descriptive statistics were assessed for each of the periods and models.

Rooting depth parameterisation for water stress conditions

The sandy loam soil layer of the lysimeter ended at 1.4 m depth. For the second run, it was assumed that – under water stressed conditions – grass can use the water stored in the entire sandy loam soil profile. Consequently, for the second model run the parameter z_{rz} (Eq. 7) was extended to a value representing the maximal possible rooting depth (1400 mm).

Potential stress conditions were determined for both basic and extended rooting depth.

In order to estimate periods with potential water stress, a simple water balance was established. The resulting values – calculated as potential *PET* minus $SOIL_M$ – are illustrated in Figure 8. Potential water stress is defined to occur if the deficits are positive and else exceeding soil moisture values.

RESULTS AND DISCUSSION

Model calibration and validation

Plotting monthly values of evapotranspiration from lysimeter measurements ($PETO_{lys}$) against values estimated using the Hamon approach (PET_{MH}) revealed that PET_{MH} considerably underestimated the evapotranspiration measured with the lysimeter (Fig. 2). Correlation during the period of dormancy is illustrated by the section on the left of the vertical dotted line (broken-line approach); however, only two values of lysimeter data (triangles) could be related to this period, so little conclusion can be drawn from that. With regard to a better accordance, the correlation parameters of Figure 2 and Table 3 were utilised to obtain calibrated potential evapotranspiration values for the model (PET_M).

Table 3. Results of the broken-line regression.

Segments	Estimated slope	Std. Error	*t* value	*Pr*(>|*t*|)
first	0.63	0.31	1.88	NA*
second	1.04	0.34	3.35	$2.3 \cdot 10^{-4}$

Pr(>|*t*|) is the p-value of the hypothesis testing of the slope. The null-hypothesis is that the slope is equal with 0. Because the p-value in our case very small we can reject the null-hypothesis.
*not available, because standard asymptotes were not applicable

The respective *NSE* value was 0.88, indicating a proper performance of the ET-model.

ET_M calculated using the weather data of the validation period (2009–2011) reflected good accordance with the measured lysimeters data (ETO_{LYS}) (Figure 4). The corresponding *NSE* value of 0.85 was similar to that of the calibration period and thus also satisfactorily. In general, calibrating *ET* data is recommended when using the Hamon approach, even though this is rarely addressed in similar studies (e.g., Keables and Mehta, 2010).

Model adjustment

A renewed $SOIL_{MAX}$ value resulting from the 7-years long adjusted and re-calibrated period was utilized to calculate the rooting depth using θ_{fc} and θ_{pwp} data from Table 4 for the first run (basic rooting depth).

$SOIL_{MAX}$ was 142.4 mm as pointed out after the calibration, and therefore z_{rz} was 890 mm (using iteration) for the first run (basic rooting depth). The interpolation was carried out iteratively for determining the location of the rooting depth between *PAW* values of 126.2 mm and 161.0 mm (Table 4).

The $SOIL_{MAX}$-value for the second run (extended rooting depth) was 233.4 mm, since the *PAW* value of the 0–140 cm profile was considered as $SOIL_{MAX}$ (Table 4). Therefore, the impact of the extended rooting (by analyzing the plant water

Bereitgestellt von University Library Bratislava | Heruntergeladen 31.01.20 12:23 UTC

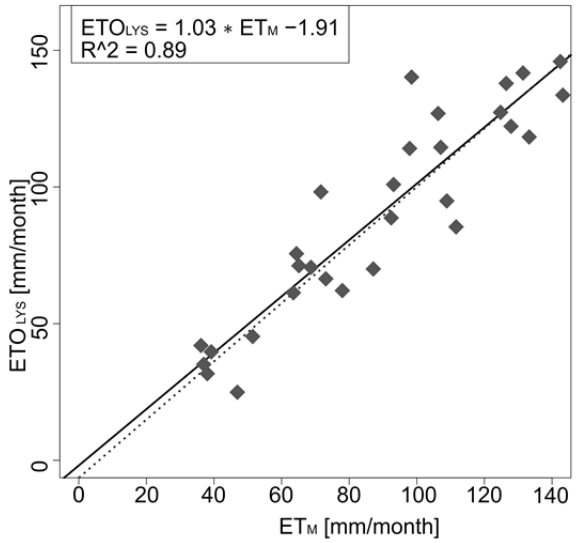

Fig. 3. Relationship between the calculated ET_M and the measured ETO_{lys} after calibration.

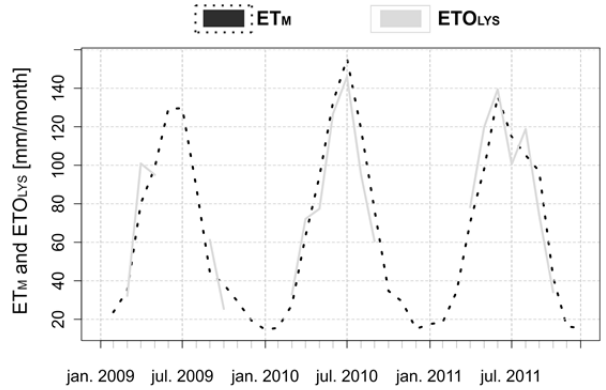

Fig. 4. Time series of the measured ETO_{LYS} and calculated ET_M values in the validation period.

uptake and water deficit stress) can be determined in order to evaluate potential adaption strategies of the plants to the warming.

Projections

Simulation results for both runs – run 1 with basic rooting depth and run 2 with extended rooting depth – are summarized in Table 6. Mean ET_M-values reproduce a slightly increasing trend, as would be expected from the predicted larger temperatures in the projection decades. However, it has to be noted that standard deviation was large. This indicates a large uncertainty that is inherent to modelled data, especially as four different RCMs were used in the given case. Differences depending on the input data are illustrated in Figure 5; the variation of ET_M data between the four RCM models was substantial (10 mm in absolute values). '2' model reproduced the greatest increase as well as the largest values, because the respective RCM projects nearly 100 mm larger precipitation values for the 2045/75 period than the average. In contrast, the '4' model shows stagnancy in evapotranspiration and even a little decrease during the first run, since this model got the smallest values of precipitation. Comparing the first run (Figure 5a) with the second run (Figure 5b) reveals minor differences, which can be associated to the simulated availability of soil water. The latter, represented by averaged $SOIL_M$-values, followed an upward tendency (Table 6), mainly because of the underlying increasing precipitations.

With regard to plant water uptake, the minimal available soil water might be of interest. Therefore, minimum $SOIL_M$-values were calculated as 10th percentile minimums. The general trend of the respective $SOIL_{M\_MIN}$*10Percentile*-values was downwards (Figure 6) with remarkably larger values (16 mm in average) for the second run (Figure 6b). It is evident that the larger soil water storage capacity, as assumed for run 2, provided better conditions for plant growth. The four RCMs revealed a similar sequence as the ET_M-values in Figure 5. Only the '2' model deviates from the general pattern in the 2045/2075-period.

Table 4. The main properties of the soil profile in the lysimeter.

Depth [cm]	θ_{fc} [vol-%]	θ_{pwp} [vol-%]	Plant available water (*PAW*) [vol-%]	Acc. *PAW** [mm]
0–20	30.1	14.9	15.2	30.4
20–40	32.7	17.2	15.5	61.4
40–60	30.4	14.7	15.7	92.8
60–80	30.2	13.5	16.7	126.2
80–100	29.7	12.3	17.4	161.0
100–140	30.0	11.9	18.1	233.4
140–250	1.7	0.8	0.9	-**

*: Accumulated plant available water (*PAW*) accumulated to the bottom of the given layer [mm].
**: non-explainable

Table 5. The calibration parameters after the re-calibration.

Result of the calibration of the PET	$PET_M = 0.54 \cdot PET_{MH} + 1.04$ (PET_{MH}–36.79)
Result of the calibration of the AET	$ETO_{LYS} = 1.04 \cdot ET_M - 2.36$ (*NSE* = 0.88)

Table 6. ET_M, $SOIL_M$, and $SOIL_{M\_MIN}10^{th}$ *percentile* values with standard deviations for the two model runs.

Parameters	1985/2015	2015/2045	2045/2075	2070/2100
	[mm]	[mm]	[mm]	[mm]
$ET_{M\ [basic\ rooting\ depth]}$	49 (34)	49 (33)	52 (34)	53 (35)
$ET_{M\ [extended\ rooting\ depth]}$	50 (33)	51 (32)	53 (33)	55 (33)
$SOIL_{M\ [basic\ rooting\ depth]}$	58 (40)	65 (43)	66 (44)	67 (48)
$SOIL_{M\ [extended\ rooting\ depth]}$	92 (51)	105 (57)	105 (58)	108 (64)
$SOIL_{M\_MIN}\ 10^{th}Percentile\ _{[basic\ rooting\ depth]}$	9 (3)	7 (2)	6 (3)	5 (3)
$SOIL_{M\_MIN}\ 10^{th}Percentile\ _{[extended\ rooting\ depth]}$	26 (6)	24 (7)	22 (6)	19 (7)

Bereitgestellt von University Library Bratislava | Heruntergeladen 31.01.20 12:23 UTC

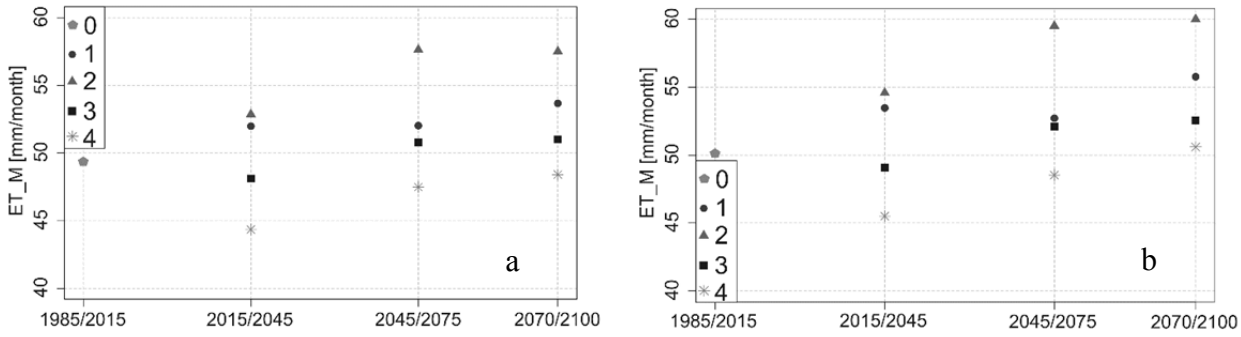

Fig. 5. The projected averages of evapotranspiration between 1985–2100; a: first run, and b: second run (the line represents the average).

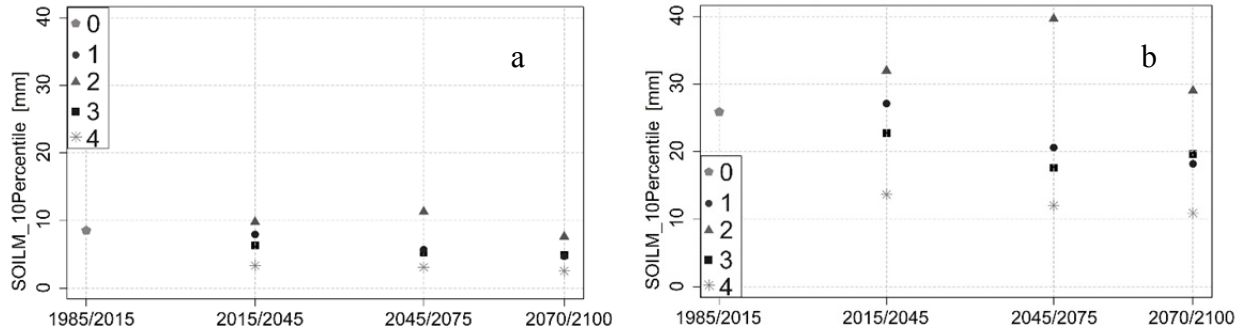

Fig. 6. The projected 10th percentile values of soil moisture between 1985–2100; a: first run, and b: second run. (The line represents average of the RCMs).

Model '1' represented the modelled averages of ET_M and $SOIL_M$ at best in both runs.

In order to analyze seasonal trends, the annual course of ET_M and $SOIL_M$ are illustrated in Figure 7 and Figure 8, respectively. The largest values of ET_M appeared in June (95–100 mm for basic rooting depth; 98–105 mm for extended rooting depth). Smallest $SOIL_M$ can be found in September (12.5–25 mm for basic rooting depth; 50–60 mm for extended rooting depth), which is typical after summer and the end of the vegetative period. The largest values of $SOIL_M$ appeared in March – at the end of the dormancy and after winter precipitation. Consequently, also the decrease of soil moisture from April to August can be typically explained by plant water uptake (Figure 7 and 8).

Beside the evident seasonal trend, Figure 8 illustrates a shift of moisture between summer and winter. While $SOIL_M$-values predicted for the period 2070/2100 are largest in winter (in relation to the other projections), $SOIL_M$ appears smallest during summer. The reason may be found on the higher precipitation rate, which will assure the replenishment of soil moisture in the dormant season, while the increasing temperature will implicate greater evapotranspiration and consequently higher rate of water consumption by the plants on the growing season. For comparison, Calanca et al. (2006) project for the period 2070–2100 a reduction in summer soil moisture over most of Europe based on GCMs with a comparatively rough spatial resolution.

With respect to the basic rooting depth as considered for run 1, potential water stress was pronounced from June to September with the largest deficit in July, when ET_M is at maximum and $SOIL_M$ is low (Figure 8a). Comparing the projection periods, the deficit is assumed to increase in future: For the 2070/2100 period it was approximately 50 mm in run 1, for instance. Consequently, periods of water stress are assumed to occur more often and shortage of the available water is assumed to increase, although more soil water might be available in total (Table 6). Similarly, Heinrich and Gobiet (2012) projected an increasing risk of dry spells for the period 2012–2050, as indicated by a negative Palmer Drought Severity Index. For the agricultural production in this area this could require adapted irrigation strategies in order to endure drought periods without loss of yield.

The larger $SOIL_{MAX}$-value of run 2 entailed larger $SOIL_M$-values (Figure 8b). As a consequence, deficit stress did not occur under these simulation preconditions. However, this hypothetical approach illustrates just the potential of reducing stress effects by improving or more efficiently using soil water storage capacity, since not only the rooting depth, but the seasonal development of aboveground biomass may change in future as well.

Nevertheless, the model works also on 1.4 m rooting depth, even if most roots are on the top 30 centimeters, and only a few located on deeper. According to Candell et al. (1996) crops can grow their roots even deeper, therefore the average of the maximum rooting depth for the globe is 2.1 ± 0.2 m in case of croplands and 2.6 ± 0.1 m for herbaceous plants.

Soil temperature is closely related to, and dependent on air temperature (Zheng et al., 1993). The projected increase in average surface temperature may also result in increased soil temperatures (IPCC, 2014), but it is more complex than the analogous changes in air temperature, since soil temperature is influenced by various factors (such as soil texture and moisture properties, the actual surface cover) (Jungvist et al., 2014). Root development may be affected directly by elevated soil temperatures, indirectly (e.g. changes in the physiology etc.) or by a mixture of those factors. Raised temperature triggers root growth rate up to a species-specific temperature optimum, and considerably alters several root architecture parameters (Gray and Bradya, 2016).

Bereitgestellt von University Library Bratislava | Heruntergeladen 31.01.20 12:23 UTC

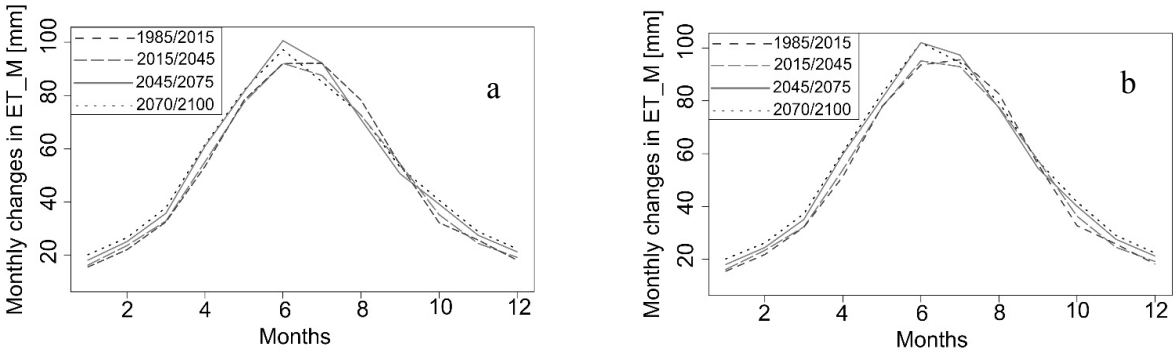

Fig. 7. Seasonal changes (mean annual courses of the different periods) of ET_M in the projection periods; a: first run, and b: second run.

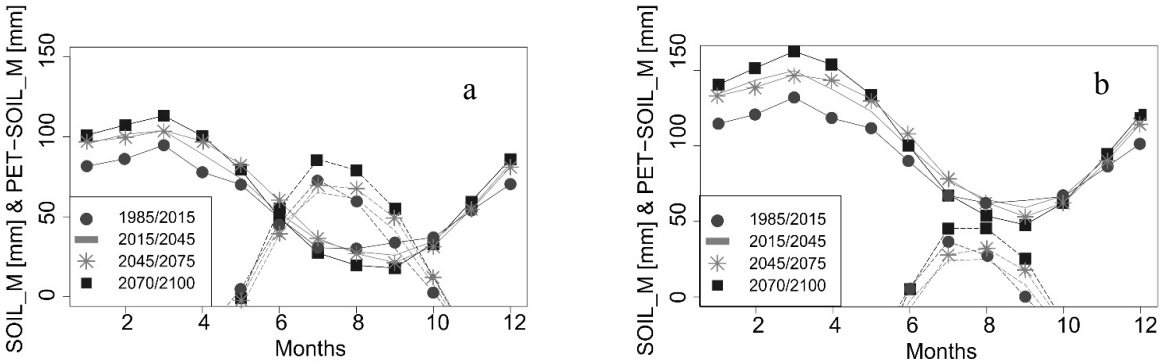

Fig. 8. Seasonal course (mean annual courses of the different periods) of $SOIL_M$ in the projection periods (solid lines) and estimated water deficit calculated as potential ET minus $SOIL_M$ (dashed lines); a: first run, and b: second run.

After intensive reviews of the scientific literature, specifically similar studies have not been found, which are exactly comparable to this work. The mentioned studies in the Introduction, namely Eitzinger et al., 2003, 2013; Strauss et al., 2012 and Thaler et al., 2012 have done crop simulations in context of water stress at Marchfeld, while in this article the grass covered surfaces was in the focus.

Nevertheless, there are impact analysis studies of water balance models (e.g., Keables and Mehta, 2010; Lutz et al., 2010; Mohammed et al., 2012; Remrová and Císlerová, 2010; Zamfir 2014) as referred in earlier, which also demonstrated that the evapotranspiration may increase, but the soil water content may decrease in the future due to the apparently increasing temperature and the decreasing precipitation. They applied mainly Thornthwaite-type, monthly-step water balance model, but basically evaluate their results annually, instead of monthly or seasonal scale as in this study. In case of their study areas there are various climates, different climate models (i.e. GCMs or RCMs), and emission scenarios with not the same investigation time series. Climate change impact studies are nevertheless always affected by uncertainties, particularly in climate model scenarios with regard to climate variability (Eitzinger et al., 2003) which makes also the comparison more difficult.

CONCLUSIONS

In this study, a Thornthwaite-type water balance model was adapted and applied to assess the future development of evapotranspiration and soil moisture in an agricultural area in the eastern part of Austria. The key new model aspect was on one hand the two-stage evapotranspiration calibration process (calibration of potential, and the calibration of the actual evapotranspiration separately). On second hand the adaption of the broken-line regression method in the calibration of the potential evapotranspiration.

The main finding was that both ET and $SOIL_M$ were predicted to become larger in future decades when assuming the results of standard climate scenarios. The remarkable shift predicted for $SOIL_M$ indicates that less soil water will be available during summer months in future. This outcome was underlined when estimating stress conditions based on periods with a negative water balance. The results of a second scenario with an extended rooting depth (i.e., larger $SOIL_{MAX}$ value) indicated that such stress periods could be avoided if the plants were able to utilize available soil water below a depth of 1 m.

The results also indicate that increasing soil water storage capacity can be an adequate adaption strategy to mitigate climate change effects in the investigated area. However, the presented simulations only provide some baseline investigations, where a relatively straightforward model approach was adapted to regional conditions and applied. Nevertheless, the developed model involves low amount of input data (precipitation and temperature); therefore it could easily be extended to larger regional scale, which requires a significant lower amount of work for input data' preprocessing for some baseline investigations than more complex models. The use of only two input parameters enables a much easier uncertainty analysis of the applied model as well. Furthermore, it ensures fast impact analysis of climate change on evapotranspiration and soil water storage.

Acknowledgement. The project was supported by EFOP-3.6.2-16-2017-00018 for the University of Sopron project.

REFERENCES

Baumer, O.W., 1992. Predicting unsaturated hydraulic parameters. In: van Genuchten, M.Th., Leij, F.J. (Eds.): Proceedings of the international workshop on Indirect methods for estimating the hydraulic properties of unsaturated soils. Riverside, California, October 11–13, 1989, 341–354.

Bereitgestellt von University Library Bratislava | Heruntergeladen 31.01.20 12:23 UTC

Calanca, P.L., Roesch, A., Jasper, K., Wild, M., 2006. Global warming and the summertime evapotranspiration regime of the Alpine region. Climatic Change, 79, 65–78.

Canadell, J., Jackson, R.B., Ehleringer, J.B., Mooney, H.A., Sala, O.E., Schulze, E.-D., 1996. Oecologia, 108, 4, 583–595. https://doi.org/10.1007/BF00329030

Christensen, J.H., Christensen, O.B., Lopez, P., Van Meijgaard, E., Botzet, M., 1996. The HIRHAM4 regional atmospheric climate model, DMI Technical Report 96-4. Available from DMI, Lyngbyvej 100, Copenhagen Ø.

Dingman, L.S., 2002. Physical Hydrology. Prentice-Hall, New Jersey, USA, 646 p.

Dobor, L., Barcza, Z., Hlásny, T., Havasi, Á., 2013. Creation of the FORESEE database to support climate change related impact studies. International Scientific Conference for PhD Students.

Eitzinger, J., Štastná, M., Žalud, Z., Dubrovsky, M., 2003. A simulation study of the effect of soil water balance and water stress on winter wheat production under different climate change scenarios. Agricultural Water Management, 61, 195–217.

Eitzinger, J., Thaler, S., Schmid, E., Strauss, F., Ferrise, R., Moriondo, M., Bindi, M., Palosuo, T., Rötter, R., Kersebaum, K.C., Olesen, J.E., Patil, R.H., Şaylan, L., Çaldağ Çaylak, O., 2013. Sensitivities of crop models to extreme weather conditions during flowering period demonstrated for maize and winter wheat in Austria. The Journal of Agricultural Science, 151, 6, 813–835. DOI: 10.1017/S0021859612000779.

Götz, B., Hadatsch, S., Kratochvil, R., Vabitsch, A., Freyer, B., 2000. Biologische Landwirtschaft im Marchfeld. Potenziale zur Entlastung des Natur- und Landschaftshaushaltes. Umweltbundesamt GmbH, Vienna.

Gray, S.B., Bradya, S.M., 2016. Plant developmental responses to climate change. Developmental Biology, 419, 64–77. https://doi.org/10.1016/j.ydbio.2016.07.023

Hamon, W.R., 1964. Computation of direct runoff amounts from storm rainfall. Intl. Assoc. Scientific Hydrol. Publ., 63, 52–62.

Herceg, A., Kalicz, P., Kisfaludi, B., Gribovszki, Z., 2016. A monthly-step water balance model to evaluate the hydrological effects of climate change on a regional scale for irrigation design. Slovak Journal of Civil Engineering, 24, 4, 27–35. DOI: 10.1515/sjce-2016-0019.

Heinrich, G., Gobiet, A., 2012. The future of dry and wet spells in Europe: A comprehensive study based on the ENSEMBLES regional climate models. Int. J. Climatol., 32, 1951–1970.

IPCC, 2007. Climate change 2007. Impacts, adaptation and vulnerability. In: Parry, M.L., Canziani, O.F., Palutikof, J.P., van der Linden, P.J., Hanson, C.E., (Eds.): Contribution of Working Group II to the Fourth Assessment Report of the Intergovernmental Panel on Climate Change. Cambridge University Press, Cambridge, UK and New York, NY, USA, 976 p.

IPCC, 2014. Climate Change 2014. Synthesis Report. Contribution of Working Groups I, II and III to the Fifth Assessment Report of the Intergovernmental Panel on Climate Change [Core Writing Team, Pachauri R.K., Meyer L.A. (Eds.)]. IPCC, Geneva, Switzerland, 151 p.

Jacob, D., 2001. A note to the simulation of the annual and inter-annual variability of the water budget over the Baltic Sea drainage basin. Meteorol. Atmos. Phys., 77, 61–73.

Jones, C.G., Ullerstig, A., Willen, U., Hansson, U., 2004. The Rossby Centre regional atmospheric climate model (RCA). Part I: model climatology and performance characteristics for present climate over Europe. Ambio, 33, 4–5, 199–210.

Jungvist, G., Oni, S.K., Teutschbein, C., Futter, M.N., 2014. Effect of climate change on soil temperature in Swedish boreal forests. PLoS One, 9, 4, e93957. https://doi.org/10.1371/journal.pone.0093957

Keables, M.J., Mehta, S., 2010. A soil water climatology for Kansas. Great Plains Research, 20, 2, 229–248.

Lenderink, G., Buishand, A., Van Deursen, W., 2007. Estimates of future discharges of the river Rhine using two scenario methodologies: direct versus delta approach. Hydrol. Earth Syst. Sci., 11, 1145–1159. DOI: 10.5194/hess-11-1145-2007.

van der Linden, P., Mitchell, J.F.B. (Eds.), 2009. ENSEMBLES: Climate Change and its Impacts: Summary of research and results from the ENSEMBLES project. Met Office Hadley Centre, FitzRoy Road, Exeter EX1 3PB, UK.

Lutz, J.A., Wagtendonk, J.W., Franklin, J.F., 2010. Climatic water deficit, tree species ranges, and climate change in Yosemite National Park. Journal of Biogeography, 37, 936–950.

Mohammed, R.K., Mamoru, I., Motoyoshi, I., 2012. Modeling of seasonal water balance for crop production in Bangladesh with implications for future projection. Ital. J. Agron., 7, 2, 146–153.

Muggeo, V.M.R., 2008. Segmented: An R package to fit regression models with broken-line relationships. R News, The Newsletter of the R Project, 8, 1, 20–25.

Nachtnebel, H.P, Dokulil, M., Kuhn, M., Loiskandl, W., Sailer, R., Schöner, W., 2014. Influence of climate change on the hydrosphere. In: Austrian Panel on Climate Change (APCC) Austrian Assessment Report Climate Change 2014 (AAR14). Austrian Academy of Sciences Press, Vienna, pp. 411–466.

Neuwirth, F., Mottl, W., 1983. Errichtung einer Lysimeteranlage an der agrar-meteorologischen Station in Groß-Enzersdorf. Wetter und Leben, 35, 48–53.

Nolz, R., Kammerer, G., Cepuder, P., 2013a. Interpretation of lysimeter weighing data affected by wind. J. Plant Nutr. Soil Sci., 176, 200–208.

Nolz, R., Kammerer, G., Cepuder, P., 2013b. Improving interpretation of lysimeter weighing data. Die Bodenkultur: Journal for Land Management, Food and Environment 64, 27–35.

Nolz, R., Cepuder, P., Kammerer, G., 2014. Determining soil water-balance components using an irrigated grass lysimeter in NE Austria. J. Plant Nutr. Soil Sci., 177, 237–244.

Nolz, R., Cepuder, P., Eitzinger, J., 2016. Comparison of lysimeter based and calculated ASCE reference evapotranspiration in a sub-humid climate. Theor. Appl. Climatol., 124, 1, 315–324.

Rao, L.Y., Sun, G., Ford, C.R., Vose, J.M., 2011. Modeling potential evapotranspiration of two forested watershed in the southern appalachians. Trans. ASABE, 54, 6, 2067–2078.

R Core Team, 2012. R: A language and environment for statistical computing. R Foundation for Statistical Computing, Vienna, Austria. http://www.R-project.org/.

Remrová, M., Číslerová, M., 2010. Analysis of climate change effects on evapotranspiration in the watershed Uhlířská in the Jizera mountains. Soil & Water Research, 5, 1, 28–38.

Strauss, F., Schmid, E., Moltchanova, E., Formayer, H., Wang, X., 2012. Modeling climate change and biophysical impacts of crop production in the Austrian Marchfeld Region. Climate Change, 111, 641. https://doi.org/10.1007/s10584-011-0171-0

Sun, G.K., Alstad, J., Chen, S., Chen, C.R., Ford, G., Lin, C., Liu, N., Lu, S.G., McNulty, H., Miao, A., Noormets, J.M., Vose, B., Wilske, M., Zeppel, Y., Zhang, Z., 2010. A general projective model for estimating monthly ecosystem evapotranspiration. Ecohydrol., 4, 2, 245–255.

Thaler, S., Eitzinger, J., Trnka, M., Dubrovsky, M., 2012. Impacts of climate change and alternative adaptation options on winter wheat yield and water productivity in a dry climate in Central Europe. The Journal of Agricultural Science, 150, 5, 537–555. DOI: 10.1017/S0021859612000093.

Thornthwaite, C.W., Mather, J.R., 1955. The Water Balance. Drexel Institute of Technology, Climatological Laboratory Publication 8. Philadelphia, USA.

Zamfir, R.H.C., 2014. The impact of climate changes on water balance from western Romania using computer tools. In: Niola, V. (Ed.): Recent Advances in Energy, Environment, Biology and Ecology. World Scientific and Engineering Academy and Society. ISBN: 978-960-474-358-2.

Zheng, D., Hunt, E.R., Running, S.W., 1993. A daily soil temperature model based on air temperature and precipitation for continental applications. Clim. Res., 2, 183–191. DOI: 10.3354/cr002183.

Received 17 May 2018
Accepted 18 March 2019

Bereitgestellt von University Library Bratislava | Heruntergeladen 31.01.20 12:23 UTC